Ureasil Architectures for Organic-Inorganic Photoactive Hybrid Materials

Ilaria Meazzini, M.Sc.

A thesis submitted to the University of Dublin, Trinity College
for the degree of Doctor of Philosophy

Under the supervision of Dr. Rachel C. Evans

School of Chemistry
Trinity College Dublin

October 2017

Declaration

I declare that this thesis has not been submitted as an exercise for a degree at this or any other university and it is entirely my own work, except where otherwise cited, referenced, acknowledged or accredited.

I agree to deposit this thesis in the University's open access institutional repository or allow the Library to do so on my behalf, subject to Irish Copyright Legislation and Trinity College Library conditions of use and acknowledgement.

.....

Ilaria Meazzini M.Sc.

Acknowledgments

There is not enough space in this page to list all the people that contributed to make this past 4 years an incredible professional and personal experience. So in my effort to thank you all, please forgive me if I forget to mention your name. None of this work would have been possible without my supervisor: Dr. Rachel Evans, whose contagious passion and enthusiasm, guided me through my entire PhD. Thanks for the endless patience and for being an amazing mentor, boss and friend.

I would also like to thank the present members of the Evans' group in Dublin. The past year has been a rollercoaster, thank you for listening to my morning rants and providing me with great music (Steve), quiet judgement on my poor sleeping routine (Elaine), cream crackers (Barry) and a smile (Camille). You made the long days of writing go faster. A special mention goes also to the past members of the Evans' group: Judith, Niamh and Adam, who made me feel welcome to this new "extended" family from the very first day.

I am extremely grateful to the entire administrative and technical staff at the School of Chemistry, in particular Dr Manuel Ruether, Dr John O'Brien and Dr Brendan Twamley, who helped me immensely during my time in Trinity.

I was also lucky enough to share this adventure with great people, Viola, thank you for being an amazing friend, I will never forget our weekends together in TBSI, Luca and Ale, thanks for saving me a spot in your couch every time I come back to Dublin or I am just too lazy to go home to bed.

I would have never been able to go this far without the friendship and support of my amazing volleyball team, in no particular order: Jen, Mamen, Ruth, Stacey, Jenny, Esther, Steph, Fenna, Katie, Heyley, Pal. You have been like a second family away from home, keep going savage girls!

And to all my friends in Italy, thank you for making me feel as if I never left every time I come back. Last but not least a special acknowledgment goes to my family, who keeps growing year after year. In particular to my parents, Elena and Stefano, who always encouraged me to push myself, even when that meant moving away from home (I am starting to think that you did not really like having me around) and to my sisters, Sara and Angela, with whom I ll always have the worst fights and the best laughter. I could not have done this without you guys!

Abstract

Ureasils are Class II organic-inorganic hybrids consisting of poly(oxyalkylene) chains covalently linked to a siliceous network *via* urea bridges. Ureasil monoliths are photoluminescent, waveguiding and photo- and thermally stable and have been used as hosts for emissive species such as lanthanides, organic dyes and conjugated polymers (CPs). CPs and conjugated organic dyes in particular, are promising materials for flexible lightweight devices such as organic light-emitting diodes and luminescent solar concentrators (LSCs). However, their solid-state morphology can significantly influence their optoelectronic properties, leading to the need for sophisticated design methodologies when trying and incorporate them into devices.

To meet this challenge, this work begins with an investigation of different incorporation strategies for π-conjugated fluorophores into ureasils. Firstly, a siloxane-functionalised poly(fluorene) (PF) (**Chapter 3**) and a perylene dicarboxdiimide (PDI) (**Chapter 4**) were covalently grafted via co-condensation to the ureasil siliceous backbone, to achieve their selective localisation within the ureasil matrix. The degree of branching and the molecular weight of the poly(oxyalkylene) backbone were also probed. In both cases, covalent grafting influenced the optical properties of the resultant material; in PF-ureasils, it results in controlled packing of the PF chains, which promotes the formation of the π-stacked β-phase, typical for PFs, which has been linked to enhanced optoelectronic properties. For PDI dyes, covalent-grafting inhibits aggregation and minimises re-absorption losses in PDI-ureasils. Moreover, the ureasil behaves as a donor for energy transfer (ET) to the PDI, enabling tuning of the emission colour.

In **Chapter 5**, a poly(fluorene-*alt*-phenylene) (PBS-PFP) copolymer containing on-chain PDI units was physically dispersed in ureasil matrices. The possibility of ET between the ureasil and/or the PBS-PFP donors to the PDI acceptor was investigated. Lifetime measurements showed that good spectral overlap, combined with efficient electronic coupling results in excitation ET from the ureasil to the PBS-PFP units. This process however, inhibits subsequent ET to the PDI chromophore, but leads to high photoluminescence quantum yields (>50%). Due to the low on chain PDI/PBS-PFP ratio, the performance of the system as an LSC is mediocre, but can be boosted by further doping with PDI using a model system. These results demonstrate that the use of an active waveguide host is a promising step towards design of next generation LSCs.

Finally, in **Chapter 6**, a new ureasil architecture is presented, through the development of hybrid nanoparticles (NPs) consisting of a ureasil core and a silica shell. Upon optimisation of the synthesis, NPs with size of ~200 nm and a polydispersity index of ~0.2, were obtained and remained stable for over 50 days. Incorporation of organic fluorophores within the NPs was investigated by: (i) a non-covalent approach, where dyes are encapsulated in the NPs and (ii) a covalent approach, where the dye is covalently grafted the NPs siliceous backbone.

These examples demonstrate that the simplicity and the versatility of the sol-gel process offer a wide range of possibilities for targeted design of fluorophore-integrated ureasil hybrids. This platform enables us to obtain a variety of hybrid architectures capable of incorporating both CPs and organic dyes, with the possibility of targeting some optoelectronic properties and/or to improve their photo- and their thermal stability, for application in both solid-state emitting devices and dye-doped NPs for imaging.

Table of Content

Abbreviations

AFM – atomic force microscopy

AIE – aggregation induced emission

APTES – (3-aminopropyl)triethoxysilane

C153 – coumarin 153

$CDCl_3$ – deuterated chorofom

CP –cross polarisation

CPs – conjugated polymers

CPEs – conjugated polyelectrolytes

DE – direct excitation

DLS – dynamic light scattering

ephen – 5,6-epoxy-5,6-dihydro-[1,10] phenanthroline

ESI – electrospray ionization

ET– energy transfer

EtOH – ethanol

FITC – fluorescein isothiocyanate

F-Na – fluorescein sodium salt

FRET – Förster resonance energy transfer

FTIR – Fourier transform infrared

FWHM – full width at half maximum

GPC – gel permeation chromatography

H_2O – water

HCl – hydrochloric acid

HPLC – high performance liquid chromatography

IC – internal conversion

ICPTES – 3-(triethoxysilyl)propyl isocyanate

IRF – instrument response function

ISC – intersystem crossing

IUPAC – international union of pure and applied chemists

Jeffamine ED-600 - *O,O'*-Bis(2-aminopropyl) polypropylene glycol-*block*-polyethylene glycol-*block*-polypropylene glycol

KBr – potassium bromide

LED – light-emitting diode

L-PLA – L-poly(lactic acid)

LEDs – light emitting diodes

LR305 – lumogen F Red 305

LSCs – luminescent solar concentrators

MALDI – matrix-assisted lased desorption/ionisation

MAS – magic angle spinning

MEH-PPV – poly[2-methoxy-5-(2'-ethylhexyloxy)-1,4-phenylenevinylene]

ND – neutral density

NLLS – non-linear least squared

NMR – nuclear magnetic resonance

NPs – nanoparticles

P3TMAHT – poly[3-(6-triethylammoniumhexyl)thiophene] bromide

PBS-PFP – poly{1,4-phenylene-[9,9-bis(4-phenoxy-butylsulfonate)]fluorene-2,7-diyl}

PBS-PFP-PDI – poly{1,4-phenylene-[9,9-bis(4-phenoxy-butylsulfonate)]fluorene-2,7-diyl} with on-chain perylenediimide

PC – polycarbonate

PdI – polydispersity index

PDI – perylenediimide

PDI-Sil – *N*,*N*-bis(3-triethoxysilylpropyl)-1,6,7,12-tetra-*tert*-butylphenoxyperylene-3,4:9,10-tetra-carboxdiimide

PEG – poly(ethylene) glycol

PEO – polyethylene oxide

PFs – poly(fluorene)

PFO – poly(9,9-di-n-octylfluorenyl-2,7-diyl)

PFO-OH – poly[(9,9- dioctylfluorene)-co-(9,9-bis(8-hydroxyoctyl)fluorene)]

PL – photoluminescence

PLED – polymer light-emitting diode

PMMA – poly methyl methacrylate

ppm – parts per million

PPO – poly(propylene oxide)

PPV – poly(*p*-phenylene vinylene)

PT – polythiopene

PV – photovoltaic

PXRD – powder X-ray diffraction

Py – pyrene

RT – room temperature

RTIL – room temperature ionin liquid

r.u. – repeat unit

SEM – scanning electron microscopy

SiNc – 2,3-naphthalocyanine bis-(trihexylsilyloxide) dye (SiNc)

ss – solid-state

TCSPC – time-correlated single photon

TEOS – tetraethylorthosilicate

THF – tetrahydrofuran

TGA – thermogravimetric analysis

TMS – tetramethylsilane

TMOS – tetramethylorthosilicate

tta – 2-thenoyltrifluoracetonate

UPTES – ureapropyltriethoxysilane

Symbols

A – acceptor

α_i – pre-exponential factor

c – degree of condensation of the siliceous network

D – donor

D_h – hydrodynamic diameter

$E(t)$ – excitation pulse

ε^0 – static dielectric permittivity

ε_A – molar absorption coefficient of acceptor

F_D – intensity of the donor emission spectrum

fi – fractional contribution for the i^{th} component of a fluorophore

f_{ic} – calculated fitted model

G – anisotropy factor

h – Planck's constant

I – intensity

$I_{ex,em}$ – emission intensity of the vertically or horizontally aligned excitation and emission polarisers

J_{DA} – spectral overlap

k – orientation factor

K_α – association constant for the formation of a non-emissive complex

k_b – Boltzmann constant

k_{nr} – non-radiative rate constant

k_Q – bimolecular quenching constant

k_{rad} – radiative rate constant

K_{SV} – Stern-Volmer quenching constant

l – orbital angular momentum

L – coherence length

λ_{em} – emission wavelength

λ_{ex} – excitation wavelength

M^* – excited-state species

$M_{n,m}$ – electric dipole moment characteristic of the transition between the n^{th} and m^{th} states

M_n – number-average molecular weight

M_w – weight-average molecular weight

n – refractive index

N_A – Avogadro's number

$n(t)$ – number of florophore units in the excited state at time t

η_{opt} – optical conversion efficiency

m/z – mass to charge ratio

$\hat{\mu}$ – dipole moment operator

p – number of floating parameters

Φ_D – donor photoluminescence quantum yield

Φ_{obs} – observed photoluminescence quantum yield

Φ_{PL} – photoluminescence quantum yield

Ψ_i – wavefunction corresponding to the i^{th} excited state

$<r>$ – fluorescence anisotropy factor

r – internuclear distance

R_0 – Förster distance

R_h – hydrodynamic radius

S – total spin angular momentum

σ_i – standard deviation

s_i – spin angular momentum

S_n – the n^{th} singlet excited state

t – time

$<\tau>$ – average fluorescent lifetime

τ_i – characteristic lifetime for the i^{th} component of a fluorophore

τ_{obs} – measured lifetime of an excited state

T_n – the n^{th} triplet excited state

v – vibrational level

χ^2 – chi squared statistic

y_i – measured data value

Chapter One

Introduction

1.1 Π-Conjugated Organic Fluorophores

During the past 30 years, the fluorescence phenomenon has become an essential research tool. The applicability and sensitivity of fluorescent molecules (*fluorophores* or more generally, *lumophores*), have driven much interest from the scientific community on the investigation and manipulation of the optoelectronic behaviour of these species. Particular attention has been focussed on π-conjugated fluorophores; a family of organic materials presenting a conjugated system. Following the *International Union of Pure and Applied Chemistry* (IUPAC) definition, a conjugated system is "*a molecular entity whose structure may be represented as a system of alternating single and multiple bonds: e.g. CH_2=CH–CH=CH_2, CH_2=CH–C≡N. In such systems, conjugation is the interaction of one p-orbital with another across an intervening σ-bond in such structures*".[1] When considering organic fluorophores, two main classes of conjugated systems have dominated this field: (i) organic dyes and (ii) conjugated polymers (CPs). Organic dyes are characterised by a small and defined molecular structure.[2] Nowadays, there is an enormous variety of organic dyes available, which can be divided into different classes according to their characteristic structure and/or the nature of the electronic transitions involved in the light-emission process. CPs instead, are characterised by a repetition of molecular units and a molecular weight distribution.[3] They are also known as *organic semiconductors* due to the linear combination of their π-orbitals, which leads to an electronic band structure similar to that of classic semiconductors. Due to their easy processability from solution, their low cost and excellent optoelectronic properties, both CPs and organic dyes have been exploited for a large variety of applications ranging from optical sensors,[4-7] to light-emitting devices.[8-11]

The focus of this work is to carefully design and characterise different novel architectures of organic-inorganic hybrid materials incorporating π-conjugated fluorophores. The first part of the thesis will be dedicated to the investigation of different incorporation strategies for organic dyes and CPs into photoactive host hybrids for application as luminescent solar concentrators (LSCs). In the second part, the same host molecules will be used for the preparation of dye-encapsulated nanoparticles (NPs) for potential application in the field of imaging.

1.1.1 Conjugated Polymers

The first record of conductivity in polymeric chains is attributed to Heeger, Shirakawa and MacDiarmid in 1977.[12, 13] The authors prepared thin films of crystalline polyacetylene (**Fig. 1.1**a) and observed a dramatic increase in their conductivity upon exposure to iodine vapours, reaching values comparable to that of metals. This discovery, for which the authors were jointly awarded the Nobel prize in Chemistry in 2000,[14] opened up an entirely new research field which linked chemistry and condensed-matter physics, introducing a new class of materials that offer the electrical and optical properties of metals, combined with the mechanical properties and processability of polymers.[15] The backbone of a CP consists of a linear combination of π-orbitals, which give rise to a band structure similar to that of a semiconductor. When excited, an electron will move from the highest occupied band (π band) to the lowest unoccupied band (π* band), leaving a "hole" in the valence band and forming a weakly bound *exciton* pair. The recombination of the electron and the hole and subsequent relaxation results in the emission of a photon of light,[16] with the energy of the photon determined by the bandgap between the valence and conduction bands of the CP. The optoelectronic properties of CPs are thus dominated by the chemical structure of their monomer repeat units and by the extent of the conjugation of their chains.

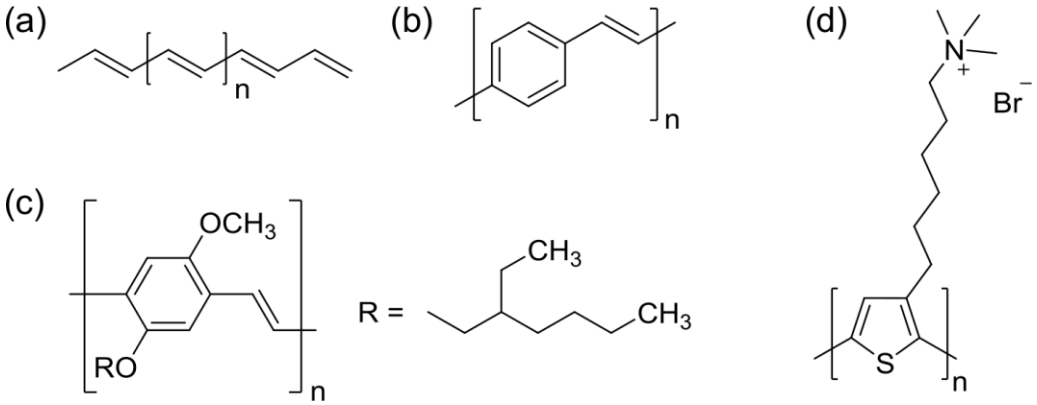

Figure 1.1. Examples of CPs and a CPE. Chemicals structures of: (a) polyacetylene, (b) PPV, (c) MEH-PPV and (d) P3TMAHT.

Since 1977, CPs have been used in a wide variety of applications, ranging from polymer light-emitting devices (PLEDs),[17-21] photovoltaic devices,[22] and transistors.[23] The very first application of a CP in a device was reported by the group of Prof. Richard Friend, where a poly(*p*-phenylene vinylene) (PPV) film was used as the emissive component for a green-yellow PLED

(**Fig. 1.1**b).[18] However, despite the great potential, strong interchain interactions between the CP backbones greatly reduced the performance of the final device. This issue, which was mainly due to the poor solubility of the CP in the solvents used to deposit the film, was a common challenge encountered for the early-stage applications of conjugated polymers in devices and urged the scientific community to push towards novel synthetic designs in order to improve the solubility of CPs in common solvents. A breakthrough into the application of CPs in PLEDs occurred in 1991, when Heeger and co-workers proposed a modified structure of PPV, namely poly[2-methoxy-5-(2'-ethylhexyloxy)-1,4-phenylenevinylene] or MEH-PPV (**Fig. 1.1**c), which presented a slightly red-shifted emission compared to PPV, but with a dialkoxy side-chain which made the final CP soluble in organic solvents.[24]

The solubility of CPs in a more diverse range of solvents was pushed even further when charged moieties were introduced onto the side-chains of the CP backbone.[25] The resulting materials, known as conjugated polyelectrolytes (CPEs), are a sub-class of CPs, which contain pendant charged units.[25] An example of a common CPE, poly[3-(6-(trimethylammoniumhexyl)thiophene] bromide (P3TMAHT) is shown in **Fig. 1.1**d. CPEs can be solubilised in polar solvents, including water, while maintaining the characteristic optoelectronic behaviour of the corresponding CP,[26] introducing an interesting prospective for applications for sensing in biological media.[27, 28] The combination of the organic conjugated backbone and the hydrophilic side chains leads CPEs to be intrinsically amphiphilic and gives them the possibility to self-assemble in solution[29, 30] and to coordinate with oppositely-charged surfactants.[31, 32]

1.2 Photoluminescence of π-Conjugated Fluorophores

1.2.1 Formation of Excited States

The phenomenon of photoluminescence refers to the emission of light from any substance presenting an electronically-excited state.[33] The excitation of the molecule occurs when an excitation source, *i.e.* a photon, of appropriate energy promotes an electron from a bonding orbital (σ, π) to an anti-bonding orbital (σ^*, π^*). Molecules containing heteroatoms, such as nitrogen or oxygen, also present non-bonding (*n*) orbitals from which electrons can be promoted to one of the aforementioned anti-bonding orbitals. The energy of these transitions corresponds to the difference

between the energy levels involved. For organic molecules, the most relevant transitions are $n \rightarrow \pi^*$ and $\pi \rightarrow \pi^*$, while the $\sigma \rightarrow \pi^*$ and $\sigma \rightarrow \sigma^*$ transitions are usually too high in energy.[34] For extended conjugated systems, such as those considered in this work, the overlap of the π-orbitals results in delocalisation of the electrons across the conjugated backbone. In particular, the energy of the low-lying $\pi \rightarrow \pi^*$ transition is a function of the extent of the delocalisation of the electrons and decreases with increasing delocalisation, leading to longer absorption wavelengths corresponding to this transition.

1.2.2 Nomenclature of Electronic States

Electronic states can be described as a function of their electronic arrangement and the combination of spin and the orbital angular moment.[35] The *multiplicity* of an electronic state is represented by $(2S+1)$, where S is the quantum number representing the total electron spin angular momentum ($S = \sum s_i$, where $s_i = +½$ or $-½$). Electrons belonging to the same molecular orbital have opposite spins; when one of them is promoted to a higher energy orbital, its spin remains in principle the same and both the ground and excited-state are called *singlet* states (S_n). The spin multiplicity for a ground or singlet state is 1 as $S = 0$. In contrast, if the electron in the excited state has a spin parallel to the electron in the ground state, then this is called a *triplet* state (T_n) and it is characterised by a multiplicity of 3 ($S = 1$).[36] A schematic representation of the electronic state energy and electron spins corresponding to a ground singlet state and excited singlet and triplet states is shown in **Fig. 1.2**.

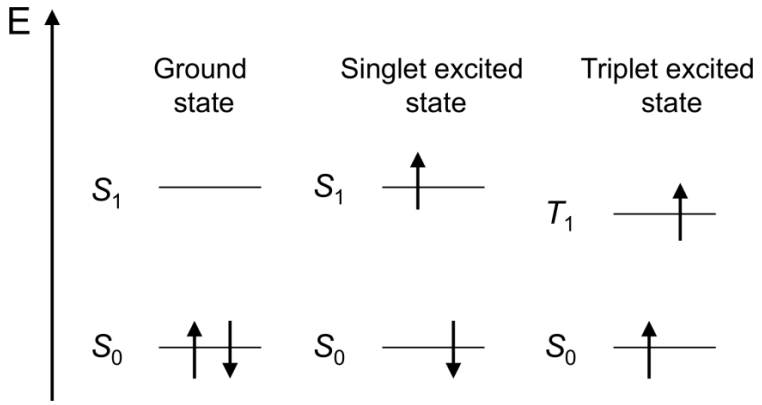

Figure 1.2. Schematic diagram representing the electron spins and energy levels characterising a ground singlet state and excited singlet and triplet states.

1.2.3 Selection Rules

The absorption of electromagnetic radiations depends on two factors: (i) the energy of the incident photon, which needs to at least match the difference in energy between the ground and the excited electronic state involved in the process and (ii) the coupling mechanism between the incident electromagnetic radiation and the dipoles of the considered system.[37] The "allowedness" of an electronic transition can be calculated from the transition dipole moment, M_{12}, which represents the electric dipole moment characteristic of the transition between the two states and is expressed by the following equation:

$$M_{12} = \int \Psi_1 \hat{\mu} \Psi_2 d\tau \qquad (\mathbf{1.1})$$

where Ψ_1 and Ψ_2 are the wavefunctions corresponding to the ground (1) and excited (2) states, $\hat{\mu}$ is the dipole moment operator, a complex vector which includes the phase factors associated with the two electronic states and represents the effect of the interaction of the electromagnetic radiation on the coupling process of the two states and the integral is calculated across the space ($d\tau$). The transition probability for the absorption process is given by $|M_{12}|^2$. This probability increases with the increase in the vector magnitude and can be equal to zero when no overlap between the wavefunctions is observed. Considering **Eqn. 1.1**, a transition is allowed when Ψ_1 and Ψ_2 overlap in space while the combination of their symmetry properties with those of the dipole operator results in an integral whose value is non-zero. Selection rules have been extrapolated from the cases where the integral is equal to zero. In the case of polyatomic organic molecules, there are two fundamental selection rules that regulate the excitation and relaxation of electronic states, describing the probability of an electronic transition:

(i) *Symmetry forbidden transitions*: For polyatomic species such as organic dyes or CPs, an electronic transition can be forbidden for symmetry reasons, *i.e.* when the electronic wavefunctions corresponding to the two states have the same parity. This rule represents an extension of the Laporte selection rule which, for a single atom, states that *s*→*s* transitions are forbidden while *s*→*p* transitions are allowed ($\Delta l = \pm 1$, where l is the orbital angular momentum quantum number). For large molecules such as CPs, the symmetry of the overall system can be associated with that of specific point groups,[38] but discussion of this is beyond the scope of this

work. Moreover, this rule applies only for completely rigid systems, as vibrations can disturb/distort the system to the point of allowing a formally forbidden transition. Such transitions will present a weaker oscillator strength and, therefore, weaker absorption and emission.

(ii) *Spin selection rule*: A transition between states presenting different multiplicities is forbidden as there can be no change in the angular momentum for transitions between "pure" states.[37] This means that transitions between singlet and triplet states are formally forbidden ($\Delta S = 0$). However, *spin-orbit coupling* between states can lead to a singlet (or triplet) wavefunction to contain a small fraction of a triplet (or singlet) wavefunction, which breaks down this selection rule and allows transitions between states of different multiplicity to some extent.

1.2.4 Optical Transitions and the Franck-Condon Principle

The difference in the mass of an electron compared to that of a nucleus allows us to consider the vibrational and rotational motion energy of the latter separate from that of an electron.[39] This enables us to describe the energy of a molecule as a sum of the contribution of rotational, vibrational and electronic energy contributions (*Born-Oppenheimer approximation*). The process of light absorption takes place on a timescale of the order of 10^{-15} s, while molecular vibrations take place between 10^{-10} to 10^{-12} s. Since nuclei are heavier than electrons, an electronic transition is therefore more likely to happen without changes in the position of the nuclei (*Franck-Condon Principle*). Therefore, the potential energy corresponding to an electronic transition can be represented by a vertical line connecting the ground and the excited states, which consist of a series of vibrational wavefunctions (**Fig. 1.3**). The amplitude of these functions is directly proportional to the probability of finding the nuclei at a specific internuclear distance, *r*. Following the Boltzmann distribution, the vast majority of the molecules will be located in the ground state at room temperature. A transition between the initial and final state will be most probable where the vibrational wavefunctions show the greatest overlap in each state (**Fig. 1.3**a). For example, in **Fig. 1.3**b, the transition from the vibrational level (v) 0 (S_0) to $v = 3$ (S_1) is the most probable. The intensity of the vibronic transition is a function of the square of the overlap integral between the

vibrational wavefunctions involved in the transition and decreases as the overlap decreases. The wavefunctions for the ground and excited states are comprised of both nuclear and vibronic components. The transition dipole moment is partly determined by the overlap of the nuclear (vibrational) wavefunctions, known as the *Franck-Condon factor*.

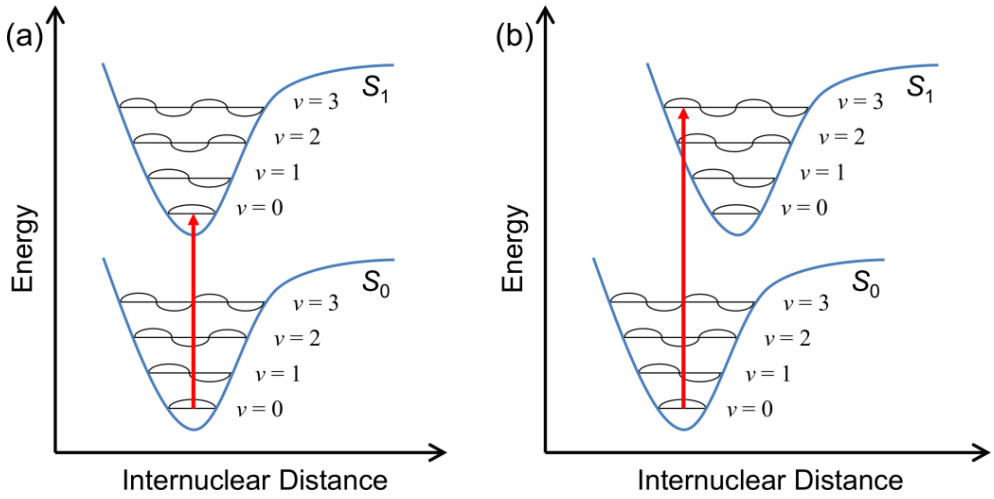

Figure 1.3. Potential energy diagrams showing the basis of the Franck-Condon principle. The vertical red arrows represent the most probable transitions for (a) the same or (b) different nuclear geometries.

The Franck-Condon principle can be used to predict the relative probabilities of the occurrence of different vibronic transitions. When numerous transitions take place over a range of energies (*i.e.* for larger molecules), the transitions merge to yield an absorption spectrum whose shape is determined by the relative intensities of each transition. For rigid aromatic systems, the individual vibrational transitions can be resolved in the absorption spectrum and the intensity of these bands is determined by the energy gap between the vibrational levels combined with the Franck-Condon factor. However, it should be noted that most fluorescent species exhibit broad or structureless absorption bands as a consequence of: (i) *homogeneous broadening*, which arises from the presence of a series of continuous sets of vibrational levels within each electronic state and (ii) *inhomogeneous broadening*, which is due to the dynamic motion of the solvent layer surrounding the molecule, which can cause changes in the local electric field and a minor re-distribution of the energies of the electronic transitions. These effects are also observed on the corresponding emission spectra of the system.

1.2.5 Deactivation of Excited States

Once a molecule is excited to a higher energy state, it relaxes back to the ground-state through a combination of radiative and non-radiative processes. A representation of the transitions and the processes involved upon the absorption of energy from a photon and subsequent deactivation pathways of the formed excited states is offered by the Jablonski diagram (**Fig. 1.4**).[40]

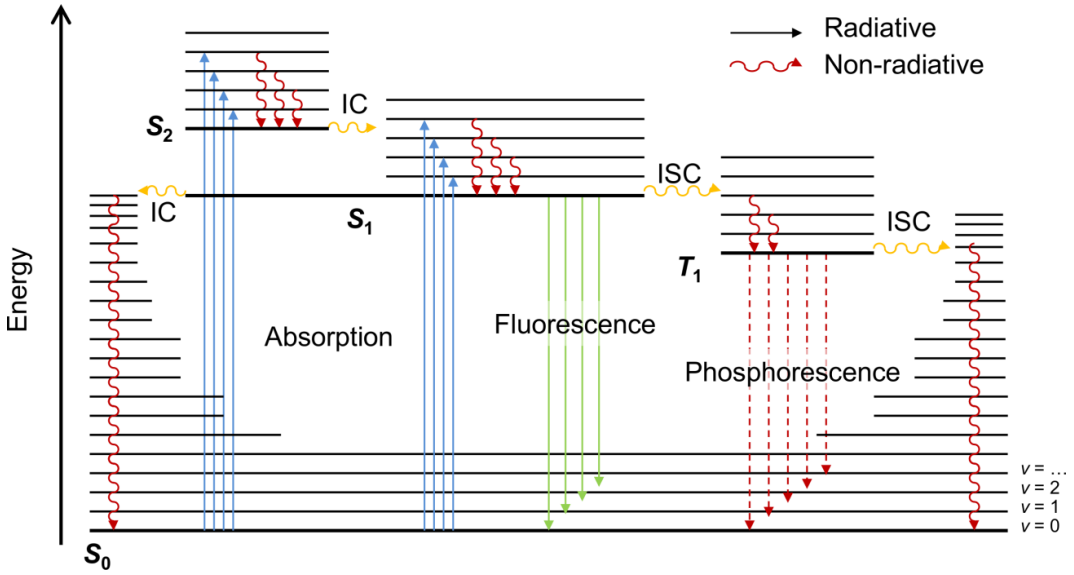

Figure 1.4. Jablonski diagram showing the processes of absorption, fluorescence, phosphorescence, internal conversion (IC) and intersystem crossing (ISC). The radiative transitions are represented by straight arrows and the non-radiative transitions are represented by red and yellow curved arrows.

Internal conversion (IC) is a non-radiative transition between electronic states of the same multiplicity. This process is normally followed by vibrational relaxation to the lowest vibrational level of the new electronic state. It is worth to note however, that vibrational relaxations can occur also before IC. For a molecule in solution, this excess energy is quickly dissipated through collisions with the surrounding solvent molecules. IC is usually more efficient for electronic energy levels that are closer in energy and although it can occur from S_1 and S_0, its efficiency is going to be much lower than any other S_n to S_{n-1} transitions. This is due to the fact that the overlap between the vibrational wavefunctions of two electronic levels, decreases with the increase of the energetic gap between the two $v = 0$ levels corresponding to the states ("energy gap law").[41] Thus, other deactivation pathways are usually preferred to the S_1 to S_0 internal conversion process.

Radiative transitions taking place in between states of the same multiplicity, *e.g.* S_1 to S_0, are known as *fluorescence*. These transitions are characterised by longer wavelengths (lower

energy) compared to that of the corresponding absorption due to the loss of energy through vibrational relaxation towards the lowest energy vibrational level in the excited state. This phenomenon is a direct consequence of the *Kasha's rule*, which states that emission occurs from the lowest excited state of a molecule, and thus the emission spectra are usually independent of the excitation wavelength. The difference between the absolute maximum of the first absorption band and the maximum of the fluorescence emission band is known as the *Stokes' shift*. Electrons in the excited state will remain in S_1 for a certain time prior to emission or other forms of deactivation. This gives rise to a characteristic lifetime of the excited singlet state, which usually ranges between 10^{-10} and 10^{-7} s.

Another non-radiative relaxation pathway that can occur is *intersystem crossing* (ISC), which is a transition that occurs between isoenergetic vibronic levels in electronic states characterised by different multiplicity, *e.g.* S_1 to T_1. Once the molecule has transitioned to T_1, it further relaxes to $v = 0$ through vibrational relaxation. Although ISC between states with different multiplicity is forbidden, it can occur if spin-orbit coupling is large, with its probability depending on the singlet and triplet states involved. The motion of an electron is known to generate a current and a magnetic field, whose magnitude depends on the nuclear charge.[38] So to greater nuclear charges correspond greater spin-orbit coupling. As such, this forbidden process will present higher rates for molecules containing an atom of high atomic number, an effect known as *heavy atom effect*.

Formally forbidden radiative transitions occurring between states of different multiplicity, *e.g.* T_1 to S_0, are known as *phosphorescence*. As they are forbidden, they are characterised by a low radiative rate constant and therefore alternative relaxation processes such as IC or vibrational relaxation are usually preferred. By reducing these effects, *i.e.* working at a low temperature or in rigid media, phosphorescence can be observed. Interestingly, when there is a small energy gap between S_1 and T_1, a reverse ISC transition from T_1 and S_1 can be observed. The emission resulting from S_1 will be characterised by a much longer decay constant compared to that of regular fluorescence, because the molecule resides in the triplet state before emitting from S_1. This relaxation process is known as *thermally-delayed fluorescence*.

The overall process of absorption of a photon and subsequent emission of light through any of the aforementioned radiative processes is known as *photoluminescence*. However, since the emission of light displayed by the fluorophores described in this work arises only from fluorescence, the terms photoluminescence and fluorescence will be used interchangeably in this thesis.

1.2.6 Excited-State Lifetime

Upon absorption of a photon and transition to a higher energy state, a system will relax back to the ground state. The length of time a system takes to return to the lowest energy state is known as the *excited-state lifetime*. Consider a dilute solution of fluorescent species *M*, characterised by a concentration of [*M*]. Upon excitation of this fluorophore with an infinitely sharp (δ-function) pulse of light, some of these molecules are brought into the excited state S_1, which will subsequently relax down to the ground state, either radiatively or non-radiatively. The rate of disappearance of the excited species (*M**) from the excited state is given by:[42]

$$-\frac{d[M^*]}{dt} = (k_{rad} + k_{nr})[M^*] \quad \textbf{(1.2)}$$

where k_{rad} is the radiative rate constant and k_{nr} is the non-radiative rate constant, which is defined as the sum of the rate constants for all non-radiative processes. Considering that [*M**] is the time-dependent concentration of *M* in the excited-state and that $[M^*]_0$ is the concentration of excited species at time $t = 0$ after the excitation pulse, **Eqn. 1.3** can be integrated over time, giving:

$$[M^*] = [M^*]_0 \exp(-\frac{t}{\tau_{obs}}) \quad \textbf{(1.3)}$$

where τ_{obs} is the measured lifetime of the excited state S_1, and can be defined as:

$$\tau_{obs} = \frac{1}{k_{rad} + k_{nr}} \quad \textbf{(1.4)}$$

The photoluminescence quantum yield (Φ_{PL}) is the ratio of photons emitted to the number of photons absorbed and is related to the excited state lifetime through the following equation:[43]

$$\Phi_{PL} = \frac{k_{rad}}{k_{rad} + k_{nr}} = \tau_{obs}\, k_{rad} \quad \textbf{(1.5)}$$

1.2.7 Quenching of Photoluminescence

The term quenching refers to any process that decreases the photoluminescence intensity of a species. The deactivation pathways described in **Section 1.2.5** are intrinsic for each excited molecule. Quenching is typically the consequence of an intermolecular relaxation process that occurs in the presence of a second species known as the *quencher*. Quenching competes with the intrinsic radiative decay processes, providing a further non-radiative relaxation mechanism. As a result, the emission intensity, the excited-state lifetime or the Φ_{PL} might be affected. For bimolecular processes there are two possible modes of quenching, *static* and *dynamic*,[43] which are represented schematically in **Fig. 1.5**.

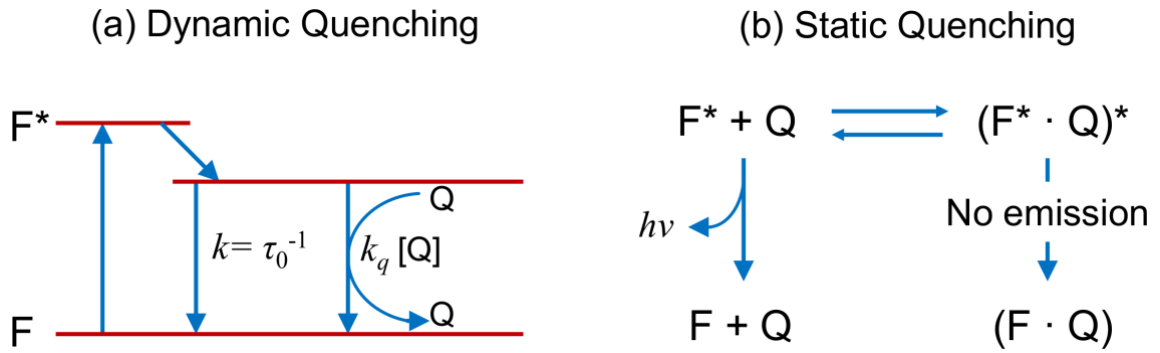

Figure 1.5. Schematic representation of bimolecular quenching modes. Deactivation of a fluorophore in the excited state by a quencher species can occur *via* (a) dynamic or (b) static modes. F is the ground-state fluorophore, F* is the fluorophore in the excited state, Q is the quencher, k is the rate constant for the deactivation of the excited state and k_q is the bimolecular quenching rate constant.

Both modes of quenching require contact between the quencher and the fluorophore in order to occur. For dynamic quenching, the quencher (Q) must diffuse to the fluorophore (F) within the lifetime of the excited state. Upon contact or collision, F will return to the ground state through a non-radiative process. Conversely for static quenching, F and Q form a ground state complex. The dynamic quenching of F can be described using the Stern-Volmer equation:

$$\frac{I_0}{I} = \frac{\tau_0}{\tau} = 1 + K_{SV}\,[Q] \qquad (\mathbf{1.6})$$

where τ_0 and τ represent the lifetime of F in the absence and presence of the quencher, respectively, and I_0 and I are the corresponding fluorescence intensities. K_{SV} is the Stern-Volmer quenching constant given by $k_q\tau_0$, where k_q is the bimolecular quenching constant. For the non-emissive

complex generated in the static quenching process, the quenching of fluorescence is described by the following equation:

$$\frac{I_0}{I} = 1 + K_\alpha [Q] \quad \textbf{(1.7)}$$

where K_α is the association constant for complex formation, given by:

$$K_\alpha = \frac{[F-Q]}{[F][Q]} \quad \textbf{(1.8)}$$

where [F-Q] is the concentration of the complex.

1.2.8 Energy Transfer

Quenching can proceed through a variety of mechanisms involving interactions between a donor (*D*) and an acceptor (*A*). One phenomenon that can manifest itself as quenching is energy transfer (ET). The transfer of excitation energy can occur both through radiative and non-radiative processes. Radiative or trivial ET consists of the emission of a photon from *D* and its subsequent absorption by *A*. This process does not require electronic coupling between the two species, but is a function of the spectral overlap between the emission of *D* and the absorption of *A* and the concentration of the species in the system.

In contrast, non-radiative energy transfer requires both electronic coupling between *D* and *A* and good spectral overlap. A schematic representation of this mechanism is presented in **Fig. 1.6**.

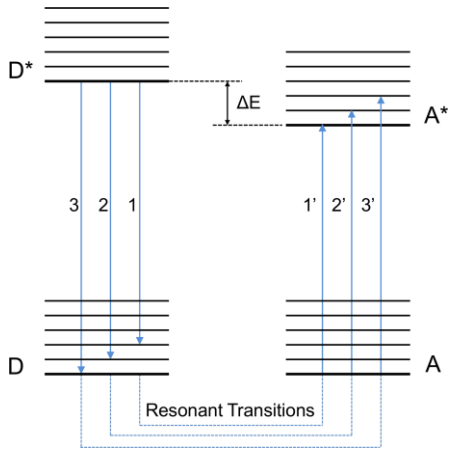

Figure 1.6. Schematic representation of the transitions and relative energetic levels involved in the resonance energy transfer process.

Non-radiative ET can occur following two distinct mechanisms: (i) Förster resonance energy transfer (FRET), a long-range dipole-dipole interaction in which the initially excited electron on *D* returns to the ground state orbital on *D*, while simultaneously an electron on *A* is promoted to the excited state.[44] A *D*-*A* system can undergo FRET when several vibronic transitions in *D* have similar energy to the corresponding transitions in *A*; these coupled transitions are said to be *in resonance* (**Fig. 1.7**a). FRET is a Coulombic interaction, and thus does not require intimate contact between *D* and *A*, but it only operates over a certain distance (≤ 100 Å). (ii) Dexter energy transfer consisting of a short-range exchange interaction in which *D* and *A* exchange an electron between either their singlet or triplet states (**Fig. 1.7**b). In this case, overlap is required between the species, which have to be in intimate contact (< 10 Å).[44] A comparison between the two mechanisms is presented in **Fig. 1.7**.

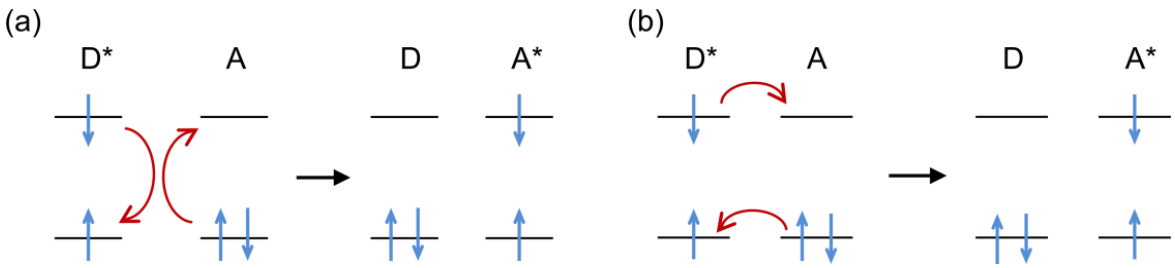

Figure 1.7. Schematic representation of the mechanisms of non-radiative energy transfer. Comparison of an excited state donor (*D**) deactivated by a ground state acceptor (*A*) *via* (a) Förster and (b) Dexter energy transfer.

The efficiency of energy transfer through the FRET mechanism is given by the following equation:

$$E = \frac{R_0^6}{R_0^6 + r^6} \qquad \textbf{(1.9)}$$

where r is the distance between the donor and the acceptor and R_0 is the Förster distance at which the efficiency of the energy transfer, E, is 50%. R_0 is given by:

$$R_0^6 = \frac{9000\ (ln10) k^2 \Phi_D J_{DA}}{128\ \pi^5\ N_A n^4} \qquad \textbf{(1.10)}$$

where k is the orientation factor, which represents the relative orientation of the transition dipoles of the *D* and the *A* and is assumed to be 2/3 for randomly oriented dipoles.[44, 45] Φ_D is the emission quantum yield of the donor, n is the refractive index of medium, N_A is Avogadro's number and J_{DA} is the spectral overlap integral and is given by:

$$J_{DA}(\lambda) = \int_0^\infty F_D(\lambda)\varepsilon_A(\lambda)\lambda^4 d\lambda \quad \textbf{(1.11)}$$

where F_D is the intensity of the donor emission spectrum at wavelength λ to $\lambda + \Delta\lambda$, with the total intensity normalised to unity and ε_A is the molar absorption coefficient of the acceptor at wavelength λ.

1.3 Relationship Between the Morphology and Optical Properties of Organic Fluorophores

The molecular packing or morphology of organic semiconductors can influence their optoelectronic properties.[3, 46] When aiming to design any light-emitting system in the solid state, particular care needs to be taken in understanding the changes of the conformation of the fluorophore upon transfer from solution. Indeed, this process often leads to quenching of the photoluminescence of the final system due to aggregation of discrete molecules and re-absorption phenomena.[47, 48] For conjugated polymers, aggregation in the solid-state is usually accompanied by a red-shift in the maximum of the emission spectrum and a decrease in the Φ_{PL} compared to the CP in a solution of a good solvent.[49, 50] This phenomenon is very common and results from an increase in the conjugation length of the polymer upon aggregation. Interactions between the π-electrons extend the conjugation and stabilise the π-electrons themselves, leading to a decrease in the energy levels of both the valence and conduction bands, and a decrease in the energy gap between S_0 and S_1. Interestingly, for some CPs, alteration of the chain morphology leads to the formation of different phases, each characterised by a specific optical fingerprint. This is the case for poly(fluorene)s (PFs),[51] which are known to exhibit different inter- and intra-molecular conformations as a function of their physical state.[52-54]

For smaller molecules, such as organic dyes, the process of aggregation can lead to similar consequences (shifts of the emission maximum and changes in the Φ_{PL}), however this is usually a

function of the relative orientation of transition dipole moments of the individual molecules.[55] Considering a simple example, aggregation of two dye molecules to form a dimeric species leads to splitting of the excited state energy level into two levels, as shown in **Fig. 1.8**. If the transition dipole moments of the two monomers are parallel, a transition to the upper excited state is most favourable and this leads to a blue-shift in the emission spectrum relative to the discrete molecule. In contrast, for perpendicular dipole moments, the most probable transition is to the lower excited state, leading to a red-shift in the emission spectrum. If the transition dipole moments are arranged in an oblique fashion, the absorption band will be split into two. The same effects are also observed for aggregates consisting of a higher number of monomer units, where a red-shift is indicative of the formation of so-called *J-aggregates*, while a blue-shift is due to the formation of *H-aggregates*.[56] Perylene bisimide dyes, such as those used in this work, are known to form *J-aggregates* in the solid-state;[57, 58] however it is hard to distinguish this process from simple re-absorption as they are both characterised by similar spectroscopic features (red-shift in emission, decrease of the Φ_{PL} and/or changes in the spectral shape).[59, 60] These features are all undesirable for light-emitting devices, which has led to the need for new design approaches to preserve and/or enhance the optical features of the dyes upon transition from the liquid to the solid-state.

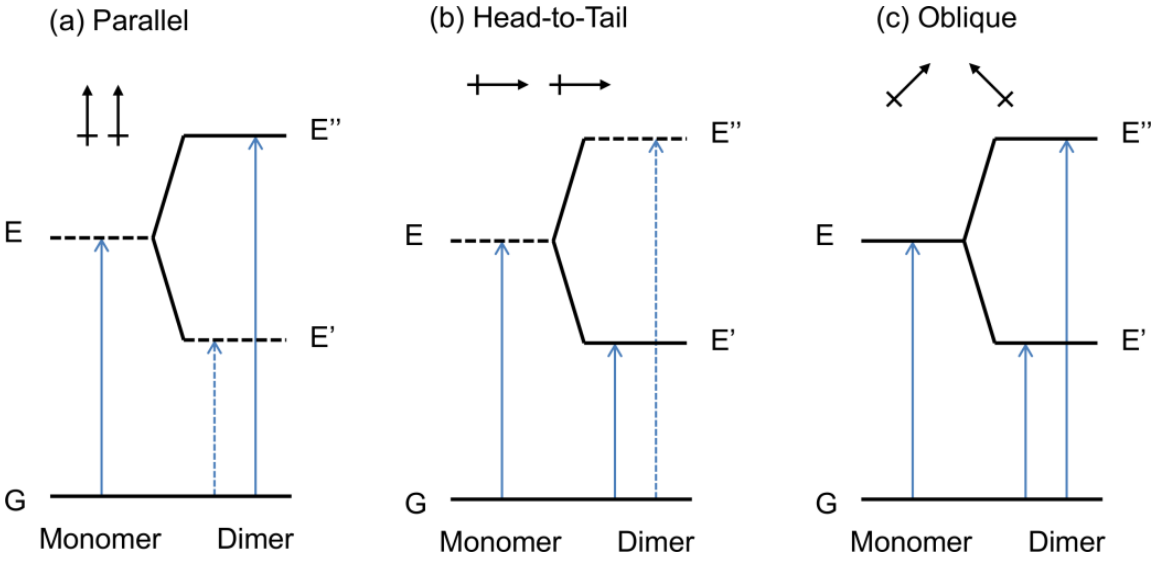

Figure 1.8. Comparison of the electronic state distribution for monomer and dimer species of conjugated organic dyes. Splitting of the energy level for molecular dimers whose dipole moments adopt (a) parallel, (b) head-to-tail and (c) oblique relative orientations. Figure adapted with permission from ref.[56]

1.3.1 Incorporation of π-Conjugated Systems in Host Matrices

Given the attractive optoelectronic properties of both CPs and organic dyes, a lot of interest has been focussed on the application of these materials as active components in light-emitting devices. However, as mentioned in the previous section, control over the solid-state morphology of the optically-active species is necessary in order to tailor their optoelectronic properties. Moreover, the lifetime of any device is dictated by the photo- and thermal stability of the CP or the dye. A proposed strategy for achieving improved stability, while simultaneously manipulating the spectroscopic features of the fluorophore is the encapsulation into a host matrix.[61, 62] The preferred route for the preparation of such materials is usually sol-gel chemistry. However, encapsulation of organic fluorophores in pure inorganic oxides can lead to a phase separation due to the incompatibility of the hydrophobic dopant with the hydrophilic host and the aqueous processing media.[63] To overcome this issue different synthetic strategies have been proposed.[46] For large CP molecules, such as PFs, for example, the targeted formation of the β-phase, was achieved through confinement of poly(9,9-dioctylfluorene) (PFO) chains into the matrix of a host system consisting of a pure inorganic silica precursor (tetraethylorthosilicate, TEOS) condensed around a room temperature ionic liquid (RTIL) template.[64] The RTIL units interact through hydrogen bonding with the free silanol moieties of the silica network, while simultaneously coordinating *via* π-π stacking, with the CP backbone guiding its localisation into hydrophobic domains within the host matrices and promoting formation of the β-phase (**Fig. 1.9**a).

Strategic localisation of CP units into sol-gel hosts can also be mediated by the use of surfactants. Non-ionic surfactants such as Pluronics™ (block-copolymers of ethylene oxide and propylene oxide) are well-known as templating agents for oxide matrices obtained in the sol-gel conditions.[65-67] The group of Frey, in particular, has worked extensively on the encapsulation of CPs into the matrices of mesostructured oxides templated by neutral block copolymers.[68-71] These materials were obtained as films by dip-coating a glass substrate in a solution containing TEOS and the surfactants, in a controlled humidity atmosphere, exploiting the evaporation-induced self-assembly of the Pluronic templates, whose structure is preserved due to the immediate hydrolysis and condensation of the silica network around them. A CP introduced into this mixture will tend to

co-assemble with the surfactant and will be incorporated in the final hybrid avoiding macrophase separation.[69, 72] This study was also extended to titania, where a Pluronic surfactant guided the formation of the cubic phase in which the conjugated polymer MEH-PPV was successfully incorporated (**Fig. 1.9**b). The resultant hybrid material showed improved photostability compared to the pure CP.

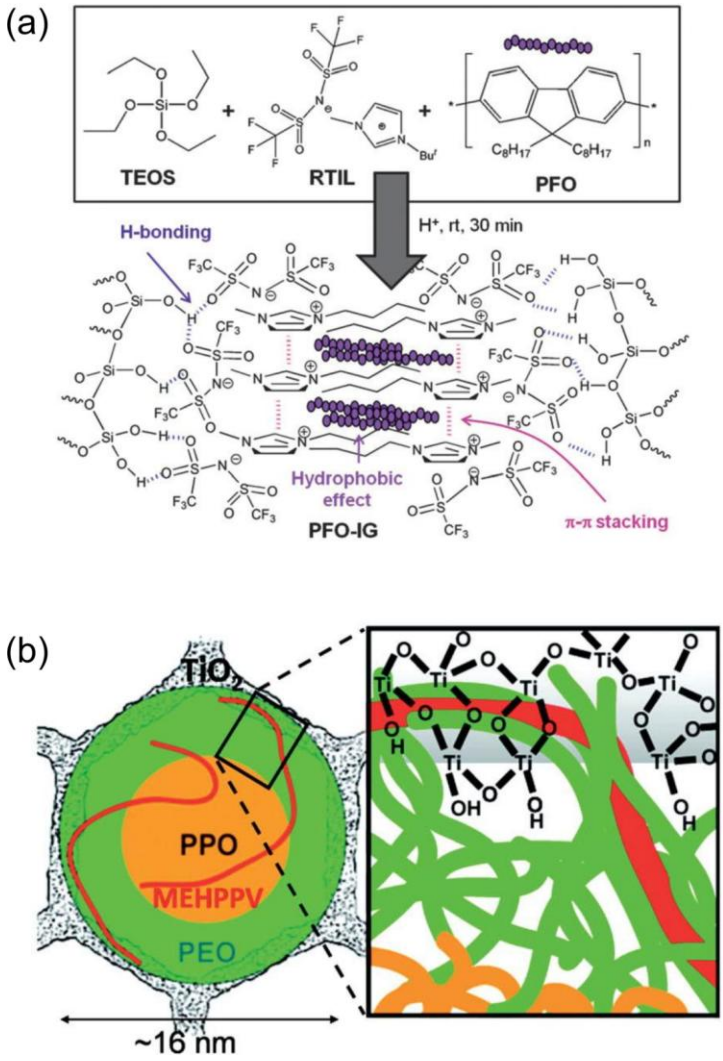

Figure 1.9. Examples of strategies for the controlled placement of CPs into host matrices. (a) Schematic representation of the local arrangement of the PFO chains into the hydrophobic domains created by the RTIL units which are aligned along the wall of a silica network. Figure adapted with permission from ref.[64] (b) Proposed structure of the titania-pluronic-CP distribution within a mesochannel. Figure adapted with permission from ref. [71]

In contrast, for CPEs, the presence of a charge on the side chain can be exploited as it confers improved solubility in the typically aqueous sol-gel medium and facilitates mixing with the network precursors (**Fig. 1.10**).

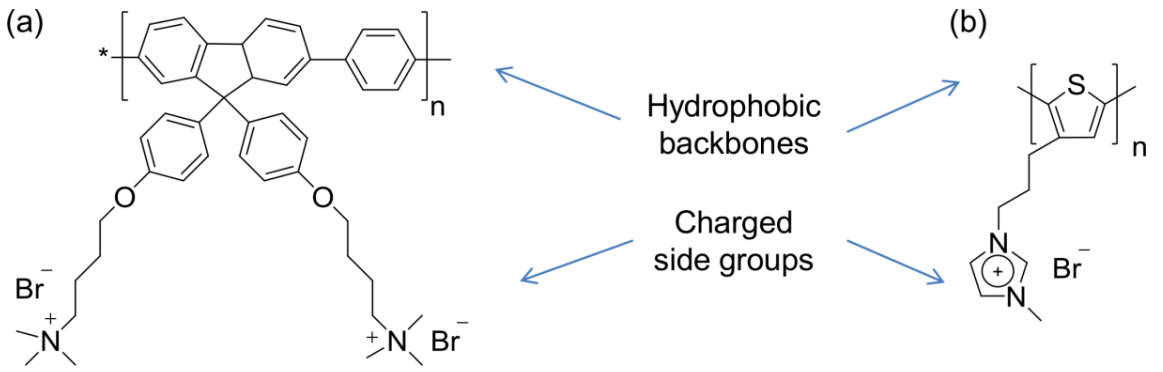

Figure 1.10. Examples of the structure of two CPEs. Chemical structures of: (a) poly(9,9-bis(6-*N*,*N*,*N*-trimethylammonium)hexyl)fluorene phenylene) and (b) poly (3-(n-(1-methylimidazolium-3-yl)alkyl)-thiophene-2,5-diyl bromide). The hydrophobic backbones and charged side groups for each CPE are also indicated.

This strategy has been successfully applied for the preparation of CPE-doped silica hybrids by exploiting the ionic interactions between the charged side chains of the CPEs and the silanol moieties on the silica host.[73] However, introduction of a high amount of ionic groups can lead to modification of the conjugation length of the CPE, affecting the overall optical properties of the fluorophore. Boury *et al.*[74] developed a synthetic approach for the preparation of poly(thiophene) (PT) molecules functionalised with ionic-liquid-like side-chains (**Fig. 1.11**a). The conformation of the final CPEs was modulated by working in an environment with different polarity, *i.e.* under hydrophilic conditions, the CPE chains adopted a micelle-like conformation consisting of a PT core, with the ioninc side chains forming the shell. Upon addition of the CPEs to a mixture containing TEOS and the sol-gel reaction initiators, the final hybrids were be spin-coated on glass supports and yielded highly transparent and regular films of 1 μm thickness (**Fig. 1.11**b). Due to the electrostatic interactions between the positively-charged imidazolium side groups and the silanol moieties, the final material consisted of a homogeneous composite where the conjugation, and hence the optoelectronic properties of the CPE, were maintained.[75]

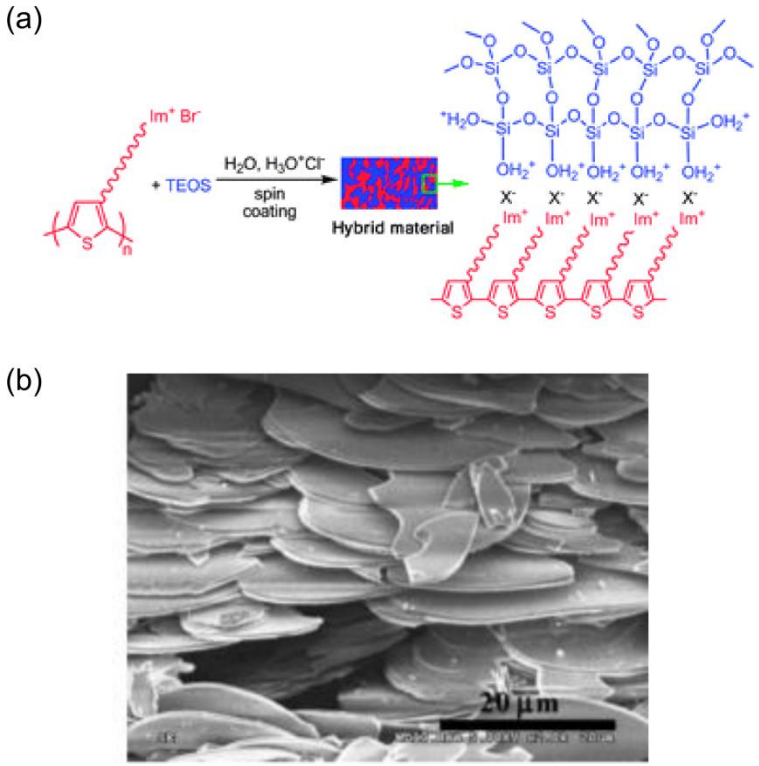

Figure 1.11. Design and macroscopic characteristics of the CPE-silica composite. (a) Schematic representation of the synthetic process for the preparation of PT-doped silica networks. (b) Scanning electron microscopy (SEM) image of the final PT-silica hybrid. Figure adapted with permission from ref. [75]

It is worth noting that each one of the examples described above consists of a system characterised by the presence of both an organic and inorganic component. Such materials are known as organic-inorganic hybrids and a detailed discussion regarding them is presented in the next section.

1.4 Organic-Inorganic Hybrid Materials

Organic-inorganic hybrid materials are nanocomposites consisting of an organic and an inorganic component.[76] These materials have attracted significant attention for their inherent characteristics arising from the possibility of combining the favourable properties of their constituents in one platform, such as the lightweight and processability of organic polymers, with the high mechanical strength and good chemical resistance of an inorganic matrix.[76] This prospective becomes even more exciting when optically-active organic species are combined with robust and chemically stable matrices.[77] The properties of hybrid materials are dictated by those of their constituents and by the interactions that hold them together.[78] In particular, organic-inorganic hybrid materials can be divided into two major classes based on these interactions:[78, 79] *Class I*

hybrids, are defined as materials where the bonds that hold together the organic and inorganic components are either non-covalent (*e.g.* van der Waals forces, hydrogen bonds or electrostatic interactions) or iono-covalent bonds.[78, 80] These materials can be prepared without the need for chemically-reactive functional groups and their final behaviour/structure can be assumed based on their physical properties, such as polarity, affinity, or π-π stacking interactions. Recently, significant interest has been focussed on Class I hybrids for the development of perovskite-based technologies and drug delivery systems.[80-82] In contrast, in *Class II* hybrids the two components are partially or totally bound together through covalent bonds.[76,78,80] To yield these materials each component must present specific functional groups that are able to react together. Due to their integrated organic backbone, Class II hybrids have found many applications from light-emitting devices,[83] to sensors.[84]

For π-conjugated fluorophores, their incorporation into the matrix of a hybrid can lead to phase separation. This is particularly true when those with extended conjugated backbones (*i.e.* CPs) are incorporated into inorganic matrices. Therefore, using a host material that combines in itself an organic and inorganic backbone could be a solution to improve the miscibility of the components forming the overall system. Moreover, in view of the application of such hybrids for the preparation of devices, a simple and efficient synthetic route would be preferred. In this context, a specific type of Class II organic-inorganic hybrids known as *ureasils* have attracted considerable attention as hosts for the incorporation of optically active species.[85-89] The inorganic framework of these materials is prepared using sol-gel chemistry, which is described in more detail below.

1.4.1 The Sol-Gel Process

For a better understanding of the overall work done in this thesis, it is of interest to recall in detail the sol-gel route for the preparation of organic-inorganic silica-based hybrids and its correlation to the pH (base vs. acid catalysed reaction) . The term *sol-gel* refers to any process occurring upon generation of a colloidal suspension, followed by the conversion *via* condensation into a gelated network.[90] The term *sol* indicates a dispersion of colloidal particles which are suspended in a fluid medium through Brownian motion and their tendency to aggregate can vary as

a function of their composition and the reaction conditions.[91] By adjusting/refining these parameters, the sol-gel method can be exploited to obtain systems presenting different organic-inorganic hybrid architectures (**Fig. 1.12**).

For a generic system consisting of silicon centres functionalised with alkyloxide chains and bound to a non-hydrolysable extremity, the steps of the sol-gel reaction are: the hydrolysis of the alkoxysilane moieties and formation of the corresponding alcohol; the condensation of the nuclei into clusters and either their precipitation as NPs or the gelation of the clusters jointed by encapsulation of the solvent (**Fig. 1.12**).[92] For the latter case, the solution becomes a viscous fluid which upon formation of the gel network, evaporation of any remaining volatile components and thermal treatment becomes a dense network.[93]

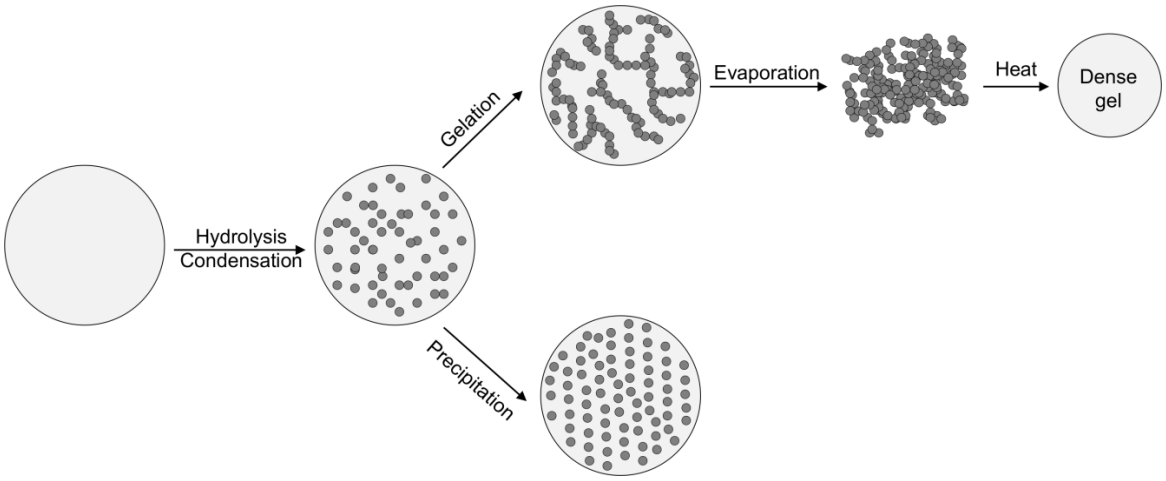

Figure 1.12. Schematic route for the sol-gel process. Description of the synthetic steps involved in the preparation of either a dense gel or NPs using the sol-gel process.

For this work, the versatility of the sol-gel method will be exploited to obtain either extended covalent ureasil networks or to yield nano-sized ureasil aggregates. The conditions for the hydrolysis and condensation processes will direct the arrangement of the final hybrid architectures. To create large ureasil monoliths, for example, acid-catalysed hydrolysis of a solution containing a relatively high concentration of the alkoxysilane precursors leads to fast conversion of units into the corresponding mono-silanol species (**Fig. 1.13**a).[90] However, since the removal of one of the electron donating –(OCH_2CH_3) groups results in a reduction in the rate of the hydrolysis reaction for a second alkoxide group, condensation can occur between partially-hydrolysed silicon centres (**Fig. 1.13**b).

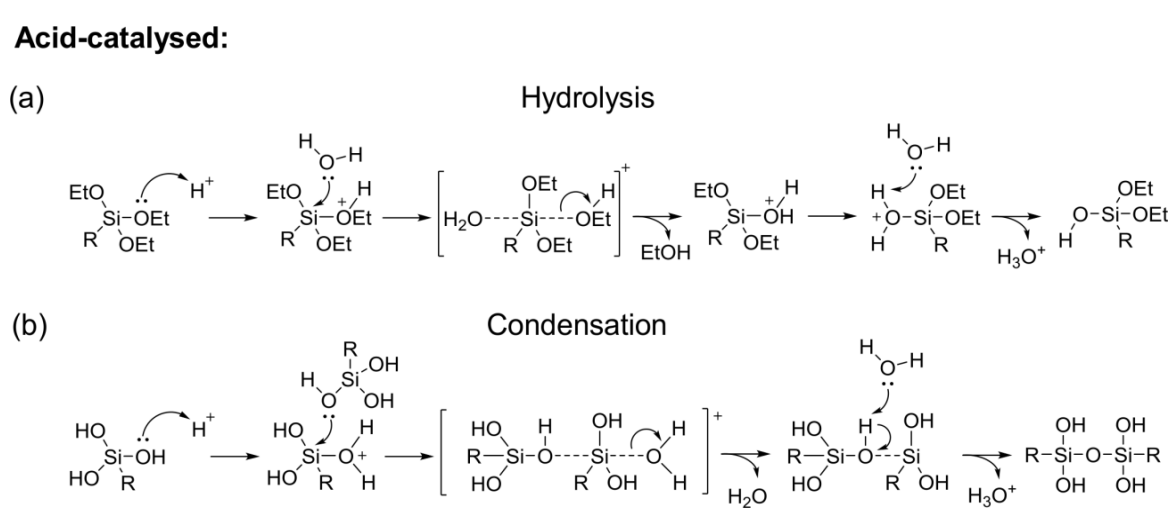

Fig. 1.13. Route for the acid-catalysed sol-gel process of alkoxysilanes. (a) Hydrolysis and (b) condensation reaction mechanisms for the preparation of the silica network. In the case of di- or tri-ureasils: R = $–(CH_2)_3–$NHCONH–Jeffamine.

This leads to elongation of the network backbone, thus resulting in the formation of extended aggregates and as a result, the final product is a homogeneous, relatively dense and compact gel. This strategy has been adopted for the preparation of ureasil monoliths.[94, 95] In contrast, base-catalysed hydrolysis is characterised by a faster rate, which increases as the electron-donating alkoxide moieties are removed. This leads to early-stage condensation between the chains, occurring even before the beginning of the hydrolysis for some of the *sol* precursors (**Fig. 1.14**).[96] The resulting hybrids are characterised by shorter networks and can yield small aggregates. This process forms the basis of the widely popular Stöber method for the preparation of silica NPs.[97]

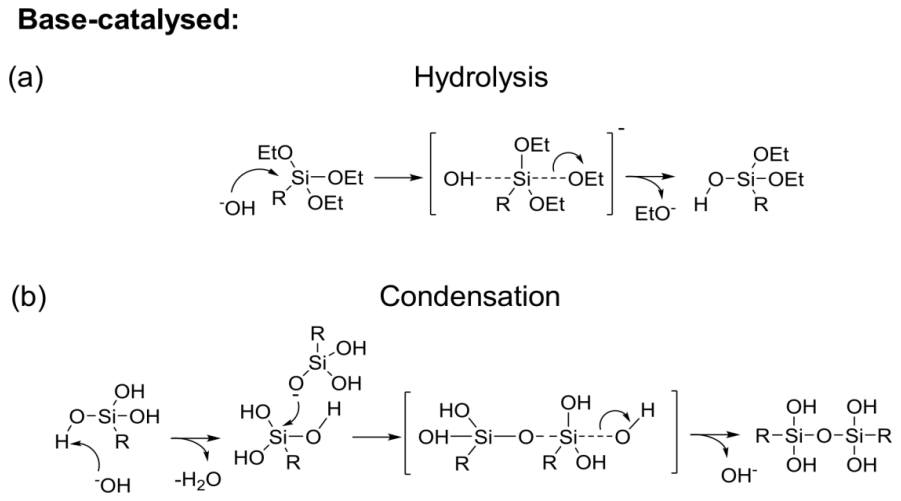

Fig. 1.14. Route for the base-catalysed sol-gel process of alkoxysilanes. (a) Hydrolysis and (b) condensation reaction mechanisms for the preparation of the silica network. In the case of di- or tri-ureasils: R = $–(CH_2)_3–$NHCONH–Jeffamine.

Most reactions using the Stöber process begin with the hydrolysis/condensation of TEOS, which is a cheap and versatile silica precursor.[98] However, the incredibly rich library of alkoxysilanes available nowadays has created infinite possibilities to design silica NPs with different architectures, such as organic-inorganic silica NPs, whose organic backbone, usually consisting of polymeric chains, can encapsulate small molecules (dyes or drugs),[80] while preserving the superior stability of a silica network.

1.4.2 Class II Hybrids: The Ureasil Family

Siloxane-based materials have attracted significant interest due to their intriguing optical properties such as photostability,[99] and electroluminescence.[100] For this work, particular attention has been placed on a family of organic-inorganic hybrid materials known as *ureasils*. Ureasils are comprised of poly(ethylene oxide) (PEO)/poly(propylene oxide) (PPO) block copolymer chains chemically bound to a siliceous network *via* urea [HN(C=O)NH] bridges.[95, 101, 102] The organic domains of ureasils are usually derived from a family of poly(etheramine)s known as Jeffamines™, which are commercially-available in a variety of branch numbers and chain lengths.[103] Therefore, ureasils can be prepared in a range of different structures, whose properties are dictated by the choice of the Jeffamine precursor. In this work, ureasils will be prepared by stoichiometric reaction of a siloxane precursor (3-isocyanatopropyltriethoxysilane, ICPTES), with either two linear Jeffamine precursors: Jeffamine ED-600 and Jeffamine D-4000, yielding *di-ureasil* hybrids or two tri-branched Jeffamine precursors: Jeffamine T-403 and Jeffamine T-5000 (**Fig. 1.15**), yielding *tri-ureasil* hybrids.

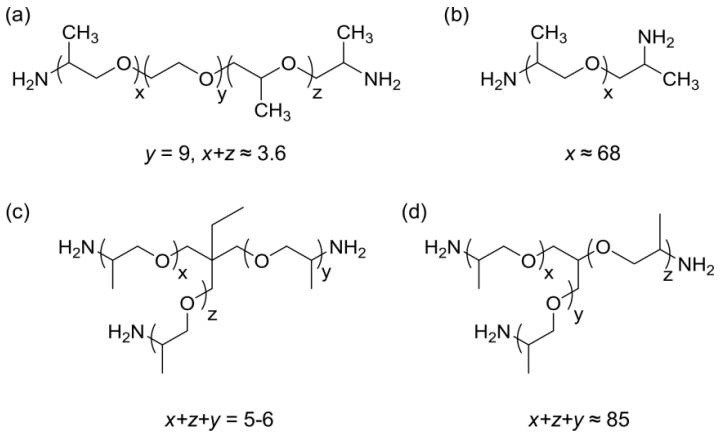

Fig. 1.15. Jeffamine precursors used in this work. Chemical structure of: (a) Jeffamine ED-600, (b) Jeffamine D-4000, (c) Jeffamine T-403 and (d) Jeffamine T-5000.

In particular, the hybrid architectures that will be investigated are ureasils as monoliths and as the core of silica-based hybrid NPs. A typical synthetic procedure for the preparation of ureasils as monoliths consists of the acid-catalysed hydrolysis and condensation of a precursor known as ureapropyltriethoxysilane (UPTES), which upon ageing, yields transparent and rubbery ureasil slabs which present a moderate refractive index (n =1.49) and good optical properties such as photoluminescence, with modest values of Φ_{PL} (ranging from 6 to 14% depending on the synthetic method used).[104-106] A schematic representation of the formation of a di-ureasil monolith is presented in **Fig. 1.16**. Since ureasils are intrinsically photoluminescent they have been used as photoactive hosts for lanthanide ions/complexes,[89, 104] molecular dyes[87] and for CPs and CPEs.[85, 86] The first study on the origin of the photoluminescence of ureasils was performed by Carlos *et al.*, on a series of ureasils consisting of ICPTES and either Jeffamine ED-600, Jeffamine ED-900 or Jeffamine ED-2001.[101] The authors noted that upon excitation in the ultraviolet (UV) (λ_{ex} = 365 nm) each sample presented a broad emission band shaped as a Gaussian curve. The emission of silicon-based materials is well-documented in the literature as well as the correlation between the presence of blue-emission and oxide moieties.[107-110] To understand the origin of the emission of ureasil, the authors deconvoluted the broad emission peak, resulting in two unshaped Gaussian components, one in the blue (~2.6 eV) and one in the purplish-blue region (~2.8-3.0 eV) of the emission spectrum. Interestingly, it was noticed that the blue component of the emission is not present for analogue hybrids made with ICPTES and poly(ethylene) glycols (PEG) chains, while the blue-purplish contribution was not detected for pure Jeffamines or for non-hydrolysed silica precursor.[102] Based on these spectroscopic observations the authors suggested that the lower energy emission is related to the presence of NH moieties and namely arises from the photoinduced proton transfer occurring in the NH groups of the urea linkages. In each urea moiety, the carbonyl groups are involved in hydrogen bonds (-C=O⋯H-N); light irradiation promotes the hydrogen-transfer from one –NH moiety to another, leading to the formation of two oppositely charged defects (-NH_2^+ and -N^-).[101, 106] These defects behave as electron and hole traps which generate the characteristic blue emission through radiative recombination. The higher energy contribution instead, is related to electron-hole recombination occurring within the siliceous nanoclusters. Although this mechanism has not been fully unravelled, electron paramagnetic resonance studies

showed that ureasil matrices present randomly located paramagnetic centres, which are most likely corresponding to peroxy-radical hole traps ·O-O-Si≡(CO_2) moieties.[111]

Moreover, it was noticed that the emission maxima of blank ureasils red-shift towards lower energy values upon increase of the excitation wavelength.[101, 102] Further investigation of this phenomenon, revealed that only the emission component related to the silica defects red-shifts upon decrease of the excitation energy,[101] and was attributed to thermal relaxation of the electrons from high-energy states in the conduction band, to the bottom of the band.[112] The possibility of tuning the emission maxima of ureasil by changing the excitation wavelength,[101, 106] can be exploited to vary the extent of energy transfer between the ureasil host and the doping agent.[85]

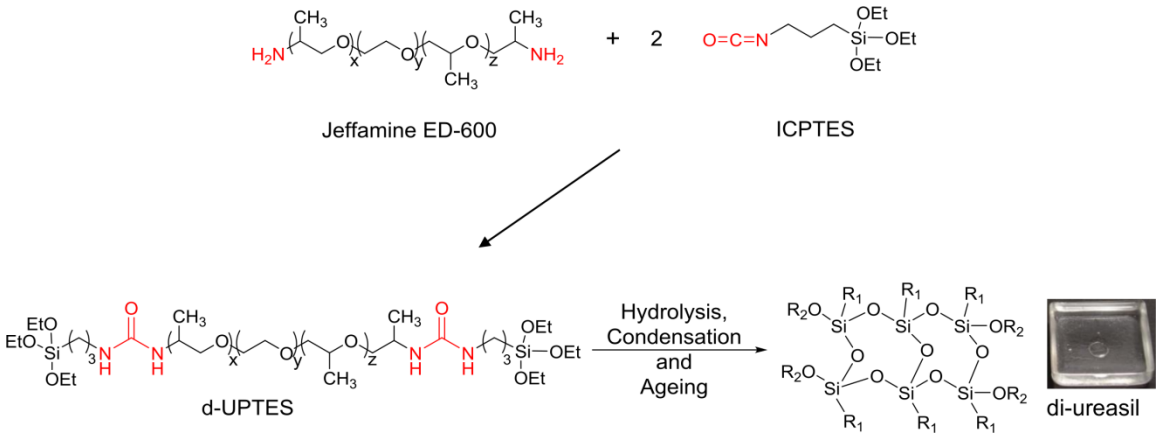

Figure 1.16. Synthetic route for the preparation of a di-ureasil monolith. Structure of d-UPTES precursor (for Jeffamine ED-600: $x+y$ = 3.6 and z = 9) and of the silica network constituting the final di-ureasil and photograph of a representative monolith under daylight. The portions of the structure in red represent the urea bridges. R_1 = –$(CH_2)_3$–NHCONH–Jeffamine and R_2= –Si–O–Si– or H).

1.4.2.1 Applications of Ureasils

The favourable mechanical and optical properties, combined with the ease of processability, make ureasils good candidates as hosts for a variety of chemical species. Ureasils have been exploited as active hosts for lanthanides;[113-115] in particular, due to their structure, their carbonyl moieties can coordinate to metal ions, enhancing their optical properties. For example, incorporation of a Eu(III)-β-diketonate complex within the matrix of a di-ureasil prepared from ICPTES and Jeffamine ED-600, leads to the coordination of the carbonyl groups of the urea bridges with the Eu^{3+} ions, replacing the ethanol molecules in the coordination sphere of the metal ions.[113, 116] Removal of the OH oscillator from the coordination sphere of the ion increases the emission quantum yield of the Eu(III) complex in the solid-state, while improving its

photostability. Moreover, the di-ureasil can function as donor for energy transfer to the metal centre.

The same undoped di-ureasil matrices have also been used as polymer electrolytes through the incorporation of a lithium perchlorate ($LiClO_4$) salt. Due to the porous structure and the flexibility of the hybrid network, the mobility of the Li^+ ions is extremely high, introducing an interesting possibility for the use of these materials as solid polymer electrolytes in lithium-ion batteries.[117, 118] Furthermore, ureasils are also capable of hosting larger species such as CPs and CPEs.[85, 86] In particular, the electronic interaction between the host and the guest species can impart interesting optical properties to the final material. In a recent example,[85] Willis-Fox *et al.* prepared a series of di-ureasil samples doped with different concentrations of a red-emitting poly(thiophene) and MEH-PPV. The exploitation of the broad spectral overlap between the ureasil emission spectrum and the absorption spectra of the CPs, combined with the strategic tuning of both the excitation wavelength and the concentration of the dopants, allowed tuning the emission of the final samples from yellow to white. In particular, the contribution of the ureasil to the emission was dominant, when exciting at higher energies. While a decrease in the excitation energy led to a red-shifted emission. The solid-state white light emission was observed when the contribution to the emission given by both the ureasil and the dopant was roughly equal. Moreover the emission could be shifted from blue to white by increasing the concentration of the dopants (**Fig. 1.17**).[85]

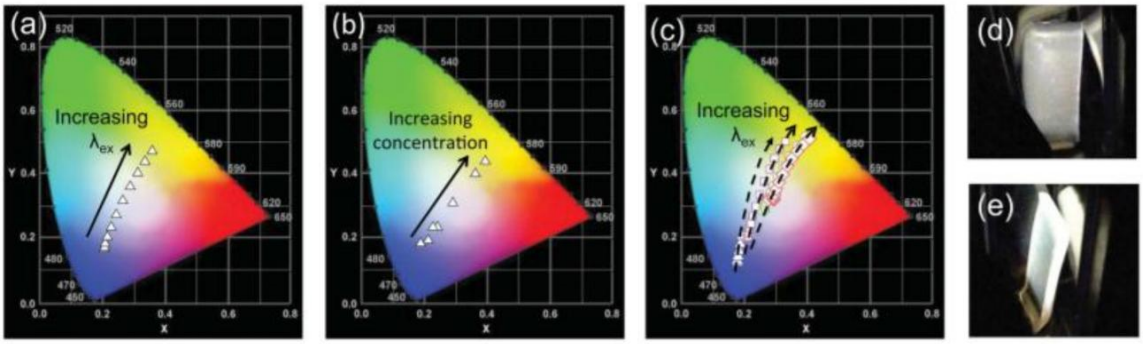

Figure 1.17. Modulation of the emission of ureasil samples doped with MEH-PPV and a poly(thiophenes). CIE x,y chromaticity diagrams for samples as a function of: (a) increase of the excitation wavelength, (b) increase of the dopant concentration and (c) increase of both. The dashed arrows serve only to guide the eye. (d) and (e) are photographs of white-emitting doped-ureasil under UV-illumination (λ_{ex} = 385 nm). Figure adapted with permission from ref.[85]

In this work, attention will be focussed on the application of ureasils as a platform for light-emitting devices, with particular interest for luminescent solar concentrators.

1.4.2.2 Ureasils as Waveguides for Luminescent Solar Concentrators

For a deeper understanding of the reasons why ureasils were chosen for the preparation of LSCs, a brief introduction to the history and to the working principle of these devices is necessary. The fast depletion of fossil fuels and the impending climatic crisis related to their use, makes it an immediate priority to invest in new technologies for energy production. Renewable energies are great candidates for this purpose, as they combine the possibility of an inexhaustible energy source with a low ecological impact.[119] In particular, solar energy is one of the renewable energy sources with the highest potential. As the European Union has decreed that all new buildings need to be near-zero energy by 2020, there is an increasing interest in the incorporation of solar energy systems into built environments.[120] Classical silicon-based photovoltaic (PV) solutions can be adapted into built environments, however their intrinsic heavy weight and limited coloration (generally black or dark blue) represent serious limitations. Moreover, these devices respond optimally to direct sunlight, while realistically, for built environments, most of the light is diffuse due to reflection and scattering by objects or clouds.[121, 122] LSCs were proposed in the 1970's as a complementary solar technology that could overcome these limitations.[122, 123] A schematic representation of a doped LSC and its working principle is presented in **Fig. 1.18**a.

In their most basic configurations, LSCs consist of a transparent waveguide plate doped with a luminescent species (lumophore). As sunlight hits the plate, a portion of it is absorbed by the lumophore (**Fig. 1.18**a), which then re-emits it at a lower frequency, *i.e.* longer wavelengths. The emitted light is then transported to the edge of the waveguide plate by total internal reflection, where it is collected by a PV cell (**Fig. 1.18**a, pathway 7). The loss mechanism associated with the device will be discussed in detail later.

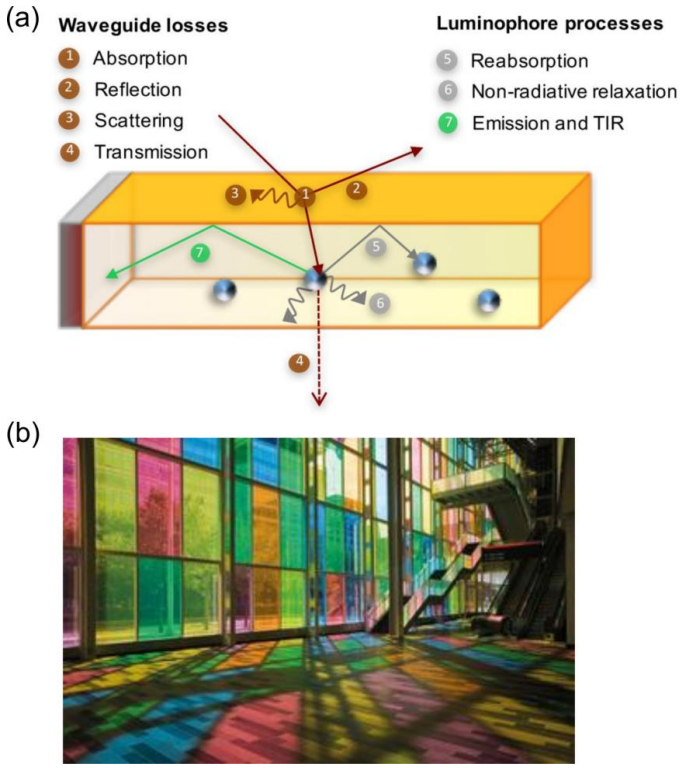

Figure 1.18. Working principle and loss mechanisms associated with a LSC and example of LSC-inspired building aesthetics. (a) Schematic representation of the components of a LSC, the working principle and the loss mechanisms (the straight arrows indicate radiative processes while the curved arrows indicate non-radiative processes) and (b) picture of the congress palace of Montreal (Canada). Figure adapted with permission from ref.[124] Photograph adapted with permission from ref.[125]

LSCs can harvest both direct and diffuse light over large areas and concentrate it into smaller areas (geometrical concentration), thus leading to a reduction of both the number and areas of PV cells required.[126] LSCs are lightweight and aesthetically pleasing, and thus, easy to integrate in the construction of energetically-neutral buildings (**Fig. 1.18**b).[122, 127] However, as the efficiency of a LSC is lower than that of a PV cell of the same area, these devices have to be considered as a complementary technology rather than a substitute to classical PV systems, which could enable the transformation of regular windows/walls into energy-harvesting machines.

LSCs can also be prepared using different architectures; for example the lumophore can be deposited as a uniform thin film or patterned on the surface of the waveguide plate.[128-131] The geometry of the waveguide can also be modify in order to achieve higher concentration factors for the same waveguide areas, for example using cylindrical optical fibers as waveguides.[132]

Despite their great potential, LSCs can be affected by several light-loss mechanisms, which have prevented them from being commercialised to date. For this thesis, the proposed examples of

ureasil-based LSCs are in a planar doped architecture (*e.g.* a lumophore homogeneously dispersed into a waveguide matrix), therefore this type of device configuration will be considered as reference when discussing the loss mechanisms (**Fig. 1.18**a). These mechanisms can be associated either with the waveguide or with the lumophore. Waveguide losses include: reflection or scattering of the sunlight from waveguide defects (**Fig. 1.18**a, pathway 2 and 3, respectively), escape cone losses which prevent the photons from being capture within the waveguide (**Fig. 1.18**a, pathway 4) and parasitic absorption (**Fig. 1.18**a, pathway 1). To reduce these losses a waveguide should be free of defects, with good values of refractive index and high transmittance in the spectral region corresponding to the solar spectrum. Lumophore-related losses include: inefficient harvesting of the solar spectrum, poor absorption and/or re-emission of light (**Fig. 1.18**a, pathway 6), poor photostability and re-absorption losses (**Fig. 1.18**a, pathway 5). Thus, to minimise these phenomena, a good lumophore should present near-unity Φ_{PL}, efficient absorption in the solar spectrum region and a large Stokes' shift, while exhibiting good thermal and photo-stability.[122, 124] At present, the most popular materials used as waveguides are: poly(methylmethacrylate) (PMMA) polymers, poly(carbonate)s (PC), transparent plastics with a refractive index of 1.49 and glasses (refractive index of 1.50).[122] Despite the impact of the waveguide losses onto the overall efficiency of a LSC, the research associated with the investigation of new materials for waveguides is limited. PMMA is a good candidate for this purpose, and is also considered the archetype material for waveguides. However, it presents poor thermal and photostability upon extensive exposure to light, resulting in the formation of photon trap sites.[133, 134] Materials like special glasses or PC display higher stability and good values of refractive indices (1.5-1.8), however they can be heavy, inflexible and difficult to handle; therefore unpractical.

New approaches for the preparation of waveguides with low ecological impacts have also been recently considered. For example, Camaioni *et al.* have investigated biodegradable polymers such as L-poly(lactic acid) (L-PLA) and silk fibroin from the *Bombyx mori* silkworm. [135,136] L-PLA proved to be a valuable alternative to classic waveguide solutions like PMMA, with good processability and transparency and similar values of refractive indices. Conversely, the use of silk

fibrons opened the possibility to the creation of fully water-processable LSC, which, once properly treated, can resist outdoor conditions.

More recently, polysiloxane-based materials were also proposed as potential waveguide solutions.[89, 137] If judiciously designed, these materials can combine the mechanical and thermal stability of a silica matrix to the possibility of yielding flexible waveguides.[138] Among the different class of polysiloxane materials, ureasils represent good candidates for applications as waveguides. The waveguiding properties of ureasils have already been exploited for the preparation of ureasil-based optical fibers and/or diffraction gratings.[139-141] Ureasils consisting of Jeffamine ED-600 and ICPTES, co-condensed with zirconium tetrapropoxide and methacrylic acid were proposed as integrated optical substrates. The refractive indices of the final materials were tuned by varying the concentration of zirconium dopant added reaching a maximum effective value of 1.52, while the design of the devices was modified through photopatterning. A detailed structural investigation of the systems showed that the zirconium-based and the silica-based domains are interconstrained and that the overall structure of the final hybrid was preserved upon incorporation of the dopant at the investigated concentration. Moreover, these systems presented thermal stability up to 70° C, meeting the thermal standards for applications as optical fibres.[141] Direct laser writing was used to create channel waveguides and Bragg gratings from zirconium oxide doped ureasils, yielding components for optical networks operating at a high bit rate.[139]

The use of ureasils as waveguides for LSCs was proposed by Nolasco *et al.* in 2013, where a β-diketonate-europium(III) complex containing 2-thenoyltrifluoracetonate (tta^-) and 5,6-epoxy-5,6-dihydro-[1,10] phenanthroline (ephen) ligands, $Eu(tta)_3ephen$ was incorporated into the matrix of a tri-ureasil hybrid formed from ICPTES and Jeffamine T-5000.[89] The complexes were added to the hybrid precursor and the final systems were processed either as monoliths or as thin films deposited onto a glass substrates. Upon creation of the LSC device, an increase in the output of the PV cell by 0.5% was observed. The same lumophore was also used to create LSC devices consisting of PMMA cylinders (diameter = 3 mm) coated with a layer of $Eu(tta)_3ephen$-doped ureasils based on Jeffamine ED-600.[142] Interestingly, this system combined the advantages of using a cylindrical geometry to increase the concentration factor of the device, with the use of flexible waveguide materials. The coating of the commercially available PMMA cylinders rather than the

homogeneous doping, is a route which allowed the use of lower amounts of lumophore, reducing the costs of the overall system. Due to the spectral region selected by the authors for the determination of the performance of these systems (300 to 380 nm), it is hard to compare the optical efficiency (the ratio between the optical power output over the four edges of the LSC and the total incident solar power on its surface) measured for these systems (20.77 ± 1.3% for the champion sample) with those of the literature. However, this example represents an intriguing possibility for application of these systems as flexible wearable solar-harvesting fabrics.[142]

Due to their organic-inorganic backbone, ureasil waveguides can also function as hosts for organic dyes. Rondão *et al.*[143] reported the preparation of a LSC device made using the same tri-ureasil hybrid doped with a near-infrared emitting dye, silicon 2,3-naphthalocyanine bis-(trihexylsilyloxide) dye (SiNc). However, due to the low Φ_{PL} of SiNc (~17%, in a THF solution), the optical efficiency of the LSC was modest (1.5%).[131] Recently, work from the Evans group showed that a ureasil hybrid prepared from ICPTES and Jeffamine ED-600 and doped with the archetypal red-emitting dye Lumogen F Red 305 can function as a LSC (**Fig. 1.19**a).[87] The dye was encapsulated into the ureasil waveguide by addition to the sol mixture before the gelation and the final hybrids were yielded as thick slabs (4 × 4 cm^2) (**Fig. 1.19**b) or spin-coated onto a PMMA support. The waveguide was attached to the PV cell using the ureasil itself as glue thus reducing the presence of an additional interface, which could cause loss of light through scattering processes. The champion device showed an optical efficiency of 14.5%, which is comparable to that of pure organic LSCs.[87, 144] Interestingly, the ureasil behaved as an efficient energy donor for the Lumogen F Red 305 acceptor, extending the window of harvested light. However, upon increasing the concentration of the lumophore over a certain threshold value (0.005%$_{w/w}$), re-absorption and/or aggregation of the dye was observed, leading to a red-shift in the maximum of the emission spectrum (**Fig. 1.19**c), a decrease in the Φ_{PL} and in the efficiency of the device.

From these results, it seems clear that despite the great potential of ureasils as waveguides, particular care needs to be taken when designing the system in respect to the choice of lumophore and the strategy by which it is incorporated into the ureasil network.

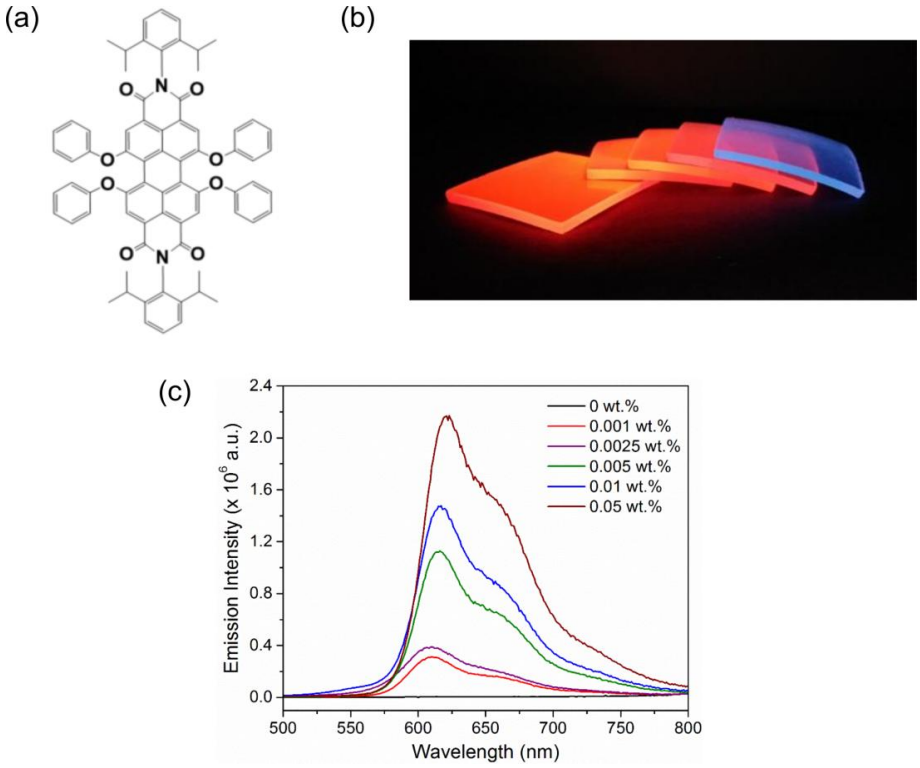

Figure 1.19. Lumogen F Red 305-doped ureasils LSCs at different loading concentrations. (a) Structure of Lumogen F Red 305, (b) photographs of dye-doped and un-doped ureasils LSCs upon excitation at 365 nm and (c) corresponding emission spectra in front-face configuration (λ_{ex}= 490 nm). Figure adapted with permission from ref.[87]

1.4.3 Organic-Inorganic Silica Hybrid Nanoparticles

As mentioned in the previous section, the versatility of the sol-gel process combined with the abundance of alkoxysilane precursors available, moved the scientific community towards the creation of novel architectures of hybrid systems, such as silica-based organic-inorganic hybrid NPs.[76, 80, 99] By doing so, the range of applications of organic-inorganic hybrids can be extended from macroscopic devices to nanosized agents,[80] able to report biological events on the cellular level in solution. To this aim, control over the colloidal stability of these NP systems is crucial.

1.4.3.1 Colloidal Stability

The process of formation of NPs is usually comprised of three key points: (i) increase of the precursor concentration, (II) nucleation and (III) growth. These stages can be explained using the well-known LaMer diagram proposed by LaMer and Dinegar, in which the concentration of the solute is monitored as a function of time (**Fig. 1.20**).[145]

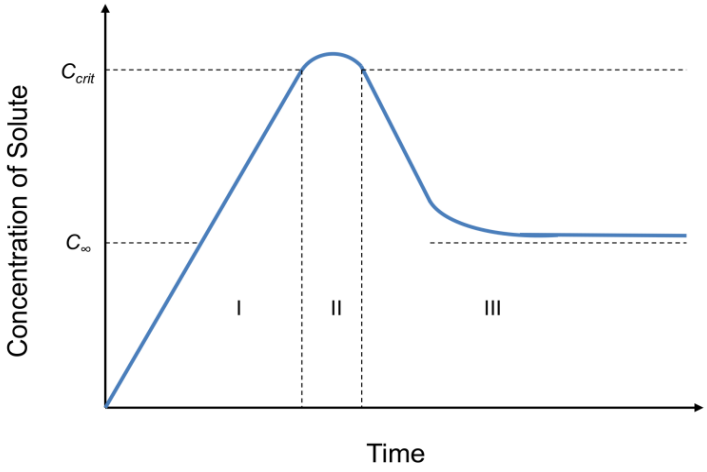

Figure 1.20. LaMer diagram for the formation of particles, showing the evolution with time of the precursor concentration during the various stages of particle preparation The critical concentration (C_{crit}) and the solubility of the solute (C_∞) are also presented.

During the first stage of the process (I) the concentration of the monomer increases until reaching a critical value (C_{crit}) (II) at which the spontaneous "burst-nucleation" of the monomers becomes significant.[146] As the precursor aggregates reach a size at which they can survive in solution without being re-dissolved (critical radius), the system enters a stage of mass balance between the supply rate of monomer and their consumption for the formation of "seeds", which result in a decrease of the concentration of monomers in solution until reaching a critical level for the nucleation process to virtually terminate. The system can then enter the growth stage (III) where the seeds act as a focus point for the accumulation of precursor, without further nucleation processes occurring.[146] The initial distribution of the size of the NPs will depend on the interplay between these steps; if the consumption of the precursor involved in the increase of the NP size is more dominant than the creation of new seeds, the final system will consist of large monodisperse NPs.[147] If the nucleation continues during the growth, the size distribution of the particles will be more polydispersed.[148] It is worth to note that these steps do not occur strictly in succession; however, the overall control over the particle distribution will be narrower if each step occurs separately.[148]

After the particles are formed, an ageing process might take place in the dispersion. Brownian motions will lead to collision between particles, which may aggregate if not sufficiently stabilised either by high surface charge or higher surface tension. Upon reaching a critical size,

these aggregates can eventually precipitate due to the effect of gravity, creating concentration gradients which can lead to further nucleation and growth mechanisms. This overall process will increase the polydispersity of the particle solution. Another phenomenon that can occur during the ageing process is known as *Ostwald ripening*,[92] during which the smaller particles in the dispersion break down into small grains, which will subsequently be attracted to the surface of the larger particles and aggregate on it, increasing the aggregate size.

Given that a number of different processes can jeopardise the stability and polydispersity of a dispersion of NPs, several approaches have been proposed in the literature to stabilise the suspension. Firstly, using a controlled synthetic method for the nucleation and growth steps increases the likelihood of obtaining higher quality systems. For this work, the NP synthesis is based on a modification of the Stöber process, which is well-known for giving reliable, monodisperse particle suspensions.[97] In this method, NPs are formed by the hydrolysis and condensation of silica alkoxide precursors through a sol-gel reaction.[97, 98] The initial favourable properties of the suspension are attributed to a nucleation-growth mechanism in which the interfacial forces are minimised, overcoming the van der Waals interactions that could lead to aggregation.[149] However, this means that once the silica particles have aggregated, the covalent bonds that held them together cannot be disrupted, and therefore particular care needs to be taken when stirring the solution as an increased frequency of collisions between the particles can lead to the formation of larger aggregates. For silica-coated NPs, like the ones that will be prepared in this work, the presence of silanol groups (-Si-OH) will impart stability to the particles. In particular, working at a pH greater than the *p*Ka of these moieties (8.4 in water) will ensure the formation of –Si-O^- groups on the surface of the NPs leading to electrostatic repulsion between adjacent particles (see **Chapter 6**).[150] When referring to these systems, the NPs are said to present a "shell" of silica on their surface. The silica shell not only improves the stability of the NPs, but also imparts solubility of the overall system into polar solvents such as water.

Other approaches can also be adopted to increase the stability of the NP suspension. The use of bulky cations offers a route to trigger both the charge and the steric hindrance on the surface of the NPs. For example, tetramethylammonium is able to enter the solvating layer of a NP through electrostatic interactions, creating a bulky and positively charged environment for the particle that

prevents aggregation.[150, 151] The reactivity of the silanol groups can also be exploited to bound bulky polymer chains which will prevent aggregation through steric effects. PEGs for example, represent an excellent candidate for stabilisation of NPs in biologically relevant matrices. For these systems, the polymer chains can bind directly to the surface of the particle *via* an esterification reaction between the silanols and the terminal alcohol group of the PEG.[152, 153]

1.4.3.2 Applications of Core-Shell Organic-Inorganic NPs

Core-shell organic-inorganic NPs are a fascinating class of materials, which have shown great potential for applications ranging from drug delivery to sensing and imaging.[80, 154] A complete discussion regarding the variety of designs in which these systems can be prepared and all their potential applications is beyond the scope of this thesis; therefore particular attention will be paid to systems presenting the following architecture: organic/hybrid core and silica shell, and on their capability of encapsulating organic molecules and dyes.

The advantages of incorporating fluorophores into the core of NPs is to potentially increase their photostability, while allowing their solubilisation in aqueous media.[155] The Stöber process allows the incorporation of dyes within the core of the NPs during their growth, without losing control over the polydispersity and the size of the final NPs.[156-158] For example, Wiesner *et al.* reported the synthesis of a series of monodispersed core-shell silica NPs consisting of a dye core and a silica shell, presenting sizes in the sub-10 nm range.[158] The dyes selected for the preparation of these NPs belong to the family of Dyomics™ dyes, which present a variety of Stokes' shifts, covering an emission range of 540 to 690 nm. The fluorophores were encapsulated within the NPs by covalent modification of each dye with a maleimide functional group and subsequent reaction of the so-obtained product with an excess of a thiol-functionalised siloxane precursor. The NPs were then obtained by hydrolysis and condensation of the final product mixture, yielding core-shell NPs with a size distribution centred at 7-8 nm, which is ideal for *in vivo* applications, in particular when considering the possibility of expulsion of the NPs through urinary excretion.[159] Moreover, due to the rigidity of the dye molecules within the silica matrix and the inherent protection from negative solvent effects in solution, the brightness of the dyes is also improved upon incorporation into the NPs. (**Fig. 1.21**).

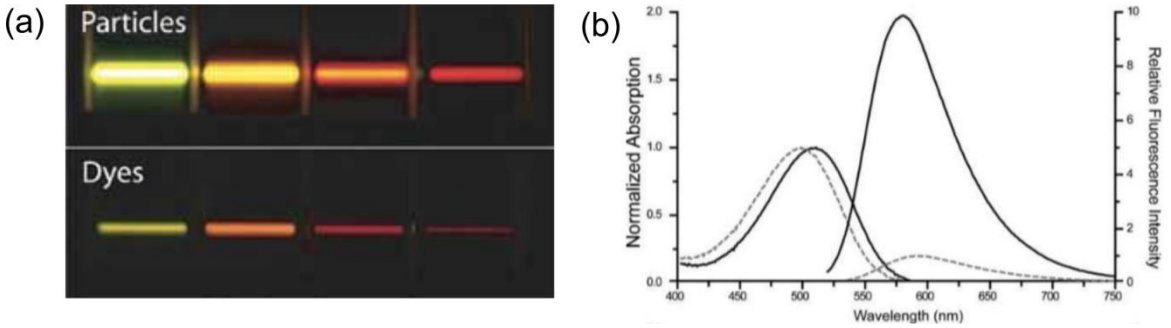

Figure 1.21. Enhancement of the emission properties of the Dyomics^{TM} dyes upon encapsulation in the NPs. (a) Pictures of the dye series upon excitation at 514 nm with a line Argon laser of the free and the encapsulated dye and (b) absorption and emission spectra of a selected dye before (dotted lines) and after (solid lines) encapsulation into the NPs. Figure adapted with permission from ref.[159]

Due to the variety of commercially-available siloxane precursors, different levels of functionalisation can occur both in the inner matrix and on the surface of the organic-inorganic hybrid NPs, for example, through functionalisation with a variety of biologically active groups. Kumar *et al.* reported the preparation of one of these systems, which consisted of a rhodamine dye covalently linked to a siloxane precursor which presented either thiol or amino groups.[160] The NPs were initially prepared through hydrolysis and condensation of the dye-grafted siloxane to yield monodisperse NPs with a diameter of ~20 nm. The free –SH or $–NH_2$ units left on the surface of the NPs were reacted with succinic anhydride and then functionalised with either transferrin, anti-claudin 4, or antimesothelin, to specifically aim at the corresponding receptor which is over expressed in pancreatic cancer cells and tissues. The efficient uptake of the targeted NPs was monitored through confocal microscopy in *in-vitro* samples and the NP system did not show any indication of cytotoxicity. These are just two of the many examples in literature, that show how organic-inorganic silica-based NPs prepared *via* the sol-gel method represent an intriguing possibility for the design of functional photoactive materials.

1.5 Aims

This thesis aims to create a series of different architectures of organic-inorganic hybrid materials based on ureasils containing π-conjugated organic fluorophores for applications ranging from light-emitting devices to luminescent solar concentrators and imaging. The optical properties of the final materials will be thoroughly investigated and correlated to the structural organisation, the composition and the architecture. In the first part of the thesis, our attention will be focussed on

ureasils fabricated as free-standing monoliths, with the incorporation of the fluorophore performed using two different approaches: (i) covalent grafting (**Chapter 3** and **Chapter 4**) and (ii) physical dispersion (**Chapter 5**).

Since the morphology of organic emitters can guide their optoelectronic properties, the first part of this work is aimed at the controlled and selective placement of the fluorophore into different ureasil matrices through covalent grafting of the dye/CP to the ureasil backbone. Two examples will be presented: in **Chapter 3**, a siloxane-functionalised PF will be bound to the backbone of either a linear or a tri-branched ureasil. The phase behaviour of the blue-emitting CP will be investigated by means of spectroscopic techniques and the extent of the different phases formed inside the ureasil network will be correlated with the local structures of the latter. In the second example, **Chapter 4**, a red-emitting perylene dicarboxdiimide dye will be covalently incorporated into ureasil matrices presenting different degrees of branching and branch lengths. The effect of the ureasil structure on the effective dispersion of the dye in the matrix will be investigated, as well as the role of each silica network onto the efficiency of energy transfer between the ureasil host and the perylene acceptor.

The second incorporation method investigated consists of physical encapsulation of the organic fluorophore, in this case a polyfluorene-phenylene copolymer containing on-chain perylene, within either a di-branched or a tri-branched ureasil hybrid (**Chapter 5**). This CPE has been chosen to extend the overall absorption and emission window of the material and to investigate potential charge/energy transfer mechanisms between the PF/ureasil donors and the perylene acceptor, which may have important implications for the application of these materials as LSCs.

The latter part of the thesis, **Chapter 6**, will be dedicated to the fabrication of ureasil-based organic-inorganic core-shell NPs. The optimisation of the synthetic process involved in the preparation of these materials will be thoroughly examined and the incorporation of a series of different organic dyes, both using covalent and non-covalent approaches, will be investigated. Finally, in **Chapter 7**, the main findings of this thesis will be summarised and the potential of these results for further work will be discussed.

1.6 References

1. P. Muller, *Glossary of terms used in physical organic chemistry (IUPAC Recommendations)*, 1994, p. 1077.
2. R. C. Evans, P. Douglas and H. D. Burrows, *Applied Photochemistry*, Springer, 2013, p. 151.
3. Z. B. Henson, K. Mullen and G. C. Bazan, *Nat. Chem.*, 2012, **4**, 699-704.
4. K. R. A. S. Sandanayake and I. O. Sutherland, *Sensor Actuat. B: Chem.*, 1993, **11**, 331-340.
5. X. Zhang, S. Rehm, M. M. Safont-Sempere and F. Würthner, *Nat. Chem.*, 2009, **1**, 623-629.
6. S. Rochat and T. M. Swager, *Angew. Chem. Int. Ed.*, 2014, **53**, 9792-9796.
7. C. Wu and D. T. Chiu, *Angew. Chem. Int. Ed.*, 2013, **52**, 3086-3109.
8. L. Ying, C.-L. Ho, H. Wu, Y. Cao and W.-Y. Wong, *Adv. Mater.*, 2014, **26**, 2459-2473.
9. P. Zalar, Z. B. Henson, G. C. Welch, G. C. Bazan and T.-Q. Nguyen, *Angew. Chem. Int. Ed.*, 2012, **51**, 7495-7498.
10. C.-L. Ho and W.-Y. Wong, *New J. Chem.*, 2013, **37**, 1665-1683.
11. M. A. Baldo, M. E. Thompson and S. R. Forrest, *Nature*, 2000, **403**, 750-753.
12. H. Shirakawa, E. J. Louis, A. G. MacDiarmid, C. K. Chiang and A. J. Heeger, *J. Chem. Soc., Chem. Commun.*, 1977, 578-580.
13. C. K. Chiang, C. R. Fincher, Y. W. Park, A. J. Heeger, H. Shirakawa, E. J. Louis, S. C. Gau and A. G. MacDiarmid, *Phys. Rev. Lett.*, 1977, **39**, 1098-1101.
14. *https://www.nobelprize.org/nobel_prizes/chemistry/laureates/2000/*.
15. A. J. Heeger, *Angew. Chem. Int. Ed.*, 2001, **40**, 2591-2611.
16. P. S. Heeger and A. J. Heeger, *Proc. Nat. Acad. Sci.*, 1999, **96**, 12219-12221.
17. G. Gustafsson, Y. Cao, G. M. Treacy, F. Klavetter, N. Colaneri and A. J. Heeger, *Nature*, 1992, **357**, 477-479.
18. J. H. Burroughes, D. D. C. Bradley, A. R. Brown, R. N. Marks, K. Mackay, R. H. Friend, P. L. Burns and A. B. Holmes, *Nature*, 1990, **347**, 539-541.
19. P. Tehrani, L.-O. Hennerdal, A. L. Dyer, J. R. Reynolds and M. Berggren, *J. Mater. Chem.*, 2009, **19**, 1799-1802.
20. F. Huang, H. Wu, D. Wang, W. Yang and Y. Cao, *Chem. Mater.*, 2004, **16**, 708-716.
21. Y. Kondo, H. Tanabe, H. Kudo, K. Nakano and T. Otake, *Materials*, 2011, **4**, 2171-2182.
22. C. J. Brabec, N. S. Sariciftci and J. C. Hummelen, *Adv. Funct. Mater.*, 2001, **11**, 15-26.
23. G. H. Gelinck, H. E. A. Huitema, E. van Veenendaal, E. Cantatore, L. Schrijnemakers, J. B. P. H. van der Putten, T. C. T. Geuns, M. Beenhakkers, J. B. Giesbers, B.-H. Huisman, E. J. Meijer, E. M. Benito, F. J. Touwslager, A. W. Marsman, B. J. E. van Rens and D. M. de Leeuw, *Nat. Mater.*, 2004, **3**, 106-110.
24. D. Braun and A. J. Heeger, *Appl. Phys. Lett.*, 1991, **58**, 1982-1984.
25. A. O. Patil, Y. Ikenoue, F. Wudl and A. J. Heeger, *J. Am. Chem. Soc.*, 1987, **109**, 1858-1859.
26. H. Jiang, P. Taranekar, J. R. Reynolds and K. S. Schanze, *Angew. Chem. Int. Ed.*, 2009, **48**, 4300-4316.
27. S. Chemburu, E. Ji, Y. Casana, Y. Wu, T. Buranda, K. S. Schanze, G. P. Lopez and D. G. Whitten, *J. Phys. Chem. B*, 2008, **112**, 14492-14499.
28. S. Rochat and T. M. Swager, *ACS Appl. Mater. Interfaces*, 2013, **5**, 4488-4502.
29. A. Gutacker, S. Adamczyk, A. Helfer, L. E. Garner, R. C. Evans, S. M. Fonseca, M. Knaapila, G. C. Bazan, H. D. Burrows and U. Scherf, *J. Mater. Chem.*, 2010, **20**, 1423-1430.
30. L. Ying, P. Zalar, S. D. Collins, Z. Chen, A. A. Mikhailovsky, T.-Q. Nguyen and G. C. Bazan, *Adv. Mater.*, 2012, **24**, 6496-6501.
31. T. Costa, L. E. Garner, M. Knaapila, A. W. Thomas, S. E. Rogers, G. C. Bazan and H. D. Burrows, *Langmuir*, 2013, **29**, 10047-10058.
32. T. Costa, D. de Azevedo, B. Stewart, M. Knaapila, A. J. M. Valente, M. Kraft, U. Scherf and H. D. Burrows, *Polym. Chem.*, 2015, **6**, 8036-8046.
33. J. R. Lakowicz, *Principles of Fluorescence Spectroscopy*, 3rd edn., 2006, p. 1.

34. R. C. Evans, P. Douglas and H. D. Burrows, *Applied Photochemistry*, Springer, 2013, p. 62.
35. R. C. Evans, P. Douglas and H. D. Burrows, *Applied Photochemistry*, Springer, 2013, p. 28.
36. B. Valeur and M. N. Berberan-Santos, *Molecular fluorescence: principles and applications*, John Wiley & Sons, 2012, pp. 20-33.
37. R. C. Evans, P. Douglas and H. D. Burrows, *Applied Photochemistry*, Springer, 2013, p. 54.
38. R. C. Evans, P. Douglas and H. D. Burrows, *Applied Photochemistry*, Springer, 2013, p. 56.
39. R. C. Evans, P. Douglas and H. D. Burrows, *Applied Photochemistry*, Springer, 2013, p. 47.
40. B. Valeur and M. N. Berberan-Santos, *Molecular fluorescence: principles and applications*, John Wiley & Sons, 2012, pp. 34-70.
41. R. C. Evans, P. Douglas and H. D. Burrows, *Applied Photochemistry*, Springer, 2013, p. 72.
42. J. R. Lakowicz, *Principles of Fluorescence Spectroscopy*, Springer, 2006, pp. 443-475.
43. J. R. Lakowicz, *Principles of Fluorescence Spectroscopy*, Springer, 2006, pp. 331-351.
44. B. Valeur and M. N. Berberan-Santos, *Molecular Fluorescence: Principles and Applications*, 2012, pp. 72-123.
45. H. Y. Byun, I. J. Chung, H.-K. Shim and C. Y. Kim, *Macromolecules*, 2004, **37**, 6945-6953.
46. R. C. Evans, *J. Mater. Chem. C*, 2013, **1**, 4190-4200.
47. T. Förster, *Discuss. Faraday Soc.*, 1959, **27**, 7-17.
48. A. C. Grimsdale, K. Leok Chan, R. E. Martin, P. G. Jokisz and A. B. Holmes, *Chem. Rev.*, 2009, **109**, 897-1091.
49. T.-Q. Nguyen, I. B. Martini, J. Liu and B. J. Schwartz, *J. Phys. Chem. B*, 2000, **104**, 237-255.
50. Z. Xu, H. Tsai, H.-L. Wang and M. Cotlet, *J. Phys. Chem. B*, 2010, **114**, 11746-11752.
51. U. Scherf and E. J. W. List, *Adv. Mater.*, 2002, **14**, 477-487.
52. M. Knaapila and A. P. Monkman, *Adv. Mater.*, 2013, **25**, 1090-1108.
53. D. W. Bright, F. B. Dias, F. Galbrecht, U. Scherf and A. P. Monkman, *Adv. Funct. Mater.*, 2009, **19**, 67-73.
54. Z.-Q. Lin, N.-E. Shi, Y.-B. Li, D. Qiu, L. Zhang, J.-Y. Lin, J.-F. Zhao, C. Wang, L.-H. Xie and W. Huang, *J. Phys. Chem. C*, 2011, **115**, 4418-4424.
55. M. Kasha, *Radiat. Res.*, 1963, **20**, 55-70.
56. R. C. Evans, P. Douglas and H. D. Burrows, *Applied Photochemistry*, Springer, 2013, p. 65.
57. T. E. Kaiser, H. Wang, V. Stepanenko and F. Würthner, *Angew. Chem. Int. Ed.*, 2007, **46**, 5541-5544.
58. F. Würthner, T. E. Kaiser and C. R. Saha-Möller, *Angew. Chem. Int. Ed.*, 2011, **50**, 3376-3410.
59. J. R. Lakowicz, *Principles of Fluorescence Spectroscopy*, Springer, 2006, p. 57.
60. A. P. Green, K. T. Butler and A. R. Buckley, *Appl. Phys. Lett.*, 2013, **102**, 133501.
61. E. Aharon, A. Albo, M. Kalina and G. L. Frey, *Adv. Funct. Mater.*, 2006, **16**, 980-986.
62. K. V. Rao, A. Jain and S. J. George, *J. Mater. Chem. C*, 2014, **2**, 3055-3064.
63. G. Kickelbick, in *Hybrid Materials*, Wiley-VCH Verlag GmbH & Co. KGaA, 2007, pp. 1-48.
64. R. C. Evans and P. C. Marr, *Chem. Commun.*, 2012, **48**, 3742-3744.
65. S.-H. Wu, C.-Y. Mou and H.-P. Lin, *Chem. Soc. Rev.*, 2013, **42**, 3862-3875.
66. D. Kuang, T. Brezesinski and B. Smarsly, *J. Am. Chem. Soc.*, 2004, **126**, 10534-10535.
67. P. Kipkemboi, A. Fogden, V. Alfredsson and K. Flodström, *Langmuir*, 2001, **17**, 5398-5402.
68. A. Keller, S. Kirmayer, T. Segal-Peretz and G. L. Frey, *Langmuir*, 2012, **28**, 1506-1514.
69. S. Kirmayer, E. Dovgolevsky, M. Kalina, E. Lakin, S. Cadars, J. D. Epping, A. Fernández-Arteaga, C. Rodríguez-Abreu, B. F. Chmelka and G. L. Frey, *Chem. Mater.*, 2008, **20**, 3745-3756.

70. S. Kirmayer, S. Neyshtadt, A. Keller, D. Okopnik and G. L. Frey, *Chem. Mater.*, 2009, **21**, 4387-4396.
71. S. Neyshtadt, J. P. Jahnke, R. J. Messinger, A. Rawal, T. Segal Peretz, D. Huppert, B. F. Chmelka and G. L. Frey, *J. Am. Chem. Soc.*, 2011, **133**, 10119-10133.
72. T. Segal-Peretz, O. Leman, A. M. Nardes and G. L. Frey, *J. Phys. Chem. C*, 2012, **116**, 2024-2032.
73. M. Kubo, C. Takimoto, Y. Minami, T. Uno, T. Itoh and M. Shoyama, *Macromolecules*, 2005, **38**, 7314-7320.
74. J.-Y. Lee, S.-H. Kim, I.-S. Song and D.-K. Moon, *J. Mater. Chem.*, 2011, **21**, 16480-16487.
75. S. Clement, A. Tizit, S. Desbief, A. Mehdi, J. De Winter, P. Gerbaux, R. Lazzaroni and B. Boury, *J. Mater. Chem.*, 2011, **21**, 2733-2739.
76. C. Sanchez, B. Julian, P. Belleville and M. Popall, *J. Mater. Chem.*, 2005, **15**, 3559-3592.
77. S. Parola, B. Julián-López, L. D. Carlos and C. Sanchez, *Adv. Funct. Mater.*, 2016, **26**, 6506-6544.
78. C. Sanchez, F. Ribot and B. Lebeau, *J. Mater. Chem.*, 1999, **9**, 35-44.
79. C. Sanchez, B. Lebeau, F. Chaput and J. P. Boilot, *Adv. Mater.*, 2003, **15**, 1969-1994.
80. C. Sanchez, P. Belleville, M. Popall and L. Nicole, *Chem. Soc. Rev.*, 2011, **40**, 696-753.
81. J. Berry, T. Buonassisi, D. A. Egger, G. Hodes, L. Kronik, Y.-L. Loo, I. Lubomirsky, S. R. Marder, Y. Mastai, J. S. Miller, D. B. Mitzi, Y. Paz, A. M. Rappe, I. Riess, B. Rybtchinski, O. Stafsudd, V. Stevanovic, M. F. Toney, D. Zitoun, A. Kahn, D. Ginley and D. Cahen, *Adv. Mater.*, 2015, **27**, 5102-5112.
82. T.-Y. Yang, G. Gregori, N. Pellet, M. Grätzel and J. Maier, *Angew. Chem. Int. Ed.*, 2015, **54**, 7905-7910.
83. A. Layek, P. C. Stanish, V. Chirmanov and P. V. Radovanovic, *Chem. Mater.*, 2015, **27**, 1021-1030.
84. D. Wencel, M. Barczak, P. Borowski and C. McDonagh, *J. Mater. Chem.*, 2012, **22**, 11720-11729.
85. N. Willis-Fox, M. Kraft, J. Arlt, U. Scherf and R. C. Evans, *Adv. Funct. Mater.*, 2016, **26**, 532-542.
86. N. Willis-Fox, A.-T. Marques, J. Arlt, U. Scherf, L. D. Carlos, H. D. Burrows and R. C. Evans, *Chem. Sci.*, 2015, **6**, 7227-7237.
87. A. Kaniyoor, B. McKenna, S. Comby and R. C. Evans, *Adv. Opt. Mater.*, 2016, **4**, 444-456.
88. A. A. Argun, P.-H. Aubert, B. C. Thompson, I. Schwendeman, C. L. Gaupp, J. Hwang, N. J. Pinto, D. B. Tanner, A. G. MacDiarmid and J. R. Reynolds, *Chem. Mater.*, 2004, **16**, 4401-4412.
89. M. M. Nolasco, P. M. Vaz, V. T. Freitas, P. P. Lima, P. S. Andre, R. A. S. Ferreira, P. D. Vaz, P. Ribeiro-Claro and L. D. Carlos, *J. Mater. Chem. A*, 2013, **1**, 7339-7350.
90. C. J. Brinker and G. W. Scherer, *Sol-gel science: the physics and chemistry of sol-gel processing*, Academic press, 2013, p. 2.
91. J. S. Duncan, *Introduction to colloid and surface chemistry*, Butterworth Heinemann: New York, 1992.
92. P. W. Voorhees, *J. Stat. Phys.*, 1985, **38**, 231-252.
93. J. D. Wright and N. A. Sommerdijk, *Sol-gel materials: chemistry and applications*, CRC press, 2000, p. 3.
94. I. Meazzini, N. Willis-Fox, C. Blayo, J. Arlt, S. Clement and R. C. Evans, *J. Mater. Chem. C*, 2016, **4**, 4049-4059.
95. V. de Zea Bermudez, L. D. Carlos and L. Alcácer, *Chem. Mater.*, 1999, **11**, 569-580.
96. J. D. Wright and N. A. Sommerdijk, *Sol-gel materials: chemistry and applications*, CRC press, 2000, p. 20.
97. W. Stöber, A. Fink and E. Bohn, *J. Colloid Interface Sci.*, 1968, **26**, 62-69.
98. M. Montalti, L. Prodi, E. Rampazzo and N. Zaccheroni, *Chem. Soc. Rev.*, 2014, **43**, 4243-4268.
99. C. Sanchez and B. Lebeau, *MRS Bull.*, 2001, **26**, 377-387.
100. T. D. d. Morais, F. Chaput, K. Lahlil and J. P. Boilot, *Adv. Mater.*, 1999, **11**, 107-112.

101. L. D. Carlos, V. de Zea Bermudez, R. A. S. Ferreira, L. Marques and M. Assunção, *Chem. Mater.*, 1999, **11**, 581-588.
102. L. D. Carlos, R. A. S. Ferreira, V. De Zea Bermudez and S. J. L. Ribeiro, *Adv. Funct. Mater.*, 2001, **11**, 111-115.
103. P. Huntsman International LLC, http://www.huntsman.com/performance_products/a/Products.
104. M. C. Gonçalves, V. de Zea Bermudez, R. A. Sá Ferreira, L. D. Carlos, D. Ostrovskii and J. Rocha, *Chem. Mater.*, 2004, **16**, 2530-2543.
105. V. T. Freitas, P. P. Lima, V. de Zea Bermudez, R. A. S. Ferreira and L. D. Carlos, *Eur. J. Inorg. Chem.*, 2012, **2012**, 5390-5395.
106. L. D. Carlos, R. A. S. Ferreira, R. N. Pereira, M. Assunção and V. de Zea Bermudez, *J. Phys. Chem. B*, 2004, **108**, 14924-14932.
107. R. D. Miller and J. Michl, *Chem. Rev.*, 1989, **89**, 1359-1410.
108. W. H. Green, K. P. Le, J. Grey, T. T. Au and M. J. Sailor, *Science*, 1997, **276**, 1826-1828.
109. M. Stutzmann, M. S. Brandt, M. Rosenbauer, J. Weber and H. D. Fuchs, *Phys. Rev. B*, 1993, **47**, 4806-4809.
110. V. C. Costa, M. J. Lochhead and K. L. Bray, *Chem. Mater.*, 1996, **8**, 783-790.
111. E. Cordoncillo, F. J. Guaita, P. Escribano, C. Philippe, B. Viana and C. Sanchez, *Opt. Mater.*, 2001, **18**, 309-320.
112. R. A. S. Ferreira, A. L. Ferreira and L. D. Carlos, *J. Non-Cryst. Solids*, 2006, **352**, 1225-1229.
113. P. P. Lima, F. A. Almeida Paz, R. A. S. Ferreira, V. de Zea Bermudez and L. D. Carlos, *Chem. Mater.*, 2009, **21**, 5099-5111.
114. M. E. Mesquita, S. S. Nobre, M. Fernandes, R. A. S. Ferreira, S. C. G. Santos, M. O. Rodrigues, L. D. Carlos and V. de Zea Bermudez, *J. Photoch. Photobio. A*, 2009, **205**, 156-160.
115. L. D. Carlos, R. A. S. Ferreira, V. de Zea Bermudez and S. J. L. Ribeiro, *Adv. Mater.*, 2009, **21**, 509-534.
116. P. P. Lima, S. A. Junior, O. L. Malta, L. D. Carlos, R. A. S. Ferreira, R. Pavithran and M. L. P. Reddy, *Eur. J. Inorg. Chem.*, 2006, **2006**, 3923-3929.
117. D. Saikia, H.-Y. Wu, Y.-C. Pan, C.-C. Liao, C.-F. Chen, G. T. K. Fey and H.-M. Kao, *Electrochim. Acta*, 2009, **54**, 7156-7166.
118. D. Saikia, Y.-H. Chen, Y.-C. Pan, J. Fang, L.-D. Tsai, G. T. K. Fey and H.-M. Kao, *J. Mater. Chem.*, 2011, **21**, 10542-10551.
119. F. G. Braun, E. Hooper, R. Wand and P. Zloczysti, *Energy Policy*, 2011, **39**, 2441-2456.
120. *Directive 2010/31/EU of the European parliament and of the council of 19 May 2010 on the energy performance of buildings.*
121. J. Aghaei and M.-I. Alizadeh, *Renew. Sustainable Energy Rev.*, 2013, **18**, 64-72.
122. M. G. Debije and P. P. C. Verbunt, *Adv. Energ. Mater.*, 2012, **2**, 12-35.
123. J. S. Batchelder, A. H. Zewai and T. Cole, *Appl. Opt.*, 1979, **18**, 3090-3110.
124. B. McKenna and R. C. Evans, *Adv. Mater.*, 2017, **29**, n/a-n/a.
125. M. Debije, *Nature*, 2015, **519**, 298-299.
126. W. G. J. H. M. van Sark, *Renew. Energy*, 2013, **49**, 207-210.
127. F. M. Vossen, M. P. Aarts and M. G. Debije, *Energ. Buildings*, 2016, **113**, 123-132.
128. G. D. Gutierrez, I. Coropceanu, M. G. Bawendi and T. M. Swager, *Adv. Mater.*, 2016, **28**, 497-501.
129. J. L. Banal, H. Soleimaninejad, F. M. Jradi, M. Liu, J. M. White, A. W. Blakers, M. W. Cooper, D. J. Jones, K. P. Ghiggino, S. R. Marder, T. A. Smith and W. W. H. Wong, *J. Phys. Chem. C*, 2016, **120**, 12952-12958.
130. P. T. M. Albers, C. W. M. Bastiaansen and M. G. Debije, *Solar Energy*, 2013, **95**, 216-223.
131. S. Tsoi, D. J. Broer, C. W. M. Bastiaansen and M. G. Debije, *Adv. Energ. Mater.*, 2013, **3**, 337-341.
132. S. F. H. Correia, P. P. Lima, E. Pecoraro, S. J. L. Ribeiro, P. S. André, R. A. S. Ferreira and L. D. Carlos, *Prog. Photovolt. Res. App.*, 2016, **24**, 1178-1193.
133. B. G. Ranby and J. F. Rabek, *Photodegradation, photo-oxidation, and photostabilization of polymers*, New York, Wiley, 1975.

134. J. Wiegman and E. Van Der Kolk, *Sol. Energy Mater. Sol. Cells*, 2012, **103**, 41-47.
135. V. Fattori, M. Melucci, L. Ferrante, M. Zambianchi, I. Manet, W. Oberhauser, G. Giambastiani, M. Frediani, G. Giachi and N. Camaioni, *Energy Environ Sci.*, 2011, **4**, 2849-2853.
136. M. Melucci, M. Durso, L. Favaretto, M. L. Capobianco, V. Benfenati, A. Sagnella, G. Ruani, M. Muccini, R. Zamboni, V. Fattori and N. Camaioni, *RSC Adv.*, 2012, **2**, 8610-8613.
137. M. Buffa, S. Carturan, M. G. Debije, A. Quaranta and G. Maggioni, *Sol. Energy Mater. Sol. Cells*, 2012, **103**, 114-118.
138. C. Pham-Van-Cang, M. A. Winnik, R. Dorigo and S. Boileau, *Eur. Polym. J.*, 1995, **31**, 227-231.
139. C. M. S. Vicente, R. A. S. Ferreira, E. Pecoraro, P. S. André and L. D. Carlos, *J. Sol-Gel Sci. Technol.*, 2011, **59**, 475-479.
140. C. M. S. Vicente, E. Pecoraro, R. A. S. Ferreira, P. S. André, R. Nogueira, Y. Messaddeq, S. J. L. Ribeiro and L. D. Carlos, *J. Sol-Gel Sci. Technol.*, 2008, **48**, 80.
141. D. C. Oliveira, A. G. Macedo, N. J. O. Silva, C. Molina, R. A. S. Ferreira, P. S. André, K. Dahmouche, V. D. Z. Bermudez, Y. Messaddeq, S. J. L. Ribeiro and L. D. Carlos, *Chem. Mater.*, 2008, **20**, 3696-3705.
142. S. F. H. Correia, P. P. Lima, P. S. André, M. R. S. Ferreira and L. A. D. Carlos, *Sol. Energy Mater. Sol. Cells*, 2015, **138**, 51-57.
143. R. Rondão, A. R. Frias, S. F. H. Correia, L. Fu, V. de Zea Bermudez, P. S. André, R. A. S. Ferreira and L. D. Carlos, *ACS Appl. Mater. Interfaces*, 2017, **9**, 12540-12546.
144. J. Graffion, A. M. Cojocariu, X. Cattoen, R. A. S. Ferreira, V. R. Fernandes, P. S. Andre, L. D. Carlos, M. Wong Chi Man and J. R. Bartlett, *J. Mater. Chem.*, 2012, **22**, 13279-13285.
145. V. K. LaMer and R. H. Dinegar, *J. Am. Chem. Soc.*, 1950, **72**, 4847-4854.
146. N. T. K. Thanh, N. Maclean and S. Mahiddine, *Chem. Rev.*, 2014, **114**, 7610-7630.
147. S. Fouilloux, A. Désert, O. Taché, O. Spalla, J. Daillant and A. Thill, *J. Colloid Interface Sci.*, 2010, **346**, 79-86.
148. E. Ruckenstein and Y. S. Djikaev, *Adv. Colloid Interface Sci.*, 2005, **118**, 51-72.
149. D. Li and R. B. Kaner, *J. Am. Chem. Soc.*, 2006, **128**, 968-975.
150. J. D. Rimer, R. F. Lobo and D. G. Vlachos, *Langmuir*, 2005, **21**, 8960-8971.
151. K. Ueno, A. Inaba, M. Kondoh and M. Watanabe, *Langmuir*, 2008, **24**, 5253-5259.
152. S.-W. Ha, C. E. Camalier, G. R. Beck Jr and J.-K. Lee, *Chem. Commun.*, 2009, 2881-2883.
153. T. Andreani, A. L. R. de Souza, C. P. Kiill, E. N. Lorenzón, J. F. Fangueiro, A. C. Calpena, M. V. Chaud, M. L. Garcia, M. P. D. Gremião and A. M. Silva, *Int. J. Pharm.*, 2014, **473**, 627-635.
154. R. Ghosh Chaudhuri and S. Paria, *Chem. Rev.*, 2012, **112**, 2373-2433.
155. D. Ma, A. J. Kell, S. Tan, Z. J. Jakubek and B. Simard, *J. Phys. Chem. C*, 2009, **113**, 15974-15981.
156. H. Ow, D. R. Larson, M. Srivastava, B. A. Baird, W. W. Webb and U. Wiesner, *Nano Lett.*, 2005, **5**, 113-117.
157. G. Alberto, I. Miletto, G. Viscardi, G. Caputo, L. Latterini, S. Coluccia and G. Martra, *J. Phys. Chem. C*, 2009, **113**, 21048-21053.
158. E. Herz, A. Burns, D. Bonner and U. Wiesner, *Macromol. Rapid Commun.*, 2009, **30**, 1907-1910.
159. A. A. Burns, J. Vider, H. Ow, E. Herz, O. Penate-Medina, M. Baumgart, S. M. Larson, U. Wiesner and M. Bradbury, *Nano Lett.*, 2009, **9**, 442-448.
160. R. Kumar, I. Roy, T. Y. Ohulchanskyy, L. N. Goswami, A. C. Bonoiu, E. J. Bergey, K. M. Tramposch, A. Maitra and P. N. Prasad, *ACS Nano*, 2008, **2**, 449-456.

Chapter Two

Experimental

2.1 Materials

2.1.1 General Chemicals

Jeffamine T-403, Jeffamine T-5000 and Jeffamine D-4000 were a kind gift from Huntsman International (www.huntsman.com). *O,O'*-Bis(2-aminopropyl) polypropylene glycol-*block*-polyethylene glycol-*block*-polypropylene glycol (Jeffamine ED-600), 3-isocyanatopropyltriethoxysilane (ICPTES, 95%), ethanol (EtOH, HPLC grade), hydrochloric acid (37% puriss), potassium bromide (FTIR grade), deuterated chloroform ($CDCl_3$) (99.8%), tetrahydrofuran (THF, HPLC grade), tetraethylorthosilicate (TEOS, ≥ 99%), (3-aminopropyl)triethoxysilane (APTES, 99%) were procured from Sigma Aldrich and used as received. Ammonium hydroxide (NH_4OH, 5.01 N solution) was purchased from Fluka and used as received.

2.2 Instrumentation

2.2.1 Powder X-Ray Diffraction (PXRD)

PXRD measurements were performed on a Bruker D2 Phaser diffractometer. The samples were exposed to the Cu K_α radiation (λ = 1.54 Å) at room temperature (RT) and measured using [100] silicon substrate to minimise background scattering. Sample were prepared by grinding the material, which was then placed onto the support. The investigated 2θ range is 5°−70°.

2.2.2 Fourier Transform Infrared (FTIR) Spectroscopy

FTIR spectra were measured on a PerkinElmer spectrum 100 FTIR spectrometer at RT and collected over a range of 4000−650 cm^{-1}, averaging 64 scans and with a resolution of 4 cm^{-1}. In a standard sample preparation, potassium bromide (175 mg) was mixed with the finely ground sample (~2 mg) and pressed into pellets.

2.2.3 Thermogravimetric Analysis (TGA)

TGA was performed using a PerkinElmer Pyris TGA thermogravimetric analyser in an air atmosphere between 30 and 900 °C, with a heating rate of 10 °C min^{-1} and using *ca.* 2-3 mg of sample placed in a ceramic crucible.

2.2.4 Solid-State Nuclear Magnetic Resonance (ss-NMR)

^{29}Si and ^{13}C cross-polarised (CP) and directly-excited (DE) magic angle spinning (MAS) NMR measurements were performed at the EPSRC National Solid-State NMR Service at Durham University by Dr. David Apperley, on a Varian VNMRS instrument operating at 79.44 MHz for ^{29}Si and 100.56 MHz for ^{13}C. Spectra were recorded at RT, against an external tetramethylsilane (TMS) standard with MAS rate of 6000 Hz. Additional ^{29}Si and ^{13}C CP and DE MAS-NMR measurements presented in **Chapter 3,** were performed by Dr. Manuel Ruether at the NMR Spectroscopy Facility of Trinity College Dublin, using an Agilent 800 MHz DD2 spectrometer operating at 158.9 MHz for ^{29}Si and 201.1 MHz for ^{13}C at 20 °C. Spectra were recorded against an external TMS standard with a MAS rate of 4200 Hz. Chemical shifts are reported in parts per million (ppm).

2.2.5 Solution Phase NMR

Solution phase ^{1}H NMR spectra were recorded on a Bruker DPX 400 spectrometer (400 MHz) on samples dissolved in $CDCl_3$ with the assistance of Dr. John O'Brien. Chemical shifts are reported in ppm.

2.2.6 Mass Spectrometry

Mass spectrometry (MS) was performed by Dr. Martin Feeney with a Q-ToF Premier Waters MALDI-quadrupole time-of-flight spectrometer equipped with a matrix-assisted laser desorption-ionisation (MALDI) source, using Glu-1-Fibrinopetide B as the MALDI matrix (reference peak of mass/charge, m/z = 1570.6774). Electrospray ionisation (ESI) mass spectrometry was performed on an ESI-TOF Q instrument in positive mode.

2.2.7 UV/Vis Absorption and Steady-State Photoluminescence (PL) Spectroscopy

UV/Vis absorption spectra on solutions were recorded in a quartz cell with a 10 mm pathlength, using either a Perkin Elmer Lambda 1050 UV/Vis scanning spectrometer with a slit width of 1 mm or a Varian Carey 50 spectrometer with a slit width of 2 nm. Solid-state steady-state PL spectroscopy measurements were performed on a Fluorolog-3 spectrometer (Horiba Jobin Yvon) using the front-face configuration. Liquid-state samples were measured using a quartz cell

of 10 mm pathlength with a FluoroMax-4 spectrophotometer (Horiba Jobin Yvon) in the right-angle configuration. The emission and excitation slits were varied depending on the different sample analysed. The emission and the excitation spectra were corrected for the wavelength response of the system and the intensity of the lamp profile over the excitation range, respectively, using the correction factors provided by the manufacturer.

2.2.8 Steady-State Fluorescence Anisotropy

Steady-state fluorescence anisotropy experiments were carried out using a Jobin-Yvon Fluorolog-3 spectrometer with right angle geometry and excitation and emission slits of 2 and 1 nm, respectively. The fluorescence anisotropy, $< r >$, is determined from:

$$< r >= \frac{I_{\parallel} - GI_{\perp}}{I_{\parallel} + 2GI_{\perp}} \qquad (\mathbf{2.1})$$

where $I_{\parallel}$ and $I_{\perp}$ are the fluorescence intensities of the vertically ($\parallel$) and horizontally ($\perp$) polarised emission when the sample is excited with vertically polarised light. Only fluorophores with a component of their absorption transition dipole moments parallel to the incoming polarised light can undergo absorption. This phenomenon is known as photoselection, and it is only from this sub-set of the molecular population that fluorescence can subsequently occur. In a perfectly aligned, rigid system in which the absorption and emission transition dipole moments are colinear, photoselection will result in highly polarised emission and the anisotropy takes a maximum value of 0.4. Fluorescence depolarisation can result from a variety of factors including rotational diffusion, reabsorption and scattering. The *G* factor corrects for the anisotropic nature of the emission polariser and is given by $G = I_{hv}/I_{hh}$, where $I_{\mathrm{ex,em}}$ is the emission intensity and *v* and *h* denote the vertical and horizontal alignment of the polarisers. *G* is experimentally determined by recording the polarised emission from a totally isotropic solution whose emission spectrum coincides with the system under investigation.

2.2.9 Photoluminescence Quantum Yield

Φ_{PL} were measured using a F-3018 integrating sphere accessory mounted on a FluoroMax-4 spectrophotometer (Horiba Jobin Yvon). The values reported are the average of three repeat

measurements and the method is accurate within 10%.[1] For solid-state samples, the Φ_{PL} values were corrected for self-absorption as described in **Section 2.3.3**.

2.2.10 Time-Correlated Single Photon Counting (TCSPC)

Fluorescence decays were measured by Camille Blayo and Dr. Rachel Evans using the picosecond time-correlated single photon counting (TCSPC) method at the Collaborative Optical Spectroscopy, Micromanipulation and Imaging Centre (COSMIC), University of Edinburgh, U.K. The excitation source was the second harmonic of the pulse-picked output of a Ti-Sapphire femtosecond laser system (Coherent, 10 W Verdi and Mira Ti-Sapphire), delivering pulses of ≈200 fs at 4.75 MHz repetition rate. Fluorescence decays were measured using an Edinburgh Instruments spectrometer equipped with TCC900 photon-counting electronics. The instrument response of the system was ≈90 ps full-width-half-maximum (FWHM). The decay curves were analysed using a standard iterative reconvolution method, assuming a multi-exponential decay function. Reconvolution and fitting of the fluorescence decays were carried out using Globals WE software package. The quality of fit was judged on the basis of the reduced chi-square statistic, χ^2, and the randomness of residuals. The fitting process is reported in **Section 2.3.4**.

2.2.11 Dynamic Light Scattering (DLS) and ζ-Potential

DLS and ζ-potential measurements were performed using a Zetasizer Nano series nano-ZS (Malvern Instruments, U.K.). The apparatus is equipped with a He-Ne laser (λ_{em}= 633 nm, power source 4.0 mW). DLS measurements were performed using the apparatus in a back-scattering configuration (175°). The hydrodynamic diameters (D_h) were calculated assuming that the shape of the particle diffusing in solution is a sphere and the reported D_h values are the mean of 3 runs of approximately 15 measurements each. The hydrodynamic radius (R_h) or diameter (D_h) used in the Stokes-Einstein equation

$$D = \frac{k_B T}{6\pi\eta R_h} \qquad (\mathbf{2.2})$$

to yield the diffusion coefficient, D, where k_B is the Boltzmann constant, T is the temperature, η is the viscosity of the medium. Cumulants analysis, a fit of the logarithm of the correlation function is

used to obtain the diffusion coefficient and a mean value for the size, together with a parameter for the size distribution. For the ζ-potential measurements, the electrophoretic mobility was recorded using a Laser-Doppler unit in the DLS machine. The ζ was calculated from the electrophoretic mobility, μ, using the Henry correction of the Smoluchowski's equation:[2]

$$\zeta = \frac{4\pi\eta}{\varepsilon^0}\,\mu \qquad \textbf{(2.3)}$$

where ε^0 represents the static dielectric permittivity.

2.2.12 Atomic force microscopy (AFM)

AFM measurements were performed by Dr. Judith Houston using an Asylum Research MFP-3D^{TM} Atomic Force Microscope mounted on an anti-vibration plinth, in the tapping mode at room temperature under ambient conditions. The silicon cantilevers used were 125 μm long, with a resonance frequency of ~150 kHz. The raw AFM images were visualised and analysed using the Gwyddion 2.31 software.

2.2.13 Optical Efficiency Measurements

The optical efficiency of the LSC was measured by illuminating the samples with a Class ABB solar simulator (Abet Technologies, Model 10500) equipped with an AM 1.5 filter, using a procedure previously reported in literature.[3] A black mask with a circular aperture (area 9.6 cm^2) was used to define the illumination area of the sample and the emission from each of the four edges was measured using a INS 125 integrating sphere coupled with a spectroradiometer (International Light Techonologies ILT950). The analysis of the data was performed with SpetrIlLight III software with the manufacturer provided calibration file for the optical power (ILT1007131U1NS125). The solar simulator was calibrated to 1 Sun (995 ± 3 W m^{-2}) using a reference silicon solar cell from ReRa Technologies. The output of the solar simulator was also measured using the spectroradiometer set-up and illuminating a circular input port of 2 cm diameter placed on the integrating sphere, which enabled accurate calculation of the power input to the LSC samples. With this method, the integrated power measured in the 250-1050 nm spectrum range, reaching the 9.6 cm^2 illuminated area of each samples is 887.0 mW.

2.3 Data Analysis

2.3.1 Non-Linear Least Square (NLLS) Fits

The fitting procedures presented in this work use non-linear least square fitting routines. This analysis requires a model that is believed to be followed by the data.[4] Upon selection of this model, the NLLS analysis will determine whether the latter is consistent with the data and the values of the parameters which will provide the best match between the measured data, y_i, and the fitted model, f_{ic}, using assumed initial parameter values. Matching between the model and the data is achieved by minimisation of the goodness-of-fit parameter, χ^2:

$$\chi^2 = \sum_{i=1}^{n} \left[\frac{y_i - f_{ic}}{\sigma_i}\right]^2 \quad \textbf{(2.4)}$$

where σ_i is the standard deviation, n is the number of data points and (y_i - f_{ic}) represents the actual deviation of the data from the fit. If the standard deviation of the experimental data from the model is proportional to the values of the data, then $\sigma_i{}^2 = y_i$ and the following equation can be stated:

$$\chi^2 = \sum_{i=1}^{n} \frac{(y_i - f_{ic})^2}{y_i} \quad \textbf{(2.5)}$$

Thus, the value of χ^2 is the sum of the squared deviations between the experimental data, y_i, and the value expected from the model, f_{ic}, divided by the square of the measured data. The fit is then run iteratively until the smallest possible sum of squares is obtained. The iteration process for the fit involves the incremental changes in the fitting parameters for each subsequent fit, to find the minimum value of χ^2. A good fit is represented by a χ^2 value of 1.

2.3.2 Gaussian Peak Fitting

2.3.2.1 ss-NMR Spectra

The degree of condensation of the siliceous network of the ureasils was calculated using Gaussian fits for each of the peaks corresponding to each of the T_n signals observed in the ^{29}Si MAS-NMR using the OriginPro 8.5 (Microcal) software (see **Section 2.4.2** for detailed explanation). The form of the Gaussian peak is given by the following equation:

$$y = y_0 + \frac{A}{w\sqrt{\frac{\pi}{2}}} e^{-2\frac{(x-x_c)^2}{w^2}} \quad \textbf{(2.6)}$$

where y_0 is the off-set from the baseline y, w is the width of the peak, x_c is the centre of the peak and A is the area of the peak.

2.3.2.2 FTIR Spectra

FTIR measurements in the Amide I region were performed to analyse the local hydrogen bonding interactions associated with the stretching of the C=O moieties of the urea groups. The deconvolution of this region (1600-1800 cm^{-1}) was performed by fitting multiple Gaussian bands using the Origin Pro 8.5 (Microcal) software. The shape of the peak is described by **Eqn. 2.6** and the quality of all Gaussian fits were assessed qualitatively by comparison of the cumulative fit peak (given by the sum of the intensity of each of the fitted peaks at a given x value) to the raw data.

2.3.2.3 PXRD Diffractograms

Gaussian fitting was performed on the PXRD diffractograms to investigate the local order of the siliceous framework of the ureasils (see **Section 2.4.3**). The fits were performed by fitting multiple Gaussian bands using the Origin Pro 8.5 (Microcal) software and the shape of the peak is described by **Eqn. 2.6**. The quality of all Gaussian fits were assessed qualitatively by comparison of the cumulative fit peak (given by the sum of the intensity of each of the fitted peak at a given x value) to the raw data.

2.3.3 Calculation of Φ_{PL}

Φ_{PL} measurements, were performed using an integrating sphere, with a method developed by Horiba specifically for the F-3018 accessory, consisting of a modification of that reported by de Mello *et al.*[9] The measured values for the soli-state samples were then corrected for reabsorption and waveguiding effects following a procedure optimised by Ahn and co-workers.[5, 6] The general expression used for the calculation of Φ_{PL} is shown in **Eqn. 2.7**:[7]

$$\phi_{PL} = \frac{\int^{cp} I(\lambda)d\lambda}{\int^{SA} I(\lambda)d\lambda - \int^{SS} I(\lambda)d\lambda \cdot 10^{\Delta OD(\lambda ex)}} \quad \textbf{(2.7)}$$

where ($\int {}^{cp}I(\lambda)d\lambda$) is the integrated area under the emission peak of the sample, ($\int {}^{SA}I(\lambda)d\lambda$) and ($\int {}^{SS}I(\lambda)d\lambda$) are the integrated areas under the Rayleigh peak of the empty sphere and the compound, respectively. As the emission of the sample is much weaker than the scattered excitation light (Rayleigh peak), the spectra were recorded using a neutral density (ND) filter to attenuate the emission intensity at the λ_{ex}. This is taken into consideration in **Eqn. 2.**7 by ($10^{\Delta OD(\lambda ex)}$) which represents the filter transmittance at the λ_{ex}. To measure the integrated area under the Rayleigh peak of the empty sphere ($\int {}^{SA}I(\lambda)d\lambda$) the selected ND filter was placed in front of the emission port and the excitation monochromator set at λ_{ex}. The emission was recorded in the range of wavelength between (λ_{ex} – 10 nm) to (λ_{ex} + 10 nm). To measure the integrated area under the emission of the sample compound ($\int {}^{cp}I(\lambda)d\lambda$), the ND filter was removed and the spectrum was recorded. Then, the emission filter was inserted in the emission port and the integrated area under the Rayleigh peak of the emission spectra of the investigated compounds, ($\int {}^{SS}I(\lambda)d\lambda$) , was measured between (λ_{ex} – 10 nm) and (λ_{ex} + 10 nm).

In the method described by de Mello,[5] three measurements were performed for the calculation of the Φ_{PL}: (a) with the empty sphere, (b) with the sample placed into the sphere and the beam directed to the wall of the sphere and (c) with the beam directed onto the sample. The value of Φ_{PL} is expressed by the following equation:

$$\phi_{PL} = \frac{P_c - (1 - A)P_b}{L_a A} \quad \textbf{(2.8)}$$

where P_c is the area under the emission profile recorded for experiment (c), A is the incident light absorbed by the sample in experiment (c), (1-A) is the fraction of the light transmitted or reflected from the sample in experiment (c), P_b is the area under the emission profile recorded for experiment (b) and L_a is the area under the Rayleigh peak in experiment (a). In the modification of the method proposed by Horiba, the fraction of the beam scattered from the sphere and absorbed by the sample is considered equal to 0. Therefore, L_a is equal to the area under the Rayleigh peak in experiment (b) (L_b) and P_b corresponds to 0. **Eqn. 2.8** can then be expressed by:

$$\phi_{PL} = \frac{P_c}{L_a A} \quad \textbf{(2.9)}$$

Following de Mello's calculations, the value of *A* can be expressed by:

$$A = \left(1 - \frac{L_c}{L_a}\right) \quad \textbf{(2.10)}$$

and where L_c represents the area under the Rayleigh peak calculated in experiment (c)

By substituting and re-arranging **Eqn 2.8**, we obtain the following expression for the calculation of the Φ_{PL}:

$$\phi_{PL} = \frac{P_c}{L_a - L_c} \quad \textbf{(2.11)}$$

which corresponds to the general expression of Φ_{PL} reported in **Eqn. 2.7**.

The measured values were then corrected for self-absorption and waveguiding effects; these phenomena occur when there is an overlap between the absorption and emission spectra.[6] In the correction method described by Ahn it is assumed that in the red-edge portion of the emission spectrum of the sample, neither of these effects are present.[6] Therefore, in this region of the spectrum, the shape of the emission profile of the fluorophore in the solid state, matches that of the fluorophore in a dilute solution of a good solvent, also known as the true spectrum, *F(λ)*.[6] The long wavelength emission can therefore be described as:

$$F'(\lambda) = \frac{F(\lambda)}{1 - a\,(\Phi_{PL})} = \alpha F(\lambda) \quad \textbf{(2.12)}$$

where *F(λ)* is the photoluminescence spectrum expressed in photons per wavelength, normalised to $\int_0^\infty F(\lambda)\, d\lambda = 1$ and a is the probability of self-absorption of an emitted photon. The factor α represents a scaling coefficient for the true spectrum, *F(λ)*, which becomes an enhanced spectrum *F'(λ)*, whose red-edge emission is matched to that of the observed PL spectrum, $F_{obs}(\lambda)$. From this, the probability of self-absorption of an emitted photon, a, is determined with the following equation:

$$\frac{\int_0^\infty F_{obs}(\lambda) d\lambda}{\int_0^\infty F'\ \ (\lambda) d\lambda} = 1 - a \quad \textbf{(2.13)}$$

which provides the equation for the corrected value of photoluminescence quantum yield:

$$\Phi_{PL} = \frac{\Phi_{obs}}{1 - a + a\,\Phi_{obs}} \quad \textbf{(2.14)}$$

where $\int_0^\infty F_{obs}(\lambda)d\lambda = \Phi_{obs}$.

2.3.4 Fluorescence Decay Fitting

2.3.4.1 Fluorescence Lifetime Theory

In an ideal case, the measurement of the fluorescence lifetime of a fluorophore consists of the excitation of the species with an infinitely sharp (δ-function) pulse of light.[8] This will promote the excitation of n_0 fluorophore units from the ground to an excited state, whose population will decay with the following rate:

$$\frac{dn(t)}{dt} = (k_{rad} + k_{nr})\, n(t) \quad \textbf{(2.15)}$$

where *n(t)* represents the number of fluorophore units in the excited state at time *t* after the excitation, k_{rad} is the radiative decay rate and k_{nr} is the non-radiative decay rate. Since the emission is a spontaneous and random event, each fluorophore in the excited state has an equal possibility of emitting in a certain period of time, meaning that the decay of the excited state population can be expressed by an exponential function:

$$n(t) = n_0 \exp(-t/\tau) \quad \textbf{(2.16)}$$

where τ is the lifetime of the excited state. **Eqn. 2.16** can be expressed as a function of the fluorescence intensity, *I*, which is measured during the experiment and is proportional to *n(t)*:

$$I(t) = I_0 \exp(-t/\tau) \quad \textbf{(2.17)}$$

where I_0 corresponds to the fluorescence intensity at time $t = 0$. The characteristic lifetime of the fluorophore, τ, is given by the inverse of the total decay rate, $\tau = (k_{rad} + k_{nr})^{-1}$. The fluorescence lifetime can be calculated by extrapolation of the slope of a plot consisting of Log *I(t) vs. t*, or by fitting of the data to an assumed model. **Eqn. 2.18** refers to the decay of a single-component system; however the systems investigated in this work often present a multi-exponential decay, represented by the following equation:

$$I(t) = \sum_i \alpha_i \exp(-t/\tau_i) \quad \textbf{(2.18)}$$

where α_i and τ_i are the pre-exponential factor and characteristic lifetime for i^{th} component, respectively. For this model, the total intensity is considered to arise from the sum of individual single exponential decays. For a single fluorophore displaying a complex decay it can be assumed that the fluorophore has the same radiative decay rate in each environment. Thus, in this case α_i represents the fraction of molecules in each environment at $t = 0$.[9] The average fluorescence lifetime $<\tau>$ can then be calculated from:

$$<\tau> = \frac{\sum \alpha_i \tau_i^2}{\sum \alpha_i \tau_i} \quad \textbf{(2.19)}$$

2.3.4.2 Reconvolution of Decay Data

In practice, the excitation pulse is not infinitely short and the response time of the detection system is not immediate. These factors define the width and the shape of the instrument response function (IRF), which represents the response of the instrument to a zero lifetime sample. Since in reality it is impossible to excite the sample with an infinitely sharp excitation pulse (δ-function) or to have a δ-function for the instrument response, the measured data is a convolution of the sample response and the lamp function.[4]

When the half-width of the IRF is comparable to the lifetime of the process under investigation, the initial part of the decay measurement deviates from the theoretical sample function, *I(t)*. In this case, the sample response function, *I'(t)* represents a convolution of the excitation pulse *E(t)* with *I(t)*. Thus, to obtain information about the sample at very short times it is necessary to reconvolute the signal using the convolution integral:

$$I'(t) = \int_0^t E(t')I(t-t')dt' \quad \textbf{(2.20)}$$

Apart from random noise, *I(t)* fully describes the measured data, *i.e.* the initial rise and subsequent decay of the measurement. This equation states that the experimentally measured intensity at time *t* is given by the sum of the intensities expected for all the δ-function excitation pulses occurring until time *t*, if the excitation pulse is considered to be formed from a series of δ-functions with

different amplitudes. This model is then fitted to the measured decay through NLLS analysis (**Section 2.3.1**). During the fitting, α_i and τ_i are varied until the value of χ^2 reaches a minimum, in order to match as closely as possible the value of the data, y_i, with the fitted point, f_{ic}.

χ^2 depends on the number of data points and its value is larger for larger data set. For this reason, the reduced χ^2 (χ_r^2) is generally preferred to evaluate the quality of TCSPC fits:

$$\chi_r^2 = \frac{\chi^2}{n-p} = \frac{\chi^2}{v} \qquad \textbf{(2.21)}$$

where n is the number of data points, p is the number of floating parameters and v is the number if degrees of freedom. For TCSPC, n is much larger than p, so that n-p can be approximated to n. If the fit is affected only by random errors, the value of χ^2 is close to unity; if the model is is a poor fit to the data, this value is expected to be much higher. The overall quality of the fit is judged by the value of the reduced χ^2 and the randomness of the residuals, which are the vertical deviation of the measured data points from the fitted curve. Non-random behaviour in the residuals plot suggests a poor fit or a hidden variable.

2.4 Structural Characterisation of Ureasil Hybrids

The structural characterisation of ureasils provides important information regarding the local organisation of the silica network within the hybrids and the possibility of changes in this arrangement upon incorporation of the fluorophores.[10, 11] For ureasils, a satisfactory overview of the structural features of the material can be provided by using a combination of techniques, in particular: FTIR in the Amide I region, ^{29}Si and ^{13}C MAS-NMR and PXRD.

2.4.1 FTIR in the Amide I Region

The detailed analysis of the Amide I region in the FTIR spectrum (1600-1800 cm^{-1}) for ureasils, was firstly proposed by Bermudez *et al.* in 1999.[12] This highly complex vibrational region, gives direct insight into the stretching vibrations of the C=O moieties which are affected by the extent and the specificity of H-bonding within the hybrid structure. Thus, the interactions between the carbonyl oxygen atom with hydrogen bonding N-H groups of the urea linkages and/or the oxygen atoms of the Jeffamine segments can be detected and quantified.[6, 12-14] A typical

Gaussian curve-fit performed on the Amide I region of a ureasil sample, consists of either three or four contributions: Peak 1, roughly centred at 1635 cm^{-1}, represents the C=O moieties involved in ordered urea-urea structures; Peak 2 and Peak 3 (centred at ~1660 and ~1710 cm^{-1}, respectively) corresponding to the urea-polyether disordered interactions of increasing strength and Peak 4 (~1760 cm^{-1}), which indicates the presence of urea moieties not involved in any hydrogen bonding interactions (**Fig. 2.1**). Depending on the Jeffamine used and on the reaction conditions, the extent of each one of these contributions can vary, leading eventually to the need for more than four Gaussians to model the spectrum.[10, 14] For this work, the investigation of the FTIR of ureasils was conducted to analyse potential changes into the network structure upon incorporation of the fluorophores and to gain a deeper understanding of the role of the host structure on the arrangement of the emitters and on the relationship between the latter and the optical properties of the materials.

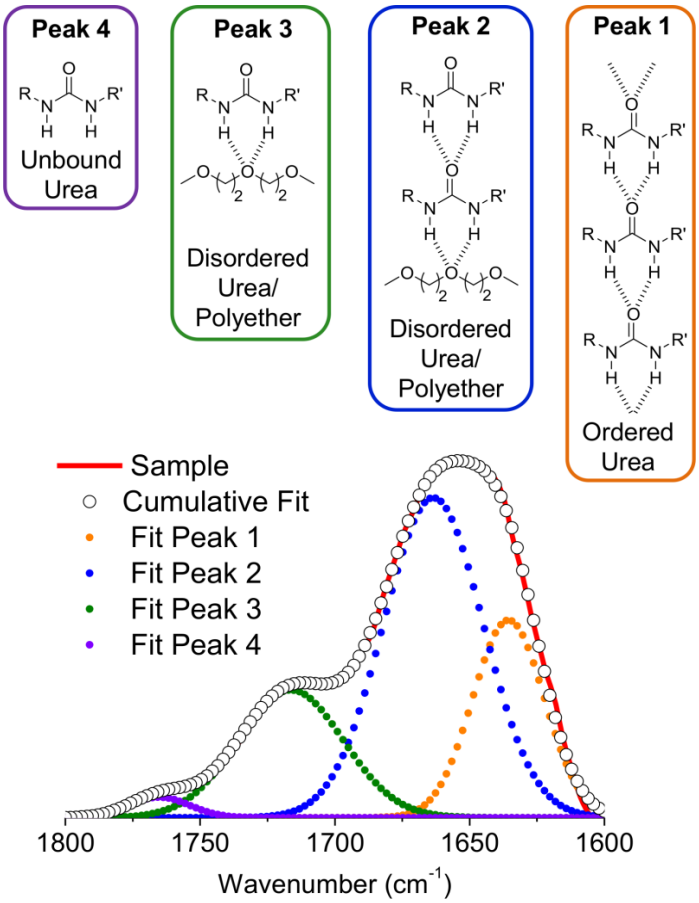

Figure 2.1. Structural investigation of a ureasil sample through FTIR spectroscopy. Schematic representation of the hydrogen-bonding associations in ureasil hybrids and corresponding Gaussian fit bands (dots) for a ureasil sample (solid line). R and R' represent the inorganic and organic portion of the hybrid structure.

2.4.2 Solid-State ^{13}C and ^{29}Si MAS-NMR and the Degree of Condensation

^{13}C and ^{29}Si MAS-NMR analyses have been used in this work to gain insight into the formation of urea linkages between the Jeffamine and ICPTES, and on the degree of condensation of the silica network. It is worth noting that the extremely low dopant concentrations used in this work, does not allow clear identification and separation of the contribution of the dye/CP from that of the ureasil, whose features dominate in the results obtained from any of the structural investigation techniques described in this work. Moreover, different ureasils can present different chain mobilities, leading to NMR spectra characterised by extremely weak signals (for higher mobility) and stronger signals for more rigid structures.[10]

The most valuable information provided by ^{13}C MAS-NMR spectroscopy performed on ureasil is the detection of a signal characteristic of carbonyl groups involved in urea bridges (~160 ppm), which confirms the successful formation of the urea linkages which hold together the organic and the inorganic domains of the hybrids.

Deeper understanding of the level of condensation of the silica network can be obtained by analysing the ^{29}Si MAS-NMR spectra of the hybrids, where a specific notation, known as the T_n notation, is used to describe the different environments surrounding the Si atoms in alkyltrialkoxysilane-based hybrids.[15, 16] The *n* number represents the number of silico-oxygen-silicon bridges. For example, a typical ^{29}Si MAS-NMR spectrum for ureasils presents the signals of T_1 = R'–Si(OSi)$(OR)_2$, T_2 = R'–$Si(OSi)_2$(R) and T_3 = R'–$Si(OSi)_3$ groups (at ~ -50, ~ -58 and ~ -67 ppm, respectively) (**Fig. 2.2**).[12, 17] A fourth signal can also be isolated (T_0), corresponding to R'-$Si(OH)_3$ moieties, which was not observed for any of the samples investigated in this work. Gaussian fits to the ^{29}Si MAS-NMR spectrum can be used to quantify the relative contribution of each of the T_n peaks and the degree of condensation of the siliceous network, *c*, can be calculated from:[18]

$$C = 1/3(\%T_1 + 2\%T_2 + 3\%T_3) \qquad \textbf{(2.22)}$$

where $\%T_n$ is the percentage contribution of the area of T_n peak to the total area. This value can provide useful information regarding the degree of the packing of the silica network before and after incorporation of the dopants.[10, 11]

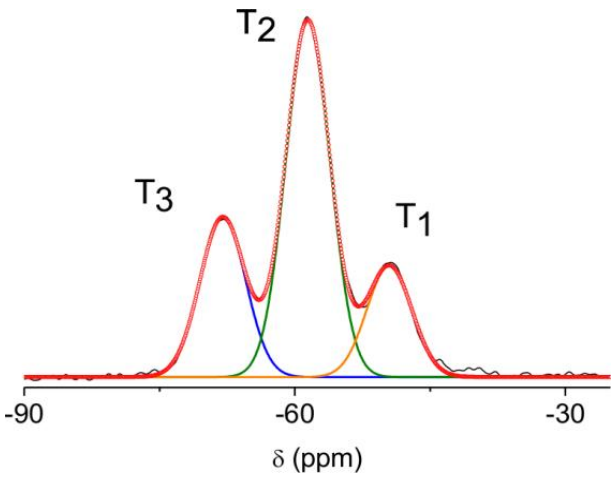

Figure 2.2. Analysis of the ^{29}Si MAS-NMR spectrum for a typical ureasil sample. The orange, blue and green solid lines correspond to the fitted T_n contributions indicated in the figure. The cumulative curve fit (open circles) and the spectrum (black solid line) are also indicated.

2.4.3 PXRD: Structural Unit Distance and Coherence Length

PXRD investigation of ureasil hybrids can provide useful information regarding the size of the inorganic domains within the matrices. The diffraction patterns for ureasils are typically comprised of a primary band centred at ~20° with a shoulder ~12-16°(**Fig. 2.3**).[10, 18] The main peak is indicative of ordering within the siliceous domains, while the lower intensity peak is ascribed to in-plane ordering of additional intra-siloxane domains.[19]

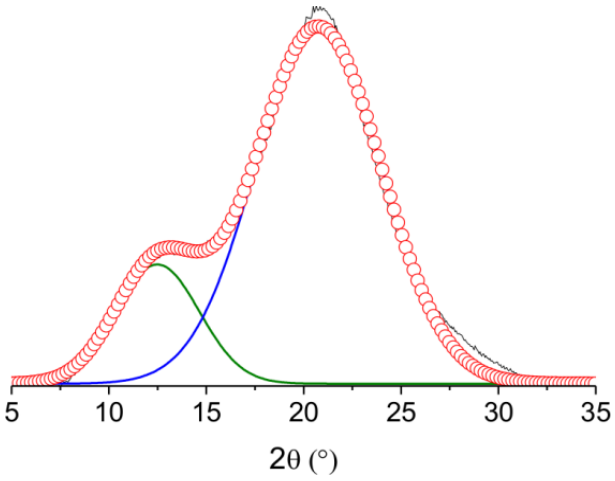

Figure 2.3. Analysis of a typical PXRD diffractogram for ureasils. The green and blue solid lines correspond to the fitted peak. The cumulative fit curve (red open circles) and the measured diffractogram (black line) are also presented.

From the main peak, the coherence length along which the structural unit survives, *L*, can be calculated using the Scherrer equation:[20]

$$L = \frac{0.94\,\lambda}{A\,cos\theta} \qquad \textbf{(2.23)}$$

where λ is the wavelength of the radiation and *A* is the full-width-half-maximum of the Bragg peak expressed in radians. It is worth noting that **Eqn. 2.23** is only true when assuming a Gaussian shape of the fitted curve and that the width of the corresponding signals can be affected by broadening effects due to both instrumental and sample contributions.[21] Therefore in this work, the results obtained using **Eqn. 2.23**, were considered meaningful only if consistent with the structural and spectroscopic evidences observed using the other aforementioned investigation techniques.

The structural unit distance, *d*, is calculated using Bragg's law:

$$2d\,sin\theta = n\lambda \qquad \textbf{(2.24)}$$

where *n* is a positive integer, λ is the wavelength of the incident wave and θ is the angle of incidencent radiation.

2.5 References

1. L. Porres, A. Holland, L.-O. Pålsson, A. P. Monkman, C. Kemp and A. Beeby, *J. Fluoresc.*, 2006, **16**, 267-273.
2. R. J. Hunter, *Zeta potential in colloid science: principles and applications*, Academic press, 2013.
3. A. Kaniyoor, B. McKenna, S. Comby and R. C. Evans, *Adv. Opt. Mater.*, 2016, **4**, 444-456.
4. J. R. Lakowicz, *Principles of Fluorescence Spectroscopy*, 2006, pp. 130-131.
5. J. C. de Mello, H. F. Wittmann and R. H. Friend, *Adv. Mater.*, 1997, **9**, 230-232.
6. T.-S. Ahn, R. O. Al-Kaysi, A. M. Müller, K. M. Wentz and C. J. Bardeen, *Rev. Sci. Instrum.*, 2007, **78**, 086105.
7. R. C. Evans, P. Douglas and H. D. Burrow, *Applied photochemistry*, Springer, 2013, p. 537.
8. J. R. Lakowicz, *Principles of Fluorescence Spectroscopy*, Springer, 2006, p. 99.
9. J. R. Lakowicz, *Priniciples of Fluorescence Spectroscopy*, Springer, 2006, p. 142.
10. I. Meazzini, N. Willis-Fox, C. Blayo, J. Arlt, S. Clément and R. C. Evans, *J. Mater. Chem. C*, 2016, **4**, 4049-4059.
11. I. Meazzini, J. M. Behrendt, M. L. Turner and R. C. Evans, *Macromolecules*, 2017, **50**, 4235-4243.
12. V. de Zea Bermudez, L. Carlos and L. Alcácer, *Chem. Mater.*, 1999, **11**, 569-580.
13. V. T. Freitas, P. P. Lima, V. de Zea Bermudez, R. A. Ferreira and L. D. Carlos, *Eur. J. Inorg. Chem.*, 2012, **2012**, 5390-5395.
14. L. Carlos, R. S. Ferreira, I. Orion, V. de Zea Bermudez and J. Rocha, *J. Lumin.*, 2000, **87**, 702-705.
15. J. D. Wright and N. A. Sommerdijk, *Sol-gel materials: chemistry and applications*, 2000, p. 71.
16. G. Engelhardt, H. Jancke, E. Lippmaa and A. Samoson, *J. Organomet. Chem.*, 1981, **210**, 295-301.
17. S. C. Nunes, V. de Zea Bermudez, M. M. Silva, M. J. Smith, E. Morales, R. A. Sá Ferreira, L. D. Carlos and J. Rocha, *Solid State Sci.*, 2006, **8**, 1484-1491.
18. L. Fu, R. Sá Ferreira, N. Silva, L. Carlos, V. de Zea Bermudez and J. Rocha, *Chem. Mater.*, 2004, **16**, 1507-1516.

19. P. Lima, R. Ferreira, S. Júnior, O. Malta and L. Carlos, *J. Photochem. Photobiol. A*, 2009, **201**, 214-221.
20. A. Guinier, *X-ray diffraction in crystals, imperfect crystals, and amorphous bodies*, Courier Corporation, 1994.
21. J. I. Langford and A. J. C. Wilson, *J. Appl. Cryst.*, 1978, **11**, 102-113.

Chapter Three

Targeted β-phase Formation in Poly(fluorene)-Ureasil Grafted Organic-Inorganic Hybrids

The work in this Chapter has been published in:
I. Meazzini, J. M. Behrendt, M. K. Turner and R. C. Evans, Targeted β-Phase Formation in Poly(fluorene)–Ureasil Grafted Organic–Inorganic Hybrids, *Macromolecules*, **2017**, 50, 4235–4243.

3.1 Introduction

In the past three decades, a family of CPs known as PFs has attracted considerable attention for their pure blue emission and high photoluminescence quantum yields,[1, 2] which have led to their widespread use as active components in polymer light-emitting diodes,[3-7] sensors and diagnostics.[8-13] The optoelectronic properties of PFs arise from the overlap of p-orbitals of their conjugated backbone and, as for every CP, are intrinsically linked to the arrangement of their individual chains. PFO in particular is known to present an incredibly rich phase diagram due to the different intra- and intermolecular conformations that it can assume in the solid, liquid and gel states.[14-16] PFO is polymorphic, with the most prevalent states including an amorphous α-phase,[17] a weakly-ordered planar β-phase[18] and the more recently discovered monoclinic γ-phase,[19] which is intermediate between the two. The formation of these phases arises from the interplay between the conformation of the polymer backbone and various inter- and intramolecular interactions: π-π stacking between the polymer backbones and van der Waals forces and hydrogen bonding between side chains. In particular, the β-phase is associated with a planarised conformation which improves the intrachain π-conjugation.[3]

Each one of the PF phases exhibits a unique optical fingerprint,[3, 20] allowing its detection by means of spectroscopic techniques. The presence of the β-phase in particular has been linked to enhanced optoelectronic properties, including improved charge carrier mobility, efficient amplified spontaneous emission and a low lasing threshold limit.[21, 22] The β-phase has been observed in polymer thin films upon specific thermal or vapour treatment,[23-25] and casting from a poor solvent.[26] However, due to the complexity of the interactions involved in the yielding of this conformation, a clear mechanism for its evolution has not yet been proposed.

Another strategy for the formation of the β-phase of PFs, consists of their incorporation into a host matrix, for example in supramolecular gels prepared from PFO in apolar organic solvents[27] or through its confinement in a silica-based ionogel,[28] or through functionalisation of the PFO side chains and *in situ* co-condensation within the host network.[29] In 2013, Marr *et al.*[27] targeted the morphology of PFO chains by strategically localising the CP at the interface of self-assembled rod-like structures consisting of: 5-di-*O*-methanesulfonyl-1,4:3,6-dianhydro-D-sorbitol (an organic gelator) and TEOS. Due to the low miscibility of PFO with both components, the CP

chains were segregated from the rest of the system and arranged themselves at the interface between the organic gelator template and the inorganic silica network. This imparted rigidity to the PFO backbone, yielding the formation of the β-phase. Targeted chain conformations of PFO can also be achieved for silica-based composites where the CP and the host are homogeneously mixed. De Francisco *et al.* [30] showed that the β-phase of PFs can be obtained by spraying a composite mixture consisting of PFO and polydimethysiloxane (PDMS) onto substrates presenting different roughness, namely: paper, glass and filtration membranes of mixed cellulose esters, to yield superhydrophobic coatings. The composite mixtures were prepared using different ratios of PFO and PDMS dissolved in toluene and sprayed onto the substrates. The investigation of the emission profile of the final samples revealed that the β-phase optical fingerprints were present in each system, regardless of the substrate used. Moreover, the extent of its formation was a function of the morphology of the coating, rather than of the substrate roughness, in particular, the β-phase was predominant in all the coatings that induced confinement of the PFO chains, like thin films or samples containing higher loading of PDMS.

Inspired by these examples, we hypothesed that targeted formation of the β-phase could be achieved by covalently grafting a functionalised PF, poly[(9,9-dioctyfluorene)-*co*-(9,9-bis(8-hydroxyoctyl)fluorene)] (**PFO-OH**, **Fig. 3.1**), onto the siliceous backbone of di- or tripodal ureasil frameworks. The organic-inorganic nature of ureasil hybrids, should allow their chemical compatibility with the **PFO-OH** chains, thus eliminating any potential phase separation, while being thermally and mechanically stable. Moreover, the physical confinement of the PFO within the ureasil framework should promote the β-phase formation, the extent of which could potentially be tuned by varying the **PFO-OH** concentration and the degree of branching of the organic backbone of the ureasil precursor.

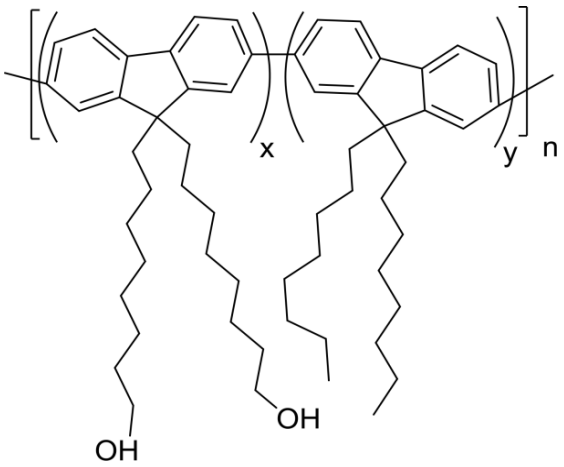

Figure 3.1. Chemical structure of PFO-OH.

3.1.1 Aims

In this Chapter, a hydroxyl-functionalised polyfluorene (**PFO-OH**) will be covalently-grafted onto the siliceous backbone of di- or tripodal ureasil frameworks to target the formation of the β-phase. The synthesis and the structural and optical characterisation of the PF-grafted di- and tri-ureasils will be discussed and from the correlation between the spectroscopic findings and the information regarding the local arrangements of two ureasil host networks, a structure of the stacking of the **PFO-OH** chains in the final hybrids will be proposed. This investigation is aimed to gain further insights into the mechanisms behind the phase behaviour of PFs, with particular interest directed to the β-phase, incorporated into hosting matrices. This approach could present a promising step towards the formation of fluorophore-grafted ureasil hybrids with tailored optical properties.

3.2 Experimental

3.2.1 Conjugated Polymer

Poly[(9,9-dioctylfluorene)-*co*-(9,9-bis(8-hydroxyoctyl)-fluorene)] (**PFO-OH**) with a number-average molecular weight M_n = 15,500 g mol^{-1} (PdI 2.3) was a kind gift from Dr. Jonathan Behrendt and Prof. Michael Turner from the University of Manchester, U.K. **PFO-OH** was prepared following a procedure previously reported in the literature.[29] The molecular ratio of hydroxyl-functionalised to non-functionalised monomer unit is 1:4.

3.2.2 Synthesis of PF-grafted Ureasil Hybrids

Samples were prepared using a method previously reported in literature.[31, 32] For undoped ureasils, each Jeffamine precursor (1.76 mmol) was dissolved in THF (5 mL) and refluxed with ICPTES at 70 °C for 12 hours (molar ratios = 1:2 and 1:3 for Jeffamine ED-600:ICPTES and Jeffamine T-403:ICPTES, respectively). Each solution was subsequently cooled to RT, before adding EtOH, HCl (0.5 M) and H_2O to initiate the acid-catalysed hydrolysis and condensation reaction, with a molar ratio of ICPTES:EtOH:HCl:H_2O of 176:350:1:265. Each solution was stirred for 2 min between each addition, before casting into a polypropylene mould and covering with Parafilm M®. After 2 days, 5 holes were pierced in the Parafilm M® to allow the slow evaporation of THF for a further 72 hours. The drying process was completed when samples were uncovered and placed in an oven at 40 °C for 48 hours. A similar approach was followed for the synthesis of PF-doped ureasils, where a fixed volume (0.193-2.081 mL) of a stock solution of **PFO-OH** in THF (1 mg mL^{-1}) was first added to ICPTES (3.52 mmol for DU-PF, 5.28 mmol for TU-PF) in THF (2.5 mL) and stirred at RT for 4 hr. The corresponding Jeffamine (1.76 mmol) and additional THF (for each sample enough to obtain a final volume of THF equal to 5.0 mL) were then added and the solution was refluxed at 70 °C for 12 hours. The volume of the **PFO-OH** stock solution was varied to yield a final concentration of either 0.01, 0.05 or 0.10 $\%_{w/w}$ of **PFO-OH** in the dry monolith. The molar ratios of the gelation reagents used in the second step and the ageing process were the same as those used for the preparation of the undoped monoliths. Samples are designated as **DU-PF-*x*** and **TU-PF-*x*** for di-ureasils and tri-ureasils respectively, where *x* represents the concentration of in $\%_{w/w}$ of **PFO-OH** in the final hybrid.

3.3 Results and Discussion

3.3.1 Grafting of the CP to the Ureasil Backbone

The grafting of the PF chains to the ureasil backbone is a process requiring three distinct steps (**Fig. 3.2**). In Step 1, **PFO-OH** (**1**) is reacted with an excess of ICPTES (**2**); the selected Jeffamine is then added to react with the unreacted ICPTES (Step 2) and the formation of the hybrids is achieved with the acid-catalysed hydrolysis of the ethoxysilane moieties and co-condensation of the functionalised PFO chains with the ureasil network (Step 3). For each sample,

the amount of ICPTES added is selected to be enough to react with both the **PFO-OH** in Step 1 and to the selected Jeffamine (molar ratio equal to 1:2 and 1:3 for Jeffamine ED-600:ICPTES and Jeffamine T-403:ICPTES, respectively) in Step 2. Each synthetic step of the reaction was monitored with different structural and spectroscopic techniques (*e.g.* TGA, ^{1}H NMR and FTIR spectroscopy).

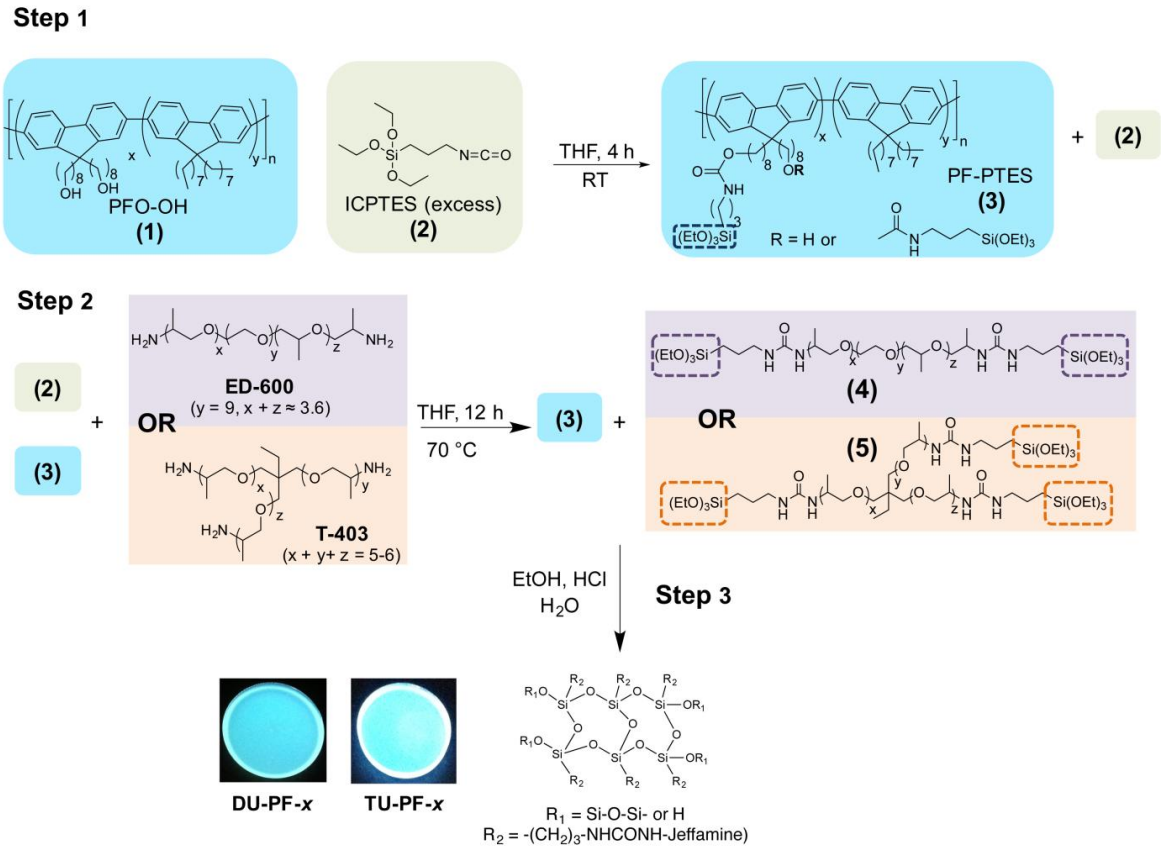

Figure 3.2. Synthetic path for the preparation of PF-grafted and undoped di- and tri- ureasils.

3.3.1.1 STEP 1: Preparation and Characterisation of the Siloxane-Functionalised PF

To ensure that the **PFO-OH** chains will be covalently bound to the ureasil network, in the first step of the reaction, the hydroxyl moieties of **PFO-OH** (**1**) were reacted with ICPTES (**2**) (**Fig. 3.2**). The reaction occurred through the formation of carbamide bonds between the two molecules, which was monitored by means of ^{1}H NMR spectroscopy and TGA analyses on a model mixture of the two reactants in a 1:1 molar ratio. This ratio was chosen to enable us to work with a sufficient concentration of the CP to follow the reaction by ^{1}H NMR spectroscopy. It was assumed that if the reaction occurs under these conditions, similar behaviour will be observed with an excess of ICPTES. To monitor the formation of a carbamide bond, the region of the ^{1}H NMR

spectrum ranging from roughly 3.20 to 4.60 ppm was investigated (**Fig. 3.3**). The spectrum of **PFO-OH** in a $CDCl_3$ solution (**Fig. 3.3**c) presents a triplet centred at 3.58 ppm, corresponding to the two hydrogen nuclei of the -CH_2- group bound to the alcohol moiety, carbon **a**.

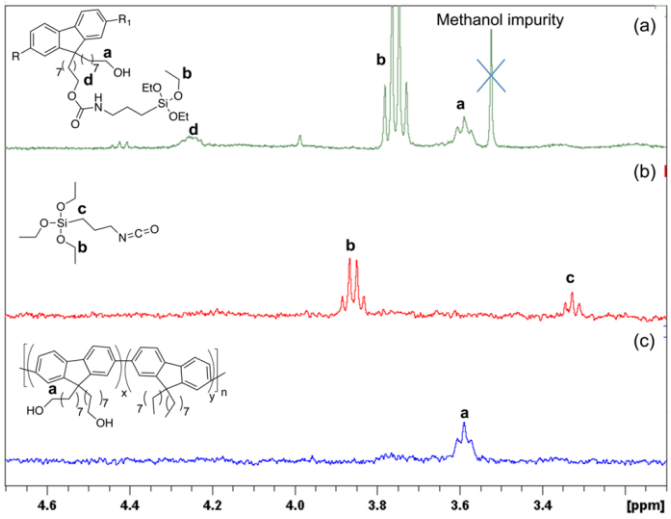

Figure 3.3.Investigation of the reaction between ICPTES and PFO-OH. ^{1}H NMR spectra (400 MHz, $CDCl_3$) of (a) PF-PTES (**3**), (b) ICPTES (**2**), and (c) PFO-OH (**1**).

The ICPTES spectrum (**Fig. 3.3**b) presents a symmetric quadruplet centred at 3.85 ppm, corresponding to the hydrogen atoms of the -CH_2- group of the ethoxy moieties bound to the silicon atom, carbon **b**. In comparison, the **PF-PTES** (**3**) spectrum (**Fig. 3.3**a) presents a new signal at 4.35 ppm corresponding to carbon **d**. As previously reported,[29] the presence of this signal confirms the formation of a carbamide group linking the branch of the CP to the siloxane precursor. It is observed that the spectrum of **PF-PTES** still presents a triplet centred at 3.58 ppm, which is typical of carbon **a**. Given the concentration of ICPTES and **PFO-OH** used the presence of this signal was expected. However, as each monomer of **PFO-OH** has two –OH moieties, the reaction with ICPTES might occur through two different mechanisms: (i) each **PFO-OH** monomer reacts with one ICPTES molecule or (ii) each **PFO-OH** monomer reacts with two ICPTES molecules. It is not possible to quantitatively confirm either of these two hypotheses with the concentration used; the ratio of –OH moieties to ICPTES molecules is 2:1, so in both cases the signals corresponding to carbon **a** and carbon **d** would be observed. Nevertheless, the ^{1}H NMR spectrum of PF-PTES confirms the formation of carbamide linkages between ICPTES and PFO-OH and as the aim of the study is to covalently bind these two species together, both reaction hypotheses would be acceptable.

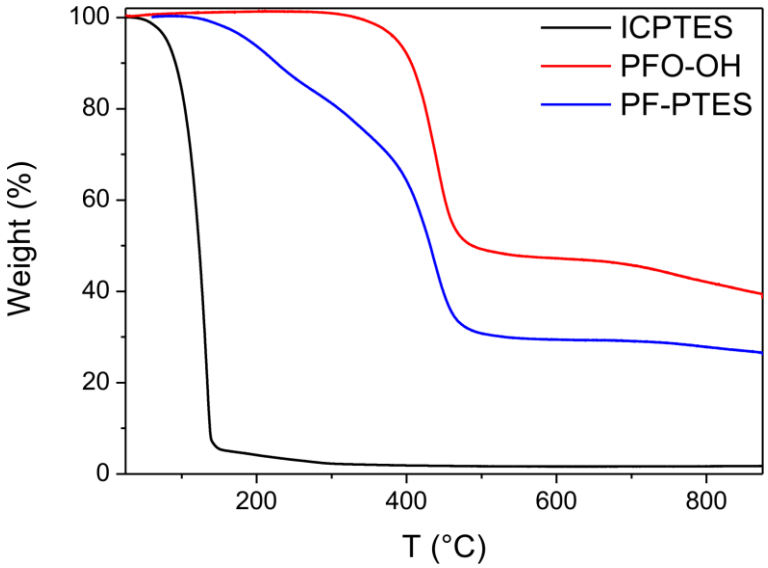

Figure 3.4. Investigation of the reaction between ICPTES and PFO-OH. Thermograms of ICPTES (black line), PFO-OH (red line) and PF-PTES (blue line) (air atmosphere, heat rate = 10 °C min^{-1}).

The thermogram of ICPTES (black line, **Fig. 3.4**) shows an abrupt weight loss of approximately 95.1% ranging between 40 and 166 °C and a further weight loss of 3.1% when the sample is heated from 166 to 870 °C. As all the measurements were performed in unsealed ceramic crucibles, the abrupt weight loss in the thermal profile of ICPTES is most likely to be due to the evaporation of the compound rather than to its thermal decomposition (flashpoint of **ICPTES** = 77 °C). For **PFO-OH** (red line, **Fig. 3.4**), TGA revealed a small increase in the weight percentage (0.5%) from 80 to 294 °C probably due to instrumental noise, followed by a major weight loss (54.1%) initiated at *ca.* 410 °C. In contrast, the TGA profile of **PF-PTES** (blue line, **Fig. 3.4**) shows a weight loss of 17.8% (onset at *ca.* 210 °C), which is higher than that corresponding to the evaporation of pure ICPTES and lower than that of **PFO-OH**, suggesting that the bonding/interaction of ICPTES with the CP has increased its stability, therefore requiring a higher temperature to thermally decompose and evaporate. A second weight loss (52.7%) corresponding to the decomposition of the polymer backbone which has lost the ICPTES residue is also observed from 325 to 689 °C. Overall, the combination of the results obtained from ^{1}H NMR and TGA confirmed the formation of carbamide linkages between the **PFO-OH** side chains and the ICPTES molecules can be achieved successfully using mild reaction conditions.

3.3.1.2 STEP 2: Preparation of d-UPTES and t-UPTES Precursors

The second step of the synthesis consists of the reaction between ICPTES and either Jeffamine ED-600 or Jeffamine T-403 in the presence of the PF-PTES precursor. This reaction is documented in the literature,[33] and occurs through the formation of urea linkages between the isocyanate moieties of ICPTES and the amine groups of Jeffamine ED-600 and Jeffamine T-403 (**Fig. 3.2**). For each sample, the reaction was followed by FTIR spectroscopy. As representative examples for the two series of ureasil hybrids, the FTIR spectra of ICPTES, Jeffamine ED-600, Jeffamine T-403 and the d- and t-UPTES precursors used to prepare samples **DU-PF-0.05** and **TU-PF-0.05**, are shown in **Fig. 3.5**a and **Fig. 3.5**b, respectively.

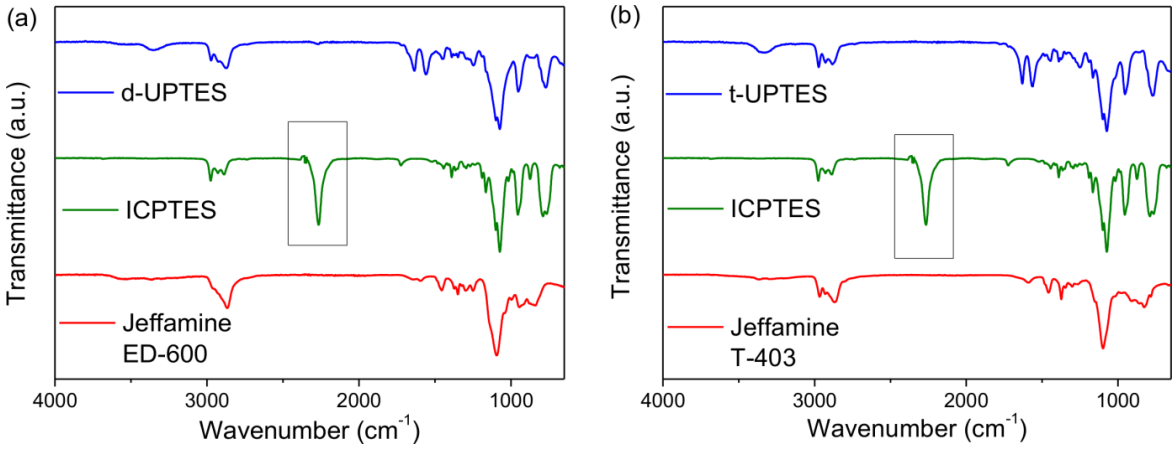

Figure 3.5. Formation of the d-UPTES and t-UPTES precursors. FTIR spectra of (a) ICPTES, Jeffamine ED-600 and d-UPTES and (b) ICPTES, Jeffamine T-403 and t-UPTES. The black rectangles indicate the asymmetric stretching of the isocyanate group of ICPTES which disappears upon reaction with either Jeffamine ED-600 or Jeffamine T-403.

The FTIR spectrum of ICPTES presents a strong vibrational band centred at 2265 cm^{-1} corresponding to the asymmetric stretching of isocyanate groups (N=C=O). The signals between 2976 and 2876 cm^{-1} are ascribed to the C-H symmetric and asymmetric stretching of the alkyl moieties, while the strong band centred at 1072 cm^{-1} is due to Si-O asymmetric stretching of –Si-O-CH_2- groups. The FTIR spectrum of Jeffamine ED-600 exhibits a broad, weak band between 3689 and 3062 cm^{-1} assigned to the asymmetric stretching of the primary amine and a strong band between 3029 and 2632 cm^{-1}, typical of symmetric and asymmetric stretching of alkyl moieties (C-H). The same features are observed for Jeffamine T-403, with the band assigned to ν_{N-H} between 3647 and 3070 cm^{-1}, and the C-H stretch between 3018 and 2706 cm^{-1}. For both Jeffamines the

signal corresponding to the C-O asymmetric stretch is centred at 1099 cm^{-1}. When ICPTES reacts with Jeffamine ED-600 or Jeffamine T-403, the formation of urea linkages causes the disappearance of the intense vibrational band corresponding to the isocyanate group (2265 cm^{-1}) and three new bands appear: one centred at 3340 cm^{-1}, corresponding to a hydrogen bonded N-H group, one centred at 1635 cm^{-1} assigned to the C=O stretching of a secondary amide, and one centred at 1561 cm^{-1} ascribed to the bending of the N-H moieties of the urea groups. The same results were observed for each sample prepared and agree with those reported in the literature.[33, 34]

3.3.2 Structural Investigation of the Hybrids

Step 3 of the synthesis consists of the acid-catalysed hydrolysis of the ethoxyl groups of the UPTES/PF-PTES units, followed by the co-condensation of the Si-O- moieties. After the completion of the sol-gel reaction and upon ageing and drying, the resulting **DU-PF-*x*** and **TU-PF-*x*** hybrids were obtained as monoliths. As the photophysical behaviour of **PFO-OH** is strictly dependent on its morphology, a detailed investigation of the local structure of the doped and undoped ureasil samples was carried out. These results should also reveal if the grafting of the CP into the two ureasil structures at the investigated concentrations also affects the arrangement of the silica network itself.

3.3.2.1 FTIR in the Amide I Region

FTIR spectroscopy in the Amide I region is a commonly used technique to investigate the effect of addition/grafting of dopants on ureasil hybrid structures.[31, 34, 35] The results of Gaussian deconvolution of the Amide I region of **DU-PF-*x*** and **TU-PF-*x*** samples are shown in **Fig. 3.6** and the peak frequencies and relative areas obtained from the Gaussian fits are reported in **Table 3.1**. For the **DU-PF-*x*** series, the following signals are isolated: Peak 3 centred at ~1710 cm^{-1} and Peak 2 centred at ~1660 cm^{-1}, corresponding to carbonyl stretching frequencies located within disordered hydrogen-bonded polyether-urea associations of increasing strength and Peak 1 (~1635 cm^{-1}) corresponding to the self-organised, hydrogen-bonded urea–urea interactions. Interestingly, for the undoped and the lowest PF concentration samples, a fourth peak at ~1775 cm^{-1} is also observed, indicating the presence of that carbonyl groups free of hydrogen-bonding.[36]

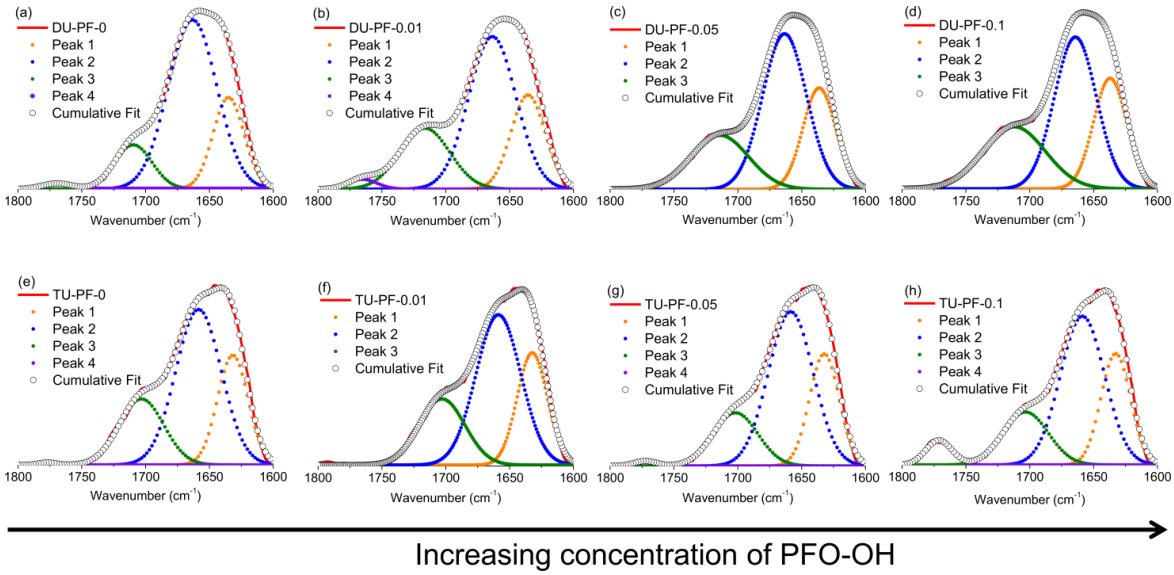

Figure 3.6 . Local structure of undoped and doped ureasil hybrids. FTIR spectra and Gaussian curve-fits of the Amide I region of: (a) **DU-PF-0**, (b) **DU-PF-0.01**, (c) **DU-PF-0.05**, (d) **DU-PF-0.1**, (e) **TU-PF-0**, (f) **TU-PF-0.01**, (g) **TU-PF-0.05** and (h) **TU-PF-0.1**. The solid red lines represents the spectra, the orange, blue, green and violet dotted lines represent the different contributions to the cumulative fit (open circles).

Table 3.1. The results of Gaussian curve-fitting to the Amide I region of the FTIR spectra of **DU-PF-*x*** and **TU-PF-*x***, showing peak position and the % contribution of each component.

Sample ID	Peak 1 / cm^{-1} Contribution (%)	Peak 2 / cm^{-1} Contribution (%)	Peak 3 / cm^{-1} Contribution (%)	Peak 4 / cm^{-1} Contribution (%)
DU-PF-0	1635 (22)	1663 (64)	1709 (13)	1777 (1)
DU-PF-0.01	1635 (23)	1663 (53)	1716 (22)	1765 (2)
DU-PF-0.05	1636 (25)	1663 (52)	1714 (23)	-
DU-PF-0.1	1637 (26)	1664 (46)	1712 (28)	-
TU-PF-0	1631 (25)	1659 (53)	1703 (22)	1777 (0)-
TU-PF-0.01	1632 (26)	1658 (51)	1703 (23)	-
TU-PF-0.05	1632 (26)	1658 (54)	1702 (19)	1773 (1)
TU-PF-0.1	1632 (25)	1659 (51)	1703 (19)	1771 (5)

This peak disappears in favour of ordered urea-urea interactions (Peak 1) when the $\%_{w/w}$ of **PFO-OH** is increased, suggesting a slight increase in the packing density of the co-condensed PF-PTES-d-UPTES network. Accordingly this change is followed by a re-arrangement of the interactions between the disordered urea/polyether chain interactions, as illustrated by the simultaneous increase and decrease in the intensities of the contributions of Peak 3 and Peak 2, respectively (**Table 3.1**). Conversely, Gaussian fits of the Amide I region for the **TU-PF-*x*** samples

shows that Peak 4 is observed for every sample, except for 0.01 $\%_{w/w}$ **PFO-OH**, indicating that there are subtle differences between the two sets of ureasils induced by the different structure of the Jeffamine precursors. For Jeffamine ED-600, its linear structure leads to a more ordered and compact conformation: the grafted PF chains occupy linear domains within the hybrid structure, whose sizes increase with the PF concentration, isolating the di-ureasil backbones and favouring the formation of disordered interactions between polyether chains and urea moieties. For **TU-PF-*x*** samples, no specific trend is observed with increasing the concentration of **PFO-OH**, suggesting that the CP chains can be accommodated without bringing major structural changes to the hydrogen-bonded array of the tri-ureasil.

3.3.2.2 Powder X-Ray Diffraction

Powder X-ray diffraction measurements were performed to further investigate the effect of the incorporation of the CP on the structure of the hybrids. PXRD patterns of both sets of samples present the characteristic features of ureasils, with a primary band between 19.9-20.7° and a shoulder at 11.8-12.5°(**Fig. 3.7**). The main peak is associated with localised order in the siliceous network,[37, 38] with a structural unit distance, *d*, of 4.4 ± 0.1 Å (calculated using Bragg's Law, **Eqn. 2.25**), while the shoulder is ascribed to in-plane ordering of the siliceous domains.[39] The coherence length calculated using the Scherrer equation (**Eqn. 2.24**) is 10.3 ± 0.8 Å and is similar to values reported in literature for ureasils.[40]

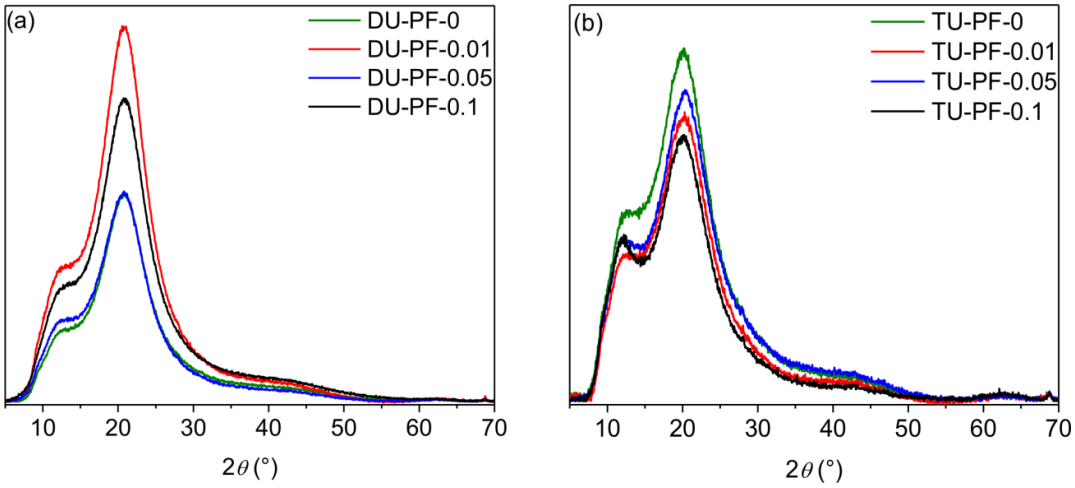

Fig. 3.7. Powder X-ray diffraction patterns for (a) **DU-PF-*x*** and (b) **TU-PF-*x*** in the range of 2θ = 5–70°.

3.3.2.3 Solid State NMR Spectroscopy

^{29}Si MAS-NMR was used to probe the degree of condensation of the siliceous network in the **DU-PF-*x*** and **TU-PF-*x*** series (**Fig. 3.8**). The peaks were assigned following the T_n notation where n=1, 2, 3 and *T* represents the number Si-bridging oxygen atoms, *i.e.* T_2 = R′Si(OSi)$_2$-(OR). Each sample presents the characteristic signals of T_1 (R′Si(OSi)(OR)$_2$, ~-50 ppm), T_2 (R′Si(OSi)$_2$(OR), ~-58 ppm) and T_3 (R′Si(OSi)$_3$, ~-67 ppm) groups, respectively. Although visual evaluation of the **TU-PF-0.1** spectrum (**Fig. 3.8**b) would suggest the presence of the T_1 signal, the signal to noise ratio prevents accurate fitting of this peak. Peak centres, relative areas and the calculated degrees of condensation, *c*, are reported in **Table 3.2**. The results of the fits show that for the undoped ureasils, the T_1 signal is more prominent in **TU-PF-0** (~5x) compared to **DU-PF-0**, suggesting that the TU-network is less condensed than the corresponding DU-system. Interestingly, for the **DU-PF-*x*** series, the degree of condensation is higher than that of the **TU-PF-*x*** samples at the same concentrations (*c*~69-79%), reaching its maximum for **DU-PF-0.1** (84%). Due to the structure of the Jeffamine precursor, **TU-PF-*x*** hybrids present a higher ratio of silica centres per ethoxy monomer compared to **DU-PF-*x*** and this imparts rigidity to the overall network, preserving its structure even upon incorporation of sterically-hindered species, such as the CP chains. This is in agreement with our hypothesis of a more distorted and less organised structure for tri-ureasil compared to di-ureasil hybrids, which is guided by the different degrees of branching on the Jeffamine precursors.

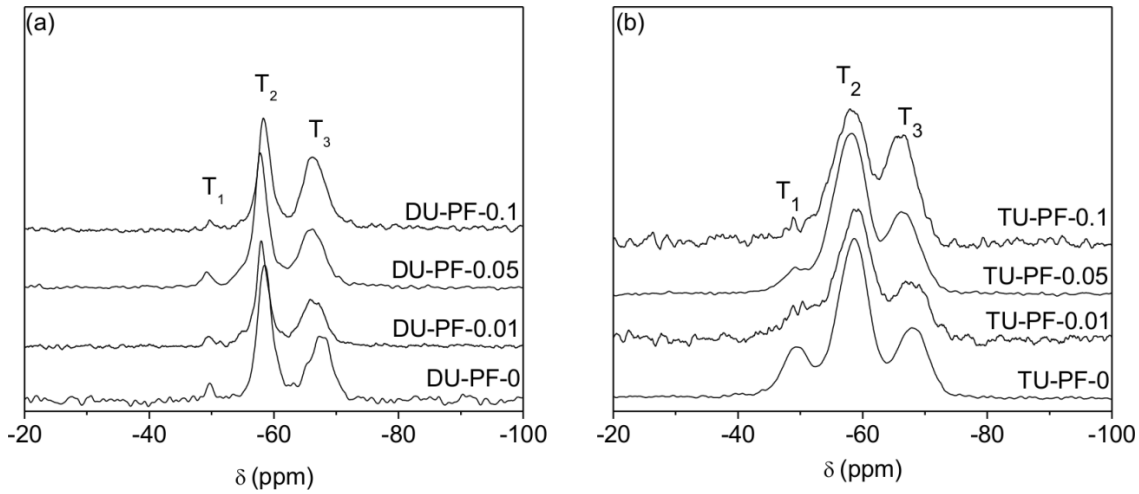

Fig. 3.8. Investigation of the extent of condensation of the siliceous network in doped and undoped ureasils. ^{29}Si solid-state MAS-NMR spectra for (a) DU-PF-*x* and (b) TU-PF-*x*.

Table 3.2. ^{29}Si MAS-NMR chemical shifts, relative T_n populations and degree of condensation, *c*, of **DU-PF-*x*** and **TU-PF-*x*** (R denotes the ureapropyl chains).

Sample ID	Peak 1 / cm^{-1} Contribution (%)	Peak 2 / cm^{-1} Contribution (%)	Peak 3 / cm^{-1} Contribution (%)	Peak 4 / cm^{-1} Contribution (%)
DU-PF-0	1635 (22)	1663 (64)	1709 (13)	1777 (1)
DU-PF-0.01	1635 (23)	1663 (53)	1716 (22)	1765 (2)
DU-PF-0.05	1636 (25)	1663 (52)	1714 (23)	-
DU-PF-0.1	1637 (26)	1664 (46)	1712 (28)	-
TU-PF-0	1631 (25)	1659 (53)	1703 (22)	1777 (0)-
TU-PF-0.01	1632 (26)	1658 (51)	1703 (23)	-
TU-PF-0.05	1632 (26)	1658 (54)	1702 (19)	1773 (1)
TU-PF-0.1	1632 (25)	1659 (51)	1703 (19)	1771 (5)

[a] $c = 1/3(\%T_1 + 2\%T_2 + 3\%T_3)$[39]

3.3.2.4 Thermogravimetric Analysis

TGA for **DU-PF-*x*** and **TU-PF-*x*** are presented in **Fig. 3.9** and are in good agreement with that previously observed in the literature for di- and tri-ureasils.[38, 41] The main decomposition event occurs at an onset temperature of ≈342−377 and ≈367−398 °C, for **DU-PF-*x*** and **TU-PF-*x***, respectively (**Fig. 3.9**), with both series of samples (**Fig 3.9**a) presenting an initial weight loss ascribed to the evaporation of residual THF and un-reacted ICPTES between 70 and 190 °C. For **DU-PF-0.1** and **DU-PF-0.01**, this weight loss occurs between 30.0 to 280.1 °C and corresponds to 3.8% and 8.3% of the weight, respectively, while for **DU-PF-0** the weight loss occurs between from 30.0 to 245.6 °C (corresponding to a decrease of 5.2%) and for **DU-PF-0.05** from 30 to 200.9 °C (corresponding to a decrease of 4.6%). For each sample, the second thermal degradation corresponds to the pyrolysis of the di-ureasil hybrids and occurs in a single step.

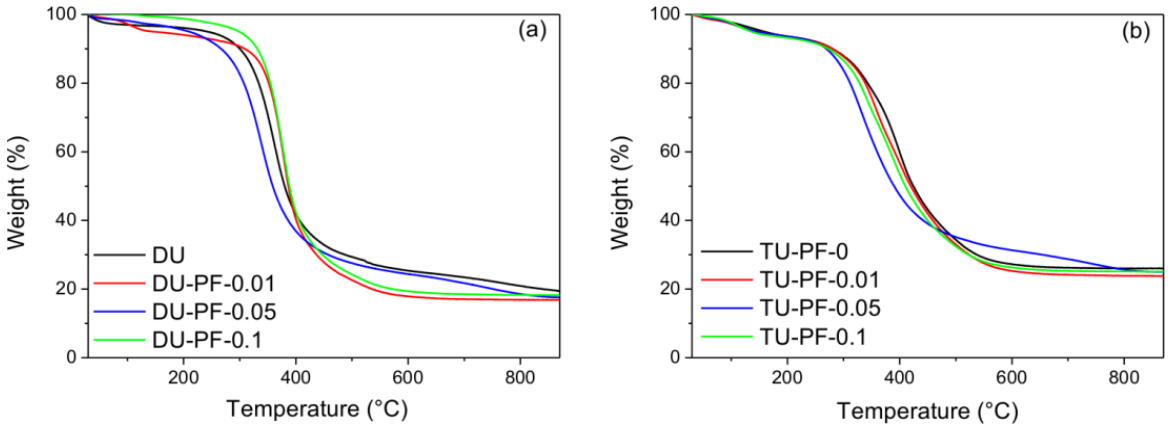

Fig. 3.9. Thermograms of (a) **DU-PF-0**, **DU-PF-0.01**, **DU-PF-0.05** and **DU-PF-0.1** and (b) **TU-PF-0**, **TU-PF-0.01**, **TU-PF-0.05** and **TU-PF-0.1** (air atmosphere, heat rate = 10 °C min^{-1}).

3.3.3 Photophysical Characterisation

3.3.3.1 Steady-State Photoluminescence Studies

The steady-state photoluminescence spectra of **DU-PF-0** are shown in **Fig. 3.10**. The emission spectrum of **DU-PF-0** consists of a broad band ranging from 340 to 600 nm whose emission maximum red-shifts to longer wavelengths with increasing excitation wavelength. This behaviour is characteristic of ureasils and arises from the nature of the emission of the undoped hybrids which arises from the combination of two distinct contributions: (i) a "blue" component, resulting from photoinduced proton transfer occurring in the NH groups of the urea bridges and (ii) a "purple" component resulting from the electron-hole recombination occurring in the siliceous domains of the hybrids.[38, 42] A similar behaviour is observed for the corresponding excitation spectra; a broad band centred between 280 and 430 nm is observed, which red-shifts with increasing emission wavelength. In this case, the red-shift of the band is accompanied by broadening, which results from preferential excitation of the purple-blue band compared to the blue one and further supports the presence of two components.[37, 43] The PL and excitation spectra of **TU-PF-0** show similar features and can be found in the Appendix (**Fig. A3.1**).

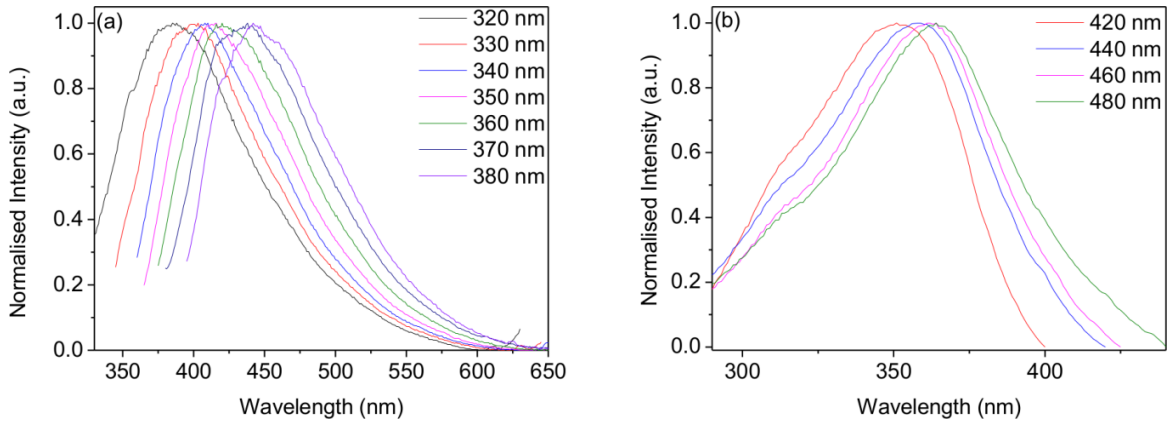

Fig 3.10. Optical features of undoped diureasils. (a) Emission and (b) excitation spectra of **DU-PF-0** measured at different excitation and emission wavelengths, respectively.

Fig 3.11a shows the normalised UV/Vis absorption and PL spectra of **PFO-OH** in THF (10^{-6} mol dm^{-3}). The UV/Vis absorption spectrum of **PFO-OH** is characterised by a broad band centred at 392 nm. The corresponding emission spectrum exhibits the characteristic features of a PF in a good solvent, with a well-structured emission band between 370 to 550 nm. The spectrum presents three vibrational maxima which can be ascribed to stretching modes associated with the -C=C-C=C- moieties of the polymer backbone.[3] The excitation spectrum of the same solution presents a broad band centred at 380 nm. As expected, these PL and absorption features are typical of the PF α-phase, where each chain of the PF is individually dissolved and adopts a rigid conformation.[44] Upon incorporation of **PFO-OH** into either the di-ureasil or the tri-ureasil matrices (**Fig 3.11**b), both the emission and the excitation spectra change dramatically.

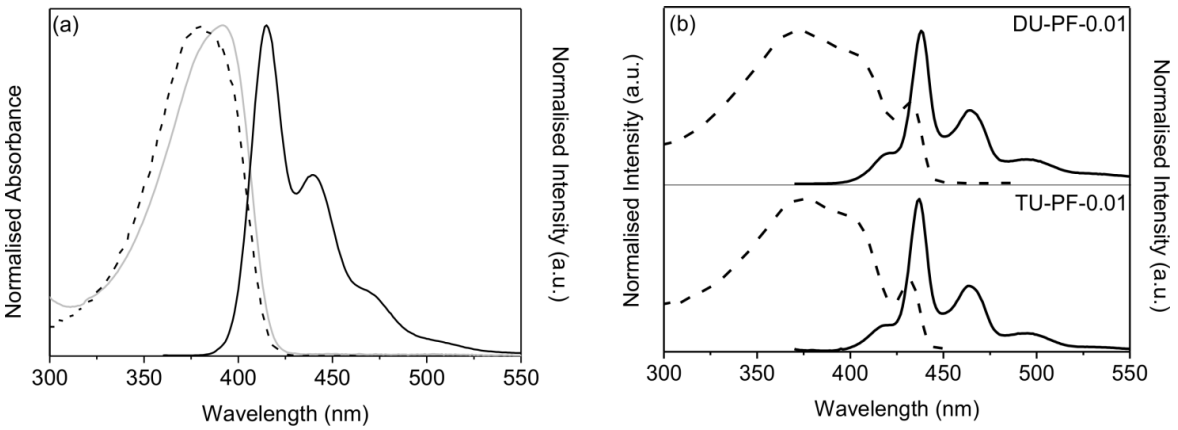

Fig. 3.11. Absorption (gray solid line), excitation (dashed line) and emission (black solid line) of (a) **PFO-OH** in THF (10^{-6} mol dm^{-3}, λ_{ex} = 350 nm, λ_{em} = 480 nm), (b) **DU-PF-0.01** and **TU-PF-0.01** (λ_{ex} = 360 nm and λ_{em} = 500 nm).

The PL profiles are dominated by the PF features, which are significantly different from those observed for **PFO-OH** in THF, with a 20 nm red-shift in the emission spectra and the simultaneous appearance of a new peak centred at 432 nm in the excitation spectrum. These optical features are typical of the PF adopting a β-phase, where the CP backbone adopts a more planar conformation.[3] Nevertheless, some of the features typical of the PF α-phase are still observed for both cases, which indicates the coexistence of the two phases. Interestingly, we observe that for both series of ureasil hybrids, the increase in the wt% of the PF leads to a broadening of the emission spectrum and a further red-shift in the position of the 0-0 vibronic transition. This would suggest the presence of self-absorption which becomes more important with the increasing CP concentration. The emission and excitation spectra of **DU-PF-0.05**, **DU-PF-0.1**, **TU-PF-0.05** and **TU-PF-0.1** are reported in the Appendix (**Fig. A3.2** and **A3.3**, respectively).

3.3.3.2 Real Time Evolution and Quantification of the PF β-phase

To further elucidate the mechanism for the formation of the β-phase in the hybrid matrix, the emission and excitation spectra and the pictures were collected for **DU-PF-0.01** along the course of the gelation process (**Fig. 3.12**). The PF chains dissolved in the sol mixture (t = 0) adopt the α-phase conformation. Upon addition of the gelation regents (EtOH, HCl and H_2O), the condensation of the silica network during the sol-gel reaction induces the formation of the β-phase. This is confirmed by an increase in the intensity of the characteristic peak of the β-phase centred at 435 nm in the excitation spectrum, and by the red-shift and the growth of a new peak centred at 480 nm in the emission spectrum. Both peaks increase in intensity with time, reaching their maximum as the condensation reaction reaches completion. The evolution of the β-phase over time is consistent with the transition from a fluid to a more confined environment for **PFO-OH** as the sol−gel transition proceeds, which promotes π−π stacking of the conjugated backbone. Similar behaviour has been observed in the literature, where the gelation process of PFO in a methylcyclohexane (MCH) solution (concentration of 1.0 wt. %) was induced by aging the sample at 20 °C.[45] Since MCH is a poor solvent for PFO, the chains of the CP already start to interact after 10 min of aging.

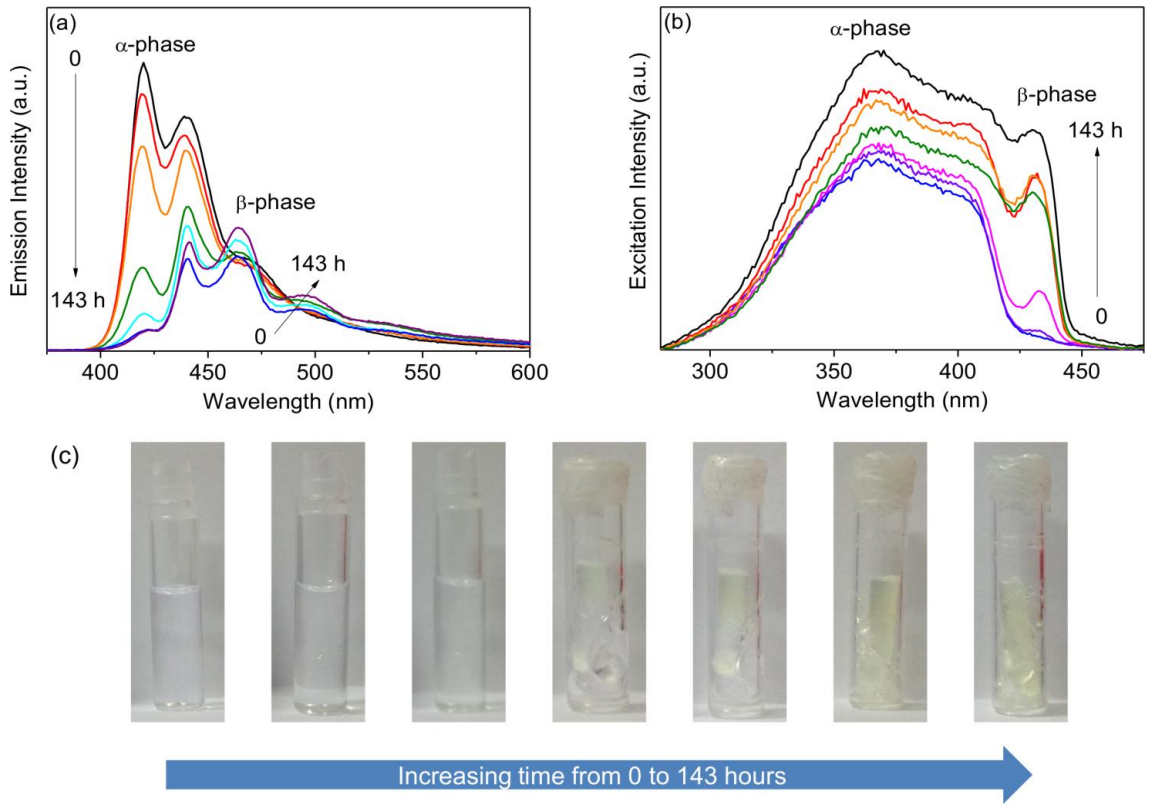

Figure 3.12. (a) Emission (λ_{ex} = 360 nm) and (b) excitation (λ_{em} = 500 nm) spectra and (c) pictures of **DU-PF-0.01** recorded as a function of time after initiation of the sol-gel process (t = 0 → 143 h).

The interactions between PFO macromolecules increase in intensity and number with time, to the point at an aging time of 2160 min, the original PFO/MCH solution had turned into a highly viscous gel.

In an attempt to quantify the contribution of the β-phase to the optical properties of each PF-grafted ureasil hybrid, Gaussian multi-peak fitting was performed on the excitation spectra. The final excitation spectrum of each PF-functionalised ureasil hybrid arises from three contributions: (i) **PFO-OH** adopting the β-phase, (ii) **PFO-OH** adopting the α-phase, and (iii) either the **DU-PF-0** or the **TU-PF-0** matrix. To take into account all of these contributions, Gaussian fits were first performed on the excitation spectrum of **PFO-OH** in solution (**Fig. 3.13**a) and on the blank ureasil (**Fig. 3.13**b). The obtained fits results were then used to provide initial values for the peak centres to fit the DU-PF-*x* and TU-PF-*x* excitation spectra. The fits for all samples can be found in the Appendix (**Fig. A3.5**).

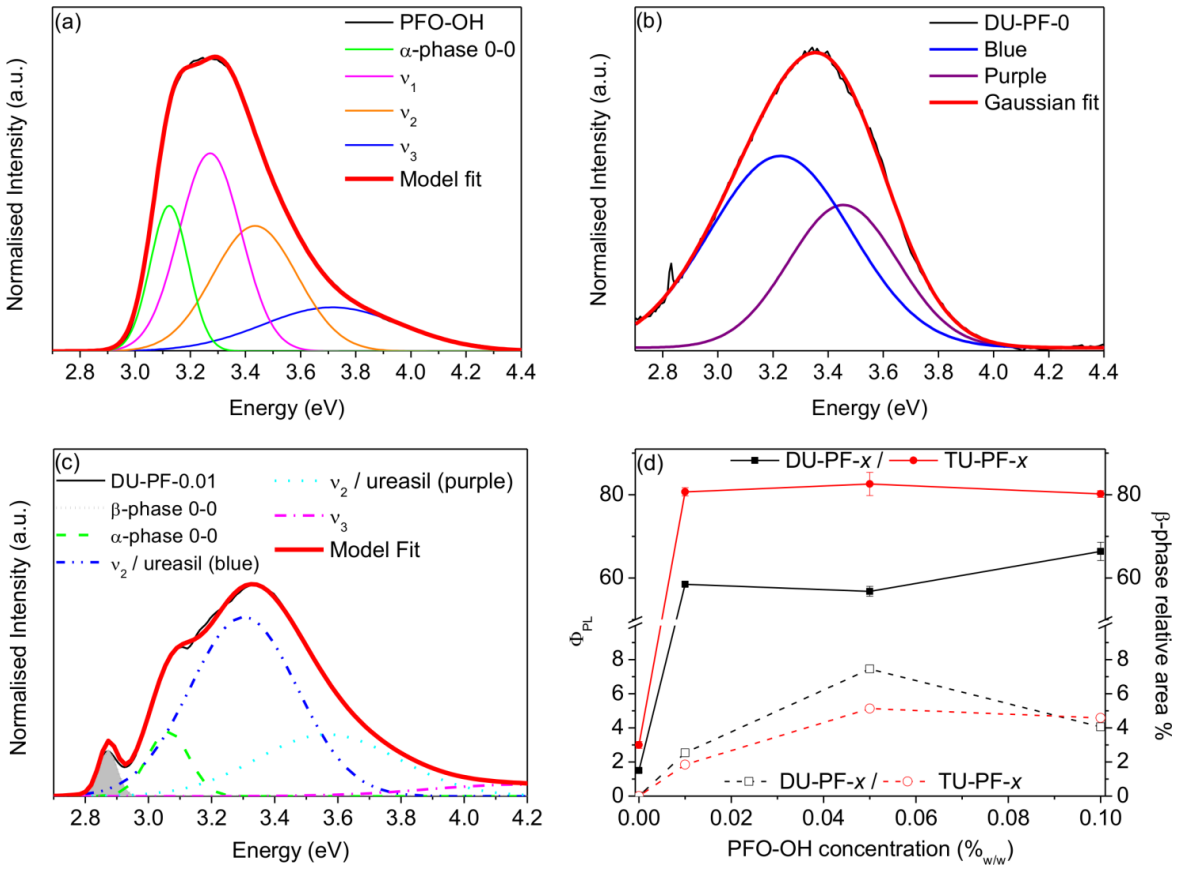

Figure 3.13. Area-normalised excitation spectrum (λ_{em} = 480 nm) and corresponding Gaussian fits of the spectral components associated with the vibronic modes of **PFO-OH**, where ν_n refers to the vibrational mode, n, and the blue and purple components of the ureasil of (a) **PFO-OH** (10^{-6} mol dm^{-3}, THF), (b) **DU-PF-0** and (c) **DU-PF-0.01**. The shaded area corresponds to the pure β phase component. (d) % β-phase contribution (open symbols) and photoluminescence quantum yields (solid symbols) as a function of the PFO-OH wt% for the DU-PF-*x* and TU-PF-*x* series. The solid and dashed lines serve only to guide the eye.

The excitation spectrum of **PFO-OH** in the isolated α-phase conformation (**Fig. 3.13**a) can be resolved into four components: the 0-0 electronic transition (~3.1 eV) and other three peaks (~3.3, ~3.4 and ~3.8 eV) which can be ascribed to the higher order vibronic contributions.[46] Analysis of the excitation spectrum of **DU-PF-0** (**Fig. 3.13**b) confirms that its emission arises from the combination of the purple component (~3.5 eV) and the blue component (~3.2 eV) as discussed previously.[42]

The components for the PF-grafted hybrids (**Fig. 3.13**c and **A3.4**) were assigned as follows: (i) the β-phase peak (~2.9 eV), (ii) the α-phase 0−0 electronic transition at ~3.1 eV; (iii) and (iv) are overlapping contributions from the ν_1 vibronic transition of the α-phase (~3.3 eV) and the ureasil emission (~2.9−3.4 eV); and (v) higher order vibronic bands (~4.2 eV) associated with the PF. We note that, while for pure PF-based systems the content of the β-phase is generally

assessed by subtraction of the absorption spectrum of the mixed-phase solution/thin film from the spectrum of the same sample adopting a pure α-phase, the strong overlap between the components of the ureasil and those of the PF prevent us for isolating each contribution in the excitation spectrum of the PF-grafted hybrids in this case. However, as previously shown by Knaapila *et al.*,[47] Gaussian fits enable us to isolate the peak corresponding to the β-phase and quantify its relative contribution to the global excitation spectrum. Similar results were obtained for samples in the entire DU-PF-*x* and TU-PF-*x* series (**Fig. A3.4**) and the percentage of β-phase in each sample is shown in **Fig. 3.13**d.

For both sets of samples, the amount of β-phase initially increases with the concentration (1.9% to 5.1% and 2.5% to 7.5% for TU-PF-*x* and DU-PF-*x*, respectively). As the concentration of the CP is further increased, the percentage of β-phase moderatly decreases to 4.1% and 4.6% for **DU-PF-0.1** and **TU-PF-0.1**. **Fig. 3.13**d also presents the photoluminescence quantum yields (Φ_{PL}) for the samples as a function of concentration. The Φ_{PL} of ureasil is 1.5 ± 0.2% and 3.0 ± 0.1% for **DU-PF-0** and **TU-PF-0** respectively, in good agreement with the literature,[37, 48] while for **PFO-OH** in THF, the Φ_{PL} is 85.3% (± 2.2%), comparable to the values reported for PFO in a dilute solution of a good solvent.[49] As mentioned above, the general decrease in intensity of the 0-0 emission peak indicates the presence of self-absorption. The values of Φ_{PL} were therefore corrected from this effect using a procedure previously described in literature (see details in Chapter 2).[50] For both di-ureasil and tri-ureasil hybrids, the incorporation of the CP results in a drastic increase in the Φ_{PL} at any of the investigated concentrations, ranging from 56.8 to 66.4% for **DU-PF-*x*** and from 80.2 to 82.6% for **TU-PF-*x*** respectively. These values indicate that the PF chains are homogeneously distributed in the ureasil matrices, which inhibits the undesired aggregation phenomena which often leads to a generalised quenching of the emission for CPs incorporated in a host material in the solid state.[51] The lowest value of Φ_{PL} was measured for **DU-PF-0.05** (56.8 ± 1.2%), to which corresponds the highest percentage of β-phase (7.5%). It has previously been shown for PF films that a high β-phase contribution can lower the Φ_{PL} due to the formation of fluorenone chemical defects in the polymer structure that are not related to the chain conformation of the polymer.[52]

3.3.3.3 Proposed Arrangement for the PF Chains in the Ureasil Network

From the combination of the structural and spectroscopic evidence gathered, it is clear that the branching of the ureasil has an important effect on the localisation and the packing of the PF chains in the hybrid host network. This directly influences the extent of the β-phase formation, and therefore the spectroscopic behaviour of these systems. **Fig. 3.14** presents a schematic representation of the proposed stacking of the PF chains in the di- and tri-ureasil structures. FTIR studies of the **DU-PF-*x*** series showed that the incorporation of **PFO-OH** results in the re-arrangement of the urea/poly(ether) chains interactions, in favour of the more ordered urea-urea H-bonding, leading to a better packed structure in the hybrid. In contrast, for **TU-PF-*x*** samples no remarkable trend in the hydrogen bonding was observed from the FTIR investigation upon incorporation of the **PFO-OH** at different concentrations.

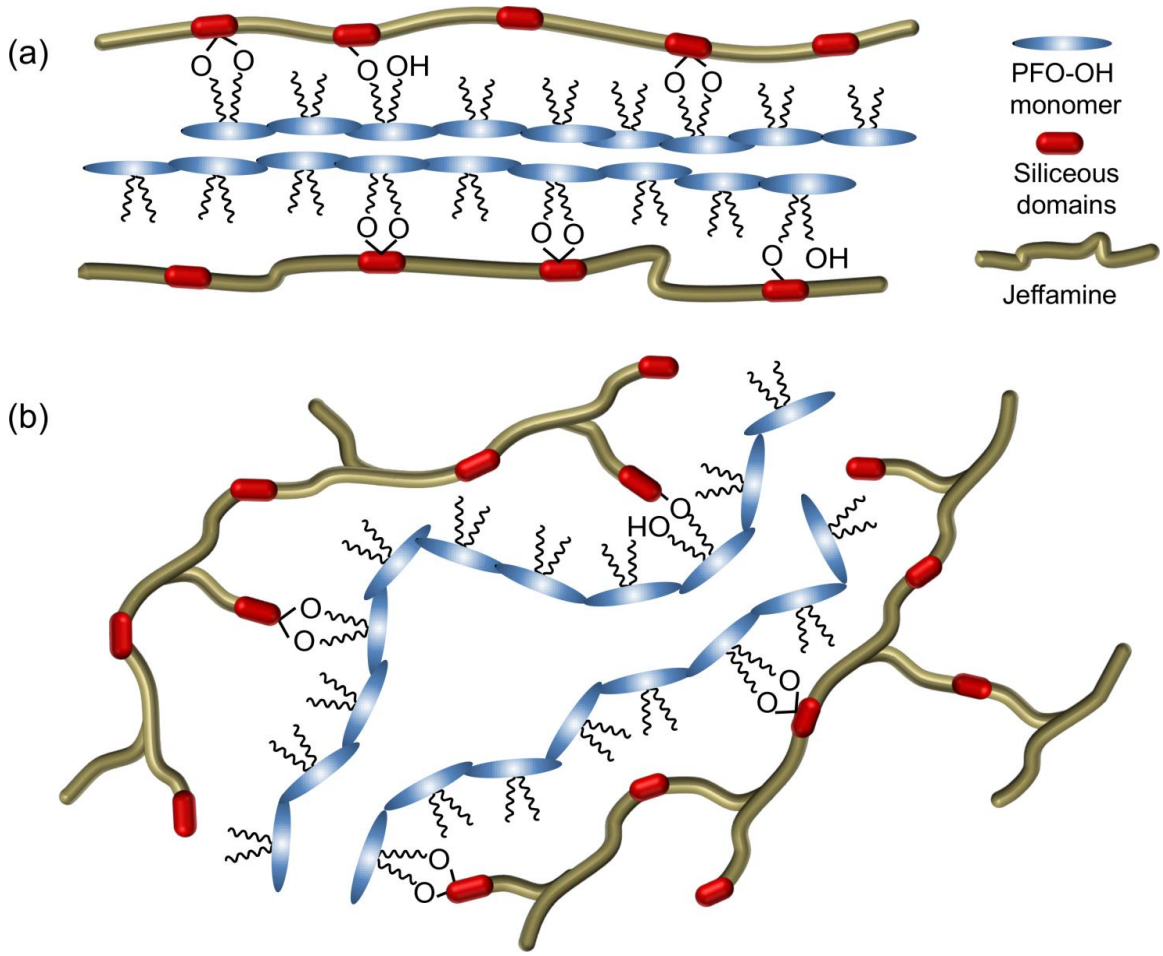

Fig. 3.14. Schematic representation of the proposed packing of **PFO-OH** in (a) **DU-PF-*x*** and (b) **TU-PF-*x*** hybrids. The image is not to scale.

These results suggest that for tri-ureasils the CP chains adapt to the rigid structure of the network and, even at higher concentrations, aggregation is inhibited to some extent by the rigidity of the silica backbone preventing a large amount of **PFO-OH** chains from being hosted in the same confined space. This assumption is reflected in the similar values of degree of condensation (from ^{29}Si MAS-NMR measurements) and of β-phase obtained for the samples (~5%) at a **PFO-OH** concentration of 0.05 and 0.1%$_{w/w}$. In contrast, the linear branching of the Jeffamine ED-600 improves the packing of **PFO-OH** in the host, by favouring the covalent grafting of the PF-PTES chains onto the di-ureasil network. This leads to an increase of the relative contribution of the T_3 peak in the ^{29}Si MAS-NMR spectrum (from 42 to 54%) jointed by a decrease of the T_1 peak intensity (from 5 to 1%) as the **PFO-OH** concentration is increased from 0 to 0.1 wt.%. This hypothesis is further supported by the red-shift in the wavelength of the 0−0 vibronic transition associated with the β-phase in the emission spectrum, which is larger and exhibits a more significant concentration dependence for the **DU-PF-*x*** series.

3.4 Conclusions

The targeted formation of the PF β-phase was achieved through covalent grafting of a hydroxyl-functionalised poly(fluorene) (**PFO-OH**) to the backbone of organic-inorganic ureasil hybrids. To gain a deeper understanding of the phase behaviour of PF in solid matrices, different structures of the network of the ureasil have been used, one containing the di-branched Jeffamine ED-600 and the other a tri-branched Jeffamine T-403. By means of spectroscopic and structural analyses, we have confirmed that the **PFO-OH** chains are covalently bound to the siloxane precursor of the ureasil and that the final network is held together by covalent bonds. Grafting of the PF chains occurs onto the siloxane domains, and the degree of branching on the Jeffamine precursor determined the packing of the **PFO-OH** chains in the hybrid, and therefore its final conformation, which is intrinsically linked to the spectroscopic behaviour of the overall material. The hydrogen bonding interactions within the hybrid structure were investigated by means of FTIR spectroscopy and revealed that the **TU-PF-*x*** samples present a more open and distorted structure which restricts the packing of the PF chains. **DU-PF-*x*** hybrids instead present generally stronger H-bonding interactions and a more compact structure. This was also confirmed by the degree of

condensation of the materials, determined from ^{29}Si MAS NMR studies, which was generally higher for the di-ureasil than the tri-ureasil hybrids. PL and UV/Vis absorption studies of **PFO-OH** in solution confirmed that in a good solvent (THF) the CP chains adopt the α-phase conformation. Upon incorporation in the ureasil matrix, the PF chains undergo a conformational change, the extent of which depends on the branching of the Jeffamine precursors, yielding the more planar β-phase and leading to distinct changes in the PL emission and excitation profiles of the samples. Real-time investigation of the PL properties of the hybrids during the gelation process further showed how the confinement of the PF chains in the ureasil network transformed the conformation of the CP chains from a pure α-phase, observed for the sol precursor, to a mixture of α- and β-phase in the hybrid. Through Gaussian multi-peak curve fitting of the excitation spectra, the contribution of the β-phase to each spectrum was isolated and quantified. The ureasil structure guides the arrangement of **PFO-OH** chains in the silica network, so that the conformation of the PF can be controlled. As there are only a few literature examples which investigate the mechanism behind the phase behaviour of PF in hybrid systems,[28, 29] the systems investigated here have provided a key insight into the role of spatial confinement and physical interactions on the formation mechanism of the β-phase. Notably, the ability to control and tune the extent of the β-phase contribution by changing the degree of branching of the organic backbone of the host has important implications in the rational design of high-performance hybrid light-emitting diodes and organic lasers, where the β-phase may be desired.[25, 53]

3.5 References

1. M. Leclerc, *J. Polym. Sci., Part A: Polym. Chem.*, 2001, **39**, 2867-2873.
2. G. M. Farinola and R. Ragni, *Chem. Soc. Rev.*, 2011, **40**, 3467-3482.
3. U. Scherf and E. J. W. List, *Adv. Mater.*, 2002, **14**, 477-487.
4. J. Luo, Y. Zhou, Z.-Q. Niu, Q.-F. Zhou, Y. Ma and J. Pei, *J. Am. Chem. Soc.*, 2007, **129**, 11314-11315.
5. J. H. Cook, J. Santos, H. Li, H. A. Al-Attar, M. R. Bryce and A. P. Monkman, *J. Mater. Chem. C*, 2014, **2**, 5587-5592.
6. K. M. Schelkle, M. Bender, K. Jeltsch, T. Buckup, K. Müllen, M. Hamburger and U. H. F. Bunz, *Angew. Chem. Int. Ed.*, 2015, **54**, 14545-14548.
7. C. Zhong, C. Duan, F. Huang, H. Wu and Y. Cao, *Chem. Mater.*, 2011, **23**, 326-340.
8. C. Zhu, L. Liu, Q. Yang, F. Lv and S. Wang, *Chem. Rev.*, 2012, **112**, 4687-4735.
9. H. Shi, H. Sun, H. Yang, S. Liu, G. Jenkins, W. Feng, F. Li, Q. Zhao, B. Liu and W. Huang, *Adv. Funct. Mater.*, 2013, **23**, 3268-3276.
10. H. Shi, X. Ma, Q. Zhao, B. Liu, Q. Qu, Z. An, Y. Zhao and W. Huang, *Adv. Funct. Mater.*, 2014, **24**, 4823-4830.
11. H. E. Cingil, I. M. Storm, Y. Yorulmaz, D. W. te Brake, R. de Vries, M. A. Cohen Stuart and J. Sprakel, *J. Am. Chem. Soc.*, 2015, **137**, 9800-9803.

12. F. Lv, T. Qiu, L. Liu, J. Ying and S. Wang, *Small*, 2016, **12**, 696-705.
13. C. S. Almeida, I. K. Herrmann, P. D. Howes and M. M. Stevens, *Chem. Mater.*, 2015, **27**, 6879-6889.
14. D. W. Bright, F. B. Dias, F. Galbrecht, U. Scherf and A. P. Monkman, *Adv. Funct. Mater.*, 2009, **19**, 67-73.
15. Z.-Q. Lin, N.-E. Shi, Y.-B. Li, D. Qiu, L. Zhang, J.-Y. Lin, J.-F. Zhao, C. Wang, L.-H. Xie and W. Huang, *J. Phys. Chem. C*, 2011, **115**, 4418-4424.
16. M. Knaapila and A. P. Monkman, *Adv. Mater.*, 2013, **25**, 1090-1108.
17. L. Huang, L. Zhang, X. Huang, T. Li, B. Liu and D. Lu, *J. Phys. Chem. B*, 2014, **118**, 791-799.
18. A. J. Cadby, P. A. Lane, H. Mellor, S. J. Martin, M. Grell, C. Giebeler, D. D. C. Bradley, M. Wohlgenannt, C. An and Z. V. Vardeny, *Phys. Rev. B*, 2000, **62**, 15604-15609.
19. M. Knaapila, M. Torkkeli, F. Galbrecht and U. Scherf, *Macromolecules*, 2013, **46**, 836-843.
20. R. C. Evans, A. G. Macedo, S. Pradhan, U. Scherf, L. D. Carlos and H. D. Burrows, *Adv. Mater.*, 2010, **22**, 3032-3037.
21. P. Prins, F. C. Grozema, J. M. Schins, T. J. Savenije, S. Patil, U. Scherf and L. D. A. Siebbeles, *Phys. Rev. B*, 2006, **73**, 045204.
22. C. Rothe, F. Galbrecht, U. Scherf and A. Monkman, *Adv. Mater.*, 2006, **18**, 2137-2140.
23. S. H. Chen, A. C. Su and S. A. Chen, *J. Phys. Chem. B*, 2005, **109**, 10067-10072.
24. D. W. Bright, K. C. Moss, K. T. Kamtekar, M. R. Bryce and A. P. Monkman, *Macromol. Rapid Commun.*, 2011, **32**, 983-987.
25. A. J. C. Kuehne, M. Kaiser, A. R. Mackintosh, B. H. Wallikewitz, D. Hertel, R. A. Pethrick and K. Meerholz, *Adv. Funct. Mater.*, 2011, **21**, 2564-2570.
26. M. J. Banach, R. H. Friend and H. Sirringhaus, *Macromolecules*, 2004, **37**, 6079-6085.
27. P. C. Marr, K. McBride and R. C. Evans, *Chem. Commun.*, 2013, **49**, 6155-6157.
28. R. C. Evans and P. C. Marr, *Chem. Commun.*, 2012, **48**, 3742-3744.
29. J. M. Behrendt, A. B. Foster, M. C. McCairn, H. Willcock, R. K. O'Reilly and M. L. Turner, *J. Mater. Chem. C*, 2013, **1**, 3297-3304.
30. R. de Francisco, M. Hoyos, N. García and P. Tiemblo, *Langmuir*, 2015, **31**, 3718-3726.
31. V. de Zea Bermudez, R. A. Sá Ferreira, L. D. Carlos, C. Molina, K. Dahmouche and S. J. L. Ribeiro, *J. Phys. Chem. B*, 2001, **105**, 3378-3386.
32. I. Meazzini, N. Willis-Fox, C. Blayo, J. Arlt, S. Clement and R. C. Evans, *J. Mater. Chem. C*, 2016.
33. Y. Cui, M. Wang, L. Chen and G. Qian, *Dyes. Pigm.*, 2004, **62**, 43-47.
34. V. de Zea Bermudez, L. D. Carlos and L. Alcácer, *Chem. Mater.*, 1999, **11**, 569-580.
35. V. T. Freitas, P. P. Lima, R. A. S. Ferreira, E. Pecoraro, M. Fernandes, V. Zea Bermudez and L. D. Carlos, *J. Sol-Gel Sci. Technol.*, 2012, **65**, 83-92.
36. L. D. Carlos, R. A. Sá Ferreira, I. Orion, V. de Zea Bermudez and J. Rocha, *J. Lumin.*, 2000, **87–89**, 702-705.
37. P. P. Lima, R. A. S. Ferreira, S. A. Júnior, O. L. Malta and L. D. Carlos, *J. Photochem. Photobiol. A*, 2009, **201**, 214-221.
38. L. D. Carlos, V. de Zea Bermudez, R. A. Sá Ferreira, L. Marques and M. Assunção, *Chem. Mater.*, 1999, **11**, 581-588.
39. L. Fu, R. A. Sá Ferreira, N. J. O. Silva, L. D. Carlos, V. de Zea Bermudez and J. Rocha, *Chem. Mater.*, 2004, **16**, 1507-1516.
40. N. Willis-Fox, M. Kraft, J. Arlt, U. Scherf and R. C. Evans, *Adv. Funct. Mater.*, 2016, **26**, 532-542.
41. S. S. Nobre, P. P. Lima, L. Mafra, R. A. Sá Ferreira, R. O. Freire, L. Fu, U. Pischel, V. de Zea Bermudez, O. L. Malta and L. D. Carlos, *J. Phys. Chem. C*, 2007, **111**, 3275-3284.
42. L. D. Carlos, R. A. Sá Ferreira, R. N. Pereira, M. Assunção and V. de Zea Bermudez, *J. Phys. Chem. B*, 2004, **108**, 14924-14932.
43. L. D. Carlos, R. A. S. Ferreira, R. N. Pereira, M. Assunção and V. de Zea Bermudez, *J. Phys. Chem. B*, 2004, **108**, 14924-14932.
44. M. Knaapila, V. M. Garamus, F. B. Dias, L. Almásy, F. Galbrecht, A. Charas, J. Morgado, H. D. Burrows, U. Scherf and A. P. Monkman, *Macromolecules*, 2006, **39**, 6505-6512.

45. C.-Y. Chen, C.-S. Chang, S.-W. Huang, J.-H. Chen, H.-L. Chen, C.-I. Su and S.-A. Chen, *Macromolecules*, 2010, **43**, 4346-4354.
46. M. Knaapila, Z. Konôpková, M. Torkkeli, D. Haase, H. P. Liermann, S. Guha and U. Scherf, *Phys. Rev. E*, 2013, **87**, 022602.
47. M. Knaapila, D. W. Bright, R. Stepanyan, M. Torkkeli, L. Almásy, R. Schweins, U. Vainio, E. Preis, F. Galbrecht, U. Scherf and A. P. Monkman, *Phys. Rev. E*, 2011, **83**, 051803.
48. V. T. Freitas, P. P. Lima, R. A. S. Ferreira, E. Pecoraro, M. Fernandes, V. de Zea Bermudez and L. D. Carlos, *J. Sol-Gel Sci. Technol.*, 2013, **65**, 83-92.
49. M. Ranger, D. Rondeau and M. Leclerc, *Macromolecules*, 1997, **30**, 7686-7691.
50. T.-S. Ahn, R. O. Al-Kaysi, A. M. Müller, K. M. Wentz and C. J. Bardeen, *Rev. Sci. Instrum.*, 2007, **78**, 086105.
51. C. Tan, E. Atas, J. G. Müller, M. R. Pinto, V. D. Kleiman and K. S. Schanze, *J. Am. Chem. Soc.*, 2004, **126**, 13685-13694.
52. A. K. Bansal, A. Ruseckas, P. E. Shaw and I. D. W. Samuel, *J. Phys. Chem. C*, 2010, **114**, 17864-17867.
53. Y. Yang, G. A. Turnbull and I. D. W. Samuel, *Adv. Funct. Mater.*, 2010, **20**, 2093-2097.

Chapter Four

Tunable Photoluminescence from Perylene Dicarboxdiimide–Poly(oxyalkylene)/Siloxane Hybrids for Luminescent Solar Concentrators

The work in this Chapter has been published in:
I. Meazzini, N. Willis-Fox, C. Blayo, J. Arlt, S. Clément and R. C. Evans, Targeted design leads to tunable photoluminescence from perylene dicarboxdiimide–poly(oxyalkylene)/siloxane hybrids for luminescent solar concentrators, *J. Mater. Chem. C*, **2016**, 4, 4049-4059.

4.1 Introduction

π-conjugated semiconductors, such as organic dyes, are promising materials for the development of flexible, lightweight devices, such as organic light-emitting displays[1, 2], organic photovoltaic devices[3, 4] and LSCs.[5, 6] They can be readily processed from solution, and due to their conjugated backbone, they conduct electricity, absorb and emit light. However, their solid-state morphology can influence their excited state energy, and as such, sophisticated design methodologies are required to yield efficient optoelectronic devices.[7, 8] A particular challenge is the transfer of a dye from solution to the solid-state, which can lead to aggregation and/or re-absorption phenomena that are usually associated with quenching of the fluorescence. This issue becomes particularly relevant when the efficiency of a device is strictly dependent on the dyes capability of re-emitting light upon absorption, which is the case for LSCs.

For organic lumophores, several strategies have been adopted to overcome this problem, most of which consist of the preparation of rationally-designed fluorophores which could align following a preferential orientation to decrease undesirable re-absorption and aggregation effects and focus the emitted light towards the edges of the LSC. For example, in an attempt to model an effective alignment angle for a lumophore in a LSC, Debije *et al.*[9] investigated the orientation of a series of dyes: rhodamine B, 4-dicyanomethylene-2-methyl-6-(*p*-dimethylaminostyryl)-4*H*-pyran and DFSB-K160 in a liquid crystal host. The "tilted" orientation of the fluorophore (an angle of 45° in respect to the waveguide plate) achieved the most efficient emission to the edges. However, the design of this system is complicated and the number of defects in the alignment has prevented practical use of this approach to date. Schenning *et al.* instead synthesised a triad dye consisting of two perylene diimide donors bridged by a perylene acceptor presenting bulky bay substituents.[10] The resulting dye could both reduce re-absorption and aggregation, and exhibit oriented emission. To exploit the latter property however, the fluorophore needed to be pre-oriented by encapsulation in a nematic liquid crystalline phase. While both of these examples represent an elegant solution to yield higher LSC efficiencies, they require significant effort in the device preparation.

Another approach proposed to reduce these losses consists in the incorporation of the dye into a host matrix, which could inhibit the intermolecular interactions and also improve the mechanical and optical properties of the fluorophore.[11, 12] However, the host and guest molecules

need to be compatible in order to achieve homogeneous mixing between the two species. This issue is especially relevant when working with silica-based materials and organic fluorophores, where compatibility can be achieved using an organic-inorganic host, which offers the advantages of host-guest chemical affinity while maintaining the stability typical of an inorganic silica network. For Class I hybrids (where the molecules are held together by physical interactions) the forces involved at the interface between the host and guest molecules (*e.g.* H-bonding, π-π stacking, van der Waals and electrostatic) can determine the goodness of the dispersion of the fluorophore in the host.[13-15] However, as shown in the previous Chapter, judicious functionalisation of the guest molecules, can introduce the possibility of covalent-grafting of the π-conjugated molecule to the backbone yielding Class II hybrids.[16-20]

In this context, *ureasils* have shown great potential as they are organic-inorganic hybrid hosts, consisting of a siliceous skeleton that is chemically-grafted to poly(oxyalkylene) chains *via* urea [NHC(=O)HN] bridges, offering the possibility of chemically reacting either their siloxane or poly(etheramine) precursors with an organic fluorophore before the overall condensation of the sol-gel mixture into a silica network.[21] Moreover, ureasils are intrinsically photoluminescent and have shown great potentials as an active host for physical incorporation of π-conjugated polymers,[22,23] and molecular dyes.[5] They can be processed as transparent free-standing monoliths or as thin films, and exhibit relatively high refractive indices (≈1.49),[24] which makes them good candidates for application as waveguides in LSCs.[5,25]

Intrigued by this possibility, in this Chapter the targeted design of a family of perylene carboxdiimide-bridged triethoxysilane (**PDI-Sil**, **Fig. 4.1**) grafted to the backbone of ureasil hybrids will be investigated. The perylene dye was selected as it presents most of the favourable properties required for a lumophore in LSCs: good photostability, high photoluminescence quantum yield and good spectral overlap between its absorption and the solar spectrum. However, LSC architectures consisting of a perylene dye simply physically dispersed within a waveguide matrix can exhibit aggregation and/or re-absorption losses influencing the overall efficiency of the device.[26, 27] In this Chapter, the possibility of tackling this issue by covalently grafting the dye to the waveguide matrix will be investigated. Moreover, using an optically active host such as a

ureasil can introduce the possibility of energy transfer between the waveguide and the lumophore, broadening the range of harvested wavelengths from the solar spectrum.

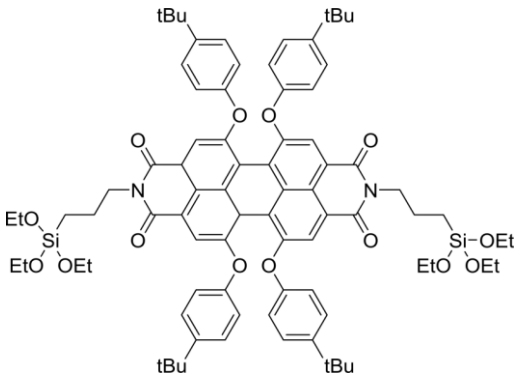

Figure 4.1. Chemical structure of **PDI-Sil**.

4.1.1 Aims

In this Chapter, the design and synthesis of a series **PDI-Sil**-grafted ureasil hybrids, is presented in an effort to obtain a homogeneous dispersion of the dye within the ureasil waveguide to reduce aggregation and re-absorption phenomena. To investigate the role of the structure of the host matrix on the spatial isolation and orientation of the lumophore molecules, four different Jeffamine precursors, two linear and two tripodal with a short and a long chain each, respectively, will be used. A combination of structural and spectroscopic characterisation techniques will be used to probe the effect of the structural framework of the ureasil on the spatial isolation of the lumophore molecules and the possibility of the energy transfer between the ureasil donor and the perylene acceptor.

4.2 Experimental

4.2.1 Synthesis of PDI-Sil

N,*N*-bis(3-triethoxysilylpropyl)-1,6,7,12-tetra-*tert*-butylphenoxyperylene-3,4:9,10-tetra-carboxdiimide (**PDI-Sil**) was a kind gift from Prof. Sébastien Clément, Université de Montpellier. It was prepared starting from 1,6,7,12-tetra-*tert*-butylphenoxyperylene-3,4,9,10-tetracarboxylic dianhydride (**1**) which was synthesised following previously reported procedures,[28, 29] and added to a Schlenk flask containing 1,6,7,12-tetra-*tert*-butylphenoxyperylene-3,4,9,10-tetracarboxylic dianhydride (503 mg, 0.51 mmol) in dry ethanol (150 mL) (**Fig. 4.2**). 3-aminopropyltriethoxysilane (1.45 mL, 6.12 mmol) was then added dropwise and the mixture was

reacted under reflux for 48 h. After cooling at room temperature, the precipitate was collected by filtration and the excess of 3-aminopropyltriethoxysilane removed thoroughly by washing with cold ethanol. **PDI-Sil** was obtained in as a dark red powder (yield=76%). The characterisation for **PDI-Sil** can be found in the Appendix (**Fig. A.4.1-3**).

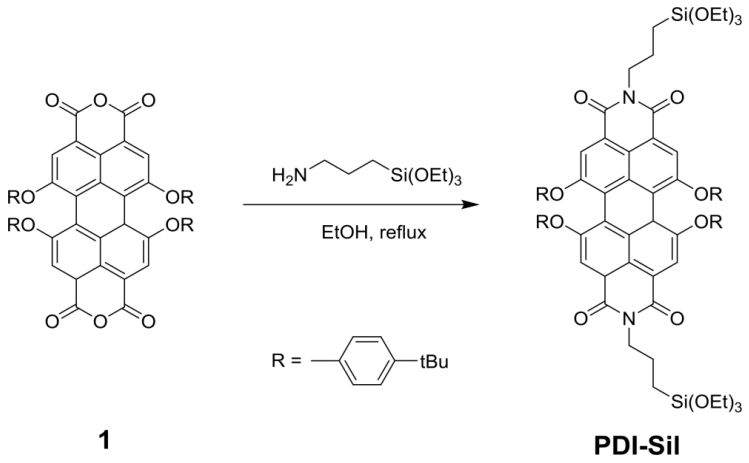

Figure 4.2. Synthetic route to **PDI-Sil**.

4.2.2 Synthesis of PDI-Sil-Ureasil Hybrids

The undoped ureasil samples were prepared using the procedure described in **Chapter 3**. In this case, the different UPTES precursors were prepared using either the diamines, Jeffamine ED-600 (M_w = 600 g mol^{-1}, ~4 OCH_2CHCH_3 and 9 OCH_2CH_2 repeat units, r.u.) or Jeffamine D-4000 (M_w = 4000 g mol^{-1}, 68 OCH_2CHCH_3 r.u.) to prepare the di-ureasils, or the triamines Jeffamine T-403 (M_w = 440 g mol^{-1}, 5–6 OCH_2CHCH_3 r.u.) or Jeffamine T-5000 (M_w = 5000 g mol^{-1}, 85 OCH_2CHCH_3 r.u.) to synthesise the tri-ureasils. Each Jeffamine, was reacted with a stoichiometric amount of ICPTES to prepare either the d- or the t-UPTES precursor and the initial amount of reagents was calculated to obtain ~2 g (mass weighed exactly for each sample) of dried monolith. The ratios of THF to Jeffamine were doubled for samples made with Jeffamine D-4000 and Jeffamine T-5000 due to their higher viscosities. We note that for di-ureasils prepared using Jeffamine D-4000 the amount of HCl used for the gelation was doubled compared to the other samples to accelerate the gelation process. The final samples are designated as d-U(*X*) for the di-ureasils and t-U(*X*) for the tri-ureasils, where *X* corresponds to the name of the starting Jeffamine polyetheramine. A similar approach was employed for the synthesis of **PDI-Sil**-ureasils, with the addition of a fixed volume of a stock solution of **PDI-Sil** in THF (0.72 mmol dm^{-3}) to the UPTES

precursor under stirring prior to addition of the gelation agents. For each sample, the volume of dye solution was optimised to obtain a concentration of 0.005%$_{w/w}$ in the final monolith. The exact quantities used for the preparation of the samples can be found in the Appendix (**Section 2.2**).

4.3 Results and Discussion

The preparation of ureasil hybrids is usually comprised of two steps (**Fig. 4.3**). In the first step, stochiometric quantities of ICPTES and Jeffamine are reacted in a THF solution for 12 h under reflux (70 °C). In the second step, the initiators for the acid-catalysed hydrolysis and further condensation of the silica network are added to the mixture and the sol is then aged. This process yields ureasils as transparent monoliths; changes in this synthetic procedure can lead to cracking of the silica network due to the intense capillary strain during the evaporation of THF.[30] Therefore, when trying to covalently incorporate the **PDI-Sil** into the ureasil network, monitoring whether the hydrolysis of the –OCH$_2$-CH$_3$ moieties, located at the **PDI-Sil** extremities, can be performed in the same conditions (water, EtOH, and HCl until pH = 2) used for the preparation of regular un-doped ureasil hybrids represents a crucial step in identifying the appropriate reaction conditions.

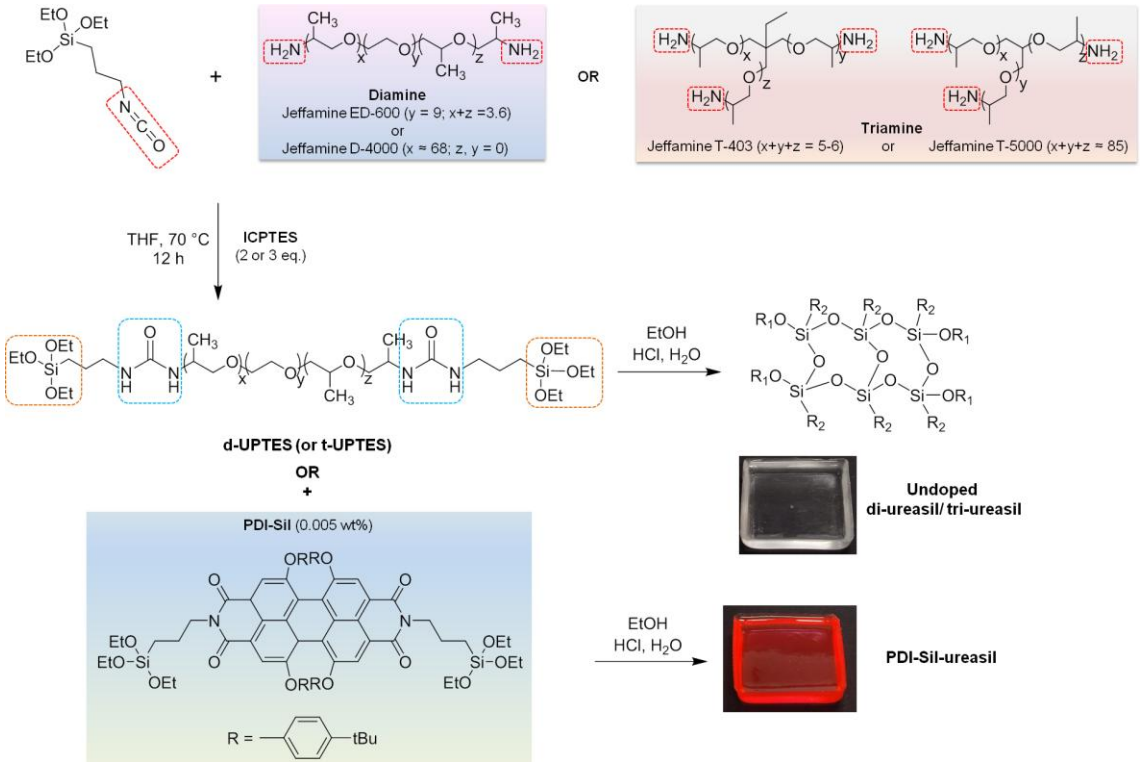

Figure 4.3. Synthesis of undoped and **PDI-Sil**-ureasils (R_1 = Si-O-Si- or H, R_2 = -$(CH_2)_3$-NHCONH-Jeffamine).

4.3.1 Grafting of PDI-Sil to Ureasil Hybrids

The acidolysis process for **PDI-Sil** was tested using four different experimental conditions: pH = 2, pH = 3, pH = 4 and pH = 5. To reproduce the experimental conditions of a regular ureasil synthesis, the dye was dissolved into THF (10^{-4} mol dm^{-3}) and the pH regulated by addition of HCl (0.5 mol dm^{-3}). As shown in **Fig. 4.4**a, the sample at pH = 2 presents a different colour compared to the others. This is likely to be due to the hydrolysis and condensation of the ethoxysilane moieties of the **PDI-Sil** molecules, which led to the formation of larger condensed dye aggregates. A similar colour trend has been previously observed in literature for perylenediimide-bridged-triethoxysilane.[31] MALDI-TOF mass spectrometry measurements were used to confirm this hypothesis (**Fig. 4.4**b and c). These results showed that upon addition of the sol-gel reactants to a solution of **PDI-Sil** dissolved in THF, the M^+ molecular peak (*m/z* 1390.66, **Fig. 4.4**b) disappears and a new peak corresponding to the completely hydrolysed dye appears at *m/z* 1222.47 (**Fig. 4.4**c). It was also noticed that a new population of peaks appears in the region ranging from 2200 to 2600 *m/z*.

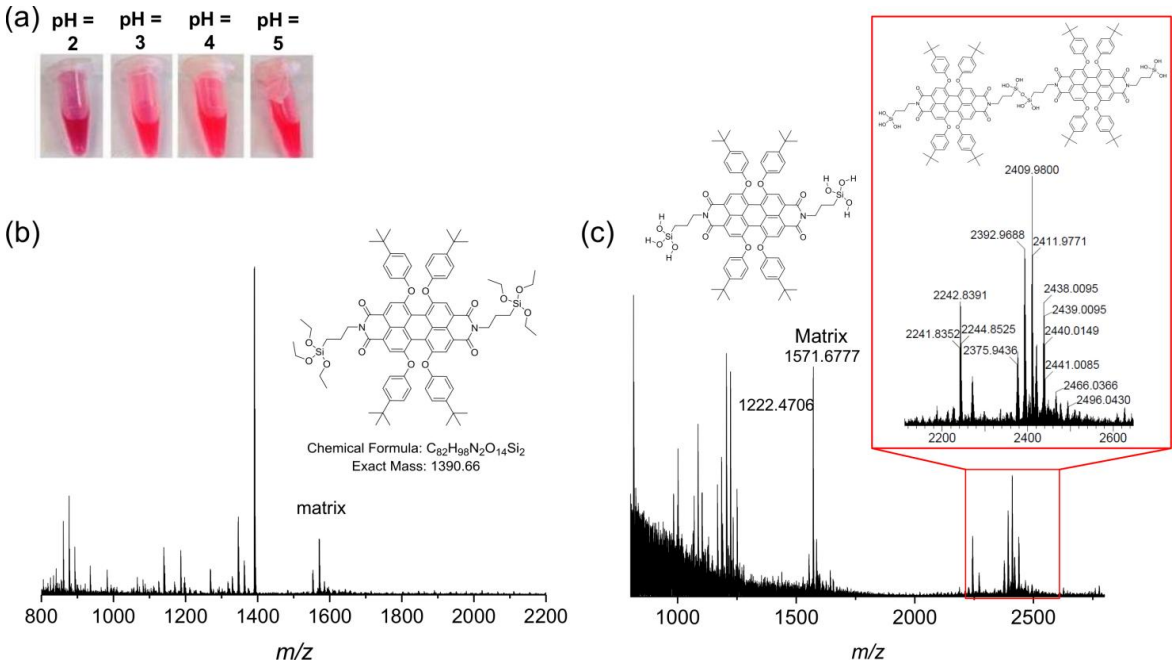

Figure 4.4. Acid-catalysed hydrolysis of **PDI-Sil** under the ureasil reaction conditions. (a) Photographs of a **PDI-Sil** solution in THF (10^{-4} mol dm^{-3}) upon ageing at different pH (24 h). (b) MALDI-TOF mass spectrum and structure of the **PDI-Sil** and (c) MALDI-TOF spectrum and structure of the **PDI-Sil** solution following addition of the catalyst (aq. HCl/EtOH).

This contribution can be ascribed to the formation of **PDI-Sil** dimers with the loss of hydroxyl moieties (*m/z* 2409.98 – 1OH, *m/z* 2392.01 – 2OH, *m/z* 2375.94 – 3OH) and *t*-butylphenyl (*m/z* 2242.84 – 3OH, 1 *t*-butylphenyl). Ito *et al.* have recently shown that the stacking of perylene dimers can lead to progressive changes in the UV/Vis absorption spectra of the final solution as a function of the concentration.[32] This further supports the colour changes that were observed for the dye at pH = 2; however this process appears to be concentration dependent as no colour change was observed upon addition of the gelation reagents to a diluted **PDI-Sil** solution (10^{-5} mol dm^{-3}, THF). Given the low concentration of **PDI-Sil** used for the preparation of the doped ureasil hybrids, no stacking effects are expected to be observed in our samples.

The rest of the synthetic process was carried out using the procedure previously described in **Chapter 3**. It is important to note that in this case, the hybrids were prepared using four different Jeffamines: the di-branched: Jeffamine ED-600 and D-4000 and the tri-branched Jeffamine T-403 and T-5000 and the same synthetic methodology was applied for each one of them to prepare the corresponding undoped ureasils (**d-U(600)**, **d-U(4000)**, **t-U(403)** and **t-U(5000)**, respectively). However, while for the ureasils prepared with Jeffamine ED-600, T-403 and T-5000 the gelation time was ranging from 10 to 25 minutes, 36+ hours were needed to achieve full gelation of **dU-(4000)**. Upon completion of the gelation/drying process the samples were obtained as transparent, free-standing monoliths. The difference in the structure of the starting Jeffamines®, is reflected in the mechanical properties of the ureasils; namely, the lower weight ratio of silica/organic domains makes **d-U(4000)-**based hybrids very flexible and resistant to contraction (**Fig. 4.4**). While the higher silica domains to poly(ether) chains domain ratio makes **t-U(403)** rigid and difficult to either cut or bend.

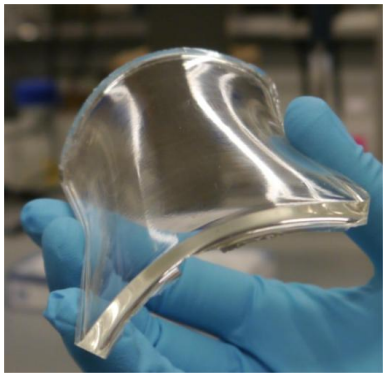

Figure 4.5. Mechanical properties of a ureasil hybrid. Picture of a sample of **d-U(4000)** while being bent.

4.3.2 Structural Investigation of Ureasil Hybrids

Structural characterisation of the hybrids was performed to analyse the effect of the different Jeffamine precursors on the arrangement of the final ureasil network and to understand whether the covalent incorporation of **PDI-Sil** units affects this organisation. Due to the low dopant concentration, it is difficult to isolate the contribution of the perylene dye compared to that of the ureasil host matrix using the following bulk characterisation methods.[22, 23]

4.3.2.1 Fourier Transform Infrared Spectroscopy and Powder X-Ray Diffraction

The Gaussian deconvolutions of the FTIR spectra in the Amide I region (1600-1800 cm^{-1}) of the **PDI-Sil**-doped and undoped samples are shown in **Fig. 4.6**a-h and the relative peak centres and percentage contribution for each band are reported in **Table 4.1**. Vibrational spectroscopy in this region provides important insight into the extent of the specific hydrogen bonding interactions associated with the urea moieties. Deconvolution of the region requires 3-5 components in order to model the Amide I band, which is typical for ureasils.[33, 34]

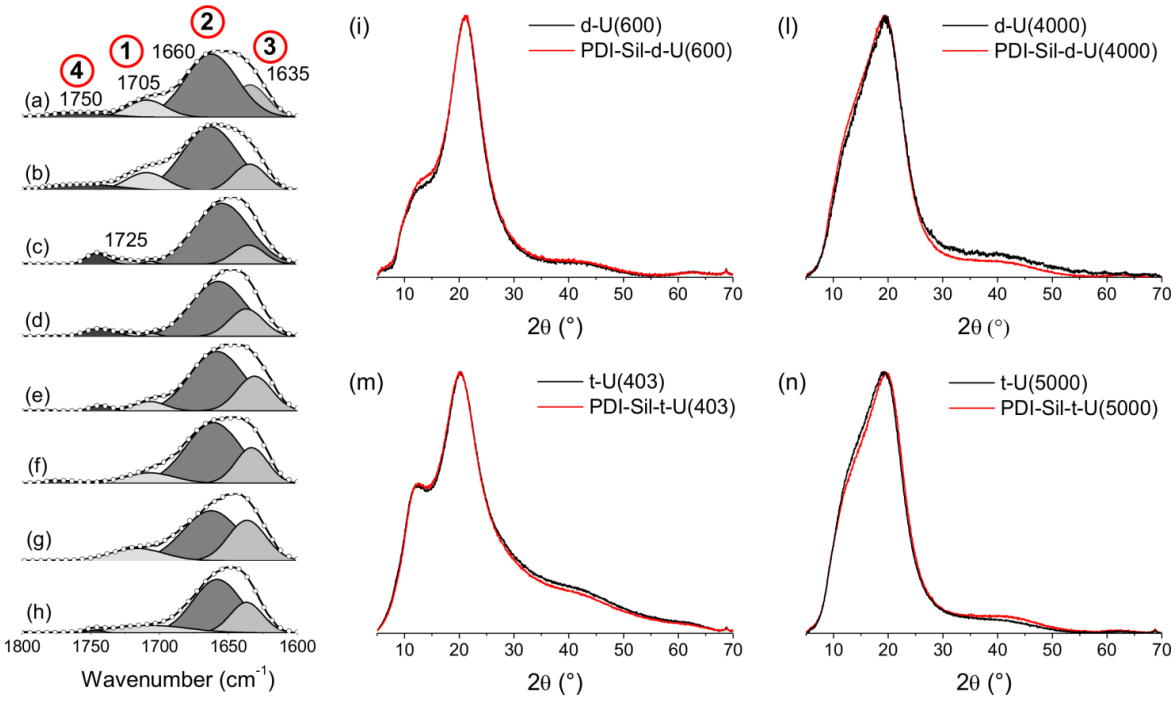

Figure 4.6. Investigation of the local structure of the ureasil hybrids. Gaussian fits to the Amide I region of the FTIR spectrum of (a) **d-U(600)**, (b) **PDI-Sil-d-U(600)**, (c) **d-U(4000)**, (d) **PDI-Sil-d-U(4000)**, (e) **t-U(403)**, (f) **PDI-Sil-t-U(403)**, (g) **t-U(5000)**, (h) **PDI-Sil-t-U(5000)**. The circled numbers represent the peaks described in the text. Powder X-ray diffraction patterns for (i) **d-U(600)** and **PDI-Sil-d-U(600)**, (l) **d-U(4000)** and **PDI-Sil-d-U(4000)**, (m) **t-U(403)** and **PDI-Sil-t-U(403)** and (n) **t-U(5000)** and **PDI-Sil-t-U(5000)**, in the range of $2\theta = 5 – 70°$.

Table 4.1. Results of Gaussian curve fitting of the Amide I band of undoped ureasils and **PDI-Sil**-ureasils, showing peak position, area and % contribution for each component resolved.

Sample ID	Peak 1 /cm^{-1} Contribution (%)	Peak 2 /cm^{-1} Contribution (%)	Peak 3 /cm^{-1} Contribution (%)	Peak 4 /cm^{-1} Contribution (%)	Peak 5 /cm^{-1} Contribution (%)
d-U(600)	1634 (21)	1663 (62)	1709 (12)	1758 (5)	-
PDI-Sil-d-U(600)	1635 (18)	1663 (59)	1709 (18)	1760 (5)	-
d-U(4000)	1635 (14)	1655 (77)	1707 (1)	1727 (3)	1746 (5)
PDI-Sil-d-U(4000)	1637 (22)	1657 (70)	1705 (1)	1722 (1)	1744 (6)
t-U(403)	1631 (25)	1658 (67)	1707 (6)	1743 (2)	-
PDI-Sil-t-U(403)	1633 (22)	1661 (66)	1707 (10)	1772 (2)	-
t-U(5000)	1637 (30)	1663 (57)	1716 (13)	-	-
PDI-Sil-t-U(5000)	1637 (23)	1658 (62)	1707 (14)	1747 (1)	-

Each sample presents the peaks centred at *ca.* 1707 cm^{-1} (Peak 1), 1660 cm^{-1} (Peak 2), corresponding to the stretching vibrations of the C=O moieties participating to H-bonding interactions with the poly(ether) chains and *ca.* 1635 cm^{-1} (Peak 3), ascribed to ordered urea-urea H-bonds.[34] A fourth contribution centred at *ca.*1745 cm^{-1} (Peak 4) is also present in every sample, with the exception of **t-U(5000)**, and indicates the presence of non-bonded urea moieties. Interestingly, a fifth contribution to the Amide I band (at *ca.* 1727 cm^{-1}, Peak 5) was observed for **d-U(4000)**-based samples. This is ascribed to the same type of interactions corresponding to Peak 1, Peak 2 and Peak 3 and is due to the higher amount of HCl used to induce gelation of this sample. It has previously been shown that changes in the HCl concentration affect the proportion of polyether/urea interactions in ureasil-type materials.[33] **Fig. 4.6**i-m shows the PXRD patterns for all the samples paired as a function of the ureasil type. Each diffraction pattern consists of a primary band centred between 19.0 and 21.1° and a shoulder at 12.2-13.5°. These results are typical for ureasils; the primary band indicates ordering within the siliceous domains,[35] while the shoulder is ascribed to in-plane ordering of the intra-siloxane domains. From the primary peak, the structural unit distance (*d*) and the coherence length (*l*) were determined using the Bragg's Law and the Scherrer equation, respectively (**Eqn. 2.24** and **2.25**, respectively). Both the values of *d* (4.4 ± 0.2

Å) and *l* (10.2 ± 0.7 Å) are characteristic of these amorphous materials. Although the resolution of the shoulder is higher for the lower molecular weight ureasils, for each set of samples the diffraction patterns are dominated by the ureasil features and no significant change was observed for any of the samples upon incorporation of the **PDI-Sil**.

4.3.2.2 Solid-State NMR Spectroscopy

The ^{13}C MAS-NMR spectra of the samples are shown in **Fig. 4.7**. As previously reported for these materials, the higher rigidity of the **t-U(403)-**based network results in stronger intensities for the corresponding NMR signals.[21, 36] Conversely, the other samples present a higher mobility leading to a generally lower signal intensity. These results match the behaviour observed macroscopically for monolith (*i.e.* **t-U(403)-**based samples are stiffer than the others). As expected, the contribution of the **PDI-Sil** cannot be directly observed due to the low loading concentration. Nevertheless, subtle changes in the intensity of the **PDI-Sil**-ureasil signals are observed in comparison to the corresponding undoped ureasil, indicating that the covalent grafting of the dye is somehow influencing the structure of the material.

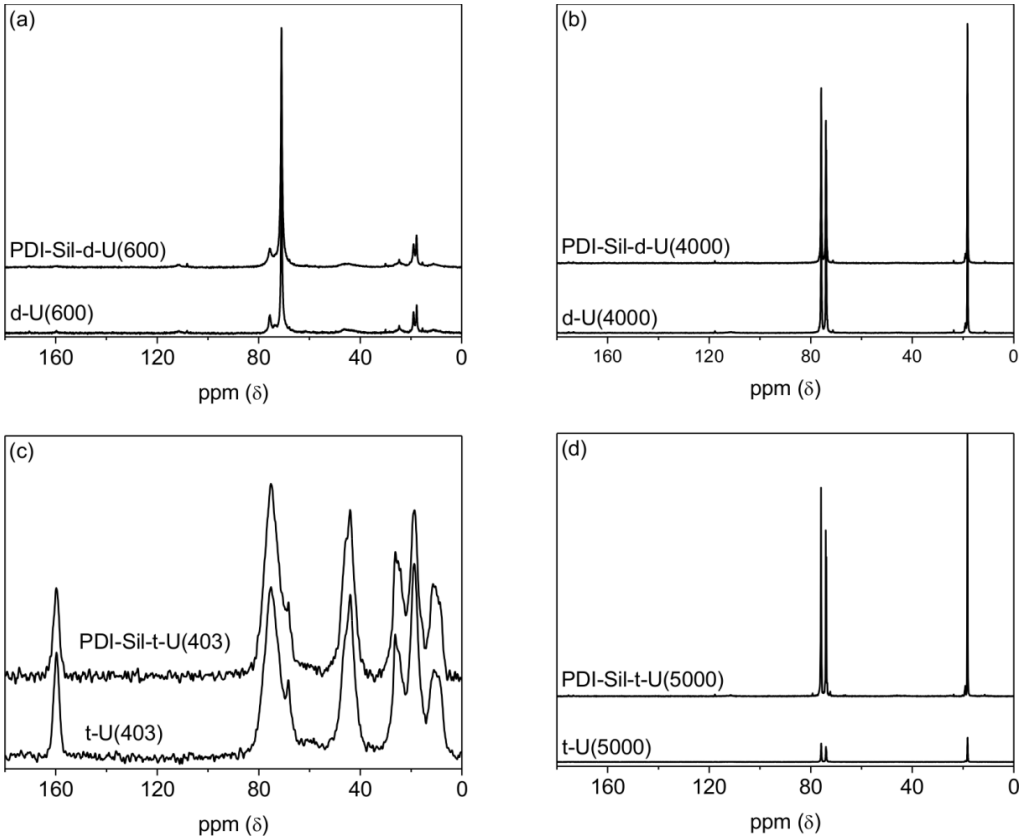

Figure 4.7. ^{13}C MAS-NMR spectra for: (a) **d-U(600)** and **PDI-Sil-d-U(600)**, (b) **d-U(4000)** and **PDI-Sil-d-U(4000)**, (c) **t-U(403)** and **PDI-Sil-t-U(403)** and (d) **t-U(5000)** and **PDI-Sil-t-U(5000)**.

Table 4.2. ^{13}C MAS-NMR chemical shifts (ppm vs. TMS) of undoped and PDI-Sil-ureasils.

Signal Assignment	d-U(600)	PDI-Sil-d-U(600)	d-U(4000)	PDI-Sil-d-U(4000)	t-U(403)	PDI-Sil-t-U(403)	t-U(5000)	PDI-Sil-t-U(5000)
C=O urea	-	-	-	-	159.7	159.7	-	-
-OCH	75.7	75.7	74.0/75.9	74.0/75.9	75.3	75.2	74.1/75.9	74.0/75.9
-(OCH_2CH_2)-	71.0	71.0			68.3	68.3		
-NCH_2- in $N(CH_2)_3$-Si	45.8	45.3	-	-	43.9	44.0	-	-
-CH_2- in $N(CH_2)_3$-Si-	24.6	24.7	-	-	26.1	26.2	-	-
-CH_3 in $OCH_2CH(CH_3)$	19.1	19.0	19.0	19.1	18.8	18.7	19.0	19.1
-CH_3 in $(CH_3CH_2O)_3Si$	17.7	17.8	18.2	18.3	-	-	18.2	18.3
-CH_2Si- in $N(CH_2)_3Si$	-	-	-	-	10.9	11.4	-	-

The ^{29}Si MAS-NMR spectra of the samples (**Fig. 4.8**) is characterised by the three signals corresponding to the T_1 (~-49 ppm,), T_2 (~-58 ppm) and T_3 (~-67 ppm), with the dominant contribution coming from the T_2 and T_3 signals. The absence of a fourth signal (T_0, at -44 ppm) indicates that none of the precursor was left unreacted. We notice that the T_1 is completely absent for **PDI-Sil-t-U(403)** and **t-U(403)** which corresponds the highest values of degree of condensation, *c*, ~80%. For the other samples, the degree of condensation ranges between 69-72% and all of these values are in reasonable agreement with those reported in literature for ureasils.[23, 37]

Solid-state NMR spectroscopy further supports our previous structural findings, indicating that the grafting of the **PDI-Sil** dye does not induce any major changes to the ureasil network which preserves its structure at the investigated loading concentration.

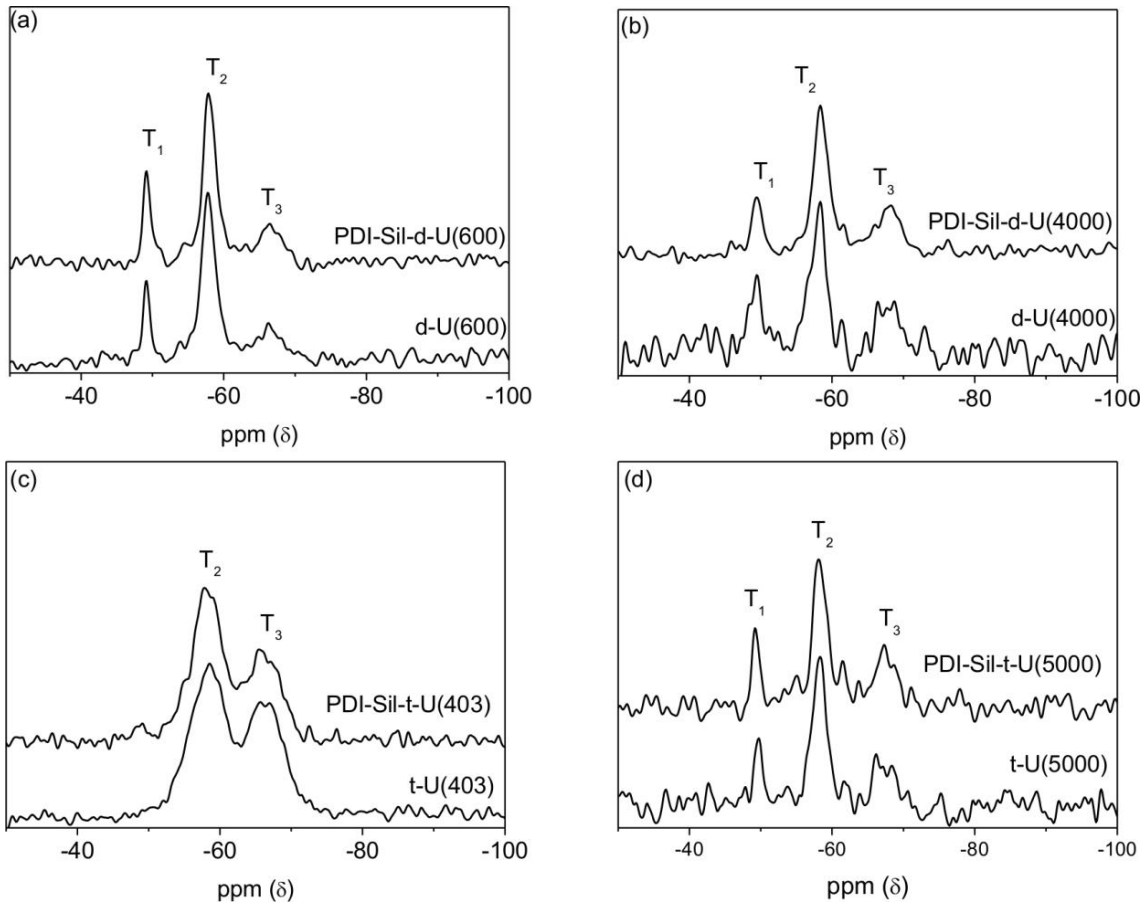

Figure 4.8. ^{29}Si MAS-NMR spectra for: (a) **d-U(600)** and **PDI-Sil-d-U(600)**, (b) **d-U(4000)** and **PDI-Sil-d-U(4000)**, (c) **t-U(403)** and **PDI-Sil-t-U(403)** and (d) **t-U(5000)** and **PDI-Sil-t-U(5000)**.

Table 4.3. ^{29}Si MAS-NMR chemical shifts (ppm vs TMS), population of different T_n species (%), and degree of condensation, *c* (%) of undoped and **PDI-Sil**-ureasils. Signals are labelled according to the T_n notation, where n (n = 1, 2, 3) is the number of Si-bridging oxygen atoms, T_1=(R′Si(OSi)-(OR)$_2$), T_2=(R′Si(OSi)$_2$(OR)), and T_3=(R′Si(OSi)$_3$).

Sample ID	T_1 (%)	T_2 (%)	T_3 (%)	*c* (%)[a]
d-U(600)	-49.2 (13.7)	-57.8 (59.8)	-65.8 (26.5)	71%
PDI-Sil-d-U(600)	49.2 (17.7)	-58.0 (58.3)	-66.1 (24.0)	69%
d-U(4000)	-49.3 (22.0)	-58.0 (54.0)	-67.9 (24.0)	67%
PDI-Sil-d-U(4000)	-49.5 (14.3)	-58.5 (57.3)	-67.8 (28.4)	71%
t-U(403)	_	-58.3 (57.5)	-66.5 (42.5)	81%
PDI-Sil-t-U(403)	_	-58.2 (61.4)	-67.2 (38.6)	80%
t-U(5000)	-49.7 (15.2)	-58.2 (60.1)	-67.2 (24.7)	70%
PDI-Sil-t-U(5000)	-49.3 (14.4)	-58.3 (53.9)	-67.3 (31.7)	72%

[a] $c = 1/3(\%T_1+2\%T_2+3\%T_3)$[38]

4.3.2.3 Thermogravimetric Analysis

The thermal stability of the samples was investigated in view of their potential application as LSCs. The thermograms of **PDI-Sil**, and of the undoped and doped ureasil samples are presented in **Fig. 4.9**.

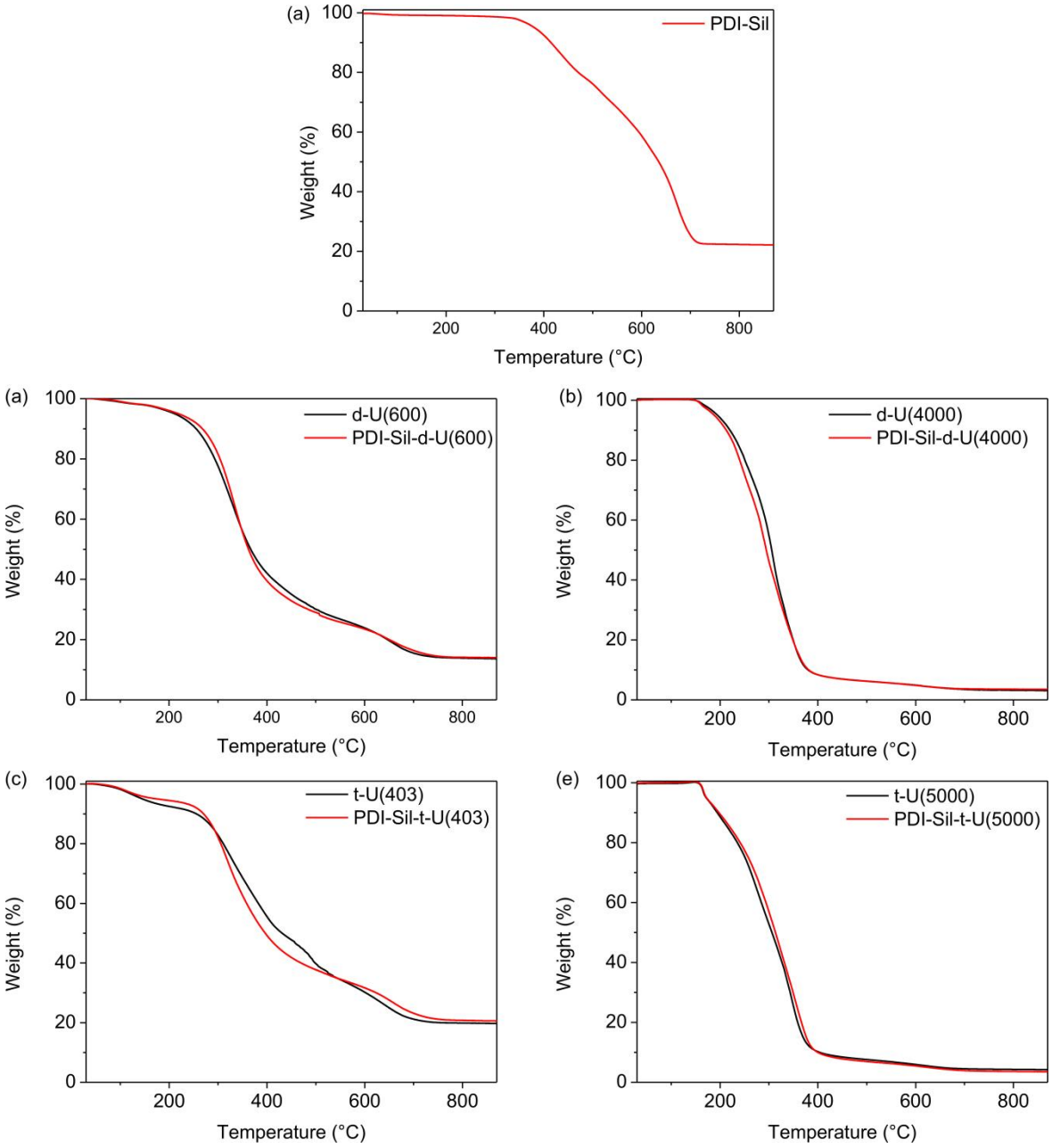

Figure 4.9. Thermograms of (a) **PDI-Sil**, (b) **d-U(600)** and **PDI-Sil-d-U(600)**, (c) **d-U(4000)** and **PDI-Sil-d-U(4000)**, (d) **t-U(403)** and **PDI-Sil-t-U(403)** and (e) **t-U(5000)** and **PDI-Sil-t-U(5000)** (air atmosphere, 10° C min^{-1}).

On its own, **PDI-Sil** (**Fig. 4.9**a) degrades in a two step process: the first weight loss (T_{onset}~380 °C) corresponds to the degradation of the alkyl chains bound to the nitrogen atoms and the bay substituent, while the second weight loss is ascribed to the thermal decomposition of the

aromatic backbone (T_{onset}~621 °C). Upon incorporation into any of the ureasil matrices, the thermal stability of the **PDI-Sil** is controlled by the ureasil (**Fig. 4.9**b-e). For each series of samples the thermograms obtained are in good agreement with the literature,[34, 39] with the main degradation event occurring at an onset temperature between ~250 and 280 °C, which is still well over the operating conditions of a standard solar cell working in hot climatic conditions (~80-95 °C).[40] As seen in the previous Chapter, **t-U(403)**-samples present a small weight loss at *ca*. T_{onset} ~115 °C, due to the evaporation of un-reacted ICPTES and/or trapped THF or gelation reagents.

4.3.3 Photophysical Investigation

4.3.3.1 Steady-State Photoluminescence Studies

Upon irradiation under UV light (λ_{ex}= 365 nm) the undoped ureasils display blue photoluminescence (**Fig. 4.10**), which is in full agreement with what reported in the literature for **d-U(600)** and **t-U(5000)**.[39, 41] Moreover, for each ureasil monolith, the emission is focussed at the edges of the slab, which is an experimental evidence of the waveguiding properties of these materials. The corresponding excitation and emission spectra for undoped ureasils are shown in **Fig. 4.11**.

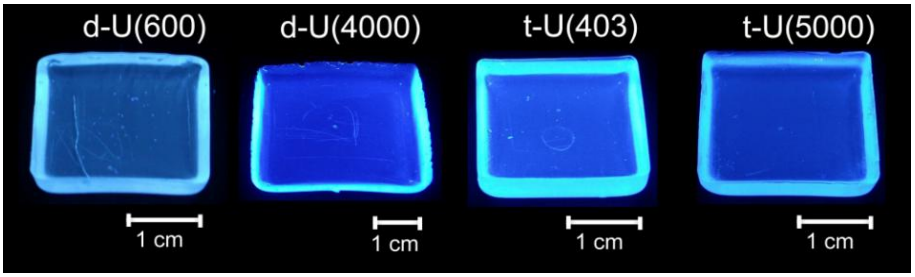

Figure 4.10. Picture of undoped ureasils under UV excitation (λ_{ex} = 365 nm).

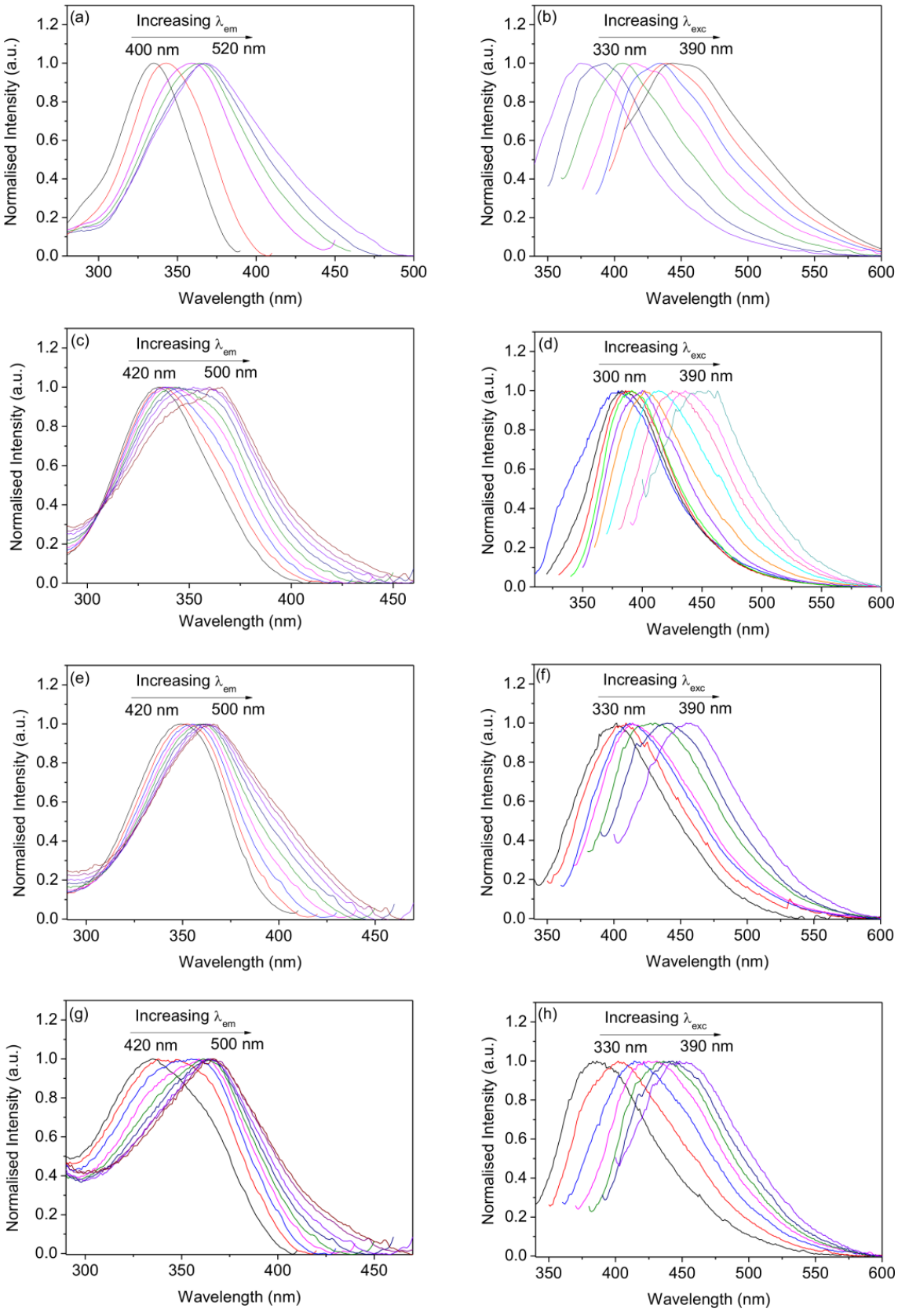

Figure 4.11. Optical investigation of the undoped ureasil hybrids. Excitation spectra of (a) **d-U(600)**, (c) **t-U(403)**, (e) **d-U(4000)** and (g) **t-U(5000)** at different λ_{em}. Emission spectra of (b) **d-U(600)**, (d) **t-U(403)**, (f) **d-U(4000)** and (h) **t-U(5000)** at different λ_{ex}.

As expected, the excitation spectra of the undoped ureasil (**Fig. 4.11**a,c,e,g) consist of a broad band ranging between 280 and 450 nm associated with the convolution of the electron-hole recombination occurring at the donor-acceptor pairs localised at the urea-bridges (*blue* component) and in the siliceous domains (*purplish-blue* component).[41] The same contributions are responsible for the corresponding emission spectra of the undoped ureasils with the characteristic broad band centred between 350-500 nm. For both sets of spectra, the maxima are strongly dependent on the excitation and emission wavelengths, as previously observed for organic-inorganic ureasil hybrids.[42] The Φ_{PL} were measured at λ_{ex}= 350 nm and range between 3.5 to 9.9 %, following this order of magnitude: **d-U(4000)** > **t-U(403)** > **t-U(5000)** > **d-U(600)**. For the linear ureasils, it has been shown that an increase in the chain-length leads to higher values of Φ_{PL}, which is consistent with what is observed in our case for **d-U(4000)** and **d-U(600)** (Φ_{PL} equal to 9.9 and 3.5%, respectively).[43]

The UV/Vis, PL and excitation spectra of **PDI-Sil** in solution are shown in **Fig. 4.12**. The dye presents the typical optical features of perylene dyes,[44] with a vibronically structured emission band displaying an absolute maximum at 600 nm. The corresponding excitation and absorption spectra show an absolute maxima centred at 567 and 570 nm, respectively, ascribed to the 0–0 vibronic band of the $S_0 \rightarrow S_1$ transition and two local maxima (529 and 440 nm) which can be attributed to the and 0–1 vibronic band of the $S_0 \rightarrow S_1$ transition and the electronic $S_0 \rightarrow S_2$ transition, respectively.[45, 46]

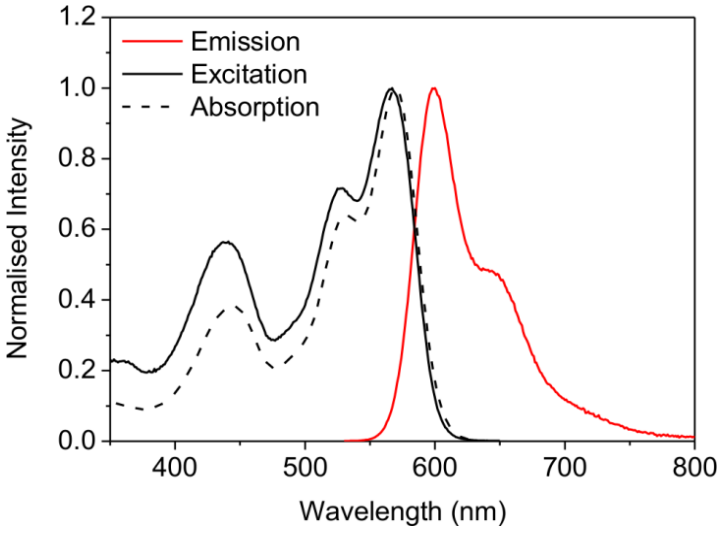

Figure 4.12. Optical properties of **PDI-Sil** in solution (10^{-6} mol dm^{-3}, THF): emission (solid red line, λ_{ex} = 520 nm), excitation (solid black line, λ_{em} = 670 nm) and absorption (black dashed line) spectra.

The PL and excitation spectra of **PDI-Sil**-ureasils are presented in **Fig. 4.13**a-d. Upon selective excitation in the UV (λ_{ex} = 330 nm), the emission spectrum of each sample presents two contributions: (i) the characteristic ureasil emission indicated by a broad band ranging between 350 and 500 nm and (ii) the **PDI-Sil** emission, associated with an intense structured band ranging between 550 and 750 nm. The corresponding excitation spectra measured at λ_{em} = 670 nm, present a similar trend, with the **PDI-Sil** contribution dominating for each spectrum.

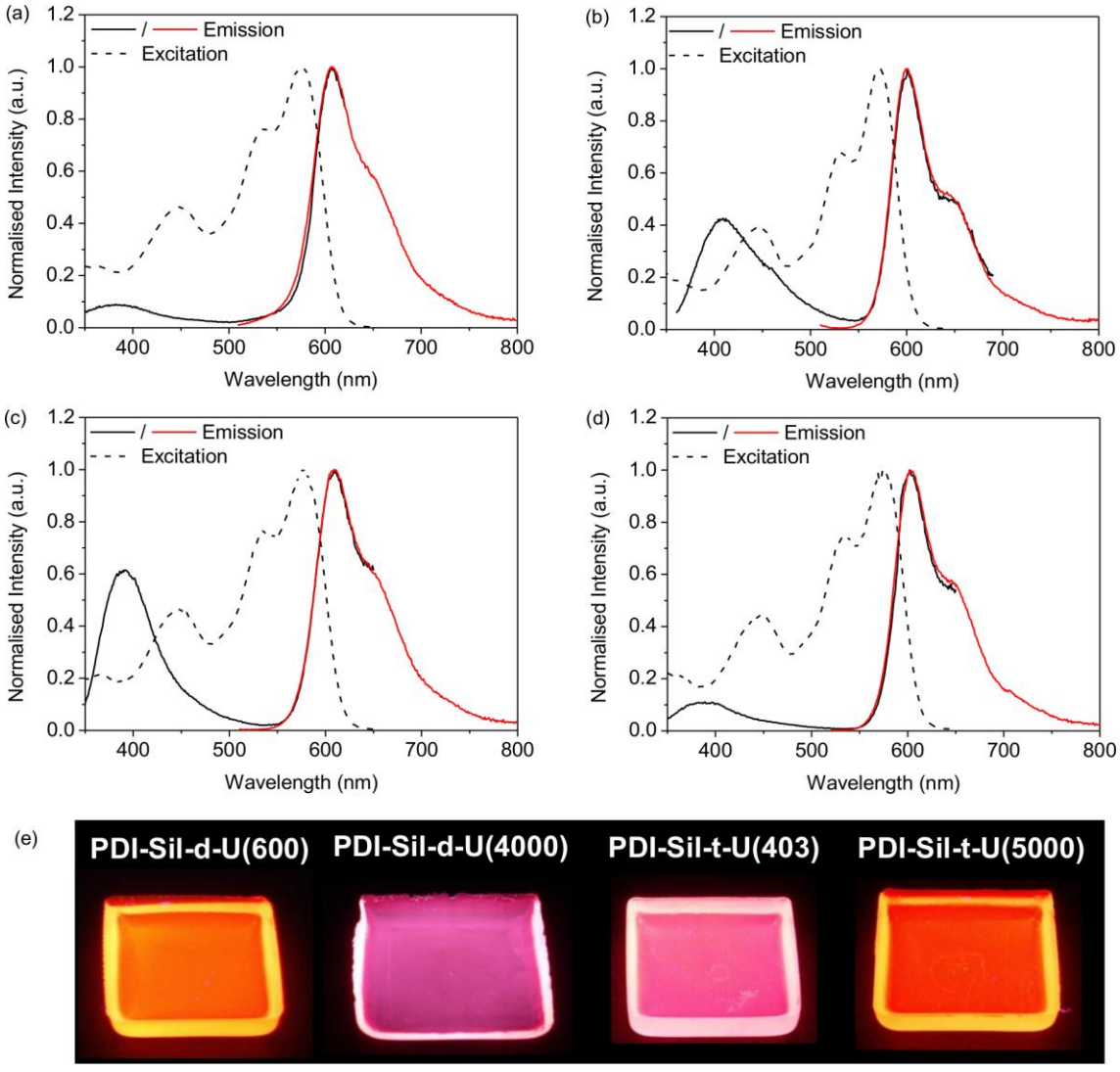

Figure 4.13. Steady-state photoluminescence properties and pictures of **PDI-Sil**-ureasils. PL emission (λ_{ex} = 330 nm, solid black line and λ_{ex}= 500 nm) and excitation spectra (λ_{em} = 670 nm, dashed black line) of (a) **PDI-Sil-d-U(600)**, (b) **PDI-Sil-t-U(403)**, (c) **PDI-Sil-d-U(4000)** and (d) **PDI-Sil-t-U(5000)**. Pictures (e) of the samples under UV irradiation (λ_{ex} = 365 nm).

Interestingly, when considering the relative intensity of the ureasil emission compared to that of the **PDI-Sil**, there are distinct differences between the samples. In particular, while for **PDI-Sil-d-U(4000)** and **PDI-Sil-t-U(403)** (**Fig. 4.13**b and c, respectively) the ureasil emission band is

relatively intense, it shows only a minor contribution in the spectra of **PDI-Sil-d-U(600)** and **PDI-Sil-t-U(5000)** (**Fig. 4.13**a and d, respectively). This trend also is also reflected in the emission colour of the samples upon irradiation under UV light (λ_{ex} = 365 nm) (**Fig. 4.13**e): **PDI-Sil-d-U(4000)** and **PDI-Sil-t-U(403)** are pink, while **PDI-Sil-d-U(600)** and **PDI-Sil-t-U(5000)** are orange. The significant overlap between the emission spectrum of ureasils and the absorption spectrum of the **PDI-Sil** introduces the possibility of energy transfer between the ureasil hybrid donors (*D*) and the perylene acceptor (*A*). The efficiency of this process will depend on the relative distance and orientation of the absorption and emission dipole moments of the species and will be discussed in details in the next section.

One of the main aims of this Chapter, is to determine whether covalent grafting of the lumophore to the backbone of the waveguide host could provide a route to reducing self-absorption and aggregation phenomena, thus decreasing optical losses. These phenomena can have a dramatic effect on the optical properties of a fluorophore and typically manifest themselves with a red-shift in the emission spectra of the optically-active species[47] and/or with a decrease in its Φ_{PL}.[48, 49] Previous work from our group showed that for Lumogen Red LR305,[5] a fluorophore presenting a very similar structure to that of **PDI-Sil**, physical incorporation into the **d-U(600)** hybrid at the same concentration used here (0.005 $\%_{w/w}$) induced a 20 nm red-shift into the emission maximum, accompanied by a decrease in the Φ_{PL}. For a dilute solution of **PDI-Sil** in a good solvent, the emission spectrum presents an absolute maximum centred at 600 nm (**Fig. 4.12**). Covalent grafting of the lumophore in any of the matrices investigated here leads to less significant red-shifts (from 1 to 8 nm), suggesting that this approach allows improved isolation of the lumophore molecules compared to simple physical incorporation. To further corroborate this hypothesis, the Φ_{PL} of **PDI-Sil**-ureasils were measured upon selective excitation of the **PDI-Sil** units (λ_{ex} = 520 nm). The measured and corrected values of Φ_{PL} are shown in **Table 4.3**. For **PDI-Sil**-ureasils the Φ_{PL} ranges between 76 and 87%. Considering that this method is accurate within 10%, we can conclude that, at the investigated concentration, the incorporation of the **PDI-Sil** into the ureasil matrices, does not lead to any significant decrease in the Φ_{PL} compared to that of the pure lumophore in a solution of a good solvent measured in the same conditions (Φ_{PL} = 90 %, in THF).

Both of these experimental observations are strong indicators of reduced aggregation and self-absorption phenomena upon covalent grafting of the lumophore to the ureasil.

Table 4.3. Measured and corrected photoluminescence quantum yields for **PDI-Sil**-ureasils (λ_{ex} = 520 nm).

Sample ID	$\boldsymbol{\Phi}_{\mathbf{PL}}$ (measured)[a]	$\boldsymbol{\Phi}_{\mathbf{PL}}$ (corrected)[b]
PDI-Sil-d-U(600)	76.3 (±1.1)	81.1
PDI-Sil-d-U(4000)	86.7 (±4.4)	88.2
PDI-Sil-t-U(403)	77.7 (±1.2)	83.8
PDI-Sil-t-U(5000)	83.4 (±0.3)	87.0

[a] Average of three independent measurements
[b] Corrected for reabsorption effects.[48]

In view of the application of these systems as LSCs, the photostability of **PDI-Sil-t-U(5000)**, which has been used as representative for the four series, was monitored upon extended exposure to UV light (λ_{ex}= 370 nm) and compared with that of the undoped **t-U(5000)** and a thin film of **PDI-Sil** spin coated from a solution (10 mg cm^{-3}, in THF) onto a cleaned glass slide at a rate of 2000 rpm. The ratios between the integrated emission intensities measured at time *t* and the integrated emission intensities measured at *t* = 0 are shown in **Figure 4.14**. Upon continuous irradiation at 370 nm over a 5 hour period, no significant decrease in the integrated intensity of the **PDI-Sil** emission was observed, for either the monoliths or the thin film sample.

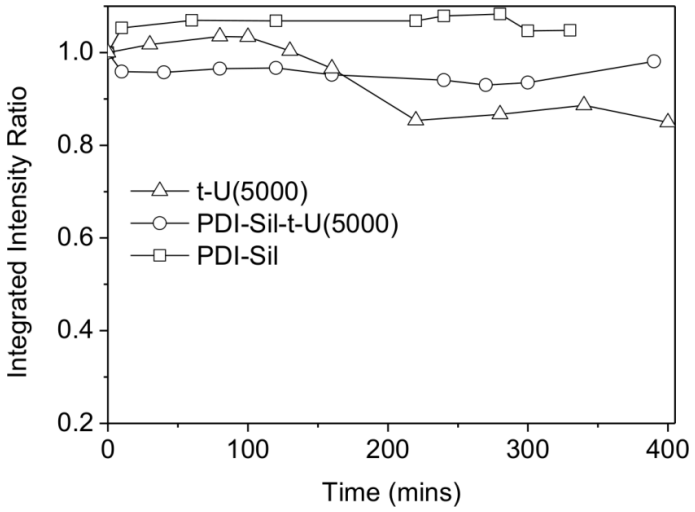

Fig. 4.14. Integrated emission intensity of a **t-U(5000)** (open triangles), **PDI-Sil-t-U(5000)** (open circles) and a **PDI-Sil** thin film (open squares) on a glass substrate irradiated at 370 nm. The solid lines serve only to guide the eye.

4.3.3.2 Possibility of Energy Transfer from the Ureasils to PDI-Sil

As briefly addressed in the previous section, the **PDI-Sil**-ureasils show remarkable differences in their emission spectra upon irradiation under UV light. In particular, the contribution of the emission from the ureasil to the overall spectra is modest for **PDI-Sil-d-U(600)** and **PDI-Sil-t-U(5000)** compared to those of **PDI-Sil-d-U(4000)** and **PDI-Sil-t-U(403)**. As optically-active hosts, ureasils can behave as an efficient energy donor to the their guest species: Willis-Fox *et al.* showed that the chains of CPEs can be dispersed through physical interactions into the matrix of a **d-U(600)** hybrid, creating emissive sites with a high recombination probability with the ureasil behaving as an energy donor for the CPEs and resulting in an overall enhancement of the Φ_{PL} of the system.[23] Kaniyoor *et al.* physically embedded Lumogen Red LR305 into a **d-U(600)** matrix and showed that efficient energy transfer through the Förster Resonance Energy Transfer (FRET) mechanism occurs between the ureasil donor and the Lumogen Red LR305 acceptor.[5] This last example is of particular interest for this study, given the chemical similarities between Lumogen Red LR305 and **PDI-Sil**. Namely, energy transfer from the ureasil donor to the **PDI-Sil** acceptor would justify the weaker emission intensity measured in the ureasil region (380 to 500 nm) for **PDI-Sil-d-U(600)** and **PDI-Sil-t-U(5000)** compared to that of **PDI-Sil-t-U(403)** and **PDI-Sil-d-U(4000)**.

The PL and excitation spectra of undoped ureasils and the PL and absorption spectra of **PDI-Sil** are shown in **Fig. 4.15** to demonstrate the regions of spectral overlap for each component. For these systems, the possible mechanisms responsible for energy transfer involved are either: radiative (or trivial) energy transfer or FRET, which both depend on the spectral overlap between the absorption spectrum of the acceptor and the emission spectrum of the donor

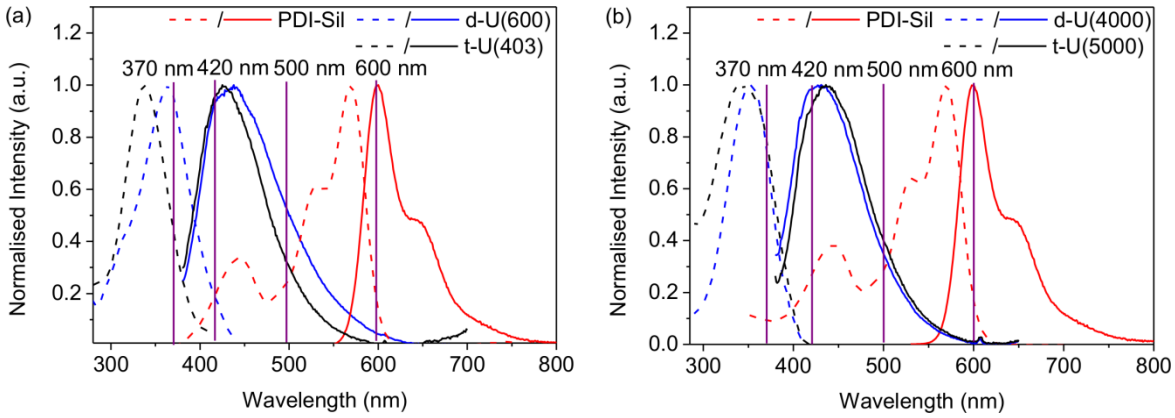

Figure 4.15. Optical properties of the donor and acceptor systems. Emission and excitation spectra for (a) **d-U(600)** (blue, λ_{ex} = 370 nm, λ_{em} = 420 nm), **t-U(403)** (black, λ_{ex} = 370 nm, λ_{em} = 420 nm) and UV/Vis absorption and emission spectra for **PDI-Sil** (red, λ_{ex} = 520 nm in THF) and (b) PL and excitation spectra for **t-U(5000)** (black, λ_{ex} = 370 nm, λ_{em} = 420 nm), **d-U(4000)** (blue, λ_{ex} = 370 nm, λ_{em} = 420 nm) and UV/Vis absorption and emission spectra for **PDI-Sil** (red, λ_{ex} = 520 nm in THF). Emission spectra are shown as solid lines and excitation and UV-Vis absorption spectra are shown as dashed lines. The purple lines highlight the excitation (λ_{ex}) and emission (λ_{ex}) wavelengths used in the TCSPC experiments.

When considering FRET, this can be quantified using the spectral overlap integral (J_{DA}):

$$J_{DA}(\lambda) = \int_0^\infty F_D(\lambda)\varepsilon_A(\lambda)\lambda^4 d\lambda \qquad \textbf{(4.1)}$$

where F_D represents the intensity of the donor (D) emission spectrum in λ–(λ+$\Delta\lambda$) wavelength range, with the total intensity normalised to unity and ε_A is the molar absorption coefficient of the acceptor (A) measured at λ. The calculated values of J_{DA} are shown in **Table 4.4**. Interestingly, the highest values of spectral overlap were calculated for **d-U(600)** and **t-U(5000)**, which matches the trend observed for the emission spectra. The corresponding Förster distance, the distance at which the energy transfer efficiency is 50% efficient, (R_0) was then calculated for **PDI-Sil-d-U(600)** and **PDI-Sil-t-U(5000)**, from:

$$R_0^6 = \frac{9000(ln10)\kappa^2\Phi_D J_{DA}}{128\pi^5 n^4 N_A} \qquad \textbf{(4.2)}$$

where Φ_D is the Φ_{PL} of the donor, n is the refractive index of the host ureasil (~1.5) and N_A is Avogadro's number.[24] The relative orientation of the transition dipole moment of the donor compared to that of the acceptor is taken into account using the κ factor, which in this case was considered equal to 2/3, and corresponds to an isotropic orientation of the donor and acceptor.[50] The calculated R_0 values are reported in **Table 4.4**.

Table 4.4. Summary of the photophysical data obtained for undoped ureasils. Φ_{PL}, J_{DA} and R_0 are the calculated spectral overlap integral and Förster distance for resonance energy transfer respectively, considering the ureasil as the donor (*D*) and **PDI-Sil** as the acceptor (*A*).

Sample ID	$\boldsymbol{J_{DA}}$ (M^{-1} cm^3)	$\boldsymbol{R_0}$ (nm)	$\boldsymbol{\Phi_{PL}}$ (%)[a]
d-U(600)	4.73×10^{-14}	2.43	3.8 ± 0.2
d-U(4000)	4.36×10^{-14}	2.82	9.9 ± 0.3
t-U(403)	4.12×10^{-14}	2.75	9.1 ± 1.7
t-U(5000)	4.72×10^{-14}	2.73	7.5 ± 0.1

[a] Calculated as the average of three independent measurements (λ_{ex} = 350 nm).

Considering the trend observed in the emission spectra, it is surprising that the calculated values for the R_0 are essentially all the same beside the one corresponding to **d-U(600)**. This result is however consistent with the hypothesis that for these system, FRET might not be the only mechanism involved in the energy transfer process, which could proceed also *via* a trivial radiative pathway. However, this could also indicate that assuming an isotropic distribution of the donor and acceptor transition dipoles (κ = 2/3) may not be applicable for our samples. To further investigate the mechanism of energy transfer, time-correlated single photon counting measurements were performed on the samples. Measurements were performed through selective excitation of either the ureasil (λ_{ex} = 370 nm) or the **PDI-Sil** (λ_{ex} = 460 nm) and the corresponding decay curves were collected at λ_{em} = 420 nm, 500 nm and 600 nm to isolate the two emission contributions of the ureasils and the **PDI-Sil** emission, respectively. The decay curves of undoped ureasils can be fitted using a tri-exponential function (**Fig. 4.16**), in good agreement with the literature.[22, 23]

The fitting data for undoped samples are reported **Table 4.5**. The three contributions (τ_i) arise from the combination of the photoinduced proton transfer in the urea moieties and the defects in the siliceous domains characteristic for ureasil-type materials. The corresponding values: $\tau_1 < 1$ ns, $\tau_2 \approx 2.5$–4.3 ns and $\tau_3 \approx 9.2$–12.9 ns are in good agreement with the values previously reported for **d-U(600)** measured in the same conditions (λ_{ex} = 370 nm and λ_{em} = 420 nm).[23, 51] The average value of the lifetime ($<\tau>$) of the samples decreases in the order: **t-U(403)** > **d-U(4000)** > **t-**

U(5000) > **d-U(600)**, which follows the trend of the photoluminescence quantum yields values.

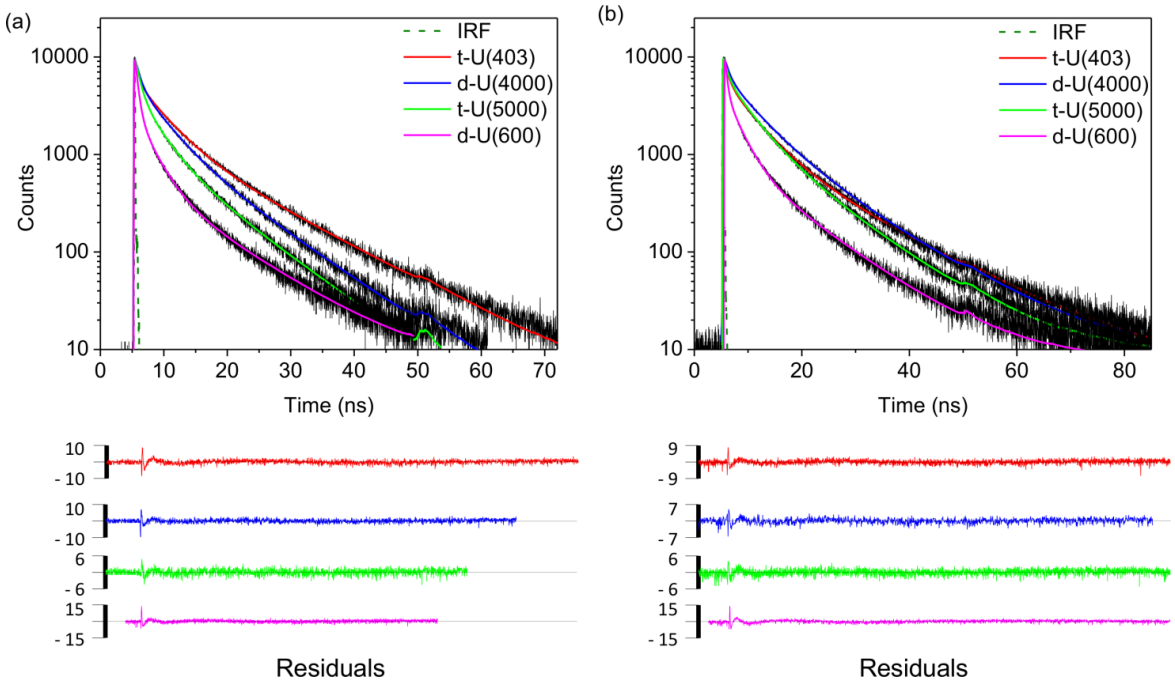

Figure 4.16. Emission decay curves (solid black lines) and fits (coloured lines) for undoped ureasils upon excitation at 370 nm and detection at (a) 420 nm and (b) 500 nm. For each fit the residuals and the instrument response function (IRF, dotted line) are also shown.

Table 4.5. PL lifetimes (τ_i), pre-exponential coefficients (α_i) and chi squared (χ^2) values obtained from fitting of the emission decays (λ_{ex} = 370 nm) of undoped ureasils at λ_{em} = 420 and 500 nm.

Sample ID	τ_1 (ns)	τ_2 (ns)	τ_3 (ns)	α_1	α_2	α_3	<τ> (ns)	χ^2
λ_{em} = 420 nm								
t-U(403)	0.53 ± 0.03	4.28 ± 0.05	12.90 ± 0.09	0.49 ± 0.22	0.40 ± 0.09	0.11 ± 0.05	7.60	1.42
t-U(5000)	0.49 ± 0.03	3.11 ± 0.04	9.22 ± 0.07	0.47 ±0.04	0.39 ± 0.03	0.15 ± 0.03	5.85	1.39
d-U(4000)	0.71 ± 0.03	3.91 ± 0.05	9.84 ± 0.07	0.48 ± 0.04	0.36 ± 0.04	0.16 ±0.04	6.35	1.24
d-U(600)	0.47 ± 0.01	2.56 ± 0.04	10.08 0.12	0.75 ±0.02	0.20 ± 0.01	0.05 ± 0.01	4.61	1.55
λ_{em} = 500 nm								
t-U(403)	1.00 ± 0.05	5.53 ± 0.06	15.68 ± 0.15	0.46 ± 0.06	0.43 ± 0.06	0.11 ± 0.05	8.97	1.28
t-U(5000)	0.71 ± 0.04	4.45 ± 0.05	11.17 ± 0.08	0.39 ± 0.05	0.43 ± 0.05	0.17 ± 0.04	7.35	1.15
d-U(4000)	0.85 ± 0.06	5.39 ± 0.06	12.72 ±0.10	0.39 ± 0.06	0.43 ± 0.06	0.18 ± 0.05	8.53	1.24
d-U(600)	0.39 ± 0.02	2.79 ± 0.05	10.90 ± 0.14	0.63 ± 0.03	0.29 ± 0.02	0.07 ± 0.02	5.91	1.66

The very same trend was also monitored for <τ> measured at λ_{em} = 500 nm. In this case, the average lifetime is also longer, which is due to the decrease in the pre-exponential factor (α_1), accompanied by an increase in both α_2, τ_2 and τ_3.This behaviour can be justified by analysis of the two components responsible for the ureasil emission. Previous time-resolved emission studies

performed at 14 K have shown that the decay term associated to the siliceous domains is generally shorter (1-5 ms) than the one assigned to the NH centres (> 10 ms).[41] Since the emission associated to the silica defects is prominent at 420 nm, it is plausible to assign this contribution to τ_1, while the emission related to the urea centres is dominant at 500 nm and can therefore be associated to τ_3. Previous work from our group, showed that for a **d-U(600)** hybrid, energy transfer can occur between the higher energy siliceous domains and the urea domains with the τ_2 term associated to the relaxation of this emissive centres followed by the population stimulated by the energy transfer.[23] In this study, a simultaneous increase in α_2 and decrease in α_1 suggested that interconversion between the two species could occur. The decay curve for the **PDI-Sil** dye in solution was obtained at λ_{ex} = 370 nm and λ_{em}= 600 nm and is shown in **Fig. 4.17** together with the corresponding fit. Despite the low absorption of the **PDI-Sil** at this λ_{ex}, it is interesting to monitor its decay behaviour under these conditions to compare it to the results obtained for the **PDI-Sil**-ureasils and further investigate the energy transfer. The decay curve for **PDI-Sil** in THF, can be fitted with a single term, τ_1 = 6.52 ns. For **PDI-Sil**-ureasils, the corresponding decay curves obtained upon the same measurement conditions can be solved with a mono-exponential term, $\tau_1 \approx$ 6.8-7.0 ns, which reflects the results obtained for **PDI-Sil** in solution. This indicates that upon hydrolysis of its ethoxysilane moieties, **PDI-Sil** co-condensed to the ureasil network without the formation of dimers or stacked aggregates, which would normally result in multi-exponential decay curves.[32]

Moreover, since re-absorption and aggregation phenomena are associated with changes in the lifetime,[52] this result further supports the conclusions from the steady-state analysis, namely covalent-grafting helps to isolate the fluorophore molecules within the host matrix. It is interesting to note that the local arrangement of the **PDI-Sil** units within the matrices of the ureasils is influenced by the host structure and in particular the use of different branching and/or different branch lengths may influence the *D-A* distance and the relative orientation/overlap of their transition dipole moments, affecting the overall efficiency of the energy transfer.

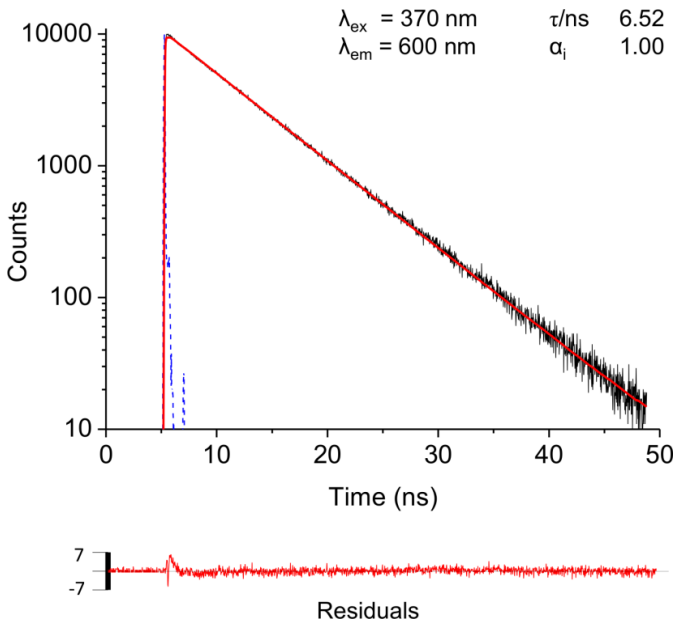

Figure 4.17. Photoluminescence decay (black line) for **PDI-Sil** in THF. The resulting decay time (τ), fit (red line), residuals and instrument response (IRF, blue dotted line) are also shown.

The results of the fittings obtained by excitation of **PDI-Sil**-ureasils at 370 nm and detection at 420 nm and 500 nm are shown in **Table 4.6**. Upon detection of the emission in the ureasil region, the decay curves can again be resolved into three components; for λ_{em}= 420 nm: τ_1 < 1 ns, $\tau_2 \approx$ 2.0–4.5 ns and $\tau_3 \approx$ 8.0-13.8 ns, while for λ_{em}= 500 nm: $\tau_1 \leq$ 1 ns, $\tau_2 \approx$ 3.3–5.0 ns and $\tau_3 \approx$ 10.3-15.1 ns. Although these lifetimes are slightly longer-lived than those obtained for the un-doped ureasils, they show the same trend of α_i and τ_i. This result is somewhat unexpected; if energy transfer occurs solely *via* the FRET mechanism from the ureasil host to the **PDI-Sil**, a decrease in at least one of these components should occur. In particular, as the absorption spectrum of **PDI-Sil** overlaps well with the urea-centred emission (2.80-3.19 eV), a change in either the α_3 and τ_3 terms would have been expected. Since this is clearly not the case, other energy transfer mechanisms must be involved, in particular radiative energy transfer. While FRET can occur only for *D-A* couples separated by a short-range distance (typically 1-10 nm) with the dipole-dipole coupling being a function of R^{-6}, the efficiency of trivial energy transfer has a less strict dependency on the distance (R^{-2}) and can operate over longer distances. The lifetime results obtained for the **PDI-Si**-ureasils, would suggest that the radiative process is the one dominating the overall energy transfer and possibly masking any short-range dipole-dipole interactions.

Table 4.6. PL lifetimes (τ_i), pre-exponential coefficients (α_i) and chi squared (χ^2) values obtained from fitting of the emission decays (λ_{ex} = 370 nm) of **PDI-Sil**-ureasils at λ_{em} = 420 and 500 nm.

Sample ID	τ_1 **(ns)**	τ_2 **(ns)**	τ_3 **(ns)**	α_1	α_2	α_3	χ^2
λ_{em} **= 420 nm**							
PDI-Sil-t-U(403)	0.56 ± 0.03	4.53 ± 0.06	13.79 ± 0.09	0.46 ± 0.05	0.39 ± 0.05	0.15 ± 0.04	1.40
PDI-Sil-t-U(5000)	0.73 ± 0.02	3.19 ± 0.04	9.18 ± 0.07	0.58 ± 0.04	0.31 ± 0.03	0.11 ± 0.03	1.15
PDI-Sil-d-U(4000)	0.58 ± 0.03	3.79 ± 0.04	9.78 ± 0.07	0.46 ± 0.04	0.38 ± 0.04	0.16 ± 0.03	1.17
PDI-Sil-d-(600)	0.42 ± 0.01	2.03 ± 0.04	8.06 ± 0.11	0.71 ± 0.03	0.24 ± 0.01	0.05 ± 0.01	1.55
λ_{em} **= 500 nm**							
PDI-Sil-t-U(403)	1.03 ± 0.04	5.02 ± 0.05	15.06 ± 0.10	0.48 ± 0.06	0.40 ± 0.05	0.12 ± 0.05	1.17
PDI-Sil-t-U(5000)	0.86 ± 0.03	4.60 ± 0.05	11.66 ± 0.09	0.49 ± 0.05	0.38 ± 0.05	0.13 ± 0.04	1.10
PDI-Sil-d-U(4000)	0.78 ± 0.05	4.98 ± 0.05	12.47 ± 0.07	0.36 ± 0.06	0.44 ± 0.06	0.21 ± 0.05	1.13
PDI-Sil-d-(600)	0.62 ± 0.02	3.31 ± 0.04	10.28 ± 0.09	0.53 ± 0.04	0.38 ± 0.03	0.09 ± 0.03	1.24

The two phenomena however, are not completely unrelated. A theory elaborated by Andrew *et al.*,[53] based on quantum electrodynamics, states that the Förster mechanism is effectively a short-range limit of a unified dipole-dipole interaction. At longer distances, the distance dependency is modified from R^{-6} to R^{-2} leading to an energy transfer model that can be classified as radiative. For our system, the difference observed for the energy transfer in different **PDI-Sil**-ureasils can therefore be assessed to a combination of the different *D-A* distances between and/or the poor coupling between the corresponding transition dipoles. The difference between the *D-A* distances is a function of the M_w and the branching of each Jeffamine precursor; for the investigated ureasils, **d-U(4000)** possess a substantial difference in the amount of r.u. per chain (~68 r.u.) compared to the other samples, with **t-U(403)** (~2 r.u.) with the shortest branch length and **d-U(600)** (~13 r.u.) and **t-U(5000)** (~28 r.u.) presenting more similar values. This could indicate that is the branch length of ureasil rather than the number of branches which exercises a higher level of control over the placement of the **PDI-Sil** dye within the ureasil network.

To elucidate the role of the relative orientation of the transition dipole moment of *D-A* on the energy transfer mechanism, preliminary fluorescence anisotropy measurements were performed on **PDI-Sil-dU(600)** and **PDI-Sil-d-U(4000)**, which exhibit opposite PL behaviours. A brief

description of the theory behind this technique can be found in **Section 2.2.8**, while the calculated values of the G factor measured for **PDI-Sil** in a THF solution are reported in **Fig. A.4.4**.

The results from the anisotropy measurements performed are presented in **Figure 4.18**. For both ureasils, the anisotropy, <*r*>, remains constant upon selective excitation and detection of the **PDI-Sil** fluorophore (<*r*> ~ 0.2) (**Fig. 4.18**a). The same trend is observed for the corresponding excitation spectra, where the <*r*> value fluctuates around 0.3 between 500 to 620 nm (which corresponds to the $S_0 \rightarrow S_1$ absorption band) (**Fig. 4.18**b). However, significant differences between the samples can be observed in the region corresponding to the ureasil excitation spectrum (380-460 nm); namely, both samples present a general decrease of the <*r*> value which reaches a minimum of ~0.1 for **PDI-Sil-d-U(4000)** and ~-0.1 **PDI-Sil-d-U(600)**. Unfortunately, due to the nature of the thick ureasil monoliths, scattering, re-absorption and waveguiding phenomena strongly affect the measurements, so that these values should not be interpreted as absolute. Nevertheless, this decrease in the <*r*> values in this region, particularly for **PDI-Sil-d-U(600)**, provides a preliminary indication that the *D-A* orientation, guided by the branch length of the ureasil, plays an important role in determining the efficiency of the energy transfer process.

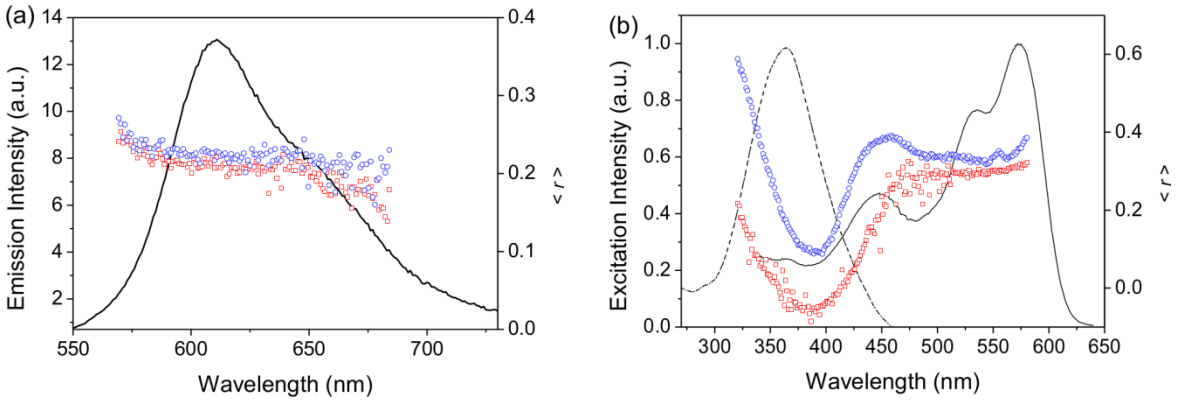

Figure 4.18. Steady-state anisotropy of the PL (a) emission (λ_{ex} = 500 nm) and (b) excitation (λ_{em} = 630 nm) of **PDI-Sil-d-U(600)** (red open squares) and **PDI-Sil-d-U(4000)** (blue open circles). The emission and excitation spectra (black lines) obtained using non-polarised light are shown for comparison.

4.4 Conclusions

In summary, a perylene dicarboxdiimide dye was grafted to the silica domains within the matrices of four different ureasil organic-inorganic ureasil hybrids. Compared to similar systems prepared only by physical encapsulation of the fluorophore into the ureasil hosts, covalent bonding of the dye to the ureasil network leads to isolation of the fluorophore units and improved dispersion of the emissive species in the matrix. By means of steady-state and time-resolved fluorescence spectroscopy, it was shown that for the investigated concentration, no relevant changes in either the emission spectra, the Φ_{PL} or the decay kinetics of the **PDI-Sil** is observed upon covalent-grafting to any of the investigated ureasil backbones, indicating that this approach significantly reduces several non-radiative deactivation pathways, including re-absorption/re-emission and formation of stacked aggregates and dimers. Investigation of the network arrangement was performed by means of MAS-NMR, PXRD and FTIR in the Amide I region, and showed that for the studied concentration, the structure of the ureasil network is not significantly influenced by grafting of the fluorophore. Interestingly, it was demonstrated that the structure of the Jeffamine precursor used for the preparation of the ureasils plays a key role in regulating the efficiency of energy transfer between the ureasil host donor and the **PDI-Sil** acceptor. Namely, this phenomenon seems to be guided by the branch length of the ureasil and potentially by the relative orientation of the transition dipole of the donor and the acceptor. Although anisotropy measurements were strongly affected by scattering effects due to the nature of the ureasil samples, subtle differences were observed when comparing the anisotropy excitation results of a sample undergoing energy transfer compared to the one that does not. These findings, combined with the good photo- and thermal stability of the **PDI-Sil**-ureasils, proved that this approach could be a valuable route towards the preparation of ureasil-based LSCs with targeted optical properties. In particular, ureasils have already shown good potential for the application as optically active waveguide for LSCs.[5, 25] However to exploit the full potential of this class of materials, direct integration of the lumophore into the waveguide, represents a step forward for the creation of LSCs with lumophores adopting preferential spatial orientation to minimise unwanted optical loss mechanisms.

4.5 References

1. H. Nakanotani, T. Higuchi, T. Furukawa, K. Masui, K. Morimoto, M. Numata, H. Tanaka, Y. Sagara, T. Yasuda and C. Adachi, *Nat. Commun.*, 2014, **5**, 4016.
2. K. S. Yook and J. Y. Lee, *Adv. Mater.*, 2014, **26**, 4218-4233.
3. A. Mishra and P. Bäuerle, *Angew. Chem. Int. Ed.*, 2012, **51**, 2020-2067.
4. J. Roncali, *Acc. Chem. Res.*, 2009, **42**, 1719-1730.
5. A. Kaniyoor, B. McKenna, S. Comby and R. C. Evans, *Adv. Opt. Mater.*, 2016, **4**, 444-456.
6. A. Sanguineti, M. Sassi, R. Turrisi, R. Ruffo, G. Vaccaro, F. Meinardi and L. Beverina, *Chem. Commun.*, 2013, **49**, 1618-1620.
7. R. C. Evans, *J. Mater. Chem. C*, 2013, **1**, 4190-4200.
8. Z. B. Henson, K. Müllen and G. C. Bazan, *Nat. Chem.*, 2012, **4**, 699-704.
9. P. P. C. Verbunt, A. Kaiser, K. Hermans, C. W. M. Bastiaansen, D. J. Broer and M. G. Debije, *Adv. Funct. Mater.*, 2009, **19**, 2714-2719.
10. J. t. Schiphorst, A. M. Kendhale, M. G. Debije, C. Menelaou, L. M. Herz and A. P. H. J. Schenning, *Chem. Mater.*, 2014, **26**, 3876-3878.
11. E. Aharon, A. Albo, M. Kalina and G. L. Frey, *Adv. Funct. Mater.*, 2006, **16**, 980-986.
12. K. V. Rao, A. Jain and S. J. George, *J. Mater. Chem. C*, 2014, **2**, 3055-3064.
13. R. C. Evans, A. G. Macedo, S. Pradhan, U. Scherf, L. D. Carlos and H. D. Burrows, *Adv. Mater.*, 2010, **22**, 3032-3037.
14. S. Clément, A. Tizit, S. Desbief, A. Mehdi, J. De Winter, P. Gerbaux, R. Lazzaroni and B. Boury, *J. Mater. Chem.*, 2011, **21**, 2733-2739.
15. R. C. Evans and P. C. Marr, *Chem. Commun.*, 2012, **48**, 3742-3744.
16. J. M. Behrendt, A. B. Foster, M. C. McCairn, H. Willcock, R. K. O'Reilly and M. L. Turner, *J. Mater. Chem. C*, 2013, **1**, 3297-3304.
17. D. Chandra, S. K. Das and A. Bhaumik, *Microp. Mesop. Mat.*, 2010, **128**, 34-40.
18. D. Chandra, T. Yokoi, T. Tatsumi and A. Bhaumik, *Chem. Mater.*, 2007, **19**, 5347-5354.
19. M. Kubo, C. Takimoto, Y. Minami, T. Uno, T. Itoh and M. Shoyama, *Macromolecules*, 2005, **38**, 7314-7320.
20. M. Schneider and K. Müllen, *Chem. Mater.*, 2000, **12**, 352-362.
21. I. Meazzini, J. M. Behrendt, M. L. Turner and R. C. Evans, *Macromolecules*, 2017, **50**, 4235-4243.
22. N. Willis-Fox, M. Kraft, J. Arlt, U. Scherf and R. C. Evans, *Adv. Funct. Mater.*, 2016, **26**, 532-542.
23. N. Willis-Fox, A.-T. Marques, J. Arlt, U. Scherf, L. D. Carlos, H. D. Burrows and R. C. Evans, *Chem. Sci.*, 2015, **6**, 7227-7237.
24. D. C. Oliveira, A. G. Macedo, N. J. O. Silva, C. Molina, R. A. S. Ferreira, P. S. André, K. Dahmouche, V. de Zea Bermudez, Y. Messaddeq, S. J. L. Ribeiro and L. D. Carlos, *Chem. Mater.*, 2008, **20**, 3696-3705.
25. M. M. Nolasco, P. M. Vaz, V. T. Freitas, P. P. Lima, P. S. Andre, R. A. S. Ferreira, P. D. Vaz, P. Ribeiro-Claro and L. D. Carlos, *J. Mater. Chem. A*, 2013, **1**, 7339-7350.
26. G. D. Gutierrez, I. Coropceanu, M. G. Bawendi and T. M. Swager, *Adv. Mater.*, 2016, **28**, 497-501.
27. J. L. Banal, K. P. Ghiggino and W. W. H. Wong, *Phys. Chem. Chem. Phys.*, 2014, **16**, 25358-25363.
28. T. Zhang, Z. Ren, X. Sun and S. Yan, *Phys. Chem. Chem. Phys.*, 2015, **17**, 23069-23073.
29. D. Dotcheva, M. Klapper and K. Müllen, *Macromol. Chem. Phys.*, 1994, **195**, 1905-1911.
30. J. D. Wright and N. A. J. M. Sommerdijk, *Sol-Gel Materials: Chemistry and Applications*, 2000.
31. B. Fouzia, J. Ferguson, K. McKenna, L. E. McNamara, N. I. Hammer and H. Rathnayake, *New J. Chem.*, 2015, **39**, 2004-2010.
32. F. Ito, H. Sato, Y. Ugachi, N. Oka, S. Ito and H. Miyasaka, *Photochem. Photobiol. Sci.*, 2015, **14**, 1896-1902.
33. V. T. Freitas, P. P. Lima, V. de Zea Bermudez, R. A. S. Ferreira and L. D. Carlos, *Eur. J. Inorg. Chem.*, 2012, **2012**, 5390-5395.
34. V. de Zea Bermudez, L. D. Carlos and L. Alcácer, *Chem. Mater.*, 1999, **11**, 569-580.

35. M. C. Gonçalves, V. de Zea Bermudez, R. A. S. Ferreira, L. D. Carlos, D. Ostrovskii and J. Rocha, *Chem. Mater.*, 2004, **16**, 2530-2543.
36. E. F. Molina, L. Marçal, H. W. Pereira de Carvalho, E. J. Nassar and K. J. Ciuffi, *Polym. Chem.*, 2013, **4**, 1575-1582.
37. P. P. Lima, R. A. S. Ferreira, S. A. Júnior, O. L. Malta and L. D. Carlos, *J. Photochem. Photobiol. A: Chem.*, 2009, **201**, 214-221.
38. L. Fu, R. A. Sá Ferreira, N. J. O. Silva, L. D. Carlos, V. de Zea Bermudez and J. Rocha, *Chem. Mater.*, 2004, **16**, 1507-1516.
39. V. T. Freitas, P. P. Lima, R. A. S. Ferreira, E. Pecoraro, M. Fernandes, V. de Zea Bermudez and L. D. Carlos, *J. Sol-Gel Sci. Technol.*, 2013, **65**, 83-92.
40. N. Grossiord, J. M. Kroon, R. Andriessen and P. W. M. Blom, *Org. Electron.*, 2012, **13**, 432-456.
41. L. D. Carlos, V. de Zea Bermudez, R. A. S. Ferreira, L. Marques and M. Assunção, *Chem. Mater.*, 1999, **11**, 581-588.
42. R. A. S. Ferreira, A. L. Ferreira and L. D. Carlos, *J. Non-Cryst. Solids*, 2006, **352**, 1225-1229.
43. L. D. Carlos, R. A. S. Ferreira, R. N. Pereira, M. Assunção and V. de Zea Bermudez, *J. Phys. Chem. B*, 2004, **108**, 14924-14932.
44. L. B. Å. Johansson and H. Langhals, *Spectrochim. Acta A Molecul. Spectrosc.*, 1991, **47**, 857-861.
45. L. Zou, A. You, J. Song, X. Li, M. Bouvet, W. Sui and Y. Chen, *Colloids Surf. A Physicochem. Eng. As.*, 2015, **465**, 39-46.
46. S. K. Lee, Y. Zu, A. Herrmann, Y. Geerts, K. Müllen and A. J. Bard, *J. Am. Chem. Soc.*, 1999, **121**, 3513-3520.
47. S. W. Leow, C. Corrado, M. Osborn, M. Isaacson, G. Alers and S. A. Carter, *J. Appl. Phys.*, 2013, **113**, 214510.
48. T.-S. Ahn, R. O. Al-Kaysi, A. M. Müller, K. M. Wentz and C. J. Bardeen, *Rev. Sci. Instrum.*, 2007, **78**, 086105.
49. D. Yan, J. Lu, M. Wei, D. G. Evans and X. Duan, *J. Phys. Chem. B*, 2009, **113**, 1381-1388.
50. H. Y. Byun, I. J. Chung, H.-K. Shim and C. Y. Kim, *Macromolecules*, 2004, **37**, 6945-6953.
51. L. Fu, R. A. S. Ferreira, M. Fernandes, S. C. Nunes, V. de Zea Bermudez, G. Hungerford, J. Rocha and L. D. Carlos, *Opt. Mater.*, 2008, **30**, 1058-1064.
52. R. O. Al-Kaysi, T. Sang Ahn, A. M. Muller and C. J. Bardeen, *Phys. Chem. Chem. Phys.*, 2006, **8**, 3453-3459.
53. D. L. Andrews, *Chem. Phys.*, 1989, **135**, 195-201.

Chapter Five

Ureasil Organic-Inorganic Hybrids as Photoactive Waveguides for Conjugated Polyelectrolyte Luminescent Solar Concentrators

The work in this Chapter has been published in:
I. Meazzini, C. Blayo, J. Arlt, A. Marques, U. Scherf, H. Burrows and R. C. Evans, Ureasil Organic-Inorganic Hybrids as Photoactive Waveguides for Conjugated Polyelectrolyte Luminescent Solar Concentrators, *Mater. Chem. Front.*, 2017, **1**, 2271-2282.

5.1 Introduction

The results obtained in **Chapter 3** and **4** showed how ureasils are capable of efficiently dispersing organic fluorophores such as CPs[1] (*i.e.* **PFO-OH**) or dyes[2] (*i.e.* **PDI-Sil**), yielding doped architectures with high values of Φ_{PL}, while using relatively low percentages of dopants ($\leq$ $0.1\%_{w/w}$ for **PFO-OH** and $0.005\%_{w/w}$ for **PDI-Sil**, respectively). Moreover, ureasils showed great potential as donors for efficient energy transfer to the **PDI-Sil** acceptor, with the efficiency of this process being regulated by the structure of the ureasil.[2] These findings represent a promising step forward for the application of fluorophore-integrated ureasils as LSCs. However, an important aspect to take into account while designing these devices is the capability of their constituents to harvest as many wavelengths of the solar spectrum as possible. For solar cells, a possible solution to increase the window for spectral absorption consists of using spectral converters.[3] These systems can be attached to the surface of the solar cell, where absorption of solar photons and exploitation of a photoluminescence process (*e.g.* downshifting,[4] singlet fission,[5, 6] upconversion[7]) leads to the conversion of the former to wavelengths that can be used more efficiently by the device.

LSCs themselves behave as spectral converters.[3] For example, in an effort to harvest the UV portion of the solar spectrum, Katsagouonos *et al*.[8] prepared a thin film LSC consisting of Eu (III) coordinated with charged β-diketonate ligand molecules as a lumophore, spin-coated onto the surface of a borosilicate glass slide. The final device absorbed light in the region ranging from 310 to 380 nm and re-emitted it efficiently between 580 and 630 nm. The combination of three LSCs glass layers made with the champion sample, led to a 28 % increase in the efficiency of the coupled solar cell. Another interesting approach considered to increase the light-harvesting capability in LSCs is to increase the dye loading either deposited on top of or embedded within the waveguide.[9] In this context, recent interest has been focused on the use of aggregation induced emitters (AIEgens),[10] a class of fluorophores whose emission is switched-on only upon aggregation. In a recent example,[11] Wong *et al.* exploited the formation of H-type aggregates based on *gem*-pyrene ethenes displaying an excimer-like emission as lumophores and exhibiting a large Stokes' shift of 1 eV. An LSC was prepared by drop-casting a solution containing a mixture of poly(methyl methacrylate) and the lumophore onto a glass substrate. Silicon PV cells were then attached around the edges of the LSC to yield a power conversion efficiency of 0.32%.

In both cases, using a non-emissive waveguide is somehow a missed-opportunity considering the potential of photoactive waveguides like ureasils. A possible strategy to increase the spectral absorption window using the systems investigated so far in this thesis (*i.e.* organic fluorophores encapsulated into ureasil matrices) could involve the use of a "cocktails" of lumophores[12-14] which can undergo energy transfer processes between the absorbing and emissive species, providing that they are electronically coupled through space and within the Förster radius in case of FRET.[15] This creates an artificial Stokes' shift which can reduce re-absorption losses. However, adding a mixture of π-conjugated fluorophores inside a host matrix could result in either non-homogeneous mixing of the different emissive species and/or aggregation, leading to the formation of isolated pockets of the same fluorophore. Covalently combining the donor and the acceptor moieties in the same molecule could be a possible solution to overcome this issue, at the expense, however, of increased synthetic demand.[16] In this context, using a photoactive waveguide that could participate as donor, as well as waveguiding the emitted photons, could provide an alternative pathway for increased solar harvesting through energy transfer. A promising lumophore candidate to exploit the advantages of energy transfer mechanisms within the LSC is represented by **PBS-PFP-PDI** (**Fig. 5.1**), a poly{1,4-phenylene-[9,9-bis(4-phenoxy-butylsulfonate)]fluorene-2,7-diyl}-based copolymer (**PBS-PFP**), functionalised with on-chain perylenediimide (PDI) moieties. Recent study from our group[17] showed that incorporating **PBS-PFP** chains into a di-ureasil host results in a dramatic increase in the photoluminescence quantum yield in the solid-state due to a synergistic electronic interaction between the photoactive host and the conjugated polyelectrolyte. While **PBS-PFP-PDI** may also exhibit this effect, it could also simultaneously offer the possibility for both on-chain intramolecular energy transfer between the **PBS-PFP** donor and the PDI acceptor[18] and interspecies energy transfer between the ureasil donor and the **PBS-PFP** and/or PDI acceptor chromophores, all of which have the potential to reduce undesirable re-absorption effects and extend the light-harvesting window of the final LSC.

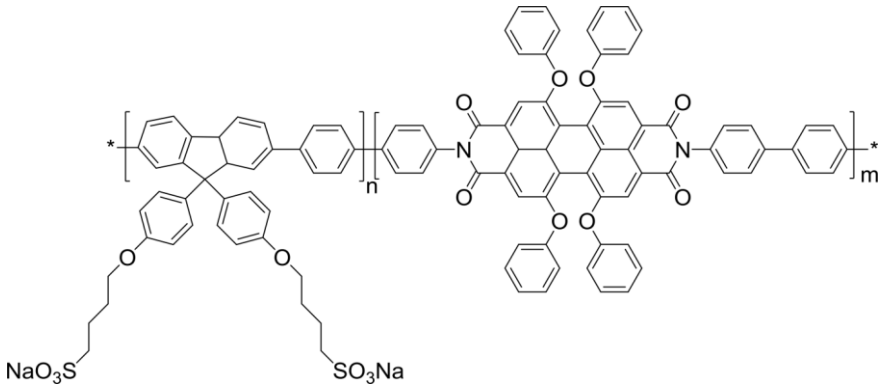

Figure 5.1. Chemical structure of **PBS-PFP-PDI**.

5.1.1 Aims

In this Chapter, LSC devices based on a **PBS-PFP-PDI** lumophore physically encapsulated into the matrices of a di-ureasil and a tri-ureasil hybrid are synthesised and tested. The overall optical properties of the materials were investigated by means of steady-state and time-resolved photoluminescence spectroscopy, with particular focus onto the possibility of energy transfer between the ureasil donor to the **PBS-PFP** acceptor and the **PBS-PFP** donor to the PDI acceptor. To probe the influence of the ureasil host on the localisation of the CPE chains, and therefore the optoelectronic properties of the system, the ureasils were prepared using both a linear and a tripodal conformation of the Jeffamine precursor, and the local arrangement of their corresponding networks was studied by means of NMR and FTIR spectroscopy and X-ray diffractometry. The optical conversion efficiencies of the resulting systems was evaluated in an effort to understand the interplay between the choice of materials and their design in order to optimise the LSC performance.

5.2 Experimental

5.2.1 Materials

PBS-PFP and **PBS-PFP-PDI** were synthesised as previously described and the associated characterisation data for this batch of the polymer can be found in the literature.[18, 19] The M_w determined by gel permeation chromatography (GPC) (NMP/LiBr, UV detection 360 nm) was 2,100 g mol^{-1} (M_w/M_n = 1.61). However, we note that GPC typically underestimates the M_w of conjugated polyelectrolytes due to polar interactions between the ionic side-chains with the column

material (as can be seen by the cutoff of the dialysis membrane at 3,500 g mol^{-1}).[19, 20] Based on the monomer/PDI ratio in the starting reaction mixture, the copolymer is expected to contain on average 5% PDI units. However, single molecule wide-field imaging studies indicate that the average incorporation of the PDI chromophore is lower (1-2%).[18] Lumogen Red F 305 was a kind gift from BASF, Germany. *O*,*O*′-Bis(2-aminopropyl) polypropylene glycol-*block*-polyethylene glycol-*block*-polypropylene glycol (Jeffamine ED-600), KBr (FT-IR grade, ≥99%), 3-(triethoxysilyl)propylisocyanate (ICPTES, 95%), THF (HPLC grade), EtOH (HPLC grade), 1,4-dioxane (HPLC grade) and HCl (37% puriss.) were all purchased from Sigma. Jeffamine T-403 was a kind gift from Huntsman International (www.huntsman.com). All chemicals were used as received.

5.2.2 Synthesis of the Ureasil Hybrids

The ureasil hybrids were prepared following the procedure reported in **Chapters 3** and **4**. Due to the limited amount of CPE available, for these sets of samples each monolith was prepared using half of the usual amount of d-or t-UPTES precursor. Briefly, either Jeffamine ED-600 or Jeffamine T-403 (4.4 mmol) were dissolved in THF (12.5 mL) and ICPTES was added in 1:2 or 1:3 molar ratio, respectively (**Fig. 5.2**). The mixture was reacted for 24 hours under reflux at 70 °C, before being cooled down to RT. For each monolith, the reagents to initiate the sol-gel process were added to either d- or t-UPTES intermediates (0.88 mmol) in the following molar ratios: ICPTES: EtOH: HCl: H_2O = 176: 350: 1: 265. The sol was then stirred for 2 minutes, poured into a polypropylene mould and covered with Parafilm M®. The drying/aging process was carried out for 2 days at RT and further 3 days in the oven at 40 °C and the ureasil hybrids were obtained as transparent, free-standing monoliths. The **PBS-PFP-PDI**-doped ureasils were prepared by addition of a stock solution of the CPE in water and 1,4-dioxane (1 mg mL^{-1}, 1:1 v/v) to each sol mixture before addition of the gelation reagents. The larger monoliths were prepared following a similar procedure, the gelation reagents and the CPE stock were added to either the d- or t-UPTES precursors (7.04 mmol) using the same molar ratios as those adopted for the smaller monoliths. As a consequence of working with higher amounts of reactants, the drying and ageing processes for these samples were performed over longer periods of time, namely, 5 days at RT followed by 3

more days in the oven at 30 °C. The conditions were purposely kept milder than those used for smaller monoliths to avoid the potential cracking of the hybrid due to strain within the silica network.[21] The di-ureasil sample containing Lumogen Red F 305 (**DU-LR305**) was prepared by addition of 616.5 μL of a stock solution of Lumogen Red F 305 (0.2 mg mL^{-1} in THF) to the d-UPTES (7.04 mmol). The sample containing both Lumogen Red F 305 and **PBS-PFP** (**DU-PBS-LR305**) was prepared by adding 616.5 μL of a stock solution of Lumogen Red F 305 (0.2 mg mL^{-1} in THF) and **PBS-PFP** (616.5 μL of a 1 mg mL^{-1}, water/1,4-dioxane (1:1 v/v)) to the d-UPTES (7.04 mmol). For both samples, the gelation reaction and the ageing process were carried out using the same quantities and procedures reported above. The samples are designated as **DU-CPE-*x*** and **TU-CPE-*x***, for di-and tri-ureasils, respectively, where *x* represents 1000 times the final concentration (in wt. %) of **PBS-PFP-PDI** incorporated (*i.e.* **DU-CPE-02** contains 0.002%$_{w/w}$ of CPE).

5.3 Results and Discussion

5.3.1 Preparation of PBS-PFP-PDI-doped ureasil LSCs

In contrast to the procedures presented so far for the synthesis of ureasil hybrids, **PBS-PFP-PDI-**doped ureasils were prepared by physical dispersion of the dopant into the organic-inorganic matrices. Therefore, the synthetic procedure consists of only two steps (**Fig. 5.2**): Step 1, is the preparation of the d- and t-UPTES precursors and Step 2, is the addition of the **CPE** (for the doped-ureasil samples) and the initiator for the gelation reaction. For both the **DU-CPE-*x*** and the **TU-CPE-*x*** sample series, four concentrations of the **CPE** were analysed (0.001, 0.002, 0.004 and 0.008 %w/w), to gather a deeper understanding of the electronic interactions between the dopant and the photoactive ureasil matrices.

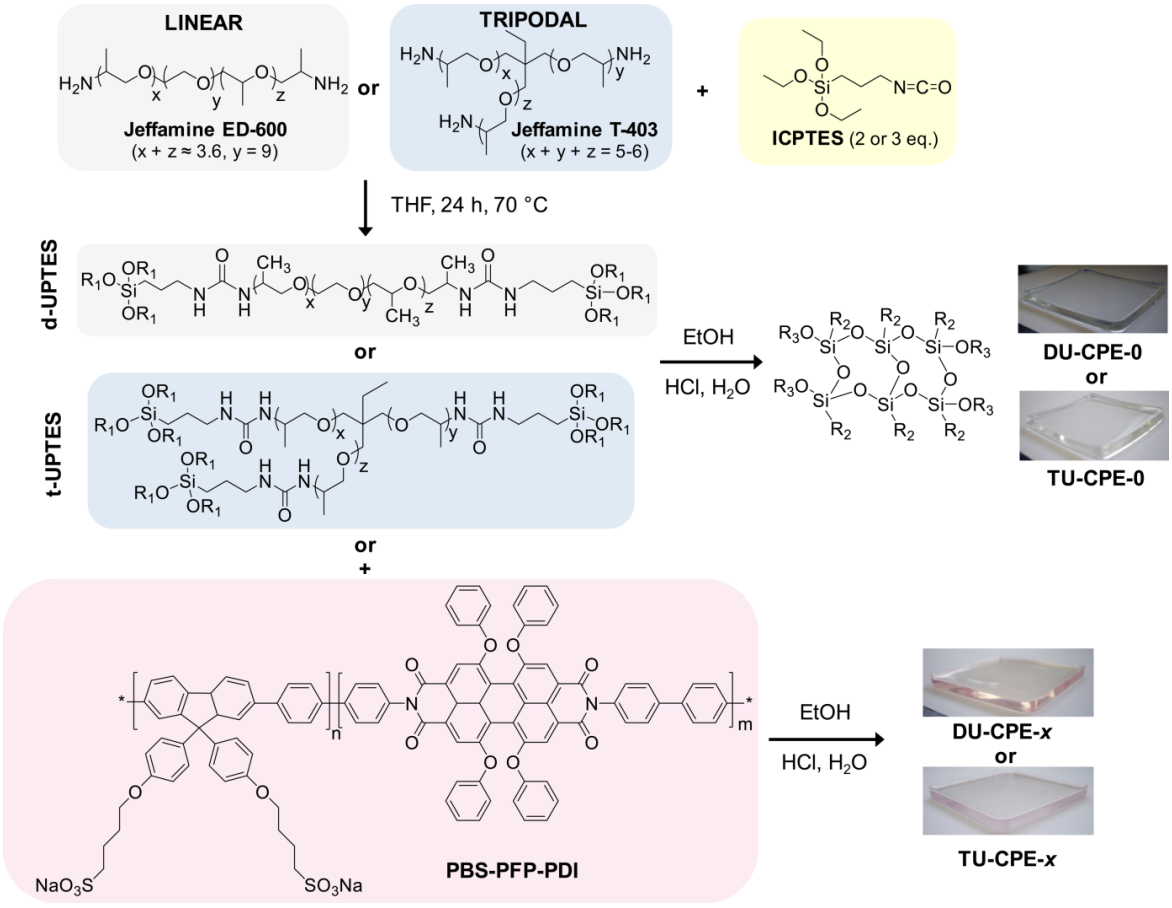

Figure 5.2. Schematic representation of the synthetic process for the preparation of undoped and **CPE**-ureasil (R_1 = –CH_2–CH_3, R_2 = –$(CH_2)_3$–NHCONH–Jeffamine and R_3 = –Si–O–Si– or H).

5.3.2 Photophysical Investigation of the Ureasil Hybrids

5.3.2.1 Steady-State Photoluminescence Studies on the CPE in Solution and on the Undoped Ureasils

Fig. 5.3 shows the steady-state optical properties of **PBS-PFP-PDI** in solution and of the un-doped di- and tri-ureasil hybrids. As expected, when the CPE is dispersed in a solution of a good solvent (water and 1,4-dioxane in 1:1 (v/v) ratio), its optical properties are dominated by those of the poly(fluorene-*alt*-phenylene) units, which constitutes ~98-99% of the **PBS-PFP-PDI** copolymer.[18] The emission spectrum of the CPE (**Fig. 5.3**a) exhibits a well-structured band between 370 to 520 nm, with an absolute maximum centred at 407 nm, typical of the poly(fluorene-*alt*-phenylene) backbone.[19] Similar behaviour is shown in the corresponding absorption spectrum, which is characterised by a broad band centred at 358 nm. Interestingly, the contribution of the on-chain PDI units to the optical properties of the CPE is only observed in the excitation spectrum, with a weak band observed between 470 and 610 nm. CPEs will typically

aggregate when dispersed in water or polar solvents, leading to a decrease of their Φ_{PL} and to a red-shift in their emission/absorption spectra.[22] For the investigated system, 1,4-dioxane is used as co-solvent to help breaking the CPE aggregates in solution, leading to a more efficient solubilisation of each individual chain.[23] As a result, the maxima of the emission and absorption spectra for **PBS-PFP-PDI** dissolved in a water/1,4-dioxane mixture (1:1 v/v) are blue-shifted by 19 and 11 nm, respectively, compared to those for the same CPE in pure water.[18]

The emission (**Fig. 5.3**b and **Fig 5.3**d) and excitation spectra (**Fig 5.3**c and **Fig. 5.3**e) of the undoped ureasils reflect the same trends reported in **Chapter 3** and **4** and the literature.[1, 24] A characteristic broad emission band is observed ranging between 380 and 470 nm, whose maximum red-shifts with increasing excitation wavelength. The corresponding excitation spectra present an analogous trend. It is of interest for improved understanding of the next section, to recall the contributions responsible for the optical properties of ureasils; each emission/excitation band can be deconvoluted in two components corresponding to (i) radiative electron-hole recombination occurring in the oxygen defects localised in the siliceous nanodomains and (ii) photoinduced proton transfer from the NH_2^+ to the N^- species in the urea bridges.[17, 24, 25]

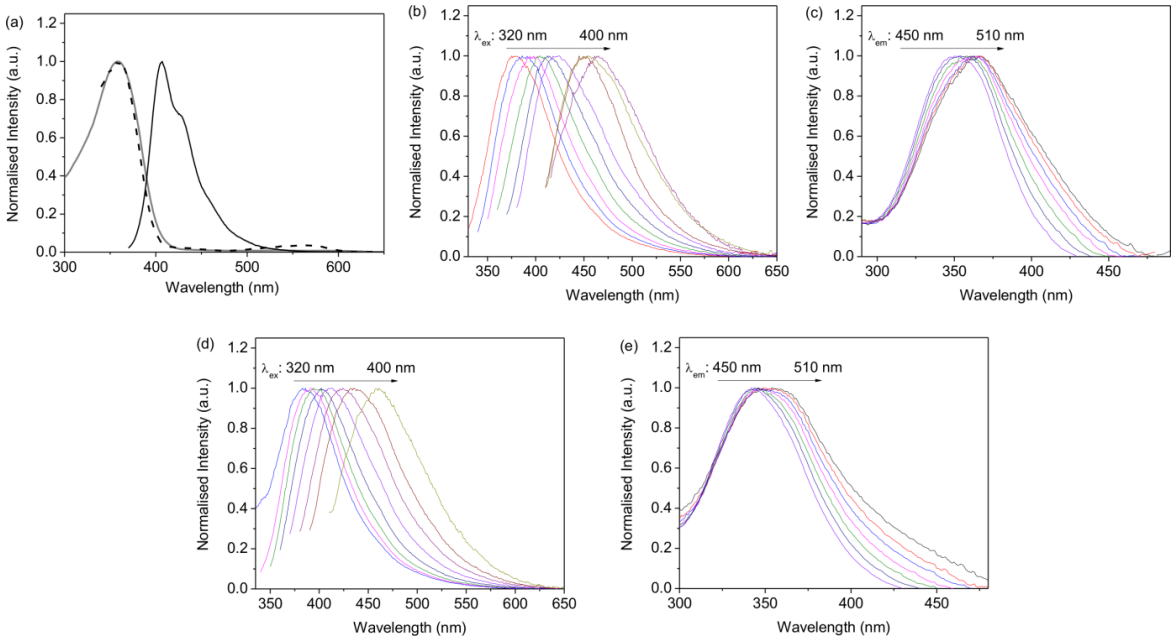

Figure 5.3. Optical properties of **PBS-PFP-PDI** and of the undoped ureasils. (a) Absorption (gray solid line), excitation (dashed line) and emission (black solid line) spectra of **PBS-PFP-PDI** (10^{-6} mol dm^{-3}, λ_{ex} = 360 nm, λ_{em}= 660 nm). Emission spectra of (b) **DU-CPE-0** and (d) **TU-CPE-0** at different excitation wavelengths and excitation spectra of (c) **DU-CPE-0** and (e) **TU-CPE-0** at different emission wavelengths.

5.3.2.2 Steady-State Photoluminescence Studies on the CPE-doped Ureasils

The emission and excitation spectra of **DU-CPE-08** and **TU-CPE-08** are shown in **Fig. 5.4**. The excitation and emission spectra of other samples can be found in the Appendix (**Fig. A5.1** and **Fig. A5.2**). For both sets of samples, the overall optical properties are dominated by emission from the poly(fluorene-*alt*-phenylene). The emission spectra of the CPE-doped ureasils (**Fig. 5.4**a and **Fig. 5.4**c and **Fig A5.1**) present an intense emission band ranging between 350 and 550 nm and centred at 409 nm for the **DU-CPE-*x*** series and at 405 nm for the **TU-CPE-*x*** series, respectively. This result provides an indication of the extent of aggregation of the CPE chains within the ureasil matrices: compared to the emission maximum observed for **PBS-PFP-PDI** dispersed in a good solvent (centred at 407 nm), the corresponding value for **DU-CPE-*x*** samples is red-shifted by 2 nm and blue-shifted by 2 nm for **TU-CPE-*x*** samples. This indicates that the matrix of the tri-ureasil network favours improved isolation of the **PBS-PFP-PDI** chains compared to its di-ureasil analogue, matching that previously observed in **Chapter 3**, where the more open and distorted structure of the tri-ureasils induced improved dispersion of **PFO-OH** chains, reducing the extent of aggregation of the CP compared to that of a linear di-ureasil.[1] The contribution of the ureasil to the emission spectra can be observed at the blue- and red-edges of the emission band, upon changing to the excitation wavelength. In particular, when exciting between 310 and 340 nm, selective for the emission of the siliceous nanodomains, a broadening of the blue-edge of the emission band is observed in each sample, while upon excitation between 350 and 400 nm, selective for the emission associated with the urea linkages, a less-pronounced enlargement of the red-edge of the emission band is observed. This excitation-wavelength dependent broadening of the emission band has been previously observed for a system consisting of **PBS-PFP** dispersed in the matrix of a d-U(600) ureasil and has been assigned to excitonic coupling between the ureasil and CPE components in a related system.[17] A similar trend in the broadening of the primary emission band is also observed for the corresponding excitation spectra (**Fig. 5.3**b, **Fig. 5.4**d and **Fig. A5.2**). The contribution of the PDI units to the optical properties of the CPE-doped ureasil hybrids is very weak, reflecting the low degree of incorporation of these moieties into the CPE chains (≈1-2%).

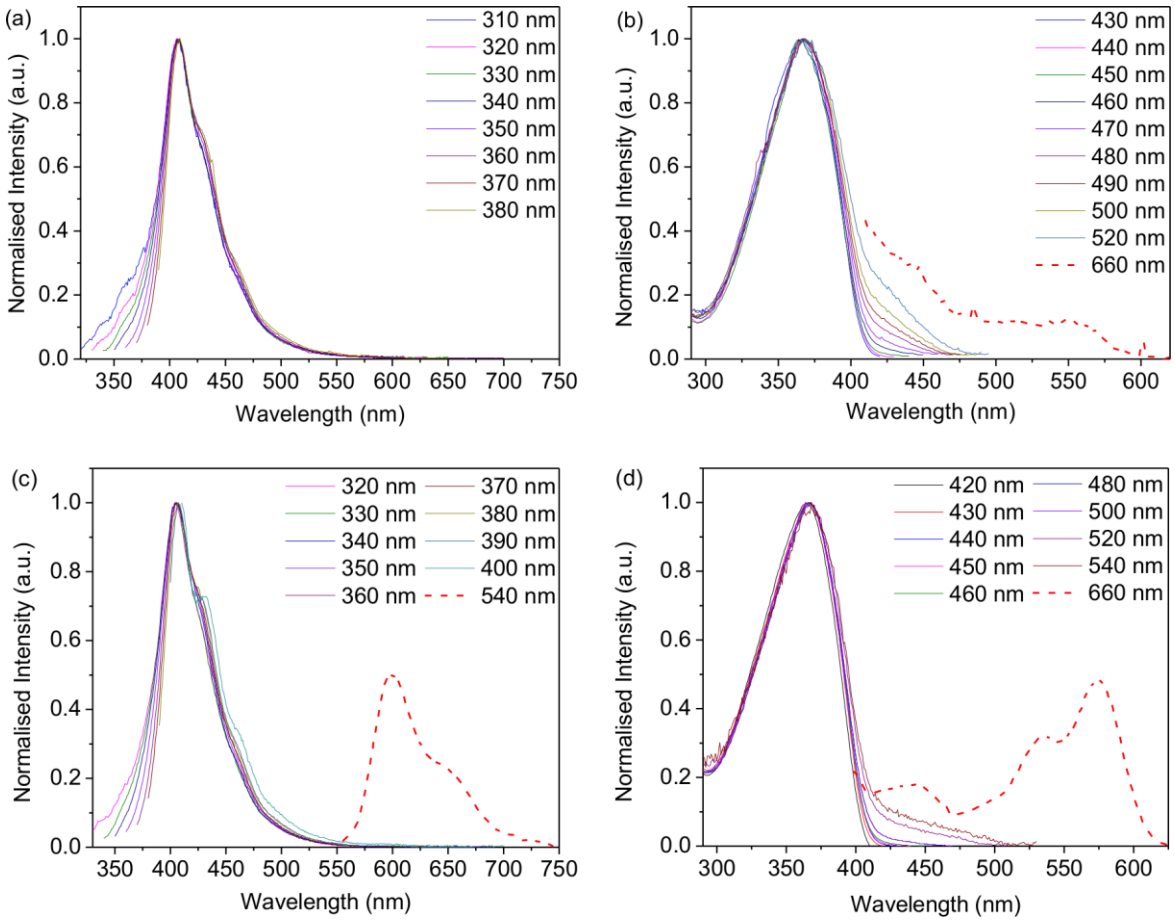

Figure 5.4. Steady-state optical properties of selected CPE-doped ureasils. Emission spectra of (a) **DU-CPE-08** and (c) **TU-CPE-08** at different excitation wavelengths and excitation spectra of (b) **DU-CPE-08** and (d) **TU-CPE-08** at different emission wavelengths.

Interestingly, the emission band corresponding to the perylene units can only be clearly isolated for the **TU-CPE-*x*** series and upon selective excitation at 540 nm and increasing the excitation and emission slit widths (from 0.75/0.75 nm to 2/2 nm). PL measurements performed in the same conditions on **DU-CPE-*x*** samples show a weaker contribution from the PDI units, frequently affected by scattering and with a lower definition. The corresponding excitation spectra for both sets of CPE-doped ureasils, show a similar trend, with the characteristic poly(fluorene-*alt*-phenylene) band observed upon detection between 420 and 520 nm. The PDI contribution is isolated upon detection at 640-660 nm and is generally more prominent for the tri-ureasils compared to the di-ureasils.

It is worth mentioning that the contribution of the PDI moieties is observed in the excitation spectra of all the samples, indicating that, even if at extremely low concentrations, the perylene units are actually present in the doped-ureasils. The results obtained for the excitation

spectra match the previous observation regarding the influence of the ureasil network on the spatial isolation of the CPE molecules. The **PBS-PFP-PDI** units seem to be more aggregated in the di-ureasil matrices, leading to quenching of the PDI emission through non-radiative relaxation of the excited state. Moreover, the emission of the PDI can now be accessed when the CPE is incorporated into the ureasil matrix rather than dispersed in solution where the presence of water and/or the aggregation can lead to radiationless relaxation pathways,[25] thus quenching of the emission.

5.3.2.3 Photoluminescence Quantum Yields Studies

The Φ_{PL} of each sample was measured upon excitation at 360 nm. The Φ_{PL} values are 6.3 ± 0.5 % and 15.7 ± 0.8 % for **DU-CPE-0** and **TU-CPE-0**, respectively. Although the value obtained for the un-doped tri-ureasil is higher than normally observed for ureasil-type materials, it is still comparable to values found in the literature.[26, 27] For **PBS-PFP-PDI** in solution (1,4-dioxane/water, 1:1 v/v) the measured value of Φ_{PL} is 68.6 ± 1.2 %, which is also slightly higher than the one reported for the same CPE in the same conditions by Marques *et al.* (Φ_{PL} = 55 %).[18] This difference can be justified considering: (i) the error associated with method used for the measurement of Φ_{PL} (10%, in our case) and (ii) the difference between the level of aggregation of the CPE chains in solution for our sample compared to the literature. The photophysical characterisation of the **PBS-PFP-PDI** solution performed by Marques *et al.* revealed that the emission (λ_{ex} = 360 nm) and absorption spectra maxima are centred at 360 and 409 nm, respectively. The values measured in the same conditions in this work are 358 and 407 nm, respectively, suggesting that in our case, the CPE chains might be, to some extent, better isolated in solution. Overall, taking into account these two factors, the obtained Φ_{PL} can be considered acceptable.

The measured and corrected values of Φ_{PL} for the **DU-CPE-*x*** and the **TU-CPE-*x*** are presented in **Table 5.1**. The CPE-doped di-ureasils present generally higher values of Φ_{PL} compared to the tri-ureasils containing the same amount of dopant. Namely, the measured values range from 32.4% to 60.5% and from 30.5% to 51.0 % for the **DU-CPE-*x*** and **TU-CPE-*x*** series, respectively. As shown in the previous Chapters, due to the nature of ureasil samples, re-absorption

and waveguiding effects can usually affect the Φ_{PL} measurements in an integrating sphere,[28] therefore the values have been corrected using the method described by Ahn *et al*.[29] leading to a 10-20% increase in each the Φ_{PL} values.

Table 5.1. Measured and corrected Φ_{PL} for **DU-CPE-*x*** and **TU-CPE-*x*** samples. (λ_{ex} = 360 nm).

Sample ID	Φ_{PL} (measured)	Φ_{PL} (corrected)
DU-CPE-0	6.3 (±0.5)	-
DU-CPE-01	32.4 (±1.8)	39.5 (±2.4)
DU-CPE-02	42.3 (±1.4)	47.7 (±1.5)
DU-CPE-04	56.4 (±1.5)	59.9 (±1.5)
DU-CPE-08	60.5 (±1.3)	65.1 (±1.7)
TU-CPE-0	15.7 (±0.8)	-
TU-CPE-01	30.5 (±0.8)	45.4 (±2.6)
TU-CPE-02	39.8 (±2.0)	51.1 (±2.5)
TU-CPE-04	48.8 (±1.4)	56.4 (±2.1)
TU-CPE-08	51.0 (±0.9)	55.5 (±0.9)

5.3.3 Investigation of the Local Structure of the DU-PF-*x* and TU-PF-*x* hybrids.

To gain a deeper understanding of the role of the ureasil host matrices on the extent of aggregation of the CPE suggested by the steady-state photoluminescence investigation, the structural features of di- and tri-ureasils were examined by FTIR spectroscopy, PXRD, solid-state MAS-NMR. Thermogravimetric analyses were also performed to test the thermal stability of the samples, which was comparable to what was previously observed for di- and tri-ureasil hybrids in the previous chapters. The thermograms can be found in the Appendix (**Fig. A5.3**).

5.3.3.1 FTIR and PXRD Studies

The FTIR spectra and the results of the Gaussian fits in the Amide I Region for the undoped ureasils are presented in **Fig. 5.5**a and **5.5**c, together with two plots presenting the trend of the relative contribution of each characteristic fitting peaks as a function of the concentration of the CPE (**Fig. 5.5**b and **5.5**d). The FTIR spectra and corresponding Gaussian fits for each sample can be found in the Appendix (**Fig. A5.4**). Comparison of the two undoped samples reveals that while three components are required to fit the Amide I band of **DU-CPE-0**, an additional component is

necessary to model this band for **TU-CPE-0**. As discussed in **Chapter 2**, these components represent the urea moieties that do not participate in H-bonding interactions.[30] Increasing the concentration of the CPE does not seem to influence the local structure of the hybrids, and the relative contribution of each peak does not show any remarkable changes or follow any particular trend when the concentration of the **PBS-PFP-PDI** is increased from 0 to 0.008%$_{w/w}$ (**Fig. 5**b and **5**d). However, it has been shown that for pure ureasils, the degree of H-bonding interactions occurring between urea moieties is directly correlated to the Φ_{PL}.[27] A decrease in this type of interaction (which corresponds to Peak 1) can lead to more efficient radiative relaxation of the urea centres due to a higher availability of the protons located in these moieties. The presence of Peak 4 in the **TU-CPE-*x*** fits indicates that the higher Φ_{PL} measured for the undoped tri-ureasils might be a direct consequence of more efficient radiative recombination localised at the urea groups.

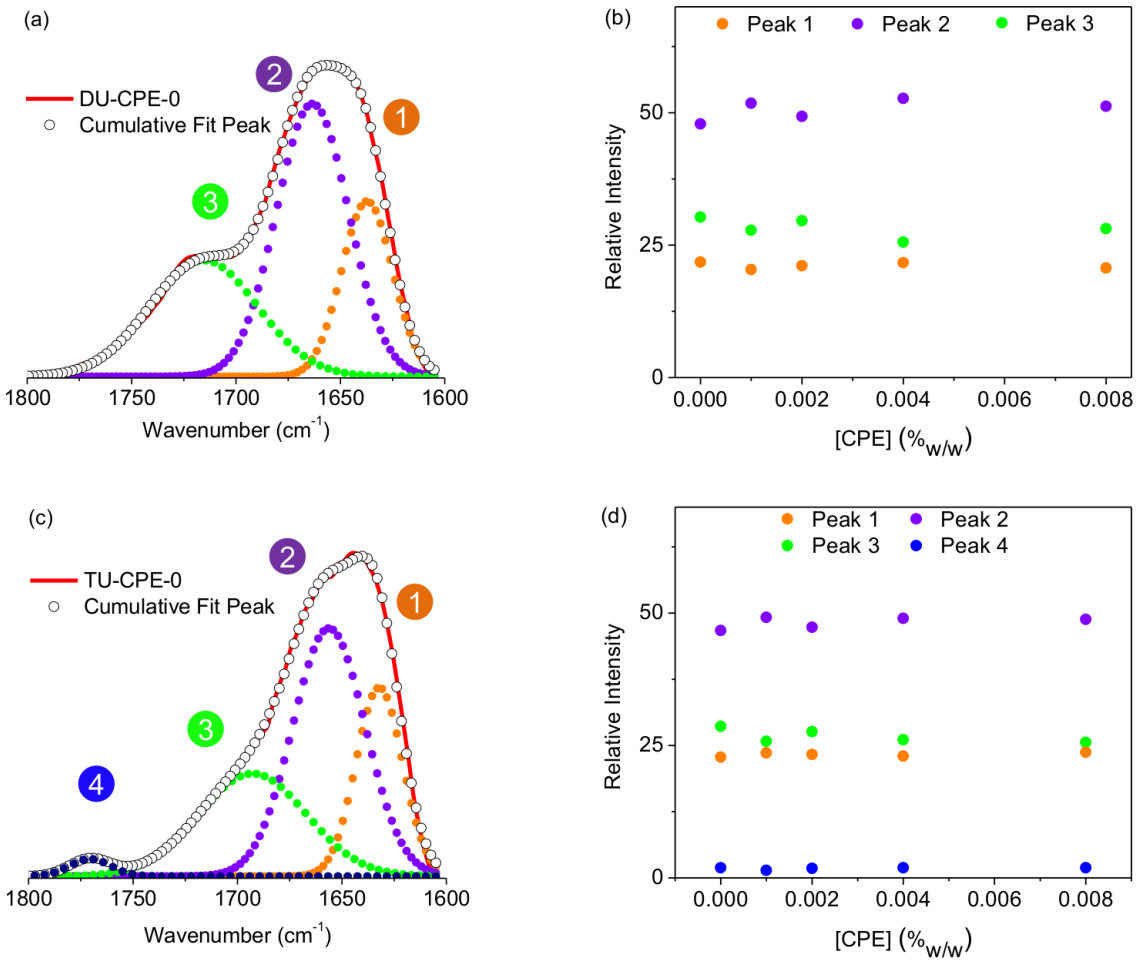

Figure 5.5. Investigation of hydrogen-bonding contributions in PBS-PFP-PDI doped di- and tri-ureasils. Gaussian fits to the Amide I region of the FTIR spectrum of (a) **DU-CPE-0** and (c) **TU-CPE-0** and relative percentage intensities of the each peak as a function of the concentration for (b) **DU-CPE-*x*** and (d) **TU-CPE-*x*** series. The circled numbers represent the peaks described in the text.

However, since the CPE-doped ureasils present in general higher values of Φ_{PL} compared to those of the corresponding CPE-doped tri-ureasils, this emission mechanism is not believed to represent a major contribution to the overall emission of the samples, which is clearly dominated by the **PBS-PFP-PDI**. Another interesting observation related to the presence of Peak 4 for tri-ureasils is that this also supports the hypothesis of a more open and distorted structure for the tri-ureasils, justifying the slight blue-shift observed in the absorption and emission spectra of the these samples compared to those of analogous **DU-CPE-*x*** samples. PXRD measurements were performed on the samples to investigate the bulk features of the structure of the di- and tri-ureasils upon incorporation of the CPE. The diffraction patterns for both sets of samples match those previously reported in literature[2, 26, 31, 32] for ureasils and are presented in **Fig. 5.6**.

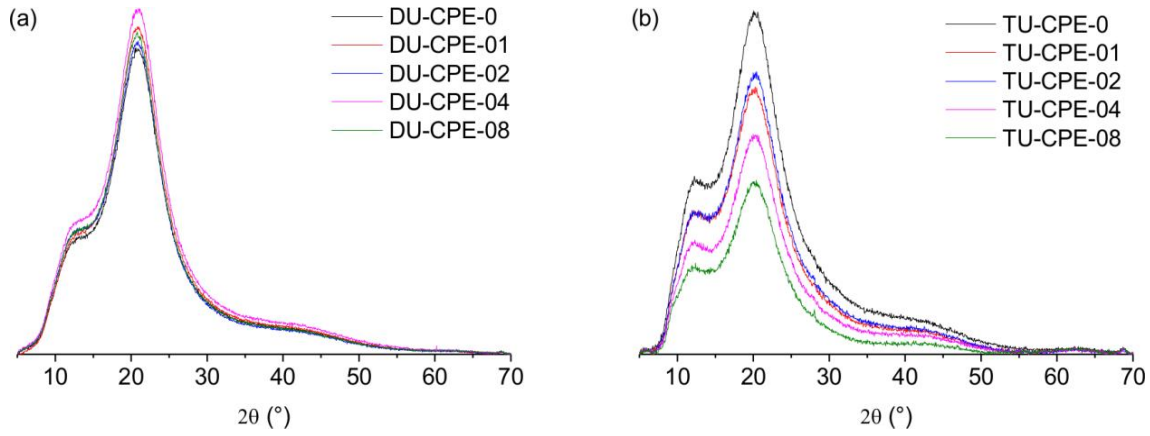

Figure 5.6. Powder X-ray diffraction patterns for (a) **DU-CPE-*x*** and (b) **TU-CPE-*x*** series, in the range 2θ = 5-70°.

The incorporation of the CPE at the investigated concentrations does not bring any significant changes to the diffractograms, which are characterised by a primary peak (Band 2) centred at 20.8° and 20.1°, with a shoulder (Band 1) at 12.5° and 11.7° for di-ureasils and tri-ureasils, respectively (**Table 5.2**). From the main peak, associated with ordering within the siliceous domains,[31] the structural unit distance, *d*, was calculated using Bragg's Law (**Eqn. 2.24**), in **Chapter 2**. The values match those typical of ureasils and are similar for both sets of samples. The coherence length, *L*, over which the structural unit survives was estimated to range between ~9.7-11.2 Å (calculated using the Scherrer equation, **Eqn. 2.23**) and are consistent with those derived from small-angle X-ray scattering experiments for the dimensions of the siliceous domains

of di-ureasils.[33] Overall, the PXRD studies suggest that the incorporation of the CPE does not affect the integrity of the structure of either the di- and the tri-ureasil matrices.

Table 5.2. Summary of PXRD data analysis: band centres, structural unit distance and coherence lengths for **DU-CPE-*x*** and **TU-CPE-*x***.

Sample ID	Band 1	Band 2	*d* (Å)[a]	*L* (Å)[b]
DU-CPE-0	12.5	20.8	4.27	11.07
DU-CPE-01	12.5	20.8	4.27	11.10
DU-CPE-02	12.5	20.7	4.29	11.14
DU-CPE-04	12.5	20.8	4.27	11.14
DU-CPE-08	12.5	20.7	4.27	11.17
TU-CPE-0	11.9	20.1	4.41	9.70
TU-CPE-01	11.9	20.0	4.43	9.69
TU-CPE-02	11.9	20.1	4.41	9.81
TU-CPE-04	11.9	20.1	4.41	9.98
TU-CPE-08	11.8	20.1	4.41	10.00

[a] From Bragg's Law [b] From the Scherrer equation

5.3.3.2 Solid-State NMR

Solid-state MAS-NMR measurements were performed to further elucidate the role of the structure of the two types of ureasil hybrids on the optical properties of the incorporated CPE. We saw above that FTIR studies revealed subtle differences on the level of disorder of the silica network imparted by the use of a linear or a tri-branched Jeffamine. This can be correlated to the degree of condensation, *c*, of the material which was calculated by means of ^{29}Si MAS-NMR spectroscopy (**Fig. 5.7**). As observed in **Chapters 3** and **4**, the ^{29}Si MAS-NMR spectra for the ureasil hybrids are characterised by the presence of peaks belonging to the T_n series centred at: ~-44 ppm, ~-52 ppm and ~-60 ppm for T_1, T_2, and T_3, respectively. Although the peak centres are similar in all samples, (**Table 5.3**), the spectra obtained for the di-ureasils show significant differences to those of the tri-ureasils. Namely, the contribution of the T_1 signal in the spectra collected for the **DU-CPE-*x*** series is extremely weak compared to that observed in the spectra of **TU-CPE-*x*** samples (**Fig. 5.7**b) and due to poor signal-to-noise ratios, it was not possible to quantify it during the fitting process and was therefore considered negligible. This observation is reflected in the calculated *c* values which were generally higher for the di-ureasils compared to the tri-ureasils (~82% *vs* ~69%).

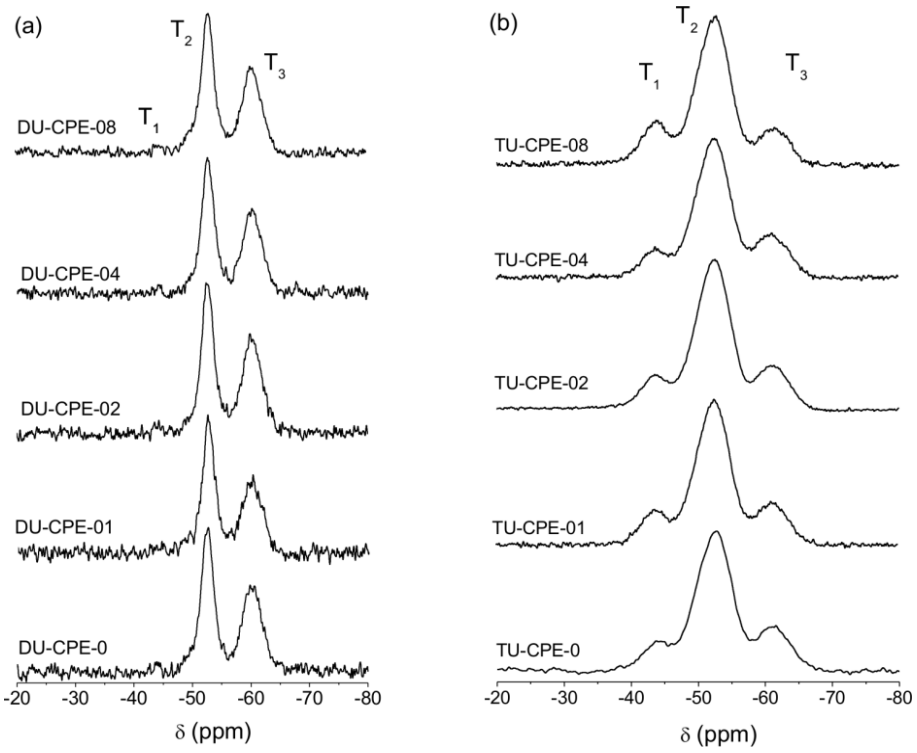

Figure 5.7. Investigation of the extent of condensation of the siliceous network in **PBS-PFP-PDI**-ureasils. ^{29}Si solid-state MAS-NMR spectra for (a) **DU-CPE-*x*** and (b) **TU-CPE-*x*.**

These finding are in agreement with our hypothesis that the more open and less condensed tri-ureasil network allows improved isolation of the **PBS-PFP-PDI** chains, compared to the more compact di-ureasil network, which favours to a small extent the aggregation of the dopant chains leading to a small red-shift in the absorption/emission spectra of the **DU-CPE-**x series compared to the CPE dispersed either in solution or the a tri-ureasil matrix. From a more general perspective and considering the work of this entire thesis, these results are consistent with those observed in **Chapter 3**, where the arrangement of the silica network guided the extent of the formation of the PF β-phase, and further support our claim that the host structure plays a crucial role in guiding the dopant conformation, hence the optoelectronic properties of the final hybrid material.

Table 5.3. ^{29}Si MAS-NMR chemical shifts (ppm), relative T_n populations and degree of condensation, *c*, for **DU-CPE-*x*** and **TU-PF-*x*** (R denotes the ureapropyl chains).

Sample ID	T_1 $RSi(OSi)(OH)_2$ (%)	T_2 $RSi(OSi)_2(OH)$ (%)	T_3 $RSi(OSi)_3$ (%)	*c* (%)[a]
DU-CPE-0	-	-52.6 (53)	-60.2 (47)	82
DU-CPE-01	-	-52.6 (54)	-59.9 (46)	82
DU-CPE-02	-	-52.6 (50)	-60.2(50)	83
DU-CPE-04	-	-52.7 (51)	-60.2 (49)	83
DU-CPE-08	-	-52.9 (53)	-60.6 (47)	82
TU-CPE-0	-44.2 (13)	-52.4 (67)	-61.3(20)	69
TU-CPE-01	-43.9 (14)	-52.4 (68)	-61.3 (18)	68
TU-CPE-02	-43.8 (14)	-52.3 (68)	-61.2 (18)	68
TU-CPE-04	-44.0 (12)	-52.4 (68)	-61.2 (20)	69
TU-CPE-08	-43.8 (18)	-52.4 (68)	-61.4 (15)	66

[a] $c = 1/3(\%T_1+2\%T_2+3\%T_3)$[26]

The ^{13}C MAS NMR spectra for the un-doped and doped ureasils hybrids are presented in **Fig. 5.8** and match those previously reported for these types of ureasils.[2, 26] Once again, no significant changes were observed upon addition of the CPE to either ureasil matrix at any of the investigated concentrations. A summary of the peak assignments can be found in **Table 5.4**.

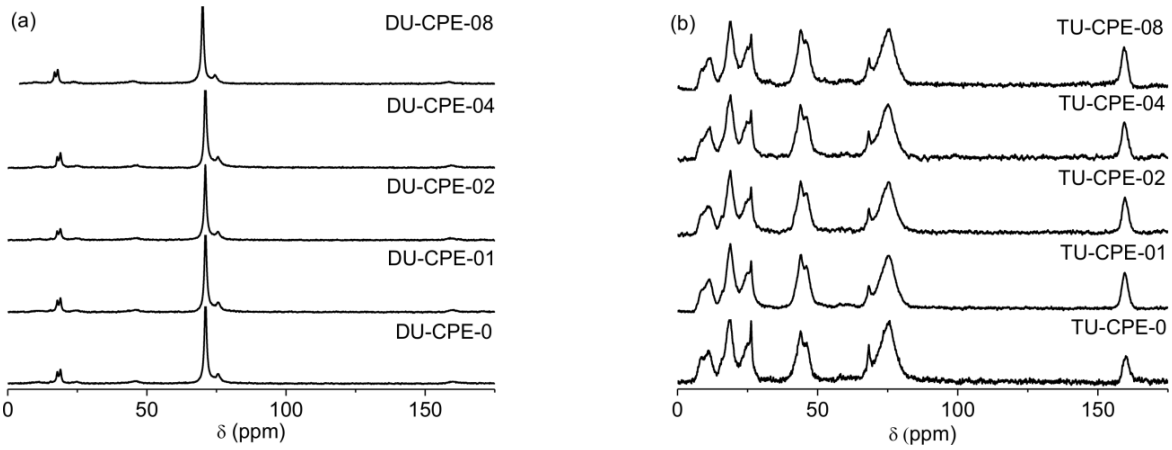

Figure 5.8. ^{13}C solid-state MAS-NMR spectra for (a) the **DU-CPE-*x*** sample series and (b) the **TU-CPE-*x*** sample series.

Table 5.4. Summary of the ^{13}C MAS-NMR chemical shifts assignment (ppm) for **DU-CPE-*x*** and **TU-CPE-*x*** samples.

Signal Assignment	DU-CPE-*x* (ppm)	TU-CPE-*x* (ppm)
C=O urea	~ 160	~ 160
-OCH	~ 75	~ 75
$-(OCH_2CH_2)-$	~ 68	~ 68
$-NCH_2-$ in $N(CH_2)_3$-Si	~ 44	~ 44
$-CH_2-$ in $N(CH_2)_3$-Si-		~ 25
$-CH_3$ in $OCH_2CH(CH_3)$	~ 19	~ 19
$-CH_3$ in $(CH_3CH_2O)_3Si$	~ 17	~ 17
$-CH_2Si-$ in $N(CH_2)_3Si$		~ 11

5.3.4 Time-Resolved Photoluminescence Studies

The aim of using **PBS-PFP-PDI** as a lumophore for LSCs is to exploit the energy transfer between the poly(fluorene-*alt*-phenylene) donor and the PDI acceptor. However, despite the good spectral overlap between these two species, the emission of the PDI was not observed upon selective excitation of the **PBS-PFP** moieties. Moreover, while Marques *et al.* demonstrated through density functional theory calculations that these two species are effectively electronically coupled,[18] the results obtained from the steady-state PL investigation suggest that energy transfer does not occur either for the CPE in solution or embedded in the ureasil matrices. However, in **Chapter 4** we demonstrated that ureasils themselves can behave as efficient excitation energy donors for perylene diimides.[34] Moreover, previous studies in our group showed that ureasils can also behave as an energy donor for efficient energy transfer to **PBS-PFP** moieties.[17] The optical behaviour observed for the current system under investigation is puzzling and further clarification on the nature of the electronic interactions between the components in their excited states was sought by means of picosecond time-correlated single photon counting emission lifetime measurements. The measurements were performed by selectively exciting the ureasil/poly(fluorene-*alt*-phenylene) components (λ_{ex}= 370 nm) or the PDI chromophore (λ_{ex}= 466 nm), while monitoring the emission at 420 nm (PBS-PFP/purplish-blue emission from ureasil) and 500 nm (blue emission from ureasil). A detailed description of the fitting procedure can be found in **Section 2.3.4**.

Due to the low amount of PDI emitters incorporated into the CPE chains (1-2%), the decay curves measured through direct excitation and detection of the perylene emission (λ_{ex}= 466 nm and λ_{em}= 600 nm) did not present good signal-to-noise ratios, resulting in poor quality fits. An example of the results obtained for the decay curve obtained at, λ_{em} = 600 nm, corresponding fits, weighted residuals and instrument response function is presented for **TU-CPE-08** in **Fig. 5.9**. The trend of the residuals and the value of χ^2 obtained would suggest a good quality fit. However, considering that under these experimental conditions the only species emitting are the PDI moieties, whose decay curve has been modelled in literature with a single term with a lifetime of ~5 ns,[35] the need to model the decay with three exponents, where the relative contributions of the un-known terms are even larger than that of the PDI, is a clear indication that the quality of the data is not sufficient to consider these results reliable. Therefore, the measurements performed under these conditions were discarded.

τ_1/ns	τ_2/ns	τ_3/ns	α_1	α_2	α_3	χ^2
0.001	1.596	5.461	0.927	0.022	0.051	1.25

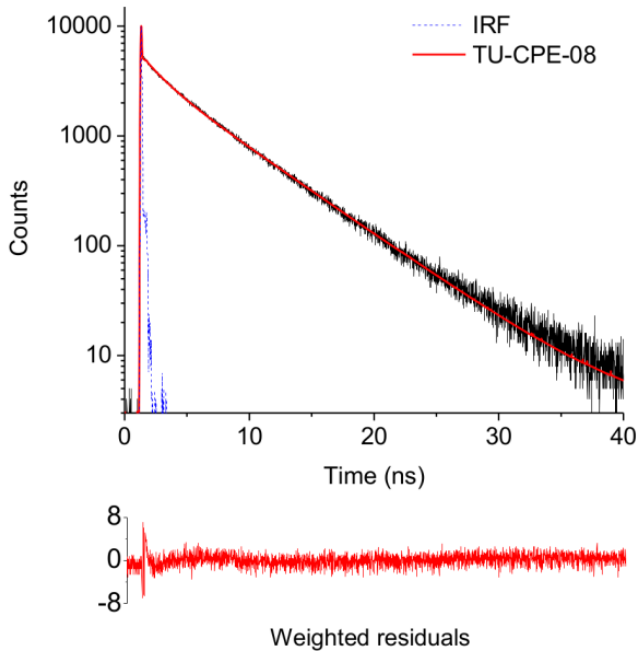

Figure 5.9. Emission decay curve (solid black line) and corresponding fit (solid red line) for **TU-CPE-08** (λ_{ex} = 466 nm, λ_{em}= 600 nm). The fitted decay times (τ_i), the pre-exponential coefficients (α_i), chi-squared (χ^2), weighted residuals and instrument response function (IRF, dotted blue line) are also shown.

The decay curves and corresponding fits for the CPE, **DU-CPE-*x*** and **TU-CPE-*x*** samples (λ_{ex} = 370 nm and λ_{em} = 420 nm) are presented in **Fig. 5.10** and the corresponding results of the fits are summarised in **Table 5.5**.

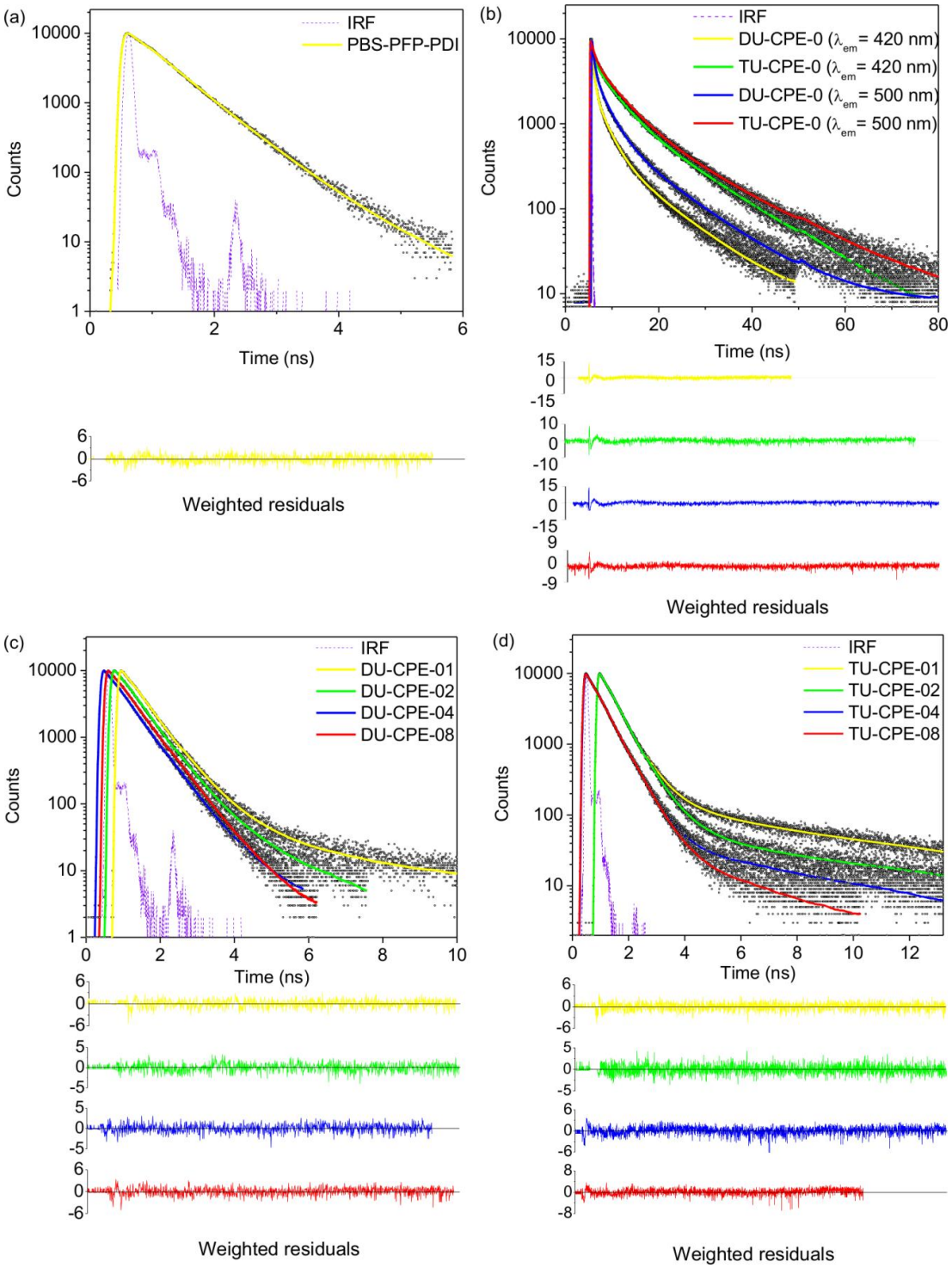

Figure 5.10. Emission decay curves (black dots), fits (coloured lines) and instrument response function (IRF) (dashed line) for **PBS-PFP-PDI** in solution (water/1,4-dioxane 1:1 (v/v)), **DU-CPE-*x*** and **TU-CPE-*x*** at selected excitation and emission wavelengths. (a) **CPE** (λ_{ex} = 370 nm, λ_{em} = 420 nm), (b) **DU-CPE-0** and **TU-CPE-0** (λ_{ex} = 370 nm, λ_{em} = 420 nm and 500 nm), (c) **DU-CPE-*x*** (λ_{ex} = 370 nm, λ_{em} = 420 nm) and (d) **TU-CPE-*x*** (λ_{ex} = 370 nm, λ_{em} = 420 nm). The weighted residuals for each fit are also shown.

For **PBS-PFP-PDI** dissolved in a solution of good solvent (water and 1,4-dioxane (1:1 v/v)) and upon selective excitation and detection of the poly(fluorene-*alt*-phenylene) units, the fluorescence decay curve (**Fig. 5.10**a) can be modelled with three terms: τ_{CPE1} ~0.03 ns, ascribed to the contributions from fast intra-/inter-chain energy migration and conformational relaxation on the PFP backbone,[35, 36] τ_{CPE2} ~ 0.55 ns, which is assigned to radiative relaxation associated with polymer aggregates[37] and $\tau_{CPE3} \approx 1.1$ ns, which is attributed to radiative decay of isolated polymer chains.[38]

Table 5.5. Decay times (τ_i), pre-exponential coefficients (α_i) and chi-squared (χ^2) resulting from analysis of the photoluminescence decays (λ_{ex} = 370 nm) of CPE, **DU-CPE-*x*** and **TU-CPE-*x*** samples (λ_{em} = 420 nm).

Sample	τ_1 **(ns)**	τ_2 **(ns)**	τ_3 **(ns)**	τ_4 **(ns)**	α_1	α_2	α_3	α_4	χ^2
CPE	0.026	0.553	1.072		-0.899	0.947	0.053		1.14
DU-CPE-0		0.47	2.56	10.08		0.75	0.20	0.05	1.55
DU-CPE-01		0.518	1.166	6.924		0.949	0.048	0.003	1.15
DU-CPE-02	0.029	0.538	1.640		-0.281	0.982	0.018		1.03
DU-CPE-04		0.537	1.545			0.990	0.010		1.32
DU-CPE-08		0.548	1.224			0.983	0.017		1.20
TU-CPE-0		0.522	4.204	12.740		0.474	0.378	0.148	1.43
TU-CPE-01		0.512	1.396	8.086		0.960	0.029	0.011	1.31
TU-CPE-02		0.513	1.050	8.103		0.943	0.052	0.005	1.12
TU-CPE-04		0.544	5.396			0.995	0.005		1.25
TU-CPE-08		0.550	3.223			0.996	0.004		1.31

For undoped di- and tri-ureasils the decay curves measured in the same conditions (**Fig. 5.10**b) can be resolved into three terms: $\tau_{U1} < 1$ ns, $\tau_{U2} \approx$2.5-4.9 ns and $\tau_{U3} \approx$10-14.5 ns, which is characteristic for these materials.[18] Each value increases when the detection wavelength is switched from 420 to 500 nm. This is a direct consequence of the spectral dependence of the two contributions responsible for the ureasil emission; at 420 nm the emission arising from the siliceous domains is predominant (τ_{U1}), switching to the urea-centred emission at 500 nm (τ_{U3}).[17] The average lifetimes ($< \tau >$) follow the same trend, increasing with increasing detection wavelength from ~4.8 ns and ~8.3 ns to ~5.9 ns and ~8.8 ns, for **DU-CPE-0** and **TU-CPE-0**, respectively. Interestingly, the undoped tri-ureasils generally present higher values of $<\tau>$ compared to the corresponding di-ureasils, which matches their higher Φ_{PL}. Unfortunately, it is

hard to unambiguously assign each one of the decay terms obtained from the fits performed on **DU-CPE-*x*** and **TU-CPE-*x*** samples. This is due to the large spectral overlap between the emission of the ureasils and the CPE at 420 nm. The fits to the decay curves of the CPE-doped ureasils require either two or three components (**Fig. 5.10**c and d, and **Table 5.5**), with all the samples presenting an intermediate lifetime τ_2~0.5 ns, which accounts for the largest contribution to the emission decay (α_2). Both the un-doped ureasils and the CPE in solution are characterised by components similar to τ_2, τ_{U1} and τ_{CPE2}, respectively. A detailed investigation by Willis-Fox *et al.*[17] showed that for a PBS-PFP-doped di-ureasil, the strong electronic coupling between the CPE and the siliceous-based emission centre of the ureasil led to efficient excitation energy transfer between the two species. Since τ_2 is predominant in each one of the investigated CPE-doped samples, a similar mechanism might be involved here as well.

The additional decay term isolated for **DU-CPE-02**, (τ_1 = 0.029 ns) is reminiscent of τ_{CPE1} (on-chain/intrachain excitation migration and/or conformational relaxation) and might arise from the presence of isolated CPE pockets inside of the ureasil networks. Similarly, for **DU-CPE-01**, **TU-CPE-01** and **TU-CPE-02**, the simultaneous presence of τ_2 ~1-1.3 ns and τ_3 ~7-8.1 ns, which are similar to τ_{CPE3} and τ_{U3}, respectively, might indicate that the two species are emitting discretely in these samples. Another component ranging between 1-6 ns is also present in all samples, and its value varies with the CPE concentration and corresponds to the same timescale as both τ_{CPE3} and τ_{U2}. For both series of samples, the values of τ_3 fluctuate with the concentration of CPE; for **DU-CPE-*x***, it first increases when the concentration of **PBS-PFP-PDI** increases from 0.001 to 0.002%$_{w/w}$ and then decreases when the concentration is further increased. For the tri-ureasil series instead, it fluctuates between 1 and 5.4 ns without following any significant trend. It is interesting to note that for the two highest concentrations of CPE, τ_3 is somewhat longer for tri-ureasils than for the di-ureasils. As mentioned above, ureasils matrices can behave as efficient energy transfer donor (from both the urea and siliceous domain centred emission) to the chains of a PBS-PFP homopolymer acceptor. This had led to an increase in the overall Φ_{PL} of the systems.[17] It is tempting to suggest that a similar mechanism is responsible for the general decrease of τ_3 with increasing CPE concentration observed here for both **DU-/TU-CPE-04** and **DU-/TU-CPE-08**.

However, this hypothesis is not consistent with the corresponding α values, which remain essentially unchanged in both series at these concentrations.

The decay curves obtained upon excitation at 370 nm and detection at 500 nm are shown in **Fig. A5.5** and **Fig. A5.6** for **DU-CPE-*x*** and **TU-CPE-*x***, respectively. and the results of the corresponding fits are presented in **Table A5.1.** For the **DU-CPE-*x*** series, the decay curves are best fitted with three components, with the exception of **DU-CPE-02** which requires a fourth term. This result strengthens the hypothesis of poor electronic coupling between the ureasil and the CPE at this concentration. The contributions isolated for each of the doped di-ureasil samples are the following: τ_1 ~20-40 ps, associated with the short-lived component of the CPE (τ_{CPE1}), τ_2 ~0.6 ns arising from the combination of the ureasil (τ_{U1}) and the CPE (τ_{CPE2}), and τ_3 ~1.4-4.1 ns, associated to a combination of the longer-lived ureasil contributions (τ_{U2} and τ_{U3}) and emission from isolated CPE chains (τ_{CPE3}). Interestingly, the long-lived ureasil component (τ_{U3}) can only be clearly isolated for sample **DU-CPE-01**, reflecting the poor coupling of the donor/acceptor pairs which was is also observed for **DU-CPE-02.** A similar trend is presented for **TU-CPE-*x*** samples, where three terms are isolated for each decay curve: τ_2 ~0.6 ns and τ_3 ~1.5-3.6 ns, while a third decay term (τ_4 ~8.8-11.6 ns) is reminiscent of τ_{U3} and is observed at all **PBS-PFP-PDI** concentrations. Each lifetime value is slightly increased compared to those observed for λ_{ex} = 420 nm. This is a consequence of the emission of the ureasil which has a more significant contribution at 500 nm.

Although the two emitters still partially overlap under these conditions, some interesting considerations can be drawn from investigating this region which is semi-selective for ureasils. For the **DU-CPE-*x*** series, the short-lived component characteristic of the CPE (τ_{CPE1}) can now be isolated for most concentrations, moreover the intensity of the contribution of the τ_2 term, increases with the **PBS-PFP-PDI** concentration, while the longest lifetime (τ_3 and τ_4) and corresponding pre-exponential factor decreases from 10.9 to 3.6 ns. A similar trend is observed for the tri-ureasil samples, with τ_4 decreasing from 14.0 to 8.8 ns (**Table A5.1**). In this case, however, the τ_{CPE1} term was not isolated at any of the investigated concentrations. This observation supports the results obtained for the steady-state photoluminescence investigation, which suggested that the tendency of the CPE to aggregate is higher in di-ureasil compared to tri-ureasil matrices, increasing the probability of on-chain energy migration. This is also in agreement with the ^{29}Si MAS-NMR data,

which showed that the structure of the di-ureasils is generally more condensed and less open compared to that of the tri-ureasils (*c*: 80 *vs* 69%). All of these observations suggest that the CPE is more homogeneously dispersed in the **TU-CPE-*x*** samples, which facilitates excitation energy migration between the host and the guest species. Moreover, the decrease of the longest lifetime component (and associated pre-exponential factor) with increasing CPE concentration, for both **DU-CPE-*x*** and **TU-CPE-*x***, supports our previous assignment of thermally-assisted excitation energy from NH-centred trap states to isolated CPE chains in these systems.[17]

5.3.5 Performance of PBS-PFP-PDI-Ureasils as Luminescent Solar Concentrators

The aim of this work is to combine an optically active waveguide with the **PBS-PDP-PDI** lumophore, which is an overall donor-acceptor system, to improve the performance of a LSC by increasing the range of harvested sun radiation and/or by initiating an energy transfer process between the species. Time-resolved photoluminescence studies confirmed energy transfer between the ureasil host and the **PBS-PFP** chains, however the direct sensitisation of the PDI units was observed only for the two samples presenting the highest CPE concentration: **TU-CPE-08** and **DU-CPE-08**, which also presented the highest value of Φ_{PL} for each series. Therefore, to test the performance of our systems as LSCs, these two samples were reproduced in a larger scale, to yield monolith of 4 cm × 4 cm size (**Fig. 5.11**a, b and c). The performance of an LSC is generally quantified by the optical conversion efficiency (η_{opt}), which is determined experimentally by measuring the optical power output summed over the four edges of the LSC (OP_{out}) with respect to the total incident solar power on the surface of the LSC (OP_{in}) according to:[39]

$$\eta_{\mathrm{opt}} = \frac{OP_{out}}{OP_{in}} \qquad (\mathbf{5.1})$$

Fig. 5.11d shows the optical power spectra emitted by the four edges of each LSC under dark (absorbing) background conditions for **DU-CPE-08** and **TU-CPE-08** and the corresponding undoped ureasils. The optical power output profiles of **DU-CPE-08** and **TU-CPE-08** are characterised by an intense band in the 380-550 nm region, which arises from the poly(fluorene) portion of the CPE and a weaker band in the 600-700 nm region which can be ascribed to the PDI units. On their own, undoped ureasils yield optical conversion efficiencies of 1.6 ± 0.1% 1.3 ±

0.3% for **DU-CPE-0** and **TU-CPE-0**, respectively, which are consistent values reported in the literature for these materials.[34] Upon addition of the CPE, the η_{opt} increases modestly to 2.4 ± 0.4% for **DU-CPE-08** and 1.8 ± 0.1 % for **TU-CPE-08**, respectively. However, the performance on a LSC, can be dramatically enhanced using different experimental conditions for the measurements. As expected, when switching to a scattering background, a significant increase in η_{opt} is observed (5-6 % for all samples, **Table 5.6**). The lower values measured for **TU-CPE-08** compared to the corresponding di-ureasil at the same CPE concentration, are consistent with its lower Φ_{PL}.

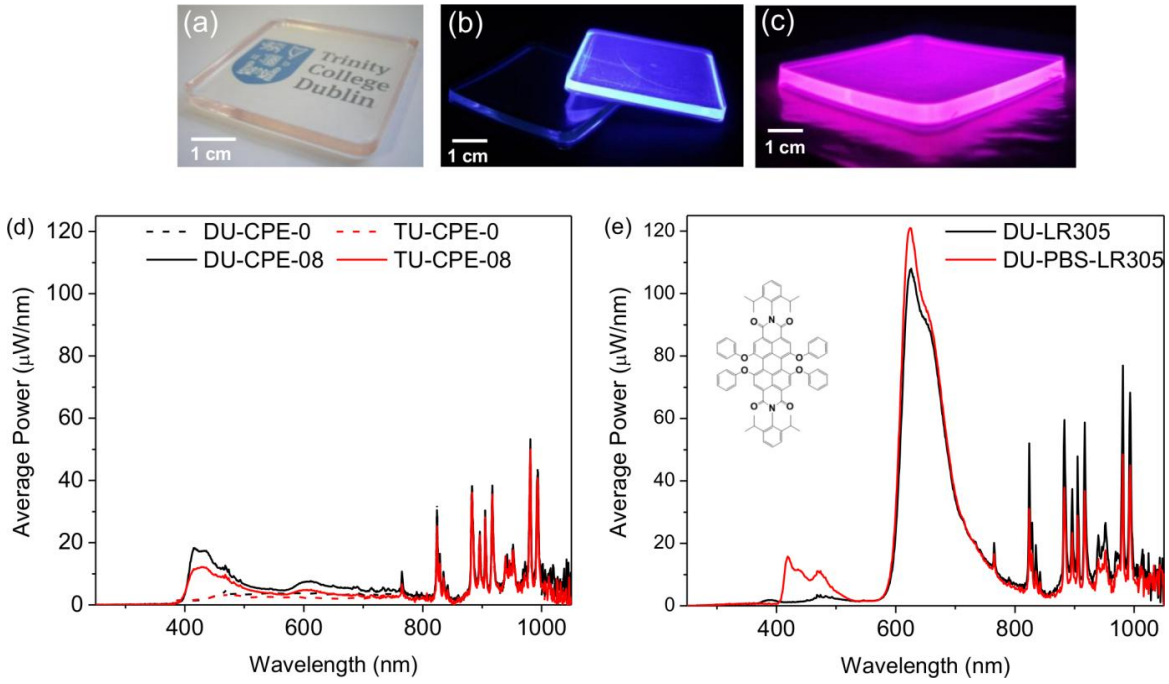

Fig. 5.11. Evaluation of the performance of **PBS-PFP-PDI**-ureasils as luminescent solar concentrators. Photographs of (a) **TU-CPE-08** in daylight, (b) **DU-CPE-0** and **DU-CPE-08** under UV irradiation (λ_{ex} = 365 nm), and (c) **DU-PBS-LR305** under UV irradiation (λ_{ex} = 365 nm). (d) Optical power spectra of **DU-CPE-0**, **DU-CPE-08**, **TU-CPE-0** and **TU-CPE-08** with a dark absorbing background. (e) Optical power spectra of **DU-LR305** and **DU-PBS-LR305** with a dark absorbing background. The chemical structure of the red luminophore LR305 is shown in the inset.

Unfortunately, it is clear that to obtain higher efficiencies, it would be desirable to have a higher percentage of PDI units incorporated into the CPE chains. The current amount of the perylene dye (1-2%) inhibits efficient energy transfer from the **PBS-PFP** units and/or the ureasil even if their good spectral overlap would suggest differently. Moreover, as observed earlier, direct excitation of the PDI units does not result in any emission in the red portion of the spectra. Ideally, being able to yield higher PDI to **PBS-PFP** ratios in the CPE, would improve the performance of our LSC.

Table 5.6. Comparison of the optical efficiency of **DU-CPE-0**, **TU-CPE-0**, **DU-CPE-08**, **TU-CPE-08**, **DU-PBS-LR305** and **DU-LR305** with an absorbing (black) and a scattering (white) background.

	Absorbing Background		Scattering Background	
Sample name	Single Edge Output (mW)	Total Optical Efficiency (%)	Single Edge Output (mW)	Total Optical Efficiency (%)
DU-CPE-0	3.5	1.6 ± 0.1	14.6	6.6 ± 0.9
TU-CPE-0	2.9	1.3 ± 0.3	12.3	5.6 ± 0.6
DU-CPE-08	5.3	2.4 ± 0.4	12.5	5.6 ± 0.5
TU-CPE-08	3.9	1.8 ± 0.1	12.2	5.5 ± 0.7
DU-PBS-LR305	13.7	6.2 ± 0.3	29.1	13.1 ± 0.5
DU-LR305	13.5	6.1 ± 0.6	36.9	16.7 ± 0.6

Due to synthetic restraints this is not possible. However, in an effort to mimic this effect and simulate a potential system which could yield better efficiencies, a model system was created by mixing the **PBS-PFP** polymer with Lumogen F Red 305 (LR305) in solution. The concentration of PDI in such system was designed to be ten times higher than that contained in **PBS-PFP-PDI**. The resulting lumophore was embedded into a di-ureasil waveguide at the same concentration used for **DU-CPE-08** and the efficiency of the final sample (**DU-PBS-LR305**) was measured. Moreover, a reference sample containing only LR305 was also prepared (**DU-LR305**). As expected, incorporation of a higher ratio of the PDI component leads to a significant increase in the optical efficiency of the LSC (from 2.4 ± 0.4% to 6.2 ± 0.3% with an absorbing background and to 13.1 ± 0.5% with a scattering background).

5.4 Conclusions

In this chapter, a CPE lumophore was embedded into two different types of ureasil waveguides, one prepared using a linear Jeffamine and one based on a tripodal Jeffamine, and the performances of the final samples as LSC were investigated. Firstly, the optical properties of the different series of ureasils were assessed by means of steady-state photoluminescence measurements, which revealed that compared to the lumophore dissolved in solution, incorporation into the ureasil networks enables the detection of the emission arising from the PDI units, due to a

reduction in the non-radiative pathways accessible to relax the excited states of the perylene in solution. Interestingly, the structure of the ureasil matrix influences this process, with the emission of the perylene moieties being more prominent for the CPE-doped tri-ureasils compared to the corresponding di-ureasils at the same dopant concentration. Solid-state MAS-NMR spectroscopy and FTIR in the Amide I region, showed that the structure of the **TU-CPE-*x*** networks is more open and distorted than that of the corresponding **DU-CPE-*x*** samples, for any of the concentrations of CPE investigated. The rigid tri-ureasil structure seems to hinder vibrational relaxation of the excited states of the perylene. Moreover, further structural investigation performed by means of PXRD showed that the overall arrangement of each silica network is not affected by the incorporation of the CPE at any investigated concentration. The optical features of the samples are dominated by the poly(fluorene-*alt*-phenylene), with the ureasil contribution detected upon varying either the emission and excitation wavelength, causing a broadening of the red- and the blue-edge of the spectra. The solid-state Φ_{PL} for **DU-CPE-*x*** and **TU-CPE-*x*** reaches a maximum value of 50-60% for the highest investigated CPE concentration. This is a promising result as it is very close to that obtained for **PBS-PFP-PDI** in a good solvent (68%). Time-resolved photoluminescence studies showed that intimate mixing of the CPE chains in the ureasil network is achieved for higher fluorophore concentrations, enabling efficient energy transfer from the emission centres of the ureasil to the **PBS-PFP** unit. TCSPC spectroscopy revealed that in every sample the largest contribution to the emission is represented by a component at ~500-600 ns, which corresponds to emission from trap sites associated with the CPE.[17] This lifetime component is, on average, slightly longer for the **DU-CPE-*x*** series, which is consistent with its higher photoluminescence quantum yield.

As the aim of this work was to test these systems as LSCs, the two most promising samples (**DU-CPE-08** and **TU-CPE-08**) were reproduced in a large scale and their optical efficiency measured. Unfortunately, as suggested by the optical investigation, the **PBS-PFP** units act as energy trap sites, impeding any further energy transfer to the PDI units and resulting in limited optical efficiencies of the final systems. This is more likely to be due to the composition of the CPE system (PDI to PBS-PFP ratio), rather than to the nature of its components, whose electronic coupling was proved by means of density functional theory calculations.[18] To confirm this

suggestion, a LSC was prepared using a model system consisting of the **PBS-PFP** units doped with higher ratio LR305 which indeed showed improved efficiencies. Nonetheless, the work in this Chapter represents a valuable example of the potential that ureasils have to offer as active waveguide for LSCs. Using **PSB-PFP-PDI** as a lumophore, which effectively combines in the same polymeric chain the features of a poly(fluorene) and of a perylene chromophore, represented a great opportunity to merge in a single system the advantages observed in **Chapter 3** and **4**, of incorporating a fluorophore into a ureasil matrix. To some extent this was actually observed, the CPE chains are well-isolated into the silica network and the extent of this isolation is guided by the nature of the ureasil backbone which behaves as a donor towards the optically active species. However, the overall low amount of on-chain PDI moieties and the energy trap behaviour of the **PBS-PFP** block any possibility of further energy transfer cascades. The results suggest that ureasil-based organic-inorganic hybrid still has much to offer in applications for LSCs in diverse constructs. As such, these results open the route towards advances in the design of new CPE/ureasil LSC architectures, with the first step being increasing the amount of on-chain PDI acceptor units to achieve a better efficiency.

5.5 References

1. I. Meazzini, J. M. Behrendt, M. L. Turner and R. C. Evans, *Macromolecules*, 2017, **50**, 4235-4243.
2. I. Meazzini, N. Willis-Fox, C. Blayo, J. Arlt, S. Clement and R. C. Evans, *J. Mater. Chem. C*, 2016, **4**, 4049-4059.
3. B. McKenna and R. C. Evans, *Adv. Mater.*, 2017, **29**, 32942-32951.
4. B. S. Richards, *Sol. Energy Mater. Sol. Cells*, 2006, **90**, 2329-2337.
5. B. Ehrler, B. J. Walker, M. L. Böhm, M. W. B. Wilson, Y. Vaynzof, R. H. Friend and N. C. Greenham, *Nat. Commun.*, 2012, **3**, 1019.
6. P. J. Jadhav, P. R. Brown, N. Thompson, B. Wunsch, A. Mohanty, S. R. Yost, E. Hontz, T. Van Voorhis, M. G. Bawendi, V. Bulović and M. A. Baldo, *Adv. Mater.*, 2012, **24**, 6169-6174.
7. J. C. Goldschmidt and S. Fischer, *Adv. Opt. Mater.*, 2015, **3**, 510-535.
8. G. Katsagounos, E. Stathatos, N. B. Arabatzis, A. D. Keramidas and P. Lianos, *J. Lumin.*, 2011, **131**, 1776-1781.
9. B. C. Rowan, L. R. Wilson and B. S. Richards, *IEEE J. Sel. Topics Quantum Electron.*, 2008, **14**, 1312-1322.
10. J. Mei, N. L. C. Leung, R. T. K. Kwok, J. W. Y. Lam and B. Z. Tang, *Chem. Rev.*, 2015, **115**, 11718-11940.
11. J. L. Banal, J. M. White, T. W. Lam, A. W. Blakers, K. P. Ghiggino and W. W. H. Wong, *Adv. Energ. Mater.*, 2015, **5**, 1-7.
12. M. G. Debije and P. P. C. Verbunt, *Adv. Energ. Mater.*, 2012, **2**, 12-35.
13. J. L. Banal, K. P. Ghiggino and W. W. H. Wong, *PCCP*, 2014, **16**, 25358-25363.
14. M. J. Currie, J. K. Mapel, T. D. Heidel, S. Goffri and M. A. Baldo, *Science*, 2008, **321**, 226-228.

15. T. Forster, *Disc. Faraday Soc.*, 1959, **27**, 7-17.
16. C. L. Mulder, L. Theogarajan, M. Currie, J. K. Mapel, M. A. Baldo, M. Vaughn, P. Willard, B. D. Bruce, M. W. Moss, C. E. McLain and J. P. Morseman, *Adv. Mater.*, 2009, **21**, 3181-3185.
17. N. Willis-Fox, A.-T. Marques, J. Arlt, U. Scherf, L. D. Carlos, H. D. Burrows and R. C. Evans, *Chem. Sci.*, 2015, **6**, 7227-7237.
18. A. T. Marques, H. D. Burrows, J. S. Seixas de Melo, A. J. M. Valente, L. L. G. Justino, U. Scherf, E. Fron, S. Rocha, J. Hofkens, E. W. Snedden and A. P. Monkman, *J. Phys. Chem. B*, 2012, **116**, 7548-7559.
19. H. D. Burrows, V. M. M. Lobo, J. Pina, M. L. Ramos, J. Seixas de Melo, A. J. M. Valente, M. J. Tapia, S. Pradhan and U. Scherf, *Macromolecules*, 2004, **37**, 7425-7427.
20. P. P. Nefedov, M. A. Lazareva, B. G. Belenkii, S. Y. Frenkel and M. M. Koton, *J. Chromatogr. A*, 1979, **170**, 11-24.
21. C. J. Brinker and G. W. Scherer, *Sol-gel science: the physics and chemistry of sol-gel processing*, Academic press, 2013, p. 386.
22. R. C. Evans, *J. Mater. Chem. C*, 2013, **1**, 4190-4200.
23. A. Albini, *Photochemistry*, 2011.
24. L. D. Carlos, V. de Zea Bermudez, R. A. Sá Ferreira, L. Marques and M. Assunção, *Chem. Mater.*, 1999, **11**, 581-588.
25. L. D. Carlos, R. A. Sá Ferreira, R. N. Pereira, M. Assunção and V. de Zea Bermudez, *J. Phys. Chem. B*, 2004, **108**, 14924-14932.
26. M. C. Gonçalves, V. de Zea Bermudez, R. A. Sá Ferreira, L. D. Carlos, D. Ostrovskii and J. Rocha, *Chem. Mater.*, 2004, **16**, 2530-2543.
27. V. T. Freitas, P. P. Lima, V. de Zea Bermudez, R. A. S. Ferreira and L. D. Carlos, *Eur. J. Inorg. Chem.*, 2012, **2012**, 5390-5395.
28. J. C. de Mello, H. F. Wittmann and R. H. Friend, *Adv. Mater.*, 1997, **9**, 230-232.
29. T.-S. Ahn, R. O. Al-Kaysi, A. M. Müller, K. M. Wentz and C. J. Bardeen, *Rev. Sci. Instrum.*, 2007, **78**, 086105.
30. V. de Zea Bermudez, L. D. Carlos and L. Alcácer, *Chem. Mater.*, 1999, **11**, 569-580.
31. L. Fu, R. A. Sá Ferreira, M. Fernandes, S. C. Nunes, V. de Zea Bermudez, G. Hungerford, J. Rocha and L. D. Carlos, *Opt. Mater.*, 2008, **30**, 1058-1064.
32. P. P. Lima, R. A. S. Ferreira, S. A. Júnior, O. L. Malta and L. D. Carlos, *J. Photoch. Photobio. A*, 2009, **201**, 214-221.
33. K. Dahmouche, L. D. Carlos, V. de Zea Bermudez, R. A. Sa Ferreira, C. V. Santilli and A. F. Craievich, *J. Mater. Chem.*, 2001, **11**, 3249-3257.
34. A. Kaniyoor, B. McKenna, S. Comby and R. C. Evans, *Adv. Opt. Mater.*, 2016, **4**, 444-456.
35. E. Fron, A. Deres, S. Rocha, G. Zhou, K. Müllen, F. C. De Schryver, M. Sliwa, H. Uji-i, J. Hofkens and T. Vosch, *J. Phys. Chem. B*, 2010, **114**, 1277-1286.
36. F. B. Dias, A. L. Maçanita, J. S. d. Melo, H. D. Burrows, R. Güntner, U. Scherf and A. P. Monkman, *J. Chem. Phys*, 2003, **118**, 7119-7126.
37. H. A. A. Attar and A. P. Monkman, *Adv. Funct. Mater.*, 2008, **18**, 2498-2509.
38. M. Monteserín, H. D. Burrows, A. J. M. Valente, V. M. M. Lobo, R. Mallavia, M. J. Tapia, I. X. García-Zubiri, R. E. Di Paolo and A. L. Maçanita, *J. Phys. Chem. B*, 2007, **111**, 13560-13569.
39. S. Tsoi, D. J. Broer, C. W. M. Bastiaansen and M. G. Debije, *Adv. Energ. Mater.*, 2013, **3**, 337-341.

Chapter Six

Synthesis of Photoluminescent Organic-Inorganic Ureasil Nanoparticles for Imaging Applications

6.1 Introduction

In the previous Chapters, the use of ureasils as active solid-state hosts has been presented. Due to the favourable combination of the organic backbone provided by the Jeffamine, bound to a robust silica network, these materials are ideal systems for the incorporation of π–conjugated fluorophores such as dyes, CP and CPEs.[1-3] However, there are other interesting architectural possibilities that can be explored while working with organic-inorganic hybrids,[4] and they can be obtained by tuning the conditions in which the sol-gel process is performed (a detailed description of the sol-gel process can be found in **Chapter 1**). For ureasil monoliths, for example, acid-catalysed hydrolysis was performed at a pH close to the isoelectric point of the silica (~2) which corresponds to a slow reaction rate, leading to the elongation of the network backbone and the formation of extended aggregates.[5] In contrast, base-catalysed hydrolysis is a process characterised by a faster rate, leading to an early stage condensation between the chains, with the resulting hybrids characterised by shorter networks and obtained as small aggregates. [6]

Base-catalysed hydrolysis is the foundation of the widely popular Stöber method used for the preparation of silica NPs.[7] Since its first report, the application of this synthetic procedure has been extensively explored for the preparation of a variety of silica-based NPs, most of which consisting of the hydrolysis/condensation of TEOS, a cheap and versatile silica precursor.[8] However nowadays, the incredibly rich library of silanes, either commercially available or that can be synthesised, has pushed the direction of the preparation of silica NPs towards more complex and exotic designs.[9, 10] In this context, organic-inorganic silica NPs represent an interesting example of the combination of the advantageous properties of a silica network, such as superior mechanical and thermal stability, and those of an organic backbone, usually consisting of polymeric chains, which can encapsulate small molecules (dyes or drugs) or present interesting properties such as fluorescence.[11, 12] For example, Kohler *et al.* optimised the synthesis of an amine-terminal PEG silane, presenting the ability to self-assemble onto the surface of metal oxide NPs.[13] The terminal silane units in the polymeric chains, were able to coordinate with the –OH moieties on the surface of the NPs while imparting improved stability to the polymeric layer surrounding the NPs. Moreover, the $–NH_2$ moieties present on the other side of the PEG chains, improved the solubility of the overall system in aqueous media, while being an easy head group to manipulate for a further

functionalisation; in this instance with folic acid, a targeting agent whose corresponding receptors are over expressed on several types of cancer cells.[13] A similar synthetic strategy can be used for the preparation of silica-based NPs covalently bound to functional polymeric chains, which are, for example, light-emissive.[14, 15]

Recently, Behrendt *et al.*[16] reported a novel strategy for the synthesis of hybrid organic-inorganic NPs, consisting of PF chains functionalised on their branches with ICPTES. These NPs were formed through nanoprecipitation of the PF derivative into a basic aqueous solution in the presence of tetramethylorthosilicate (TMOS). These conditions triggered the hydrolysis and condensation of the silica precursors, leading to the formation of NPs consisting of covalently-linked organosilica matrices, whose sizes and optical properties were controlled by the amount of TMOS added. Silica-based organic-inorganic NPs have also been made using biologically-relevant molecules such has peptides.[17] Ciccione *et al*.[18] designed a family of triethoxysilane-functionalised peptides which were reacted on the surface of fluorescent silica NPs, made of fluorescein isothiocyanate units grafted to (3-aminopropyl)triethoxysilane (APTES). The organic-inorganic hybrid NPs constituting the core of the system were synthesised using a water/oil microemulsion made of water, Triton-X, cyclohexane and ammonia to which the siloxane-grafted dye and TEOS were added. The ICPTES-grafted peptide groups were reacted by simple addition to the NPs solution in an acidic medium yielding fluorescent NPs of ~80 nm diameter and good polydispersity index (PdI ~ 0.12), with important implications for application of these systems as therapeutic or diagnostic tools.

Inspired by these examples, a novel strategy for the formation of ureasil-based organic-inorganic core-shell NPs will be presented in this Chapter, following a procedure that combines nanoprecipitation[19, 20] and the Stöber method.[7] Attention will be paid to the optimisation of the synthetic procedure to allow the preparation of NPs with enhanced colloidal stability, while remaining in the same size range. Although ureasils are photoluminescent in the solid-state,[21] their low Φ_{PL} in solution necessitates the doping of these NPs with a fluorophore if they are to be utilised for fluorescence imaging. The incorporation process needs to be efficient and to preserve the photophysical properties of the fluorophore, while maintaining the colloidal stability of the NPs.

6.1.1 Aims

The aim of this Chapter is to develop a robust method for the preparation of a new class of organic-inorganic core-shell hybrid ureasil NPs consisting of a ureasil core coated with a silica shell and to investigate the possibility of incorporation of dyes either in the core or onto the shell. In the first part of this work, the synthesis of the NPs will be optimised, with particular attention to: (i) the concentration of the base catalyst, (ii) the concentration of the TEOS and (iii) the rate of addition of the TEOS, which will be varied while monitoring their effect on the diameter and PdI of the NPs. Once the synthetic strategy is optimised, two different incorporation methods for organic dyes will be investigated: (i) a non-covalent approach, where the organic dyes (pyrene and coumarin 153) are encapsulated in the NPs through hydrophobic interactions and (ii) a covalent approach, where the dye (fluorescein isothiocyanate) is covalently grafted to the siliceous domains of the NP (**Fig. 6.1**).

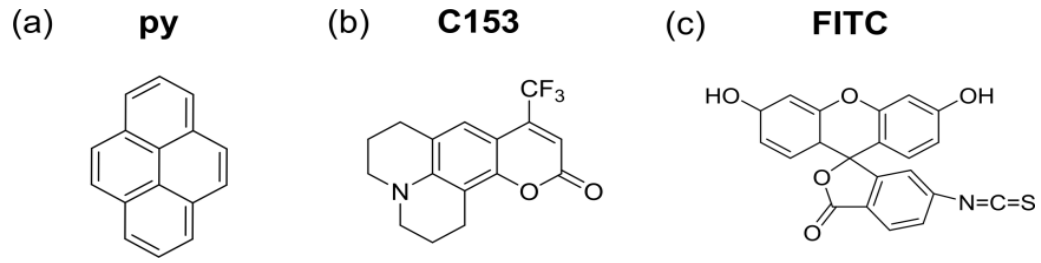

Figure 6.1. Selected dyes for incorporation into ureasil core-shell NPs: (a) pyrene (**py**), (b) coumarin 153 (**C153**), (c) fluorescein isothiocyanate (**FITC**).

6.2 Experimental

6.2.1 Reagents and Materials

O,O'-bis(2-aminopropyl)polypropylene glycol–*block*–polyethylene glycol-*block*–polypropylene glycol (Jeffamine ED-600), 3-(triethoxysilyl)propyl isocyanate (ICPTES, 95%), tetraethylorthosilicate (TEOS, ≥ 99%), (3-aminopropyl)triethoxysilane (APTES, 99%), ammonium hydroxide (NH_4OH, 5.01 N solution) and the fluorescent dyes: **py**, **FITC** and **C153** were all purchased from Sigma-Aldrich or Fluka and used as received. All solvents were obtained from Sigma-Aldrich or Fischer Scientific and used without further purification. Water was filtered three times through a 0.25 μm nylon filter before use. The dialyses were performed using snake skin pleated dialysis tubing from Thermoscientific with a M_w cut-off of 3,500 Da. The d-UPTES

solution was injected using a 2 mL BRAUN disposable syringe with a BRAUN Sterican needle (diameter 0.45 mm and length 25 mm) into a soda glass tube (diameter 25 mm and length 75 mm). For DLS measurements, 100 μL of the solution of NPs were dissolved in 900 μL of triple filtered water in an acrylic cuvette (Sarstedt, 10 mm pathlength). ζ-potential measurements were performed in disposable capillary cells (DTS1070) purchased from Malvern Instruments.

6.2.2 Synthesis of the Ureasil Core-Shell NPs

6.2.2.1 Synthesis of the di-Ureapropyltriethoxysilane (d-UPTES) Hybrid Precursor

The organic-inorganic hybrid precursor (d-UPTES) was synthesised in quantitative yield by reacting the terminal amine functionalities of Jeffamine ED-600 with the isocyanate group of an alkoxysilane precursor as reported in detail elsewhere (**Fig. 6.2**a).[22, 23] In brief, ICPTES (0.91 mL, 3.7 mmol) was mixed with Jeffamine ED-600 (1 mL, 1.8 mmol) in THF (5 mL) and reacted for 24 h at room temperature. Reaction completion was confirmed by recording the FTIR spectra over the 4000-650 cm^{-1} range. The presence of the broad N-H stretch (~ 3400-3600 cm^{-1}) and C=O stretch (1610-1770 cm^{-1}) IR signals and the concomitant disappearance of the isocyanate N=C=O stretch at 2265 cm^{-1} are both indicative of urea linkages and thus, formation of the d-UPTES (**Fig. A6.1**).[24]

6.2.2.2. Method A

For Method A, the first batch of NPs was prepared by diluting 54.8 μL (0.03 mmol) of the d-UPTES precursor stock (0.56 mol dm^{-3}) in THF (671.2 μL) in an Eppendorf. Then, a solution consisting of TEOS (12.0 μL, 0.05 mmol) and THF (12.0 μL, 0.01 mmol) was added to the mixture. The content of the Eppendorf was syringe-sprayed into a glass sample tube containing 2.988 mL of water and 12 μL of NH_4OH (0.06 mmol). The removal of the THF was subsequently performed using a rotary evaporator at RT for 10 minutes.

6.2.2.3 Method B

The initial synthesis of NPs prepared using Method B consisted of mixing the d-UPTES precursor stock (54.8 μL, 0.03 mmol) in THF (671.2 μL) in an Eppendorf. The content of the Eppendorf was syringe-sprayed into a glass sample tube containing 3.0 mL of a solution of water and 12 μL of NH_4OH (0.06 mmoles). 120 μL of a solution of TEOS in THF ($5\%_{v/v}$, 0.03 mmol)

was then added dropwise to the mixture under stirring. This concentration was chosen upon investigation of different samples, prepared by varying the concentration of the stock solution of TEOS (in THF) from 0 to 20%$_{v/v}$. The THF was removed 20 minutes after spray-injection of the d-UPTES, using a rotary evaporator at RT for 10 min. Optimisation of the base concentration for NH_4OH was performed by varying the volume of NH_4OH (5.01 mol dm^{-3}) added to the water to yield 3.0 mL of either a 10, 20, 60 or 120 mM solution, respectively.

6.2.2.4 Method C

For the NPs prepared with Method C, 54.8 μL (0.03 mmol) of the d-UPTES precursor stock (0.56 mol dm^{-3}) were added to THF (671.2 μL) in an Eppendorf and syringe-injected into a glass sample tube containing 3.0 mL of NH_4OH (0.03 mmol) in water. TEOS in THF (5%$_{v/v}$, 0.03 mmol) was then added dropwise in two steps (60 μL each) to the mixture under stirring. This rate of addition was chosen upon the testing of two different rates as described below.

6.2.2.5 Preparation of Dye-Doped NPs

Py-doped NPs were prepared using the same quantities and concentrations of d-UPTES, TEOS and NH_4OH used in Method C. 24.6 μL of the dye stock solution (7.38×10^{-5} mmol, in THF) were added to the d-UPTES/THF mixture before being spray-injected into the water and ammonia solution. The volume of THF used to dilute the d-UPTES stock solution was adjusted from 671.2 μL to 646.6 μL in order to match the same overall d-UPTES concentration used for the undoped particles.

For **C153**-doped NPs a stock solution of **C153** (36.0 μL, 3×10^{-3} mol L^{-1}, in THF) was mixed with the d-UPTES precursor and the volume of added THF adjusted to obtain the same d-UPTES concentration used in optimised Method C. The overall synthesis was continued using the procedure described for Method C.

For the preparation of the **FITC**-doped NPs, **FITC** (0.0135 mmol) was pre-reacted with APTES (0.405 mmol) in 1 mL of EtOH at RT, in the dark and under an N_2 atmosphere for 24 hours. Although the reaction between the two species occurs in a 1:1 molar ratio, an excess of APTES to **FITC** (30:1 molar ratio) was used to ensure that the silica precursor is grafted to all the dye molecules. The reaction mixture was centrifuged (7 min, 10,000 rpm) and the supernatant

collected. The synthesis of the NPs was performed using the same quantities and conditions described in Method C until. During the second addition of TEOS, an aliquot of the supernatant (either 3, 6 or 15 μL) was co-added with the TEOS into the reaction mixture. The same aliquot was subtracted by the volume of TEOS added (*e.g.* 3 μL of supernatant + 57 μL of TEOS) in order to keep the volume of added solvent constant. The THF and EtOH were then removed with a rotary evaporator (10 min, RT).

6.2.3 Time-Resolved Spectroscopy Measurements

The fluorescence lifetime measurements presented in this Chapter, were performed by Dr. Steve Comby using a Horiba Jobin Yvon Fluorolog FL 3-22 spectrometer equipped with a FluoroHub v2.0 single photon controller using the time-correlated single photon counting method. The sample solutions were excited at 458 nm with a pulsed nanosecond light-emitting diode (NanoLED®). The time distribution of the lamp pulse (< 1.3 ns) was recorded prior to lifetime measurements in a separate experiment using a scattering solution (Ludox, Sigma Aldrich) and the decays were analysed using the IBH DAS6 software.

6.3 Results and Discussion

6.3.1 Design Strategy Used to Obtain Ureasil Core-Shell NPs

Fig. 6.2 presents the synthetic strategy followed to obtain ureasil core-shell NPs. Firstly, the d-UPTES precursor is synthesised from Jeffamine ED-600 and ICPTES in THF (good solvent) as described in the previous chapters (**Fig. 6.2**a). An aliquot of the d-UPTES precursor is then sprayed onto the surface of a solution of a bad solvent (water) and base, to yield the core of the NP (**Fig. 6.2**b, step [1]). Due to their higher hydrophilicity, the ethoxysilane moieties attached at the extremities of the d-UPTES chains are expected to be exposed on the surface of the more hydrophobic core.

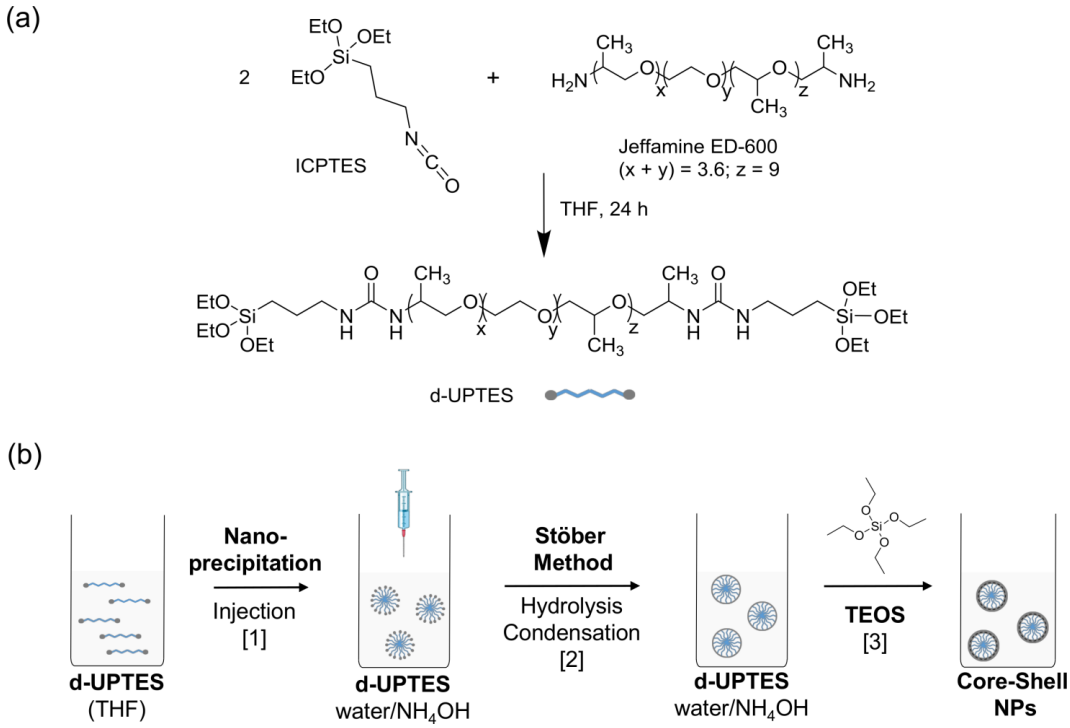

Figure 6.2. Description of the synthetic route to ureasil core-shell NPs. (a) Reaction scheme for the synthesis of the d-UPTES precursor and (b) schematic representation of the synthetic steps used to obtain ureasil NPs.

The presence of the base catalyst (ammonium hydroxide) in the solution is used to trigger the hydrolysis-condensation reaction of the surface siloxane groups (**Fig. 6.2**b, step [2]), and results in subsequent formation of a silica shell during the nanoprecipitation process, yielding hybrid core-shell nanoparticles *via* a rapid, one-pot procedure. TEOS is subsequently added to control the size of the NP shells and to eventually improve the stability in solution (**Fig. 6.2**b, step [3]).[25] The final nanocomposite system consists of an organic-inorganic core made of ureasil, surrounded by an inorganic silica shell.

6.3.2 Optimisation of the Synthetic Procedure for Ureasil Core-Shell NPs

As mentioned in the aims, a large portion of the work carried out in this Chapter is dedicated to the optimisation of the synthetic parameters to develop a reproducible method for the preparation of ureasil-based core-shell NPs. To be used as imaging agents for biological matrices, the diameter of the NPs should typically be smaller than 250 nm;[26] however the NP cores should be large enough to host small organic dye molecules. Size, however, is not the only parameter responsible for the uptake of NPs into cells or to avoid their aggregation into biologically relevant media. The surface charge of the NPs plays on equally important role in these processes.[27]

Considering our synthetic route and conditions, the surface of the ureasil NPs will consist of negatively-charged -(SiO^-) silica moieties. However, the literature does not present a unanimous answer for the optimum size/charge combination required to obtain stable NPs, as this is largely dependent on the specific application of the final system. Lu *et al.* for example, investigated the uptake capability of a series of NPs consisting of fluorescein molecules grafted to the surface of TEOS cores with sizes ranging from 30 to 280 nm and monitored the efficiency of their uptake on cultures of human cervical cancer cells (HeLa).[28] Using confocal lasing scanning microscopy, they observed that the highest cellular uptake occurred for NPs of 50 nm size.[28, 29] On the other hand, the use of larger NPs facilitated the delivery of macromolecules. In a more recent study, Kim *et al*. prepared large mesoporous silica NPs by hydrolysis and condensation of a solution of TEOS in the presence of a templating agent (Pluronic P104).[30] Once the NPs were prepared, the templating agent was removed and the NP surface was covered with a thin layer of cross-linked poly(methacrylic acid), yielding positively-charged NPs with a diameter ranging from 500 to 600 nm and pores of ~12 nm. The NPs were then loaded with fluorescein-grafted dextran molecules, which are typically membrane impermeable, and the final system was used for the controlled release of the macromolecules into the membrane of HeLa cells which was monitored with confocal microscopy. Despite their large size, the NPs maintained their stability throughout the process and functioned as trans-membrane carriers inside of living cells.[30] Moreover, the size of the silica NPs is also directly related to their cytotoxicity.[31] These are just two of the many examples of dye-loaded silica-based NPs that can be found in literature. As it is hard to predict the size of the ureasil core, in the first instance the concentration of TEOS will be used to manipulate the diameter of the NPs, which will be aimed between 50-200 nm.

Our design strategy to obtain ureasil core-shell NPs consists of a modification of the Stöber method, which allows for good control over the size and the possibility of working in an aqueous medium, without the need for surfactant.[7] However, there are a number of synthetic parameters and steps which must be considered and controlled to yield stable and useful core-shell NPs. Transferring the d-UPTES from a good solvent such THF to water (a bad solvent) should drive the aggregation of the precursor into nuclei due to hydrophobic effect (nanoprecipitation), from which the NPs can grow.[32] The ammonium hydroxide present in the aqueous medium acts as a catalyst

for the hydrolysis and condensation process of the ethoxysilane moieties at the extremities of the d-UPTES chains. Considering the chemical structure of d-UPTES, it is expected that the nuclei of the NPs would be formed by the poly(ether) chains, with the ethoxysilane extremities exposed to the surface of the NPs. Under these conditions, the additional TEOS is expected to co-condense with the exposed ethoxysilane groups and reinforce the silica shell. However, it cannot be excluded that some of the ICPTES units could be on the inside of the NPs, rather than only on their surface. Moreover, it is possible that a second population of pure silica NPs form. The ureasil NPs are expected to be stabilised by the presence of silanol units on the surface, which will be negatively charged upon partial dissociation of the –OH moieties in the basic water solution and therefore repel each other. The final step of the process consists of the removal of THF. Its presence in solution could enhance the possibility of Ostwald ripening, due to the tendency of the smaller particles to re-dissolve in the THF pools and subsequently re-deposit onto the surface of the larger ones.[33] This process leads to an overall increase in the size of the NPs.[34-36] The overall evolution of the synthetic method adopted to prepare the NPs is summarised in **Fig. 6.3**; each method will be described in detail in **Sections 6.3.2.1-3**.

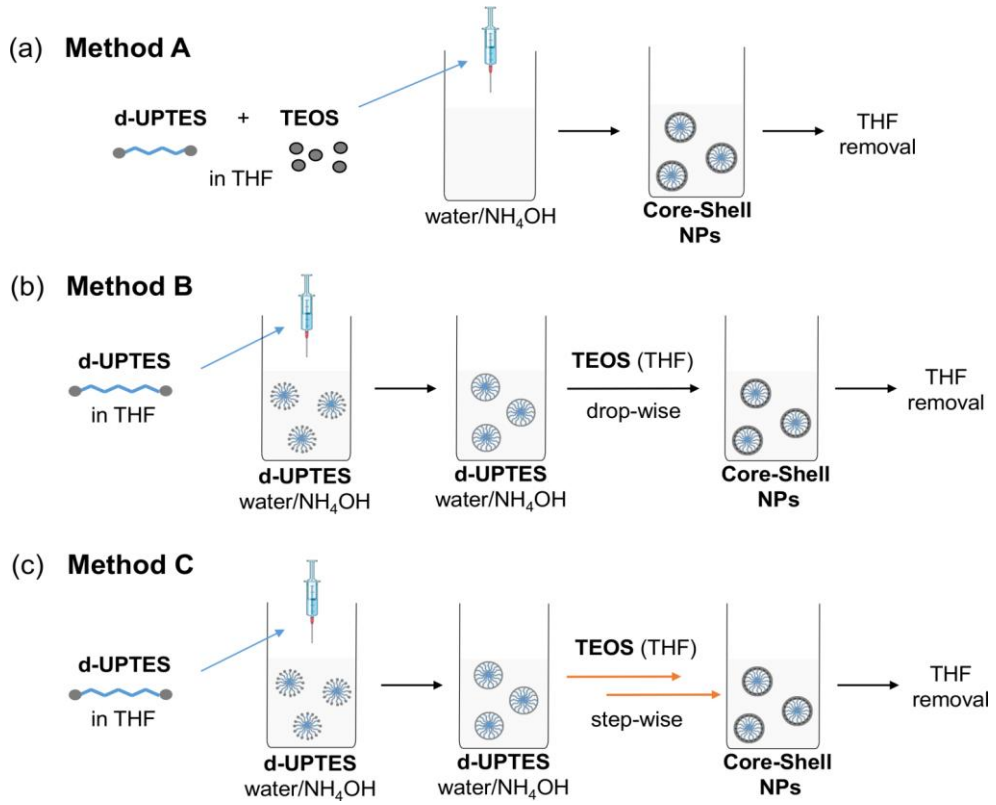

Figure 6.3. Evolution of the synthetic method adopted for the preparation of ureasil core-shell NPs. Schematic representation of (a) Method A, (b) Method B and (c) Method C.

6.3.2.1 Method A: Effect of Good Solvent Removal and co-Mixing d-UPTES/TEOS

As illustrated in **Fig. 6.3**a, the initial synthetic approach adopted for the preparation of the NPs (Method A) consisted of a two-step process: (i) spraying of a mixture containing the d-UPTES stock, TEOS and THF onto the surface of a solution containing triple-filtrated water and NH_4OH and (ii) removing of the THF using a rotary evaporator. Although this synthetic procedure may seem very straightforward, it involves a considerable number of variables that require optimisation. For Method A, the d-UPTES precursor and TEOS are mixed and added to the poor solvent at the same time (**Fig. 6.3**a). In an effort to create a robust procedure and to allow a consistent investigation of the effect of each one of these parameters, the initial concentration of d-UPTES (20,000 ppm), volume of water (3.0 mL), base (12 μL, 0.06 mmol) and TEOS (24.0 μL, 0.05 mmol, 50%$_{v/v}$ in THF) concentrations were arbitrarily decided and kept constant. As shown in **Fig. 6.4**, the NPs obtained using Method A present an average hydrodynamic diameter (D_h) ranging between 122-164 nm and a polydispersity (PdI) of 0.11. Moreover, the synthesis is reproducible, yielding every time NPs with similar features.

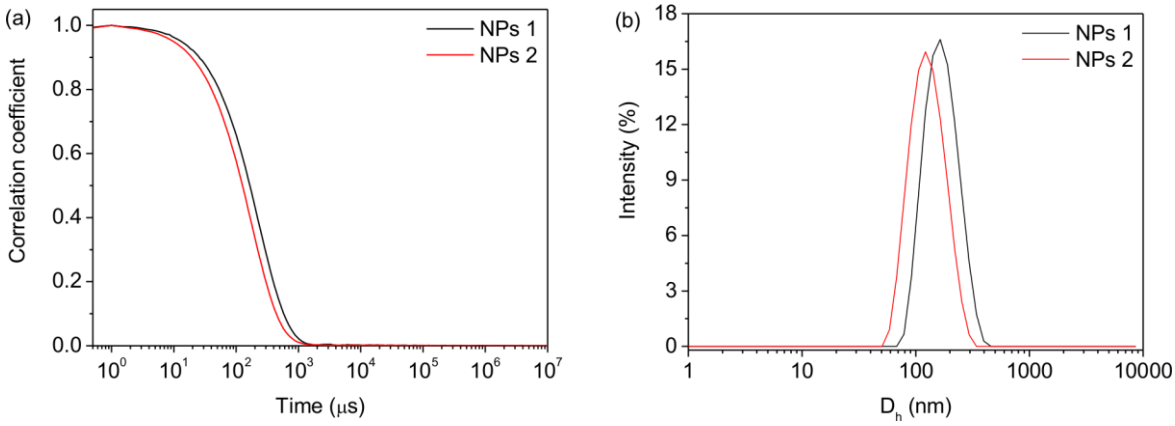

Figure 6.4. Comparison of the reproducibility of ureasil core-shell NPs obtained using Method A. (a) Correlation function and (b) size distribution of two batches of NPs (1, red line and 2, black line) prepared on different days using Method A.

As mentioned above, removal of the "good solvent" upon preparation of the NPs following the Stöber method is a common practise to improve the stability of the final system. For example, Liu *et al.*[37] investigated the effect of the solubility of β-carotene on the rate of the Ostwald ripening in water/THF mixtures.[34, 36] The ratio of the solvent was changed between 1:4 to 1:20 (*v:v*, THF:water), corresponding to a reduction in the solubility of β-carotene in the solvent mixture and

leading to 10-time decrease in the rate of particle growth. It is therefore important to consider the effect of the THF removal on the NP stability. With this aim, three sets of samples were prepared following the aforementioned Method A and their stability was monitored upon evaporation at different times of the THF after the spray-injection of the d-UPTES precursor. The D_h and PdI of the NPs upon evaporation of THF at different times are presented in **Table 6.1**. When the THF is evaporated after 20 minutes, the average diameter of the NPs is 127 nm, with PdI values ranging from 0.13 to 0.15. A general increase in both the average size (D_h = 173 nm) and PdI (0.20) of the NPs is observed when the evaporation is delayed to 3 hours after syringe-spraying. Upon removal of the THF after 10 hours, the size of the NPs is similar to those measured initially (D_h = 121.3 nm), while an increase of the PdI to 0.22 is observed. Although these results meet the target requirements for the NPs (PdI $\leq$ 0.2 and D_h = 50-200 nm), the best results are obtained upon evaporation of the THF after 20 minutes, which is selected as part of the protocol for the optimised synthetic method.

Table 6.1. Hydrodynamic diameter (D_h) and polydispersity (PdI) of ureasil core-shell NPs prepared with Method A upon evaporation of THF at different times after spray-injection. Samples prepared in triplicate from the same d-UPTES precursor batch at room temperature.

Time	**D_h (nm)**	**PdI**
20 minutes	129	0.15
	126	0.15
	125	0.13
3 hours	175	0.23
	173	0.19
	169	0.17
10 hours	124	0.23
	120	0.24
	120	0.19

However, despite the promising results for the size and polydispersity obtained for the NPs using Method A, their stability over time was extremely poor. It was noticed that upon storage of the NPs for 3-5 days at RT, the solution became opaque and showed occasionally a white precipitate. DLS measurements were performed on samples prepared following the optimised Method A over the course of 75 hours. The corresponding average D_h and PdI are shown in **Fig. 6.5**. The NPs seem to maintain their initial characteristics in the first 46 hours after the synthesis,

with a minor increase in the D_h from 149 to 153 nm and in the PdI from 0.08 to 0.11. However, a sharp increase in both parameters is observed at the beginning of the third day, reaching sizes of 177 nm and a PdI of 0.29 after 75 hours. This result clearly shows that upon ageing the NPs tend to aggregate. This is probably due to an insufficient stabilisation provided by the negatively-charged silica shell, indicating that co-injection of the d-UPTES and TEOS might not be the best approach to obtain core-shell NPs.

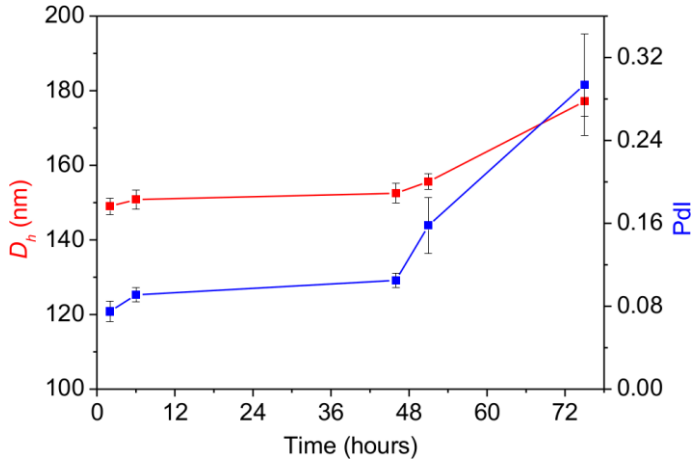

Figure 6.5. Investigation of the stability of ureasil core-shell NPs prepared using Method A as a function of time. The change in the hydrodynamic diameter (D_h) (red squares) and the PdI (blue squares) of 3 samples as a function of time are reported. The solid lines serve only to guide the eyes.

6.3.2.2 Method B: Stepwise Addition of TEOS and Effect of Concentration

Although Method A yielded ureasil NPs of the desired size and PdI, the lack of colloidal stability suggests that modifications to the synthetic procedure are necessary. It was initially hypothesised that co-addition of the d-UPTES precursor and TEOS could lead to self-compartmentalisation of the organic polyether chains to form the core, with the TEOS molecules spontaneously arranging themselves around it to form a shell. This synthetic approach is at the heart of strategies for the formation of dye-doped core-shell silica NPs.[38] However, while it might work efficiently for highly apolar species, the chains of the d-UPTES precursor also present ethoxysilane moieties, which have a higher polarity compared to the materials commonly used (*i.e.* aromatic systems). A method of encapsulation for organic-inorganic systems has previously been proposed by Ricka *et al.* in 1993 and is referred to as "heterogeneous nucleation".[39] In this case, the authors added a stock solution of siloxane-functionalised fluorescein into a water/base mixture containing tetramethoxysilane "seeds". The silica nuclei in solution functioned as seeds for the

reaction of the dye, which was grafted to the NP surface at the end of the synthesis. This method yielded monodispersed NPs with sizes < 100 nm, which could be tuned by addition of different amount of the silica seeds to the solution. A few years later, Weisner and co-workers revisited this synthetic approach using the dye molecules themselves as seeds.[40] Tetramethyl rhodamine isothiocyanate was reacted with APTES and dropped into a solution of water and ammonia. TEOS was then added dropwise to the dye "seeds" to yield core-shell NPs consisting of a mainly organic core and an inorganic shell. The addition of the TEOS in the second step allowed improved control over the formation of the silica shell and its thickness. This system is very similar to ours, an organic chain functionalised with terminal ethoxysilane units that needs to be encapsulated within a silica shell.

Inspired by these examples, the synthetic approach was modified and divided in two separate steps: first the d-UPTES precursor was sprayed into the water/base solution, then a solution of TEOS in THF was added dropwise into the mixture (Method B, **Fig. 6.3**b). The hydrophobic effect should promote the formation of the d-UPTES nuclei and the TEOS molecules should subsequently co-condense around the core to form a homogeneous shell. The NPs were prepared using different amounts of TEOS and their stability over time was investigated. Namely, the concentration of the stock solution of TEOS (in THF) was varied from 0 to 20%$_{v/v}$, while the overall added volume (120 μL) was kept constant. The PdI and D_h were monitored over the course of 4 days (**Fig**. **6.6**). As expected, the largest sizes and PdI were measured for the NPs prepared without TEOS (0 %), with both the D_h and PdI increasing during the first two days after preparation, from 133 nm to 245 nm and from 0.25 to 0.38, respectively, and then stabilising.

These trends suggest that the silica shell provided only by the d-UPTES is not sufficient to prevent the ageing of the NPs either through Ostwald ripening or aggregation. The sample prepared using the highest concentration of TEOS (20%) shows an initial diameter of 145 nm, which decreases to 129 nm after 1 day, and further increases to 170 nm from day 1 to day 4. Again, the PdI follows a similar trend, with a good initial value of 0.11 which increases to 0.36 after 4 days, which is due to the formation of a separate population of NPs consisting of only TEOS, as shown by the corresponding distribution graph (**Fig. A6.2**).

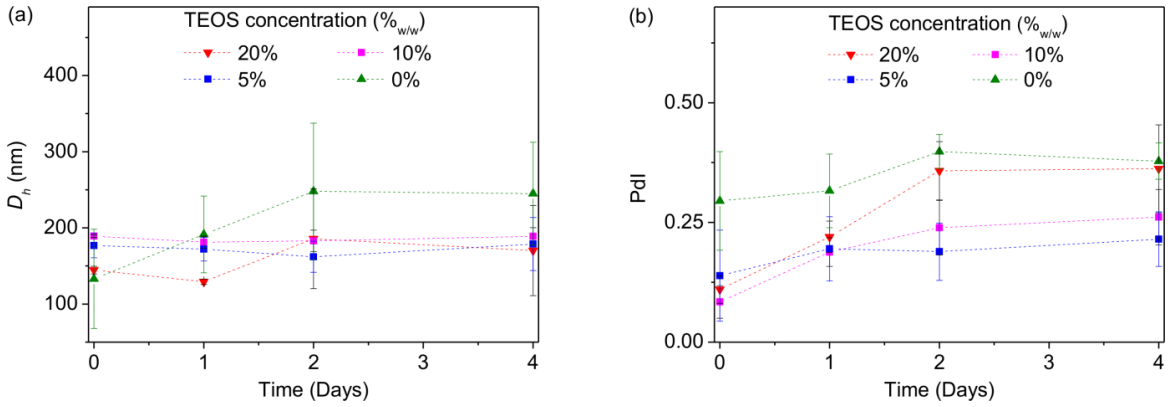

Figure 6.6. Stability studies of ureasil core-shell NPs prepared using Method B at different TEOS concentrations. Evolution of (a) hydrodynamic diameter (D_h) and (b) polydispersity (PdI) as a function of time. The dashed lines serve only to guide the eyes. Results are the average of the values obtained for three samples.

Finally, NPs prepared with a TEOS concentration of 5 and 10% $_{v/v}$ are stable with time, with an average D_h that never exceeds 190 nm. In both cases, the increase of the PdI, which was observed for all samples, is much less pronounced compared to that of the samples containing the highest amount of TEOS or no TEOS at all (**Fig. 6.6**b). The overall tangible increase in stability shown by these samples, confirmed the importance of the silica shell in preventing the ageing of the NPs. Considering the generally lower values of D_h and PdI, a concentration of TEOS equal to 5% $_{v/v}$ was chosen as the optimum value.

In an effort to further improve the colloidal stability, the concentration of NH_4OH used for the preparation of the NPs was also investigated. As previously explained, the stabilisation of the NPs occurs due to the electrostatic forces of repulsion between the negatively-charged NP surfaces. The charges are due to the de-protonated silanol groups ($-SiO^-$), whose pKa is 8.4.[41] Therefore working at pH values above 8.4, should ensure the stability of the NPs. As the concentration of NH_4OH used so far is 20 mM, a range of concentrations from 10 to 120 mM was subsequently investigated (**Fig. 6.7**) and the stability of the NPs monitored over the course of 10 days. As shown in **Fig. 6.7**, the initial size and PdI of the NPs does not seem to be significantly affected by the change in the base concentration. At t=0 days, the NPs present similar sizes, ranging from 120 to 140 nm and the corresponding PdI values do not exceed 0.19. These features seem to be maintained until the end of day 1, after which, a general increase in both the D_h and PdI is observed, followed by the stabilisation of both parameters from day 6 to day 10.

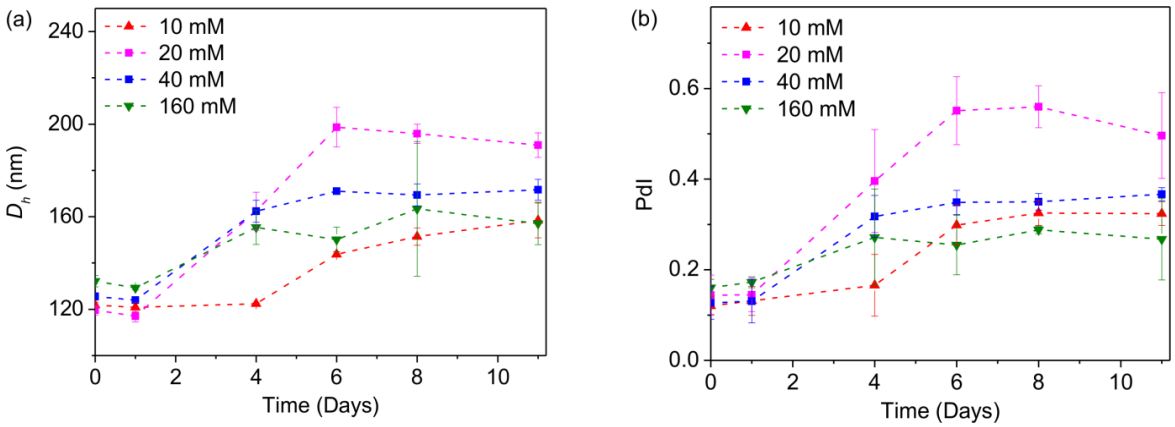

Figure 6.7. Stability studies of core-shell ureasil NPs prepared with Method B using different concentrations of NH_4OH. Evolution of (a) hydrodynamic diameter (D_h) and (b) polydispersity (PdI) as a function of time. The dashed lines serve only to guide the eyes. Results are the average of the values obtained for three samples.

Interestingly, the sizes for each sample are always < 200 nm, while the PdI values are far from optimum. Although it is hard to isolate an unambiguous trend between the concentration of ammonia and the stability of the NPs, it is clear that in these conditions, the lowest concentration of base (10 mM) is the one that gives the best results. Indeed, this parameter not only controls the surface charge of the NPs, but also the kinetics of the sol-gel reaction. An increase in the hydrolysis rate, could lead to the formation of isolated TEOS NPs, which effectively translates into a subtraction of –Si-O^- moieties from the surface of the ureasil NPs, leading to the overall destabilisation of the system, with aggregation phenomena observed two days after the preparation of the NPs. FTIR analysis of the d-UPTES batch used in these experiments confirmed the successful reaction between ICPTES and Jeffamine ED-600. Therefore, the colloidal stability issue observed for these samples is not due to the purity of the d-UPTES itself. Based on these results, the best size/PdI combination is obtained for the samples prepared from the lowest and the highest ammonia concentration (10 mM and 160 mM, respectively), which after 10 days yields NPs with an average diameter of ~160 nm and a PdI of ~0.3. Previous reports showed that an increase in the concentration of ammonia is usually correlated to an increase in the rate of both the hydrolysis and condensation reactions,[42] leading to an increase in the concentration of the intermediate semi-hydrolysed products of the reaction. When the system reaches the supersaturation limit, the consumption rate of the intermediate units through condensation reactions will also be very fast and this can lead to a decrease in the nucleation period,[43] yielding lower numbers of critical nuclei

in solution and larger particle sizes compared to those observed in the same systems with a lower catalyst concentration.[44] Based on this knowledge and the experimental data obtained, the base concentration was fixed at 10 mM for subsequent iterations of the synthetic procedure.

6.3.2.3 Method C: Effect of Rate of TEOS Addition

Despite optimisation of the number of synthetic steps and the quantities of TEOS and base involved in the preparation of the NPs, and the improvement observed from Method A to Method B, the colloidal stability of the system is still not sufficient. This is most likely to be due to a poor coverage of the TEOS shell on the d-UPTES cores. This can arise from the formation of pure TEOS NPs with similar sizes as targeted for the ureasil core-shell ones, which will aggregate either by ageing or Ostwald ripening. In order to create a homogeneous TEOS shell, while avoiding the formation of secondary nuclei upon addition of the reactant to the mixtures, a further modification to the synthetic process seems necessary. The formation of secondary TEOS nuclei is a common problem encountered when trying to prepare monodisperse silica NPs on an industrial scale. Good results have been obtained using the so-called "semi-batch" process, in which TEOS or some other silica precursor is added as a continuous stream into the reaction vessel containing the initial nuclei and the sol-gel process initiators,[45-47] and reacts progressively, allowing a better coverage and improved size control of the final NPs. This can be performed on a smaller scale (*i.e.* in a research laboratory) using a syringe pump. This process was simulated by dividing the addition of the TEOS into a series of steps (**Fig. 6.3**c) and allowing time between each addition. Two samples were prepared: the first with the TEOS solution ($5\%_{v/v}$, in THF) added as aliquots of 30 μL every 30 minutes and the second through addition of TEOS as two aliquots of 60 μL every 60 minutes. The stability of the resultant NPs was investigated for 50 days (**Fig. 6.8**). As shown in **Fig. 6.8**, the size and PdI of the NPs measured immediately after their preparation using Method C are very promising, with an average D_h of ~130-155 nm and PdIs below 0.15. Interestingly, these features are preserved for samples prepared upon addition of the TEOS solution in two steps of 60 μL every 60 minutes even 50 days after the synthesis.

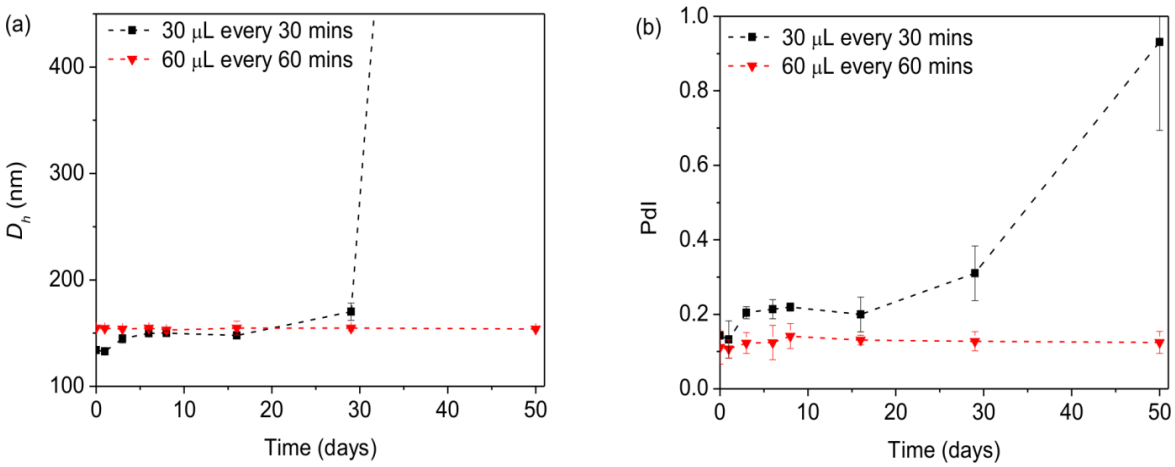

Figure 6.8. Stability studies of core-shell ureasil NPs prepared with Method C and different rates and volumes of TEOS addition. Evolution of (a) hydrodynamic diameter (D_h) and (b) polydispersity (PdI) as a function of time. The dashed lines serve only to guide the eyes. Results are the average of the values obtained for three samples.

Given the improved stability and the consistency of the values of both the average D_h and PdI over time, the synthetic procedure adopted for the preparation of this sample was considered as our optimised method. The ζ-potential of samples prepared using the optimised method was measured to be -51.3 ± 3.3 mV, which is indicative of good colloidal stability.[48] The NPs were imaged using AFM (**Fig. 6.9**). Interestingly, both the phase-contrast and the height-contrast AFM images show that the NPs are characterised by the expected core-shell structure. However, the diameter of the NPs imaged by AFM is ~240 nm, which is larger than that measured with DLS (usually less than 200 nm). This result is somewhat surprising considering that, smaller diameters are usually expected for AFM measurements compared to DLS, due to the absence of the solvent layer around the NPs. Although it can be argued that the observed diameter is still included in the size range measured with DLS (56-344 nm), none of the NPs imaged in the AFM seem to present a diameter that is comparable to the average D_h observed for this sample with DLS. This can be due to several reasons. Firstly, the preparation method of the sample; for AFM imaging of the NPs, the best images were obtained using a dilute solution of the NP stock (1:50 volume dilution in water). This leads to a decrease in the pH of the solution, which might affect the surface charge and thus the stability of the NPs.[49] Moreover, while AFM is a quick and relatively inexpensive imaging method, it can be affected by different artefacts when working with NPs. For example, as the sample dries upon deposition, the retreating liquid meniscus can cause the formation of NP

aggregates.[49] Klapetek *et al.* formulated a theoretical model for the investigation of the deviation of the measured and the real sizes of NPs imaged *via* AFM in non-ideal conditions (*i.e.* rough surfaces, aggregated NPs and different tip shapes).[50] The simulation revealed that a combination of non-ideal measuring conditions and human error can results in an inaccuracy of ± 7 nm for NPs with a true size of 30 nm. Contact with the substrate or with the tip can also cause deformation of the NPs.[51] AFM images performed on another sample prepared and measured in the same conditions, showed how the contact of the tip with the core of the NPs leads to a deflection of the NPs centre, while the shell is left intact (**Fig. A.6.3**). These NPs however still presented a diameter exceeding that measured by DLS (> 200 nm).

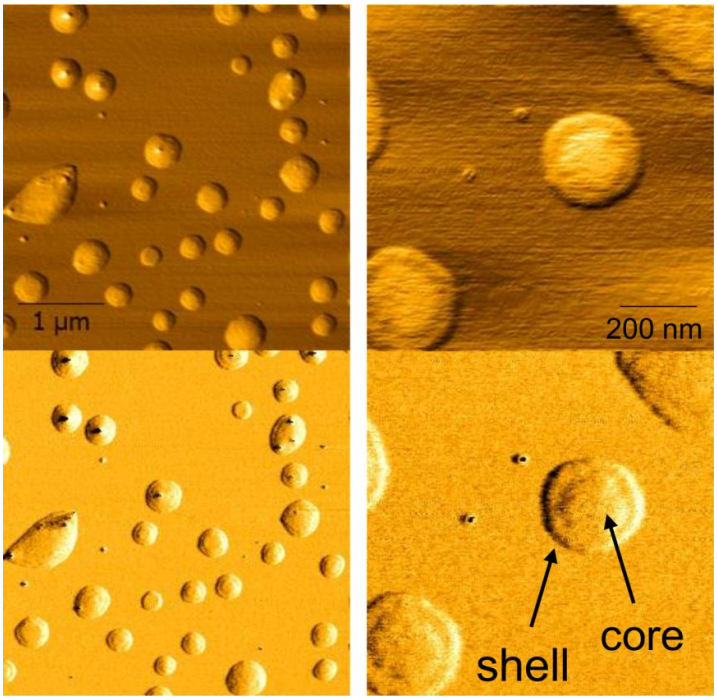

Figure 6.9. Tapping-mode AFM images of a solution of ureasil core-shell NPs prepared using method C: top panels - height-contrast images, lower panels - phase contrast images. The expected core-shell structure is clearly visible.

6.3.3 Fluorescent Ureasil Core-Shell NPs via Dye Encapsulation

Once the synthetic procedure for the preparation of un-doped ureasil core-shell NPs was optimised, the encapsulation of different organic dyes was investigated in view of the potential use of these system for sensing and/or imaging applications. Dye incorporation was investigated using both non-covalent and covalent approaches.

6.3.3.1 Dye Encapsulation: Non-Covalent Approach

For this approach, the key to successful incorporation of the dye into the NPs is to exploit the higher hydrophobicity of the NP core compared to the water/base solution. The selected dye was mixed with d-UPTES and co-sprayed into the water/base solution. The synthetic procedure was then continued following Method C (**Fig. 6.10**).

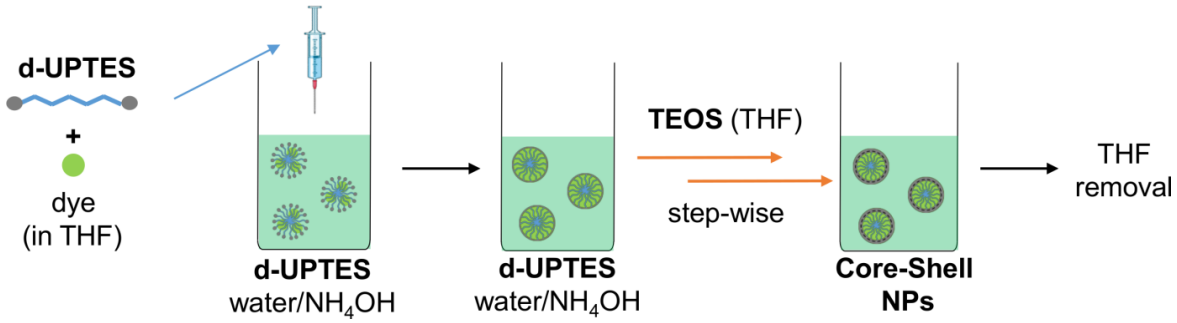

Figure 6.10. Schematic representation of the step-by-step procedure applied for dye incorporation *via* a non-covalent approach using Method C.

The dyes selected for this type of incorporation are **py** and **C153** (**Fig. 6.2**a and b, respectively). Both fluorophores present photoluminescence properties dependent on the polarity of the surrounding environment and therefore their incorporation into the NPs can be followed using fluorescence spectroscopy.

Py is rather insoluble in water (solubility = 0.135 mg L^{-1}) with a Φ_{PL} of 65% in ethanol.[52,53] The sensitivity of **py** to the polarity of the local environment can be extrapolated from two main features: (i) the ratio between the emission intensities of the third and the first peak in the PL spectra (I_3/I_1 ratio) and (ii) the presence of a broad band centred at ~465 nm, which is indicative of the formation of an excimer and is usually present when the dye aggregates (*i.e.* in confined environments).[54, 55] Considering the structure of the Jeffamine, the polarity of the core of the ureasil NPs can be compared to that of ethanol. The emission properties of **py** in a mixture of EtOH/water at different ratios were therefore monitored to investigate the typical value of the I_3/I_1 ratio in the two environments (**Fig. 6.11**). The emission spectrum of **py** in EtOH (**Fig. 6.11**a, red line) is characterised by an intense emission band ranging from 350 to 450 nm and consisting of four vibronic maxima. The corresponding emission spectrum at the same concentration in water presents the same band structure. In addition, a strong emission band centred at ~470 nm is

observed, which is typical of emission from the pyrene excimer and suggests that the **py** molecules are aggregated.[54] This hypothesis is also confirmed by the appearance of the solution of **py** in pure water, which was cloudy compared to the other samples investigated.

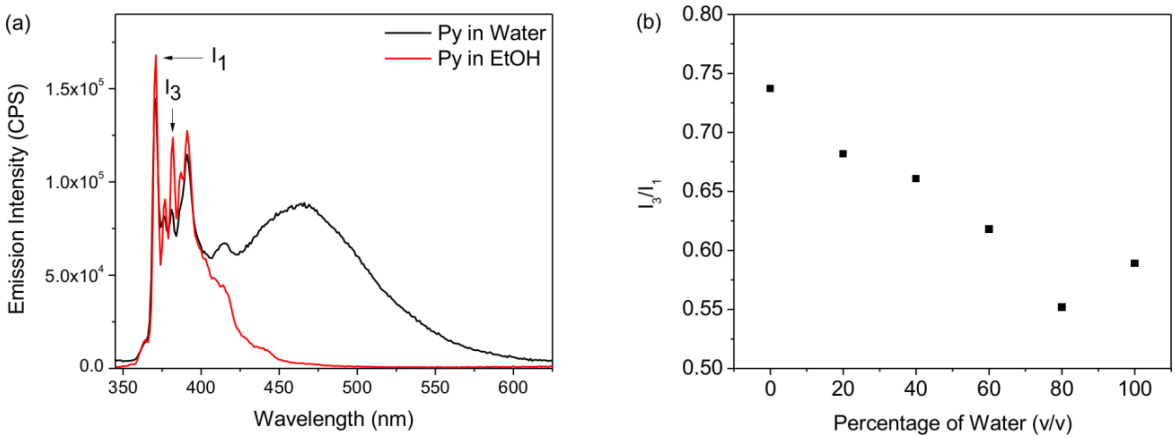

Figure 6.11. Investigation of the PL properties of pyrene in environments with different polarity. (a) Emission spectra (λ_{ex} = 335 nm) of a solution of **py** (2.5×10^{-5} mol L^{-1}) in water (black line) and EtOH (red line). The I_1 and I_3 emission lines are labelled. (b) I_3/I_1 intensity ratios for **py** in a water/ethanol mixture at different volume percentage of water.

A series of solutions containing different water/EtOH volume ratios was prepared and upon addition of the same aliquots of **py** stock the I_3/I_1 ratio were calculated for each mixture. The results are presented in **Fig. 6.11**b. The I_3/I_1 ratio decreases from 0.74 to 0.55 as the concentration of the water is increased from 0 to 80%, respectively. The I_3/I_1 value for **py** in water, however, is slightly higher than expected. This result, might be due to the presence of a contribution of the emission coming from the excimer which can overlap with that of Peak 3, leading to an increase in the intensity of the latter. **Py**-doped ureasil NPs were prepared following Method C, through addition of the same volume of a stock solution of **py** as that used for the calibration curve, to the d-UPTES/THF mixture. The NPs prepared with this method show D_h of 149±2 nm and PdI of 0.08±0.01. The emission spectrum of the **py**-ureasil NPs and the corresponding I_3/I_1 ratio were monitored over the course of two days (**Fig. 6.12**). All the doped-NP samples present an emission spectra characterised by the typical features of the **py** monomer, with a well-structured emission band ranging between 350 and 450 nm. In addition, the emission of the excimer is also observed at ~470 nm. The intensity of this contribution, increases from t = 2 h to 6 h, and then decreases progressively with time (**Fig. 6.12**b). Accordingly, in the same time range, the corresponding I_3/I_1

ratio presents a main decrease from 0.68, which is higher than that of the pyrene in water, to 0.64 and then continues to decrease in time reaching 0.59 after 48 hours. A small increase in both the size and the PdI of the doped-NPs was also observed over the course of the 48 hours, from 149 to 177 nm and from 0.08 to 0.26, respectively.

Both the emission spectra and the I_3/I_1 ratio values indicate that upon incorporation in the NPs, **py** presents an intermediate optical behaviour between that observed for the dye in pure EtOH and in pure water (**Fig. 6.12**). From these results, it seems that the fluorophore is initially incorporated inside the NPs however, it spontaneously leaches out with time. It would be tempting to assume that the presence of the excimer emission for the **py**-doped NP samples, is on its own indicative of the confinement of **py** units into the NP cores. However, the aggregation of the dye is clearly observed in water as well so in this instance, the I_3/I_1 ratio is a preferred diagnostic tool to investigate the local environment surrounding the dye, suggesting that pyrene leaches out spontaneously from the NPs with time. This might be due to the inherent polarity of the Jeffamine units, which is higher than that of pure aliphatic chains. The I_3/I_1 ratio, however, is still higher than that recorded for pyrene in a $100\%_{v/v}$ water solution which represents a promising initial result to start from for the optimisation of the non-covalent dye-encapsulation approach.

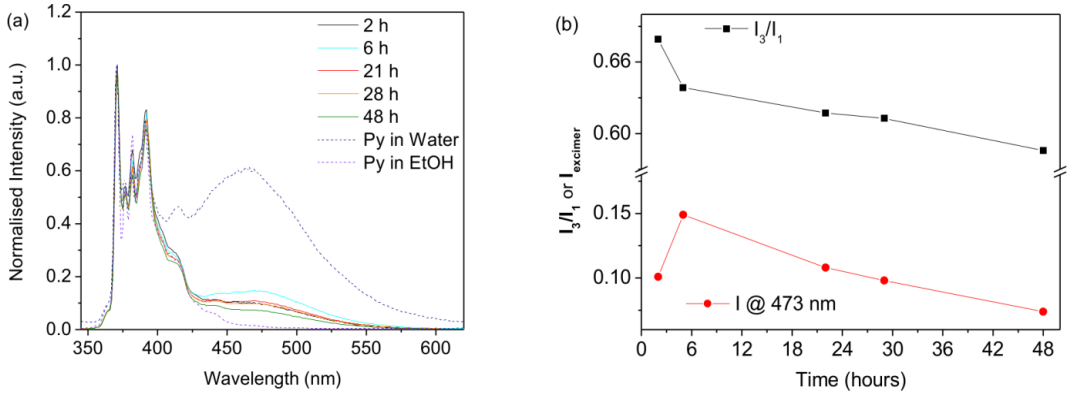

Figure 6.12. In time evolution of the PL properties of the **py**-doped NPs. (a) Normalised emission spectra of the **py**-doped NPs in time (λ_{ex} = 335 nm) and **py** in water and in EtOH (dashed lines) and (b) I_3/I_1 intensity ratio (black dots) and normalised PL maxima of the excimer emission (red dots). The lines serve only to guide the eyes.

The second dye that was encapsulated through the non-covalent approach is **C153**. The emission of this fluorophore is known undergo a blue-shift when the polarity of the environment is decreased.[56, 57] **C153** was incorporated into the NPs using the same process described above. The

obtained NPs present a D_h of 117±2 nm, with a PdI of 0.14±0.03. The emission spectrum of **C153** in water (**Fig. 6.13**a) consists of a broad band between 430 and 680 nm, with a maximum centred at ~549 nm. The PL spectrum of **C153-**doped NPs presents comparable features but is slightly blue-shifted (2 nm), suggesting a change in the polarity of the local environment of the dye. The corresponding excitation spectra for both samples present very similar features; a broad band from 330 to 500 nm with the maxima centred at 411 nm. From these results, it seems that the properties of both samples are dominated by that of the dye dissolved in a water solution. The main spectroscopic differences between the two samples are observed in the absorption spectra (solid lines), whose maximum is red-shifted for the solution of **C153** in water compared to that of the **C153**-doped NPs (429 nm *vs* 418 nm, respectively), indicating that the dye might be surrounded by a more apolar environment upon incorporation into the NPs.[58] To test this hypothesis, the solution of NPs was dialysed for 24 hours against a NH_4OH/water solution (pH = 9) and the emission spectrum was measured again (**Fig. 6.13**b).

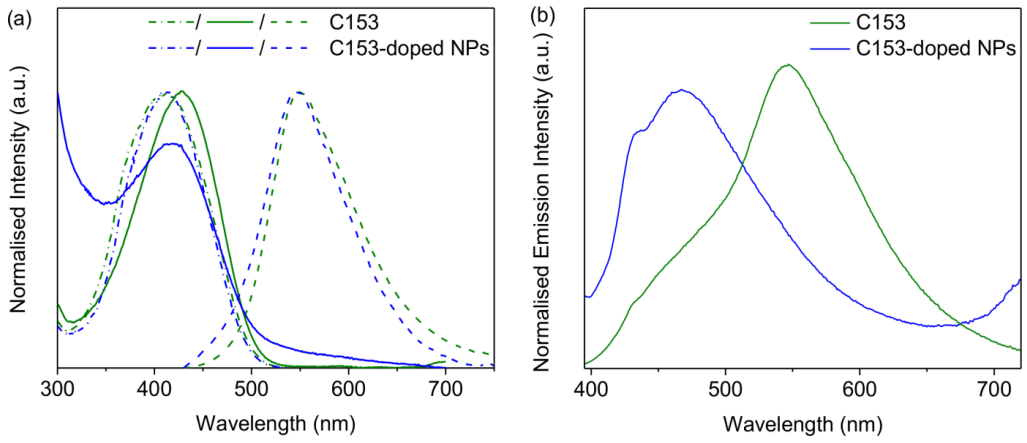

Figure 6.13. PL properties of **C153** in water, upon incorporation into ureasil core-shell NPs and upon dialysis. (a) Normalised absorption (solid lines), emission (λ_{ex}= 420 nm, dashed lines) and excitation (λ_{em}= 550 nm, dashed-dot lines) spectra of **C153** in water (green) and in ureasil NPs (blue) (3.6×10^{-5} mol L^{-1}). (b) Normalised emission spectrum (λ_{ex}= 390 nm) of **C153** in water (green) and in the NPs (blue) after dialysis.

When comparing the normalised emission spectra of **C153** in water and of **C153-**doped NPs after dialysis, it is clear that the dye is present in two very different local environments, as demonstrated by the dramatic blue-shift in the emission maximum of the **C153-**doped NPs sample after dialysis (from 547 to 468 nm). Although this value is an indication that the dye is surrounded by the a more apolar environment compared to water, it is hard to strictly correlate the polarity of this surrounding to that of the core of the NPs. Models, such as the Lippert-Mataga relationship,[59]

can be of aid when trying to predict the entity of the Stokes' shift of a fluorophore as a function of the polarity of the environment. However, it is extremely difficult to model the polarity of the nanoparticle interior and exterior environments, which includes contributions from the poly(propylene) chains, the silica shell, the encapsulated water and the ammonia.

6.3.3.2 Fluorescent NPs via Dye Grafting: Covalent Approach

The previous section showed how two different dyes can be encapsulated into the core of ureasil NPs without requiring any major changes to the optimised synthetic procedure (Method C). Another approach commonly found in the literature for incorporation of dyes into silica NPs is through the covalent bonding of fluorophore to the NPs. In this case, the dye needs to have a functional group able to react with one of the components of the NP. In an effort to preserve as much as possible the optimised synthetic procedure to yield NPs of controlled size and PdI, **FITC** was the chosen dye as it presents a isothiocyanate moiety. Isothiocyanates react readily with the amino group of a siloxane precursor such a APTES, which can then undergo hydrolysis and condensation and bind to the silica shell of NPs.[60, 61]

The reaction proceeds through the formation of a thiourea bridge, as shown in **Fig. 6.14**a. Interestingly, the addition of APTES to a solution of **FITC** leads to the immediate formation of a bright orange precipitate whose quantity increases at the reaction reaches completion. Upon centrifugation, the supernatant containing the APTES-grafted **FITC** (**FITC-PTES**) was added to the NPs mixture during the second addition of TEOS (Method C), to co-condense within the silica shell (**Fig. 6.14**b). However, it cannot be excluded that some of the dye molecules can react on the surface of the silica shell, leading to changes in the relative sizes/charge of the NPs. Three different concentrations of **FITC-PTES** were tested for the preparation of the doped NPs and reference samples containing only APTES were also prepared to investigate whether the potential presence of $-NH_2$ groups onto the NPs surface could affect the stability. The composition of the prepared samples is reported in **Table 6.2**. For each composition, three samples were prepared and the presented results that follow refer to the average of the values obtained for samples of the same composition. The size and PdI of both the APTES and the **FITC-PTES** functionalised NPs are between 100-210 nm and 0.01-0.21, respectively.

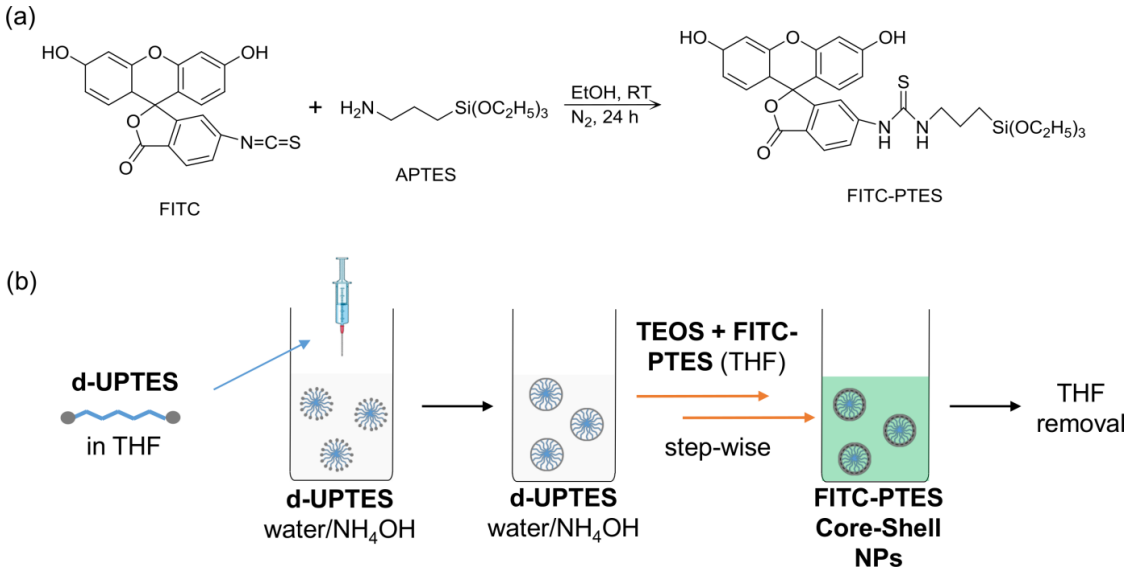

Figure 6.14. Encapsulation of **FITC** in the NPs using a covalent approach. (a) Synthesis of **FITC**-PTES and (b) schematic representation of the modification to method C to obtain the **FITC**-grafted ureasil NPs.

Table 6.2. Composition of **FITC-PTES**-doped NPs and reference samples prepared using the covalent approach.

Sample ID	**Step 1**	**Step 2**		
	TEOS (5%$_{v/v}$)	**TEOS (5%$_{v/v}$)**	**APTES (2%$_{v/v}$)**	**FITC-PTES (22%$_{v/v}$)**
NP0-3	60 µL	57 µL	3 µL	-
NP0-6	60 µL	54 µL	6 µL	-
NP0-15	60 µL	45 µL	15 µL	-
FITC0-3	60 µL	57 µL	-	3 µL
FITC 0-6	60 µL	54 µL	-	6 µL
FITC 0-15	60 µL	45 µL	-	15 µL

The stability of the NPs was monitored after 13 days, proving that the size and PdI of the NPs were still in the desired range. The emission of the **FITC**-doped NPs was monitored before and after dialysis (**Fig. 6.15**) to determine if the dye is effectively grafted into the silica shell. The emission spectra of the **FITC**-doped NPs before dialysis exhibit the typical optical features of fluorescein,[60] with a band between 480 and 625 nm and an absolute maximum at 516 nm (**Fig 6.15**a). The emission spectra of the corresponding dialysed samples measured under the same conditions (slit widths, excitation wavelength *etc*.) display very similar properties, with the emission centred at 516 nm. However, there is a general decrease in the emission intensity. The aim of the dialysis was indeed to remove any excess un-bound dye from the solution; however, some interesting conclusions can also be drawn considering that the intensity seems to decrease by

80-85% for each sample. This might be an indication that the synthetic procedure for the preparation of the APTES-grafted dye did not occur successfully or yields only 15-20% of the desired product. Although the procedure used is well-documented in literature,[61] it was impossible to obtain higher yields through further repetition of the reaction.

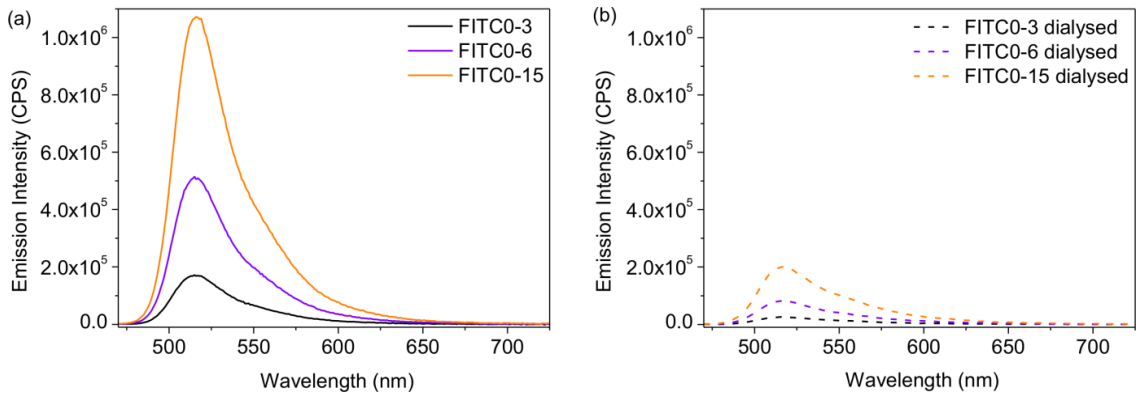

Figure 6.15. Verification of grafting of **FITC** within the silica shell of ureasil core-shell NPs. Emission spectra (λ_{ex} = 465 nm) of samples FITC0-3, FITC0-6 and FITC0-15 (a) before and (b) after dialysis (24 hours in water).

To ensure that the observed emission properties for the NPs are due to **FITC** moieties that are actually grafted onto the NPs and not only unbound in solution, lifetime measurements were performed on sample FITC0-3. Santa *et al.*[60] conducted a detailed study on the fluorescence lifetime of FITC-based silica NPs to investigate the distribution of the dye within the core or the shell of the final NPs. While the decay curves of both **FITC** and **FITC-PTES** in solution could be modelled by a monoexponential decay curve (τ_1 ~ 4.0 ns), an additional contribution (τ_2 ~ 2.4 ns) was needed to fit the decay curves of **FITC**-grafted SiO_2 NPs. The authors attribute this difference to the change in environment of the dye molecules from solvated regions (either the solution or the porous TEOS shell of the NPs), to a dry environment such as the NP core.

For this study, several reference samples were prepared in order to be able to compare the differences between a system containing fluorescein, both bound and unbound to APTES, and the effect of the presence of the ureasil core-shell NPs. Firstly, a sample containing fluorescein sodium salt (**F-Na**) and APTES in the same molar ratios and conditions used to form the **FITC-PTES** precursor was prepared and the resultant **F-Na-APTES** solution was used to synthesise NPs (**F-Na-APTES NPs**) in the same concentration as **FITC0-3**. Although no reaction is expected to occur between the two species, the APTES is expected to graft onto the surface of the NPs, thus

influencing the system stability and/or the **F-Na** distribution to some extent. The decay curve, fits and residuals are presented in **Fig. 6.16,** while the results of the lifetime fittings for the aforementioned samples before and after multiple dialyses are presented in **Table 6.3**.

As expected, the decay curve of **F-Na-APTES** is comparable to that of pure fluorescein in solution and is characterised by a single term, τ_1 = 4.06 ns (**Fig. 6.16**a). [60] The incorporation method described in **Fig. 6.14**b seems not to be effective for **F-Na-APTES**, which might not be able to penetrate the first layer of silica formed by the TEOS added in step one, possibly due to the higher solubility of **F-Na** in water, due to its ionic nature, compared to **C153** and **py**.[52, 62] The emission decays of **F-Na APTES NPs** are also characterised by a single term, τ_1 ~4.0 ns, which remained unchanged even when measuring the solution after the first and second dialysis(**Fig. 6.16**a). It is worth of note that the solution progressively loses most of its green emission during the dialysis processes.

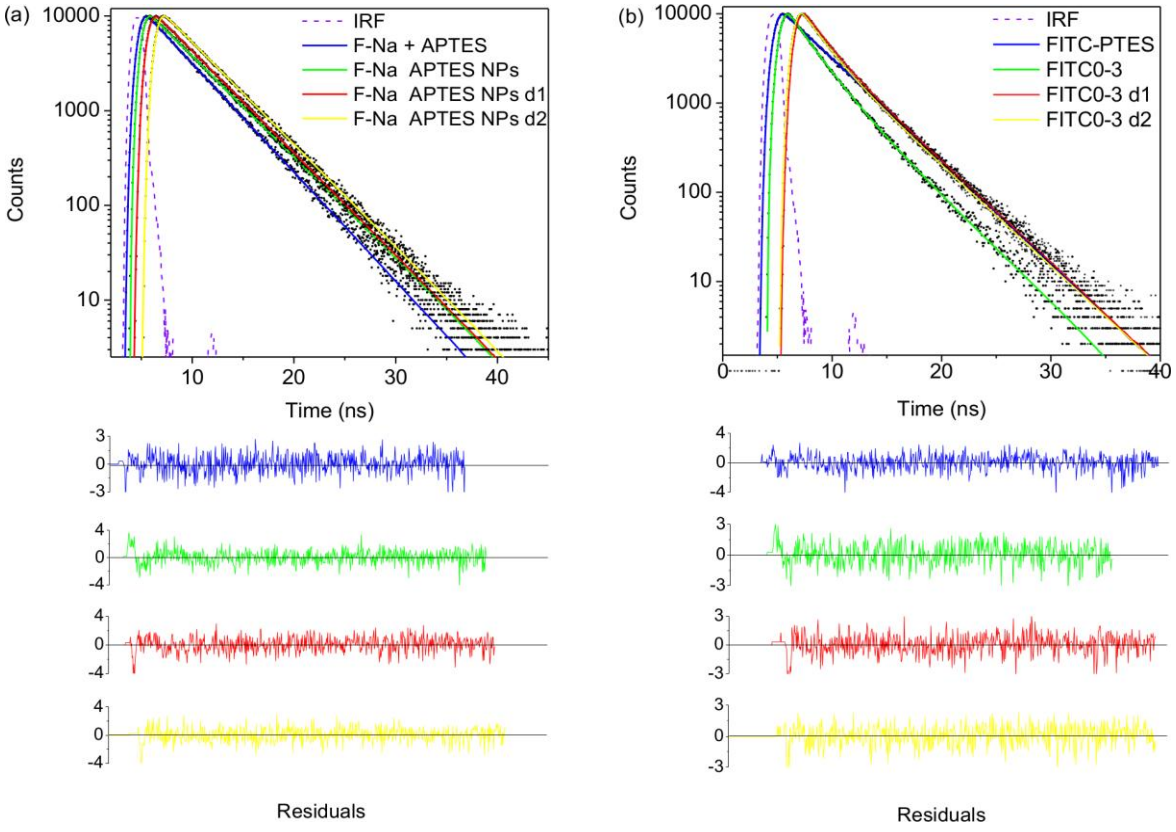

Figure 6.16. Time-resolved fluorescence investigation of **F-Na** and **FITC**-doped NPs. Emission decay curves (black dots) and fits (coloured lines) for (a) **F-Na+APTES** and **F-Na APTES NPs** and (b) **FITC-PTES** and **FITC0-3** before and after dialysis 1 (**d1**) and dialysis 2 (**d2**) (λ_{ex}= 458 nm and λ_{em}= 515 nm). The weighted residuals for each fit and the instrument response function (IRF, dotted line) are also shown.

Table 6.3. Time-resolved photoluminescence analyses of **FITC**-grafted ureasil NPs. Decay times (τ_i), fractional contributions (f_i) and chi-squared (χ^2) resulting from analysis of the photoluminescence decays (λ_{ex} = 458 nm) of **F-Na-APTES**, **FITC-PTES**, **F-NA-APTES NPs** and **FITC0-3** before and after dialysis 1 (**d1**) and dialysis 2 (**d2**) (λ_{em} = 515 nm).

Sample ID	τ_1 (ns)	f_1	τ_2 (ns)	f_2	χ^2
F-Na + APTES	4.06 (±0.01)	1.00 (±0.02)			1.03
F-Na APTES NPs	4.08 (±0.01)	1.00 (±0.01)			1.01
F-Na APTES NPs d1	4.03 (±0.01)	1.00 (±0.01)			1.08
F-Na APTES NPs d2	4.02 (±0.01)	1.00 (±0.02)			1.02
FITC-PTES	3.78 (±0.01)	1.00 (±0.04)			1.03
FITC0-3	3.78 (±0.02)	0.44 (±0.01)	2.08 (±0.04)	0.56 (±0.01)	1.06
FITC0-3 d1	3.86 (±0.01)	0.67 (±0.05)	1.75 (±0.04)	0.33 (±0.03)	1.11
FITC0-3 d2	3.85 (±0.01)	0.65 (±0.05)	1.73(±0.02)	0.35 (±0.03)	1.05

The fits to the **FITC-PTES** decay curve reveal that it is characterised by a single component (τ_1 = 3.8 ns) (**Fig. 6.16**b), which is similar to that of **F-Na-APTES**. Interestingly, upon incorporation into the NPs, the decay curve can only be modelled using a biexponential fit (τ_1 ~3.9 ns and τ_2 ~ 2.0 ns), which is in good agreement with that observed in the literature for fluorescein surrounded by different environments.[60] A slight redistribution of the f_i values is observed after the first dialysis with an increase of f_1 (from 0.44 to 0.67) and a concomitant decrease in f_2 (from 0.56 to 0.33). These values remained constant upon the second dialysis and could indicate a re-distribution of the **FITC** molecules onto the NP surface. Although these data cannot unravel the exact location of the **FITC** units in the NPs, they can give us further insights into their organisation in solution and on the NPs. It is plausible to assume that a portion of the **FITC** molecules is grafted onto the inner silica shell of the NPs, occupying the vacant holes in the ureasil cores left uncovered by the first TEOS addition. A second population of **FITC** molecules could actually be located on the surface of the NPs, with the APTES extremity covalently grafted onto the outer silica shell. It is also possible that some of the fluorescein molecules might be stacked onto the surface of the NPs, interacting with the covalently bound **FITC-PTES** units on the NPs surface. Since during the dialyses we noticed that the volume of the bag increased progressively with time, the dilution of the NPs sample could have led to re-dispersion of the dye into the solution, inhibiting the stacking.

Overall these data showed that the **FITC-PTES** exists in two different environments within the NP solution and are a further indication that covalent grafting can yield **FITC**-doped ureasil core-shell NPs.

6.4 Conclusions

The synthesis of ureasil core-shell NPs was successfully optimised and the incorporation of organic dyes has been achieved through both a covalent and a non-covalent approach. Several synthetic pathways were considered to reach the optimum reaction conditions. The optimised synthetic conditions for the final un-doped NPs were found to be: (i) d-UPTES concentration of 20,000 ppm (ii) base concentration equal to 10 mM NH_4OH, (iii) concentration of added TEOS equal to $5\%_{v/v}$ in THF and (iv) rate of addition of TEOS equal to 60 μL/ 60 minutes. The NPs obtained following this method present sizes of ~150 nm and PdI < 0.2, which are within the desired features that were aimed for this work and are stable for over 50 days. The core-shell structure of the system was proved using AFM imaging and their stability confirmed by means of ζ-potential measurements.

The encapsulation of organic dyes using a non-covalent approach was monitored by fluorescence spectroscopy. For **py**-loaded NPs, the dye tended to leach out of the aggregates roughly two days after encapsulation. This phenomenon was attributed to the inherent polarity of the Jeffamine chains which constitutes the NP cores. **C153** instead could be efficiently encapsulated into the NPs and remained encapsulated even after dialysis. Moreover, the NPs were also successfully loaded with **FITC** through a covalent approach. In this case, the dye was functionalised with a siloxane precursor and reacted on the surface of either the inner or outer silica shell of the NPs. Lifetime measurements revealed that the spectroscopic behaviour of the **FITC** grafted to the NPs is different to that of the pure dye, with the decay curve of the former characterised by two terms, indicating that the dye is surrounded by different environments, *i.e.*. the core of the NPs and the solution.

Overall these results highlight the versatility of the sol-gel method and the use of ureasils in general, to yield different organic-inorganic hybrid architectures which are able to host emissive species for potential applications in imaging, sensing and possibly as delivery agents.

6.5 References

1. I. Meazzini, J. M. Behrendt, M. L. Turner and R. C. Evans, *Macromolecules*, 2017, **50**, 4235-4243.
2. I. Meazzini, C. Blayo, J. Arlt, A.-T. Marques, U. Scherf, H. D. Burrows and R. C. Evans, *Mater. Chem. Front.*, 2017, DOI:10.1039/C1037QM00264E.
3. I. Meazzini, N. Willis-Fox, C. Blayo, J. Arlt, S. Clement and R. C. Evans, *J. Mater. Chem. C*, 2016, **4**, 4049-4059.
4. P. Judeinstein and C. Sanchez, *J. Mater. Chem.*, 1996, **6**, 511-525.
5. C. J. Brinker and G. W. Scherer, in *Sol-Gel Science*, Academic Press, San Diego, 1990, pp. 96-233.
6. J. D. Wright and N. A. Sommerdijk, *Sol-gel materials: chemistry and applications*, CRC press, 2000.
7. W. Stöber, A. Fink and E. Bohn, *J. Colloid Interface Sci.*, 1968, **26**, 62-69.
8. M. Montalti, L. Prodi, E. Rampazzo and N. Zaccheroni, *Chem. Soc. Rev.*, 2014, **43**, 4243-4268.
9. C. Rosu, A. J. Gorman, R. Cueto, K. M. Dooley and P. S. Russo, *J. Colloid Interface Sci.*, 2016, **467**, 321-334.
10. C. Sanchez, B. Julian, P. Belleville and M. Popall, *J. Mater. Chem.*, 2005, **15**, 3559-3592.
11. C. Sanchez, P. Belleville, M. Popall and L. Nicole, *Chem. Soc. Rev.*, 2011, **40**, 696-753.
12. C. Sanchez, B. Lebeau, F. Chaput and J. P. Boilot, *Adv. Mater.*, 2003, **15**, 1969-1994.
13. N. Kohler, G. E. Fryxell and M. Zhang, *J. Am. Chem. Soc.*, 2004, **126**, 7206-7211.
14. J. Feng, Y. Li and M. Yang, *Sensors and Actuators B: Chemical*, 2010, **145**, 438-443.
15. K. Ogawa, S. Chemburu, G. P. Lopez, D. G. Whitten and K. S. Schanze, *Langmuir*, 2007, **23**, 4541-4548.
16. J. M. Behrendt, A. B. Foster, M. C. McCairn, H. Willcock, R. K. O'Reilly and M. L. Turner, *J. Mater. Chem. C*, 2013, **1**, 3297-3304.
17. S. Jebors, S. Cecillon, C. Faye, C. Enjalbal, M. Amblard, A. Mehdi, G. Subra and J. Martinez, *J. Mater. Chem. B*, 2013, **1**, 6510-6515.
18. J. Ciccione, T. Jia, J.-L. Coll, K. Parra, M. Amblard, S. Jebors, J. Martinez, A. Mehdi and G. Subra, *Chem. Mater.*, 2016, **28**, 885-889.
19. H. Fessi, F. Puisieux, J. P. Devissaguet, N. Ammoury and S. Benita, *Int. J. Pharm.*, 1989, **55**, R1-R4.
20. C. E. Mora-Huertas, H. Fessi and A. Elaissari, *Int. J. Pharm.*, 2010, **385**, 113-142.
21. L. D. Carlos, V. de Zea Bermudez, R. A. Sá Ferreira, L. Marques and M. Assunção, *Chem. Mater.*, 1999, **11**, 581-588.
22. D. C. Oliveira, A. G. Macedo, N. J. O. Silva, C. Molina, R. A. S. Ferreira, P. S. André, K. Dahmouche, V. D. Z. Bermudez, Y. Messaddeq, S. J. L. Ribeiro and L. D. Carlos, *Chem. Mater.*, 2008, **20**, 3696-3705.
23. V. de Zea Bermudez, L. D. Carlos and L. Alcácer, *Chem. Mater.*, 1999, **11**, 569-580.
24. Y. Cui, M. Wang, L. Chen and G. Qian, *Dyes Pigm.*, 2004, **62**, 43-47.
25. R. Ghosh Chaudhuri and S. Paria, *Chem. Rev.*, 2012, **112**, 2373-2433.
26. M. Di Paola, A. Quarta, F. Conversano, E. A. Sbenaglia, S. Bettini, L. Valli, G. Gigli and S. Casciaro, *Langmuir*, 2017, **33**, 4490-4499.
27. T. S. Hauck, A. A. Ghazani and W. C. W. Chan, *Small*, 2008, **4**, 153-159.
28. F. Lu, S.-H. Wu, Y. Hung and C.-Y. Mou, *Small*, 2009, **5**, 1408-1413.
29. C. He, Y. Hu, L. Yin, C. Tang and C. Yin, *Biomaterials*, 2010, **31**, 3657-3666.
30. T.-W. Kim, I. I. Slowing, P.-W. Chung and V. S.-Y. Lin, *ACS Nano*, 2011, **5**, 360-366.
31. D. Napierska, L. C. J. Thomassen, V. Rabolli, D. Lison, L. Gonzalez, M. Kirsch-Volders, J. A. Martens and P. H. Hoet, *Small*, 2009, **5**, 846-853.
32. E. Ruckenstein and Y. S. Djikaev, *Adv. Colloid. Interface Sci.*, 2005, **118**, 51-72.
33. P. W. Voorhees, *J. Stat. Phys.*, 1985, **38**, 231-252.
34. V. Kumar and R. K. Prud'homme, *Chem. Eng. Sci.*, 2009, **64**, 1358-1361.
35. I. M. Lifshitz and V. V. Slyozov, *J. Phys. Chem. Solids*, 1961, **19**, 35-50.
36. T. K. N. Hoang, L. Deriemaeker, V. B. La and R. Finsy, *Langmuir*, 2004, **20**, 8966-8969.
37. Y. Liu, K. Kathan, W. Saad and R. K. Prud'homme, *Phys. Rev. Lett.*, 2007, **98**, 036102.

38. E. Rampazzo, S. Bonacchi, M. Montalti, L. Prodi and N. Zaccheroni, *J. Am. Chem. Soc.*, 2007, **129**, 14251-14256.
39. R. Nyffenegger, C. Quellet and J. Ricka, *J. Colloid Interface Sci.*, 1993, **159**, 150-157.
40. H. Ow, D. R. Larson, M. Srivastava, B. A. Baird, W. W. Webb and U. Wiesner, *Nano Lett.*, 2005, **5**, 113-117.
41. J. D. Rimer, R. F. Lobo and D. G. Vlachos, *Langmuir*, 2005, **21**, 8960-8971.
42. G. H. Bogush and C. F. Zukoski, *J. Colloid Interface Sci.*, 1991, **142**, 1-18.
43. S.-L. Chen, P. Dong, G.-H. Yang and J.-J. Yang, *Ind. Eng. Chem. Res.*, 1996, **35**, 4487-4493.
44. K.-S. Chou and C.-C. Chen, in *Innovative Processing and Synthesis of Ceramics, Glasses and Composites VIII*, John Wiley & Sons, Inc., 2006, pp. 57-67.
45. K. D. Kim and H. T. Kim, *Mater. Lett.*, 2003, **57**, 3211-3216.
46. K. Nozawa, H. Gailhanou, L. Raison, P. Panizza, H. Ushiki, E. Sellier, J. P. Delville and M. H. Delville, *Langmuir*, 2005, **21**, 1516-1523.
47. S. Kang, S. I. Hong, C. R. Choe, M. Park, S. Rim and J. Kim, *Polymer*, 2001, **42**, 879-887.
48. *Zetasizer Nano Series User Manual*, Malvern Instrument Ltd., 2004.
49. R. Brydson, A. Brown, C. Hodges, P. Abellan and N. Hondow, *Journal of Microscopy*, 2015, **260**, 238-247.
50. P. Klapetek, M. Valtr, D. Nečas, O. Salyk and P. Dzik, *Nanoscale Res. Lett.*, 2011, **6**, 514.
51. G. Dan, X. Guoxin and L. Jianbin, *J. Phys. D: Appl. Phys.*, 2014, **47**, 013001.
52. M. M. Miller, S. P. Wasik, G. L. Huang, W. Y. Shiu and D. Mackay, *Environ. Sci. Technol.*, 1985, **19**, 522-529.
53. T. Medinger and F. Wilkinson, *Trans. Faraday Soc.*, 1966, **62**, 1785-1792.
54. K. Kalyanasundaram and J. K. Thomas, *J. Am. Chem. Soc.*, 1977, **99**, 2039-2044.
55. V. R. Kaufman and D. Avnir, *Langmuir*, 1986, **2**, 717-722.
56. M. Horng, J. Gardecki, A. Papazyan and M. Maroncelli, *J. Phys. Chem.*, 1995, **99**, 17311-17337.
57. P. Sen, D. Roy, S. K. Mondal, K. Sahu, S. Ghosh and K. Bhattacharyya, *J. Phys. Chem. A*, 2005, **109**, 9716-9722.
58. M. Ferrer and P. Lianos, *Langmuir*, 1996, **12**, 5620-5624.
59. J. R. Lakowicz, *Principles of Fluorescence Spectroscopy*, 2006, p. 208.
60. S. Santra, B. Liesenfeld, C. Bertolino, D. Dutta, Z. Cao, W. Tan, B. M. Moudgil and R. A. Mericle, *J. Lumin.*, 2006, **117**, 75-82.
61. G. Durgun, K. Ocakoglu and S. Ozcelik, *J. Phys. Chem. C*, 2011, **115**, 16322-16332.
62. H. Shirota and E. W. C. Jr., *J. Chem. Phys.*, 2000, **112**, 2367-2376.

Chapter Seven

Conclusions

This thesis has explored the optical and structural properties of a series of organic-inorganic hybrid architectures based on ureasils and doped with π-conjugated fluorophores towards the design of efficient light-emitting platforms.

The first part of this work was focused on the preparation of ureasils as free-standing monoliths and on the investigation of different methods for the incorporation of CPs and dyes into their matrices, with the aim of enhancing the overall emission properties of the fluorophore, while conferring to it improved photo- and thermal stability. Different structures of ureasils, obtained through judicious selection of the Jeffamine organic precursor, were used to study the effect of the network arrangement on the morphology of the dopant and to target specific optical properties.

In **Chapter 3**, the incorporation of **PFO-OH** into both di- and tri-ureasil was successfully achieved through grafting of the CP to the backbone of the hybrids. NMR spectroscopy confirmed that the side chains of the CP were covalently linked to the silica precursors and subsequently co-condensed to the inorganic domains of both sets of ureasil hybrids. A combination of structural investigation techniques, namely, PXRD, FTIR and ^{29}Si and ^{13}C MAS-NMR, revealed that the packing of the hybrids is more open and distorted for tri-ureasils compared to di-ureasils and that while the overall network integrity is preserved upon grafting of the CP chains, a slight re-arrangement of the H-bonding interactions within the hybrid network, was observed for di-ureasils upon doping. The PL properties of the systems were monitored during the gelation process, and revealed that while prior to the hydrolysis/condensation reaction the **PFO-OH** chains adopt the α-phase conformation, the gelation induced conformational changes leading to the targeted formation of the β-phase. Gaussian multi-peak fits to the corresponding excitation spectra were used to isolate and quantify the contribution of the β-phase, showing that the extent of its formation, depends on the structure of the ureasil used.

A similar incorporation approach was also used in **Chapter 4**, where a perylene dicarboxdiimide dye presenting siloxane extremities was covalently-bound to the silica domains of four different ureasil hybrids. Detailed investigation of the optoelectronic properties of each sample through steady-state and time-resolved spectroscopy showed that grafting of the fluorophore leads to improved dispersion and better isolation of the dye units within the host matrices. This reduced the undesirable effects of re-absorption/aggregation phenomena on the PL

properties of the materials, which present values of Φ_{PL} comparable to that of the dye in a dilute solution of a good solvent. Detailed investigation of the local-arrangement of the ureasil network revealed that the overall structure of each ureasil hybrid is preserved upon incorporation of the **PDI-Sil**. TCSPC experiments, combined with steady-state PL spectroscopy, showed that energy transfer can occur between the ureasil donor and the **PDI-Sil** acceptor. Interestingly, the structure of the Jeffamine precursor, which is responsible of the overall macroscopic features for each hybrid, seems to determine the extent of the efficiency of this process. Namely, the branch length appears to be the key determining factor.

For both examples, covalent grafting of the fluorophore to the hybrid backbone, seems to be a versatile synthetic route to yield organic-inorganic ureasil hybrids in which the fluorophore is homogeneously dispersed. This leads to values of Φ_{PL} for the final materials which are comparable to those of the fluorophore in solution, using a relatively low concentration of dopant ($\leq 0.1\ \%_{w/w}$) and preserving the integrity of the host network. Moreover, integration of both the CP and the perylene dye into the hybrid network led to an improvement of both the photo- and the thermal stability of the fluorophores, while enhancing their optoelectronic properties.

In **Chapter 5** instead, another incorporation approach was investigated for a fluorene-phenylene conjugated polyelectrolyte functionalised with perylene diimide units. In this case, a stock solution of the fluorophore was added to the reaction mixture prior to addition of the sol-gel initiator agents, leading to physical dispersion of the CPE within the matrices of either a di- or a tri-ureasil. Steady-state photoluminescence measurements revealed that inclusion into the ureasil matrix reduces the non-radiative pathways available to the PDI units, enabling their detection in the emission spectrum. In particular this phenomenon is prominent for tri-ureasil compared to di-ureasils, confirming again the importance of the structural surrounding provided by the host for targeting specific optical properties of the dopant. By means of solid-state MAS-NMR spectroscopy and FTIR in the Amide I region the structural features of the ureasils were again unravelled, showing that for Jeffamines with similar chain lengths but different number of branches, tri-ureasils generally present a more distorted and open structure compared to the di-ureasils. Due to the low concentration of on-chain PDI units (1-2%), the optoelectronic features of the final system are largely dominated by the contribution of the **PBS-PFP** backbone. The CPE is

well-dispersed into the ureasil network, yielding Φ_{PL} values comparable to that of the polymer in solution. However TCSPC measurements showed that the global emission of each system is dominated by a component with a lifetime of ~500-600 ns, which correspond to trap sites on the **PBS-PFP** chains, leading to impossibility of energy transfer to the PDI units. This resulted into mediocre values of optical efficiencies obtained when the sample was used as a LSC device.

Although this CPE was chosen to combine the advantageous optical features observed for the fluorophores investigated in **Chapter 3** and **Chapter 4**, due to the low ratio of PDI to **PBS-PFP** units inherent of the synthetic design of the CPE, this goal could not be fully achieved. However, recent reports in literature have shown that upon judicious selection of different CP lumophores, energy transfer can be exploited to reduce re-absorption losses in LSC devices.[1] This, combined with the intriguing possibility of using a photoactive waveguide like ureasils, represents a promising step towards the design of novel CP-integrated LSC architectures.

Overall, both covalent grafting and physical encapsulation, proved to be simple and efficient approaches to yield fluorophore-integrated ureasil monoliths. For each example presented, the optoelectronic properties of the final materials resulted from the combination of those of the ureasil host and of the dopant and are mediated by a fine interplay between the structural arrangement of each fluorophore and their electronic interactions with the host, which can trigger phenomena such as energy transfer or reduced re-absorption.

In the final part of this work (**Chapter 6**), the synthesis of organic-inorganic NPs based on a ureasil core and a silica shell was optimised and the resulting systems were loaded with different organic dyes. The NPs were prepared using a synthetic route that combines nanoprecipitation with the Stöber method, through spray-injection of the d-UPTES precursor into a solution of a bad solvent containing a base catalyst, that can trigger both the hydrolysis and condensation of the alkoxysilane extremities of the d-UPTES. TEOS was also added to densify the silica shell around the ureasil core and to improve the overall stability of the system. The optimisation of the synthetic route to obtain this architecture was achieved by careful investigation of the synthetic parameters and the NPs prepared with the optimised strategy proved to be stable for over 50 days, maintaining their sizes and PdI within a suitable range for potential applications as imaging agents (D_h ~200 nm and PdI < 0.2). Moreover, the encapsulation of different organic dyes was investigated either by (i)

non-covalent and (ii) covalent incorporation. For the first method, steady-state spectroscopy measurements revealed that the encapsulation can occur by pre-mixing of the d-UPTES precursor and subsequent synthesis of the NPs following the optimised method. While dye leaching was observed for the incorporation of pyrene, this approach seems to be more efficient for coumarin 153. The covalent grafting of the dye to the NPs was achieved by functionalisation of fluorescein isothiocyanate with a siloxane and subsequent condensation within the NP shell and was confirmed by lifetime measurements on the system before and after incorporation. As the design of the ureasil NPs allows for the incorporation of dyes on both their hydrophobic core (*via* the non-covalent approach) and their hydrophilic shell (*via* the covalent approach), an interesting prospect for future work on these systems is the simultaneous encapsulation of two emissive species, one for each environment. Judicious selection of the two dyes, could lead to energy transfer between the fluorophores enabling a higher signal to noise ratio for the emission of the final NPs.[2]

The overall results obtained throughout this thesis highlight how a simple and versatile synthetic process such as the sol-gel method can open a variety of architectural possibilities for ureasil hybrids. For each presented example, the rational design of the system, achieved by control over of the Jeffamine precursor, the fluorophore and the synthetic conditions, open the prospective towards yielding systems whose potential applications range from light-emitting devices to LSCs to imaging agents.

Future work on these system will focus on the encapsulation of a new class of emitters known as *Aggregation Induced Emission* (AIE) agents into both ureasil-based waveguides and NPs. Due to their characteristic emission which is switched-on upon aggregation, AIE emitters could overcome the undesirable effects of lumophore aggregation within a waveguide, while allowing high dye loading concentrations.[3] For ureasil NPs instead, monitoring the emission of the AIE agents during the NP formation, could provide an interesting route to gain a deeper understanding of the encapsulation process of luminescent species within ureasil NPs.

7.1 References

1. G. D. Gutierrez, I. Coropceanu, M. G. Bawendi and T. M. Swager, *Adv. Mater.*, 2015, **28**, 497-501.
2. W. Lin and W. Tan, *Nano Lett.*, 2006, **6**, 84-88.
3. J. L. Banal, J. M. White, K. P. Ghiggino, W. W. Wong, *Sci. Rep.*, 2014, **4**, 436.

Appendix

1.1 Chapter 3

Figure A3.1. PL and PL excitation spectra of undoped tri-ureasils.

Figure A3.2. PL spectra of **DU-PF-0.01**, **DU-PF-0.05**, **DU-PF-0.1**, **TU-PF-0.01**, **TU-PF-0.05** and **TU-PF-0.1**.

Figure A3.3. PL excitation spectra of **DU-PF-0.01**, **DU-PF-0.05**, **DU-PF-0.1**, **TU-PF-0.01**, **TU-PF-0.05** and **TU-PF-0.1**.

Figure A3.4. Results of fittings o f the PL excitation spectra of **DU-PF-0.05**, **DU-PF-0.1**, **TU-PF-0.01**, **TU-PF-0.05** and **TU-PF-0.1**.

1.2 Chapter 4

Figure A4.1. ^{1}H NMR spectrum of **PDI-Sil** in $CDCl_3$.

Figure A4.2. $^{13}C\{^{1}H\}$ NMR spectrum of **PDI-Sil** in $CDCl_3$.

Figure A4.3. $^{29}Si\{^{1}H\}$ NMR spectrum of **PDI-Sil** in $CDCl_3$.

Figure A4.4. Calculated *G* values for a dilute solution of **PDI-Sil** in THF (λ_{em} = 630 nm).

1.3 Chapter 5

Figure A5.1. PL spectra of **DU-CPE-*x*** and **TU-CPE-*x***.

Figure A5.2. PL excitation spectra **DU-CPE-*x*** and **TU-CPE-*x***.

Figure A5.3.Thermal stability of **DU-CPE-*x*** and **TU-CPE-*x***.

Figure A5.4. Results of FTIR spectra and Gaussian curve-fits for the Amide I region of **DU-CPE-*x*** and **TU-CPE-*x***.

Figure A5.5. Emission decay curves and fits for **DU-CPE-*x***.

Figure A5.6. Emission decay curves and fits for **TU-CPE-*x***.

Table A5.1. Photoluminescence lifetimes (τ_i), pre-exponential coefficients (α_i), and chi squared (χ^2) values obtained from fitting of the emission decays (λ_{ex} = 370 nm) at λ_{em} = 420 and 500 nm for **DU-CPE-*x*** and **TU-CPE-*x*.**

1.4 Chapter 6

Figure A6.1. FTIR measurements on d-UPTES, ICPTES and Jeffamine ED-600.

Figure A6.2. Intensity *vs* the size (nm) of NPs prepared with Method B.

Figure A6.3. AFM images of a ureasil core-shell NP prepared using Method C.

1.1 Chapter 3

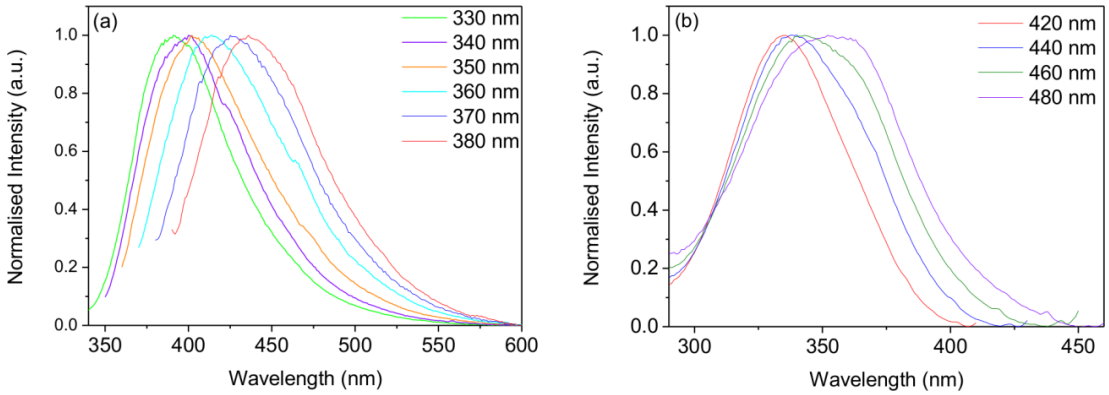

Figure A3.1. Optical features of undoped tri-ureasil. RT (a) emission and (b) excitation spectra of **TU-PF-0** measured at different excitation and emission wavelengths, respectively.

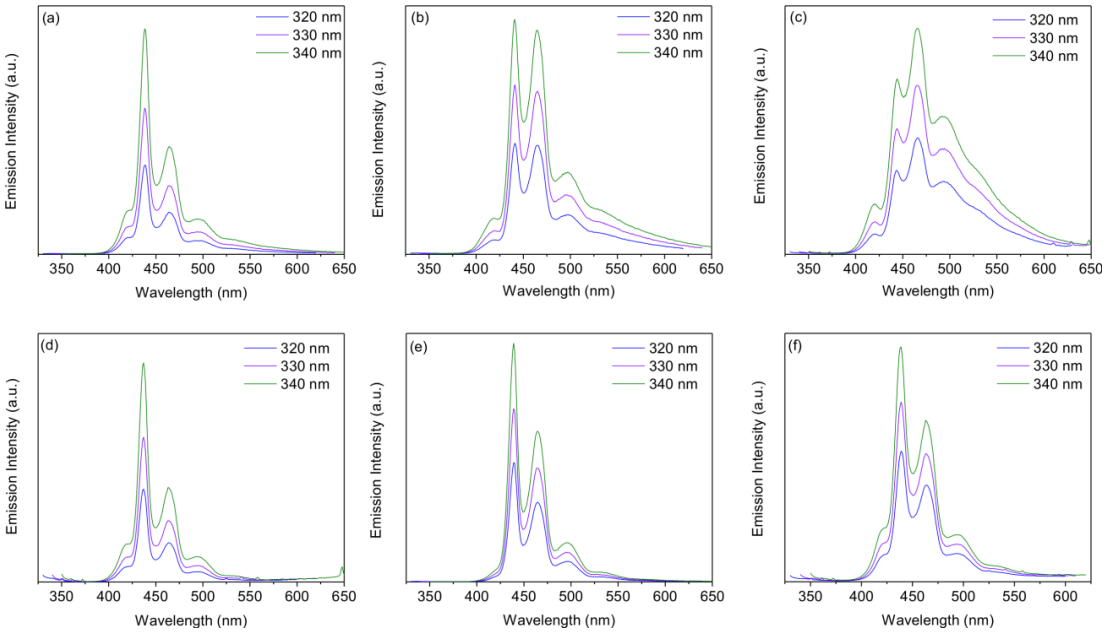

Figure A3.2. Optical features of PF-doped ureasils. Emission spectra of (a) **DU-PF-0.01** (b) **DU-PF-0.05**, (c) **DU-PF-0.1**, (d) **TU-PF-0.01**, (e) **TU-PF-0.05** and (f) **TU-PF-0.1** measured at different excitation wavelengths.

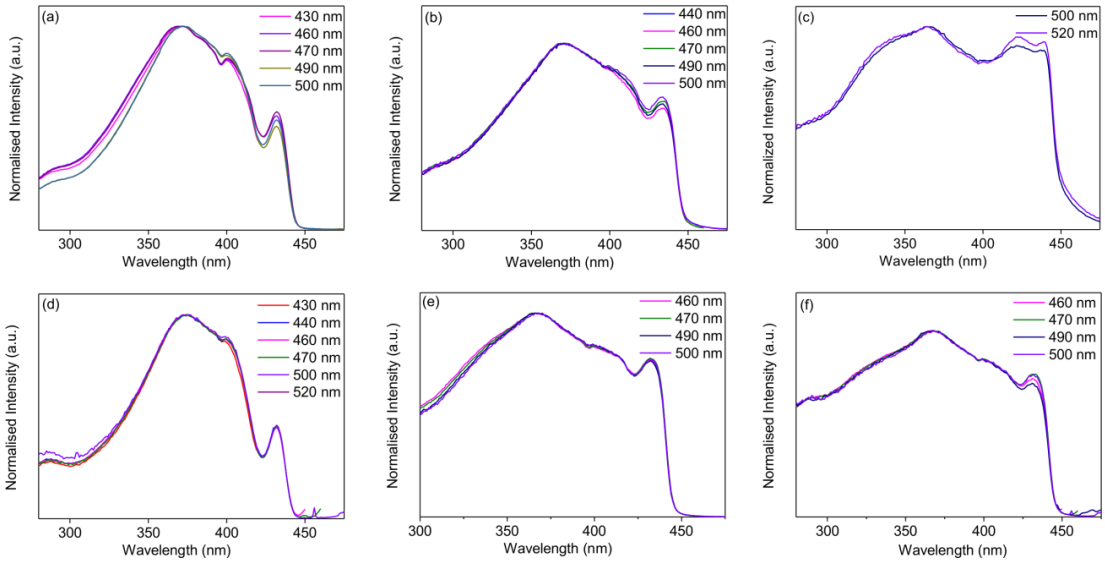

Figure A3.3. Optical features of PF-doped diureasils. Excitation spectra of (a) **DU-PF-0.01** (b) **DU-PF-0.05**, (c) **DU-PF-0.1**, (d) **TU-PF-0.01**, (e) **TU-PF-0.05** and (f) **TU-PF-0.1** measured at different emission wavelengths.

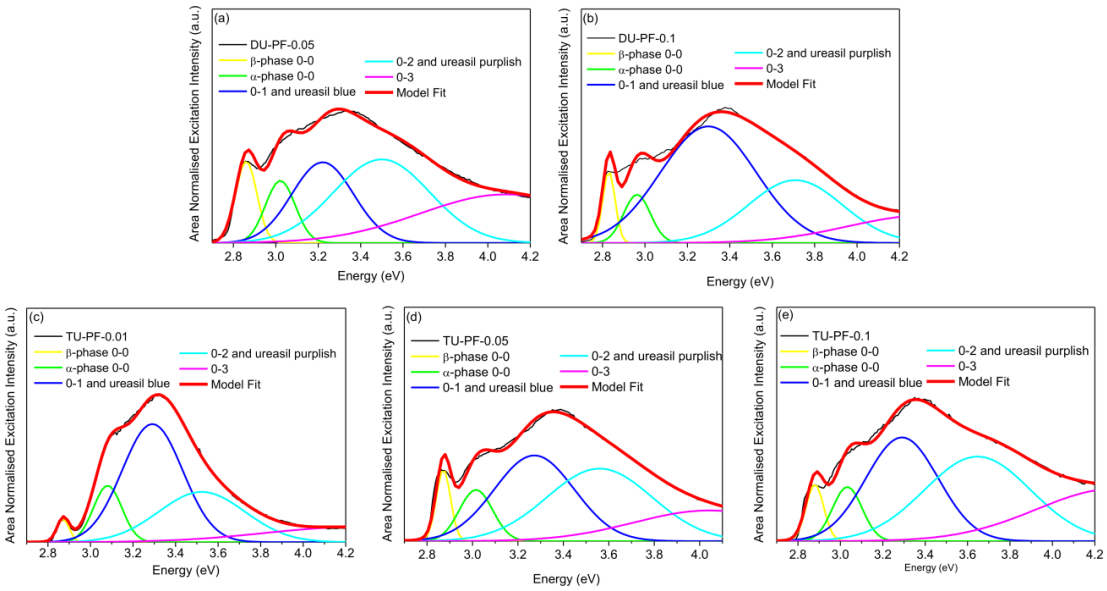

Figure A3.4. Area normalised excitation spectra (λ_{em} = 480 nm) of (a) **DU-PF-0.05**, (b) **DU-PF-0.1**, (c) **TU-PF-0.01**, (d) **TU-PF-0.05** and (d) **TU-PF-0.1** and corresponding Gaussian-fits of the spectral components 0-0, 0-1, 0-2, 0-3 and the ureasil blue and purplish components.

1.2 Chapter 4

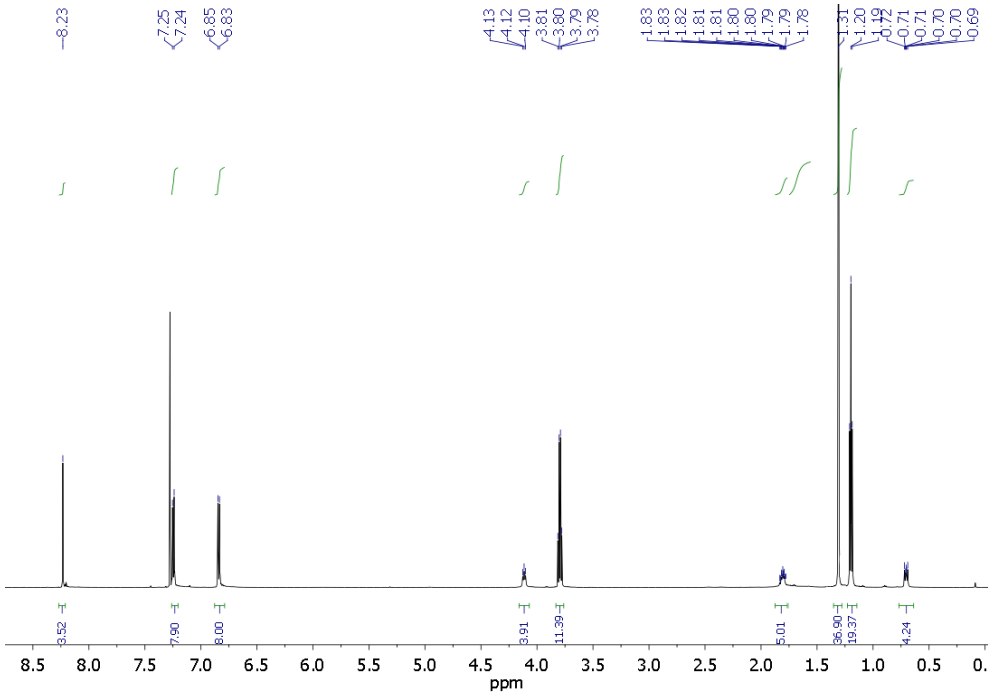

Figure A4.1. ^{1}H NMR spectrum of **PDI-Sil** in $CDCl_3$.

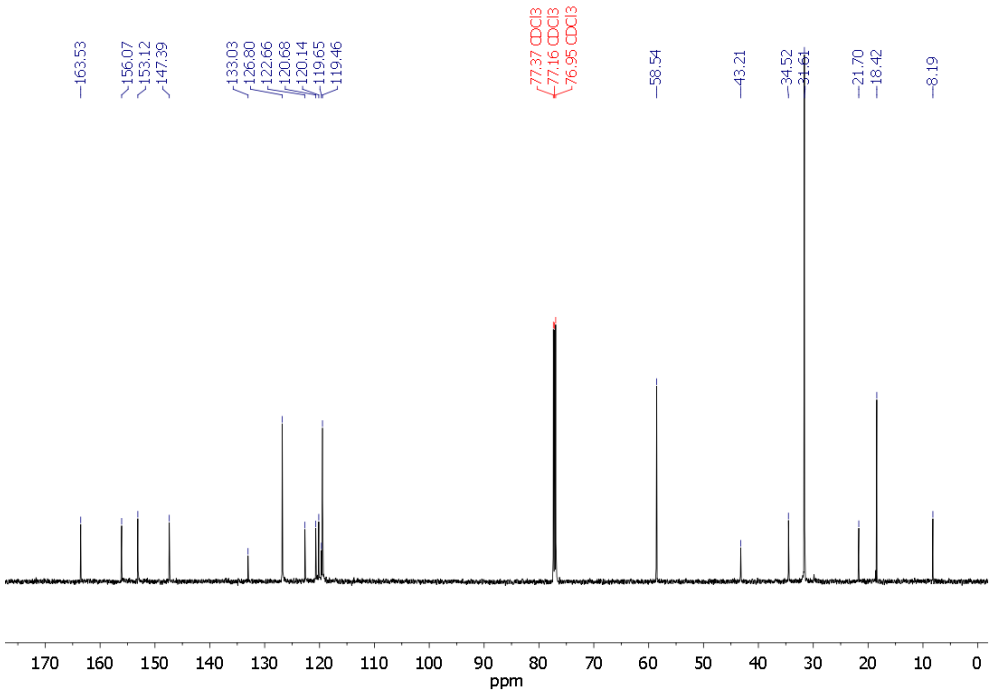

Figure A4.2. ^{13}C{^{1}H} NMR spectrum of **PDI-Sil** in $CDCl_3$.

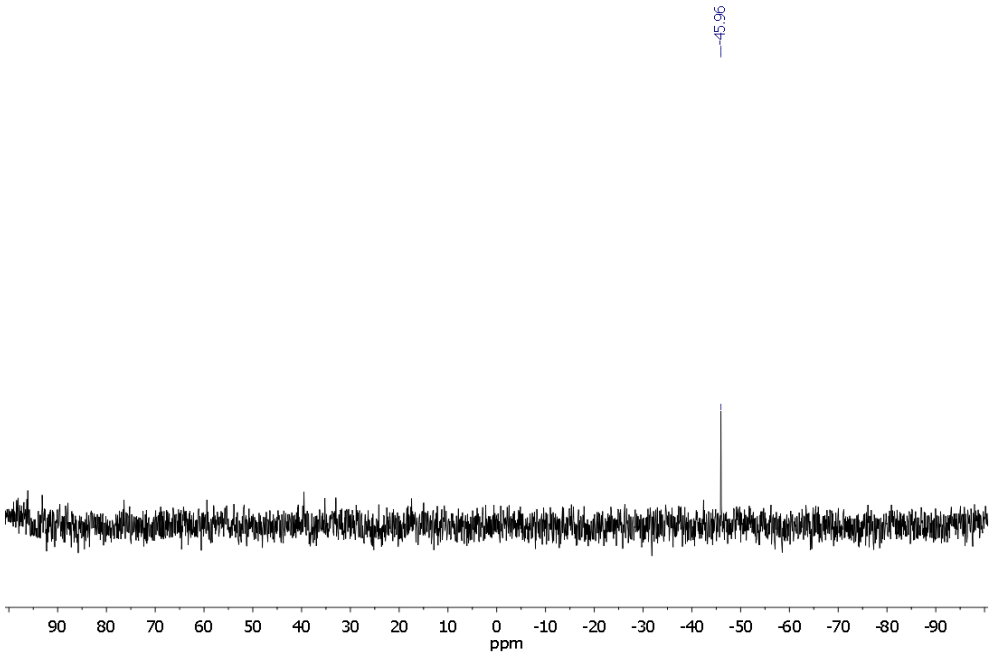

Figure A4.3. $^{29}Si\{^{1}H\}$ NMR spectrum of **PDI-Sil** in $CDCl_3$.

Synthetic Details for the Preparation of PDI-Sil-ureasils

As a representative example for the preparation of the hybrids, the synthesis of **t-U(403)** and **PDI-Sil-t-U(403)** is presented. Jeffamine T-403 (0.792 ml, 1.76 mmol) was mixed with THF (5 mL), and ICPTES (1.307 mL, 5.28 mmol) was added under stirring. This corresponds to 1:3 stoichiometric equivalents. The mixture was refluxed at 70 °C for 12 hours, allowed to cool to RT, before the addition under stirring of the gelation agents in the following order: of EtOH (0.614 mL), HCl (0.5 M, 0.060 mL) and water (0.142 mL) to initiate the sol formation. The molar ratio of ICPTES : EtOH : HCl : H_2O was 176 : 350 : 1 : 265. The resultant solution was cast in a polypropylene mould and covered with Parafilm M®. The sample was aged for 2 days at RT, after which the film was pierced to evaporate the THF from the sample for a further 24 hours. Finally, the sample was dried in an oven at 40 °C for 48 hours, yielding the resultant **t-U(403)** tri-ureasil as a free-standing, transparent monolith. **t-U(5000)** was prepared using the same procedure through substitution with the corresponding Jeffamine T-5000 (1.76 mmol) and addition of 5.28 mmol of ICPTES. Compared to the synthesis of **t-U(403)**, a larger THF volume (10 mL) was required to dilute the more viscous, higher M_W Jeffamine T-5000. For **d-U(600**) and **d-U(4000**), the ICPTES: Jeffamine were reacted in a 2:1 molare ratio (3.52:1.76 mmol of ICPTES: Jeffamine). A larger volume of THF (10 mL) was required to dissolve the more viscous D-4000. Moreover, the HCl concentration was doubled to accelerate the gelation (ICPTES : EtOH : HCl : H_2O ratio was 176 : 350 : 1 : 26588 : 175 : 1 : 132.5) and an ageing time of 5 days was required for this sample.

For PDI-Sil-ureasils, the synthesis was carried using the same procedure described for the undoped sample, by adding a fixed volume (100 μL) of stock solution of **PDI-Sil** (THF, 0.72 mmol dm^{-3}) under stirring prior to addition of the gelation agents. The mass of gelled precursors was chosen to obtain 2 g of dried monolith, with the volume of dye solution optimised to ensure a concentration of 0.005 $\%_{w/w}$ in the final sample.

G Factor for PDI-Sil in Solution

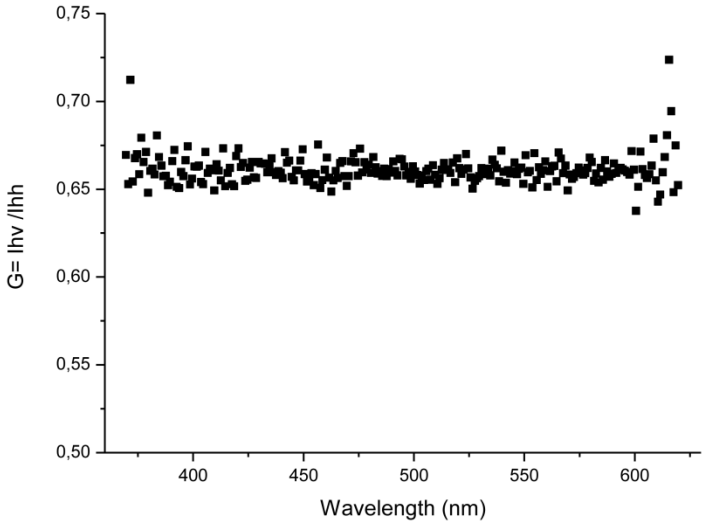

Figure A4.4. Calculated *G* values for a dilute solution of **PDI-Sil** in THF (λ_{em} = 630 nm).

1.3 Chapter 5

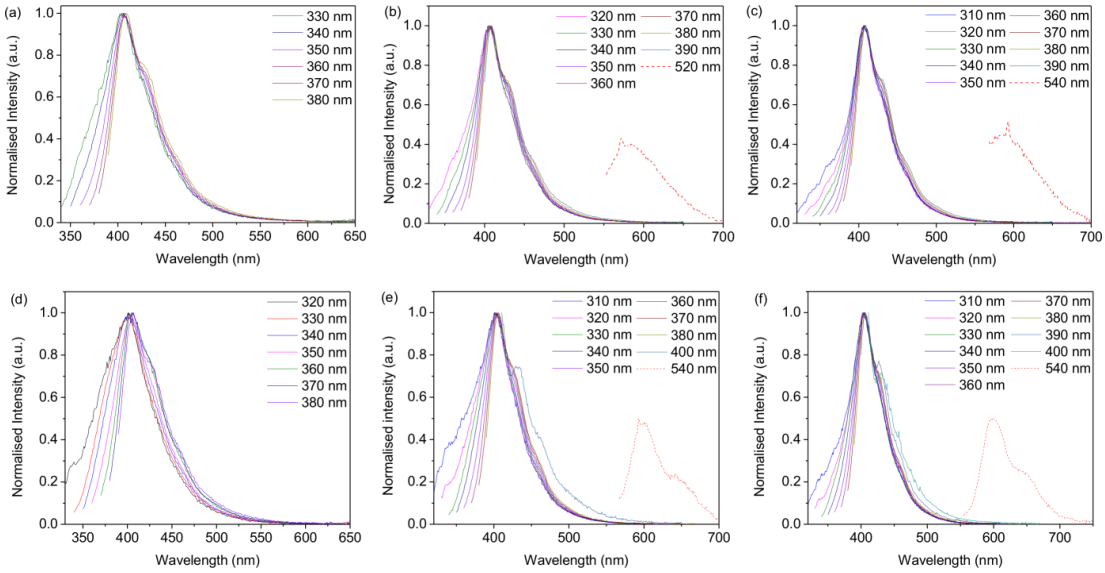

Figure A5.1. Emission spectra of (a) **DU-CPE-01**, (b) **DU-CPE-02**, (c) **DU-CPE-04**, (d) **TU-CPE-01**, (e) **TU-CPE-02** and (f) **TU-CPE-04** at different excitation wavelengths.

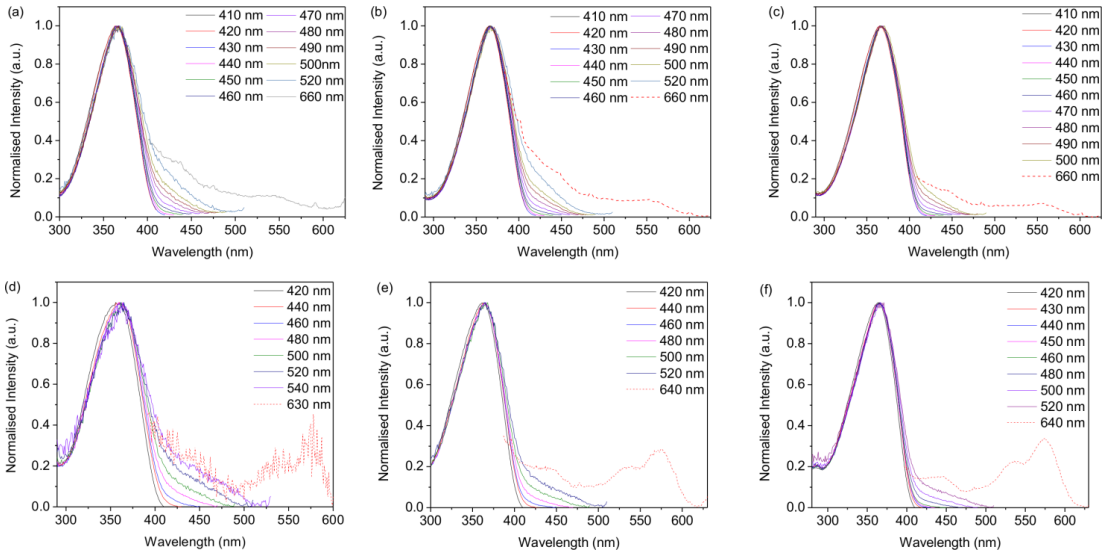

Figure A5.2. Excitation spectra of (a) **DU-CPE-01**, (b) **DU-CPE-02**, (c) **DU-CPE-04**, (d) **TU-CPE-01**, (e) **TU-CPE-02** and (f) **TU-CPE-04** at different emission wavelengths.

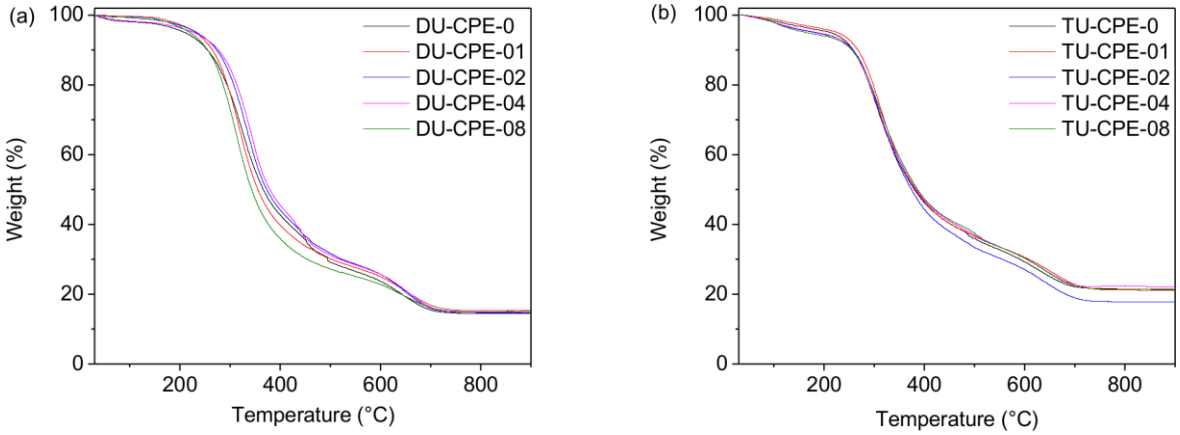

Figure A5.3.Thermal stability of the doped and undoped ureasil samples. Thermograms of (a) **DU-CPE-*x*** and (b) **TU-CPE-*x*** measured in an air atmosphere (heat rate = 10 °C min^{-1}).

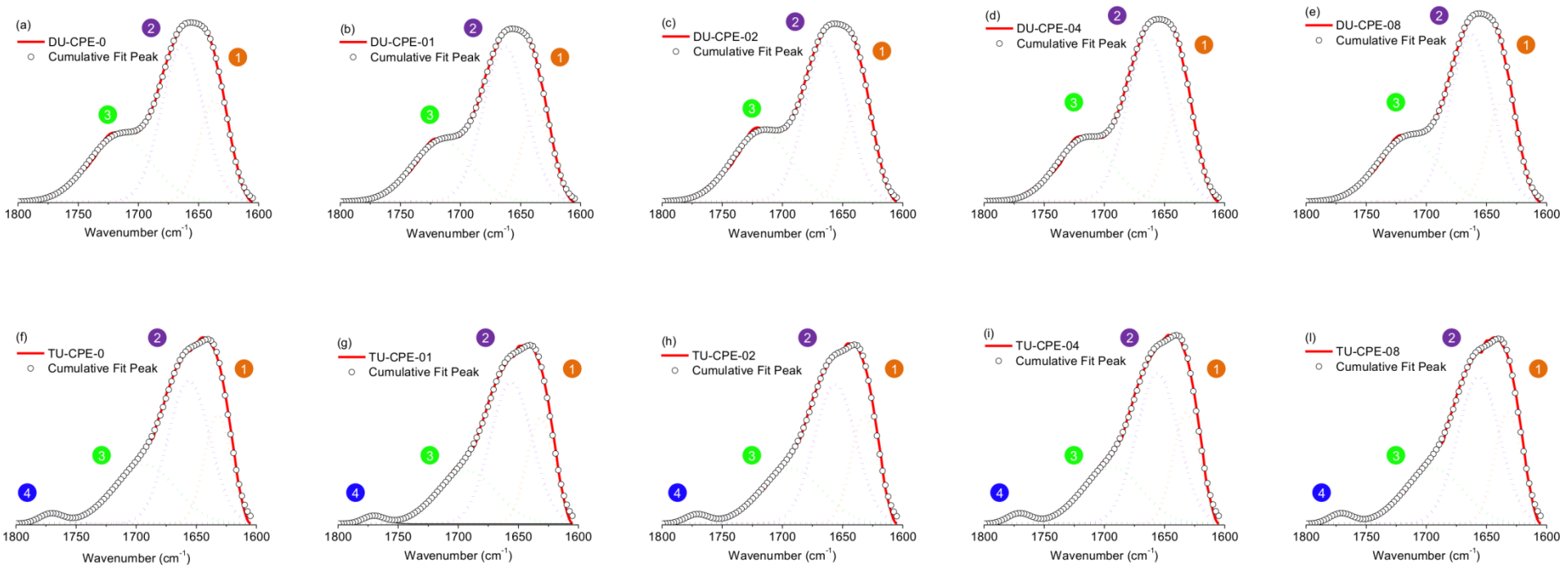

Figure A5.4. FTIR spectra and Gaussian curve-fits for the Amide I region of: (a) **DU-CPE-0**, (b) **DU-CPE-01**, (c) **DU-CPE-02**, (d) **DU-CPE-04**, (e) **DU-CPE-08**, (f) **TU-CPE-0**, (g) **TU-CPE-01**, (h) **TU-CPE-02**, (i) **TU-CPE-04** and (l) **TU-CPE-08**.

τ_1/ns	τ_2/ns	τ_3/ns	α_1	α_2	α_3	χ^2
0.65	1.61	7.72	0.76	0.23	0.01	1.01

τ_1/ns	τ_2/ns	τ_3/ns	τ_4/ns	α_1	α_2	α_3	α_4	χ^2
0.04	0.56	1.43	6.98	-0.18	0.94	0.05	0.01	0.99

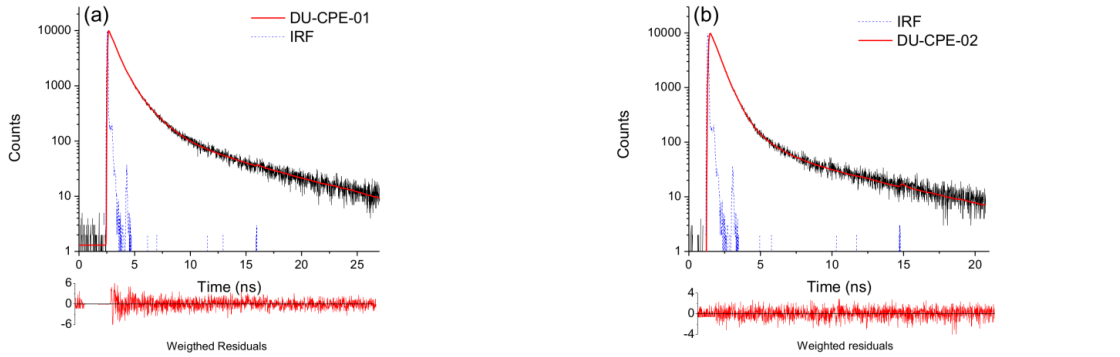

τ_1/ns	τ_2/ns	τ_3/ns	α_1	α_2	α_3	χ^2
0.02	0.60	4.11	-0.78	0.99	0.01	1.25

τ_1/ns	τ_2/ns	τ_3/ns	α_1	α_2	α_3	χ^2
0.02	0.62	3.62	-0.73	0.99	0.01	1.18

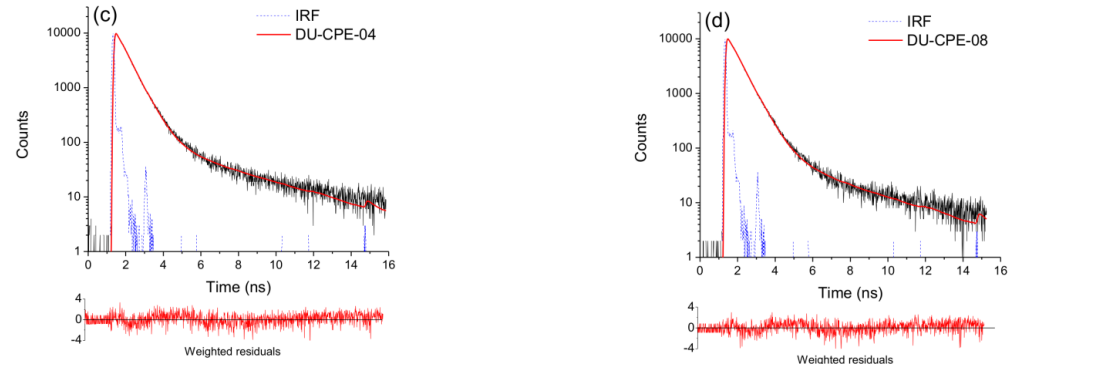

Figure A5.5. Fluorescence emission decay curves and corresponding fits for (a) **DU-CPE-01**, (b) **DU-CPE-02**, (c) **DU-CPE-04** and (d) **DU-CPE-08** upon excitation at 374 nm (λ_{em} = 500 nm). The fitting data, weighted residuals and IRF are also shown.

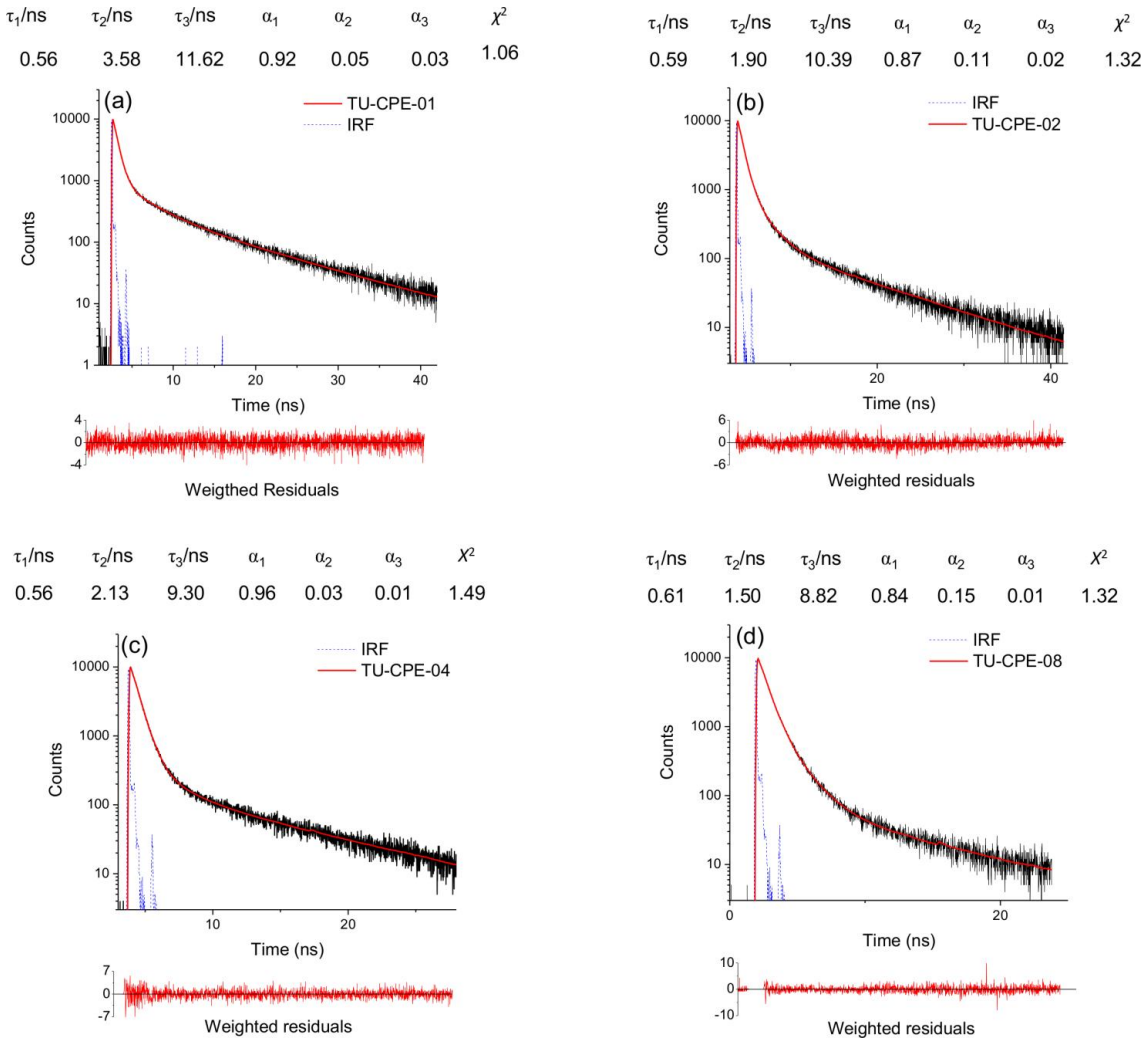

Figure A5.6. Fluorescence emission decay curves and corresponding fits for (a) **TU-CPE-0**, (b) **TU-CPE-02**, (c) **TU-CPE-04** and (d) **TU-CPE-08** upon excitation at 374 nm (λ_{em} = 500 nm). The fitting data, weighted residuals and IRF are also shown.

Table A5.1. Photoluminescence lifetimes (τ_i), pre-exponential coefficients (α_i), and chi squared (χ^2) values obtained from fitting of the emission decays (λ_{ex} = 370 nm) at λ_{em} = 420 and 500 nm for **DU-CPE-*x*** and **TU-CPE-*x*.**

λ_{em} = 420 nm

Sample	τ_1 (ns)	τ_2 (ns)	τ_3 (ns)	τ_4 (ns)	α_1	α_2	α_3	α_4	χ^2
CPE	0.026±0.001	0.553±0.002	1.072±0.020		-0.899±0.001	0.947±0.001	0.053±0.001		1.14
DU-CPE-0		0.47 ± 0.01	2.56 ± 0.04	10.08±0.12		0.75 ±0.02	0.20 ± 0.01	0.05 ± 0.01	1.55
DU-CPE-01		0.518 ± 0.003	1.166 ± 0.026	6.924±0.519		0.949±0.003	0.048±0.002	0.003±0.001	1.15
DU-CPE-02	0.029±0.005	0.538 ± 0.002	1.640 ± 0.037		-0.281±0.004	0.982±0.002	0.018±0.001		1.03
DU-CPE-04		0.537 ± 0.002	1.545 ± 0.068		0.990±0.002	0.010±0.001			1.32
DU-CPE-08		0.548 ± 0.002	1.224 ± 0.045		0.983±0.002	0.017±0.001			1.20
TU-CPE-0		0.522 ± 0.030	4.204 ± 0.052	12.740±0.089		0.474±0.005	0.378±0.003	0.148±0.001	1.43
TU-CPE-01		0.512 ± 0.004	1.396 ± 0.045	8.086±0.158		0.960±0.004	0.029±0.002	0.011±0.001	1.31
TU-CPE-02		0.513 ± 0.003	1.050 ± 0.029	8.103±0.025		0.943±0.003	0.052±0.002	0.005±0.001	1.12
TU-CPE-04		0.544 ± 0.003	5.396 ± 0.187			0.995±0.003	0.005±0.001		1.25
TU-CPE-08		0.550 ± 0.003	3.223 ± 0.141			0.996±0.003	0.004±0.001		1.31

λ_{em} = 500 nm

Sample	τ_1 (ns)	τ_2 (ns)	τ_3 (ns)	τ_4 (ns)	α_1	α_2	α_3	α_4	χ^2
CPE	0.034±0.003	0.582±0.002	1.364±0.028		-0.491±0.002	0.967±0.016	0.033±0.001		1.07
DU-CPE-0		0.39 ± 0.02	2.79 ± 0.05	10.90 ± 0.14		0.63 ± 0.03	0.29 ± 0.02	0.07 ± 0.02	1.66
DU-CPE-01		0.653 ± 0.008	1.611 ± 0.018	7.719 ± 0.145		0.759 ±0.04	0.230 ± 0.002	0.011 ±0.001	1.01
DU-CPE-02	0.041±0.003	0.556±0.004	1.431±0.025	6.980±0.191	-0.184±0.001	0.941±0.001	0.052±0.001	0.007±0.001	0.99
DU-CPE-04	0.022±0.003	0.597±0.004	4.106±0.116		-0.782±0.002	0.989±0.001	0.011±0.001		1.25
DU-CPE-08	0.024±0.003	0.618±0.004	3.624±0.112		-0.732±0.002	0.991±0.002	0.009±0.001		1.18
TU-CPE-0		0.792±0.030	4.845±0.052	14.213±0.102		0.425±0.005	0.431±0.003	0.144±0.001	1.24
TU-CPE-01		0.556±0.006	3.572±0.085	11.625±0.139		0.915±0.005	0.057±0.002	0.028±0.001	1.06
TU-CPE-02		0.593±0.006	1.904±0.037	10.390±0.167		0.873±0.004	0.112±0.002	0.015±0.001	1.32
TU-CPE-04		0.563±0.003	2.125±0.087	9.297±0.204		0.957±0.002	0.030±0.001	0.013±0.001	1.49
TU-CPE-08		0.605±0.007	1.504±0.030	8.819±0.240		0.840±0.004	0.153±0.003	0.007±0.001	1.32

1.4 Chapter 6

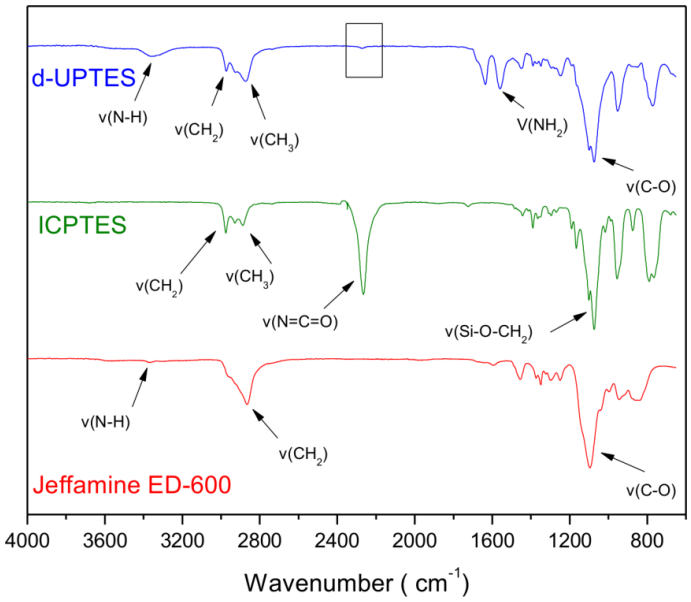

Figure A6.1. Confirmation of the successful reaction between Jeffamine ED-600 and ICPTES. FTIR spectra of: d-UPTES (blue), ICPTES (green) and Jeffamine ED-600 (red). The main contribution to the spectra are indicated and assigned. The region were the signal corresponding to the N=C=O stretching disappeared, is marked in the d-UPTES spectrum.

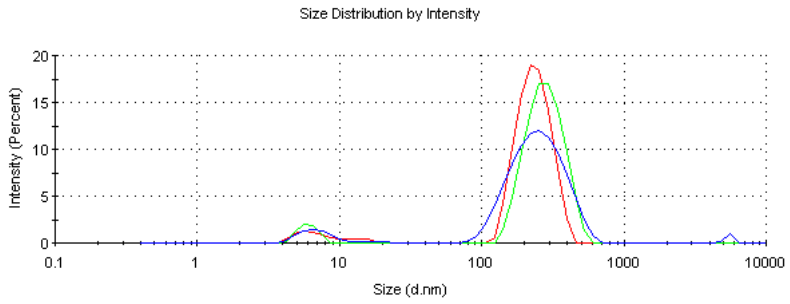

Figure A6.2. Investigation of the effect of the TEOS concentration on di-ureasil NPs prepared with Method B. Intensity *vs* the size (nm) of samples prepared using 20%$_{v/v}$ TEOS after 4 days of ageing. The peak centred at ~5 nm represent a population of pure TEOS NPs while those centred at ~200 nm represent the di-ureasil core-shell NPs. A smaller contribution probably due to dust is also observed at ~6000 nm.

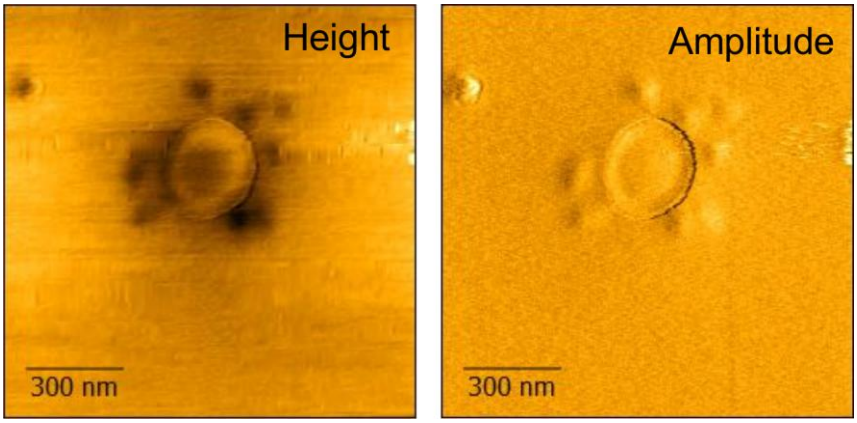

Figure A6.3. Tapping-mode AFM images of a ureasil core-shell NP prepared using Method C. The amplitude image shows how the NPs core seem to bend upon contact with the AFM tip while the external silica shell remained intact.